Centrifugal Casting and Fast Curing of Polydimethylsiloxane (PDMS) for the Manufacture of Micro and Nano Featured Components

by

Aaron D. Mazzeo

S.M., Mechanical Engineering (2005)
Massachusetts Institute of Technology

S.B., Mechanical Engineering (2003)
Massachusetts Institute of Technology

Submitted to the Mechanical Engineering Department
in partial fulfillment of the requirements for the degree of

Doctorate of Philosophy

at the

MASSACHUSETTS INSTITUTE OF TECHNOLOGY

June 2009

Author .....
Mechanical Engineering Department
May 2009

Certified by .....
David E. Hardt
Ralph E. and Eloise F. Cross Professor of Mechanical Engineering
Thesis Supervisor

Accepted by .....
David E. Hardt
Ralph E. and Eloise F. Cross Professor of Mechanical Engineering

Centrifugal Casting and Fast Curing of Polydimethylsiloxane (PDMS) for the Manufacture of Micro and Nano Featured Components

by

Aaron D. Mazzeo

Submitted to the Mechanical Engineering Department
on May 2009, in partial fulfillment of the
requirements for the degree of
Doctorate of Philosophy

Abstract

The thermosetting resin polydimethylsiloxane (PDMS) is commonly used to prototype micro and nano featured components. In the field of microfluidics, PDMS-based devices have been used for cell sorting, cell culturing, microbioreactors, DNA sequencing, and immunoassays. In energy-related applications, PDMS has been used in fuel cell assemblies and as a material for transferring carbon nanotubes in the construction of solar cells. In addition, PDMS is the fundamental material of soft lithography and microcontact printing.

Given the widespread use of PDMS in micro/nano technology, biology, and chemistry, the motivation of this thesis is to outline a viable manufacturing process for thermosetting resins such as PDMS that could be scaled-up for the large-scale production of micro/nano featured components. With respect to rate of PDMS device production, the two time-limiting steps in the typical prototyping process are degassing (bubble removal) and curing. To improve the degassing step, a novel centrifugal casting method is introduced, which permits simultaneous patterning of multiple surfaces and precise thickness control of a PDMS part. To improve the curing step, a custom-designed thermal management system heats and cools the PDMS.

In centrifugal casting, the spinning time required to produce a bubble-free part is dependent on a distribution of critical bubble sizes, the centrifuge's spin speed profile, geometry, and fluid properties. A physical model predicting the spin time for bubble removal is verified by high speed video imaging and the production of bubble-free parts. In addition to producing bubble-free parts, the PDMS centrifugal casting technique is utilized to produce micro and nano featured components.

Thesis Supervisor: David E. Hardt
Title: Ralph E. and Eloise F. Cross Professor of Mechanical Engineering

Acknowledgements

I would like to thank Professor David Hardt for advising me throughout this work. He has been kind, considerate, understanding, wise, smart, and helpful. He has been incredibly supportive in my quest to research unconventional polymer processing techniques. He has also been incredibly patient in picking out themes and ideas from my many streams of consciousness.

My thesis committee of Professors David Hardt, Jung-Hoon Chun, Todd Thorsen, Joel Voldman, and Sangeeta Bhatia has also been a tremendous help. They have been great at letting me explore various ideas but have also helped me focus and search for answers to questions I might have glossed over. Their extra prodding caused me to explore diffusion mechanisms and to develop a better understanding of the underlying physics concerning bubble growth and dissolution. Dr. Brian Anthony, director of the Singapore-MIT Alliance Manufacturing, Science, and Technology program, has been a tremendous help with his insights in image processing and high speed videography. Dr. Jim Bales of the MIT Edgerton Center also helped me take my first high speed images and also made it possible for me to participate in the Edgerton Center's summer course on high speed imaging. Professor Gareth McKinley was very gracious in meeting with me to discuss the empirical behavior of bubble growth and dissolution. Professor Kamal Youcef-Toumi, an active participant in the Singapore-MIT Alliance, has been very supportive and kind in listening to my work during a number of research meetings. Professor David Roylance took the time to listen to some of my thoughts about centrifugal casting and provided insights as well. With respect to helping me figure out my post-PhD life, I want to thank Professor Thomas Eagar. He has been extremely generous with his time and resources in helping me have a wonderful MIT experience. I appreciate Professor David Trumper for his support in letting me continue my graduate studies toward a PhD. I learned a tremendous amount from him as a Masters student in the Precision Motion Control Lab, and he helped me bridge the gap between my undergraduate and graduate studies.

I would like to thank AJ Schrauth for helping me get on track with a thesis topic. I will never forget running around the office cubicle frustrated with bubbles entrapped in one of my PDMS parts and then hearing AJ suggest spinning the PDMS in a centrifuge. I do not know if I would have ever thought about centrifugal casting without his comment.

Even though he is not in the Polymer Microfabrication Lab, his concern for my research was evident, and I am very grateful for his insights. In addition to AJ, I have had the opportunity to work with other great students in the Laboratory for Manufacturing and Productivity, the Mechanical Engineering Department, and MIT at large. Matt Dirckx helped me out tremendously when I started in the lab, and we have had the privilege of working on papers together. Eehern Wong has been a great sounding board, and I think his research will illuminate the limits associated with high temperature curing of PDMS or other liquid resins. Hayden Taylor has also been a tremendous help in various discussions and in producing mold materials in MIT's Microsystems Technology Laboratory. I would also like to thank Melinda Hale, Vikas Srivastava, David Lee Henann, JP Urbanski, Sumeet Kumar, Nancy Diaz, Dan Lorenc, Stuart Rossen, Xin (Cindy) Wang, Mike Kozlowski, and other students I have gotten to know and work with while at MIT.

I would like to thank the members of the MIT staff that have been extremely helpful in my research. The LMP/MIT Machine Shop has been a tremendous asset. Specifically, Gerry Wentworth, Pat McAtamney, Dave Dow, and Fred Cote helped me machine, build, and test various components. Fred Cote suggested using tie rods, nuts, and plates to build the heating and curing system. In addition to the machine shop, I want to thank Erica McDaniel Nofi and Rachel Russell for helping me purchase, acquire, and manage many of the administrative details associated with this research. David Rodriguera and Richard Brickman have also been great supports in keeping the administrative business details straight.

From an industrial perspective, I would like to thank the wonderful people at Fusion Optix, who helped prepare me for my return to MIT for the PhD. Dr Zane Coleman, Steve Akey, Dr. Chris Scott, and Dr. Terry Yeo all served as mentors for me and shared their polymer processing knowledge and experience with me. While at Fusion Optix, I also had the wonderful privilege of working with Mark Chu and Kate Awad. Their patience and understanding with me helped me enjoy my time while there, embrace polymer processing, and ease back into MIT. Don Leone from Ashby Cross, Bill Kyle (Thinky mixer representative) from Janus Tech Sales, Ed Stein from Brandywine Associates, David Corneau from Albright Technologies, and David Midgley from Welch Fluorocarbon were also very helpful over the phone or in personal meetings. Bill Kyle let us test one of the Thinky mixers, and Ed Stein donated many of the static mixers used in this research.

I would like to thank the Singapore-MIT Alliance (SMA) Flagship Research Program

(FRP) for funding me and this research for almost three years. I enjoyed visiting Singapore and being able to collaborate with faculty at Nanyang Technological University, including Professors Tor Shu Beng and Lam Yee Cheong. In addition to the faculty, I had the opportunity to work and visit with students/postdocs Loke Yew Weng (Gabriel), Yeo Lip Pin, Dr. Gang Fu, and others. Overall, the SMA FRP has been a wonderful experience and has allowed me to learn from the academic and manufacturing worldwide communities.

I would like to thank my wife, Jonina, for being a great support, listening to many one-sided dinner conversations about PDMS, letting me have fun in lab, letting me run simulations on her laptop, and refraining from complaint in spite of a hectic graduate student lifestyle. Getting married a couple of years ago has turned out to be a very wonderful and fortunate decision. I love her and am anxiously awaiting the arrival of our first child. Indeed, it has been a rather productive couple of years. My parents, George and Sharon, along with my siblings, Brian and Celeste, and Brian's wife Maren have been very supportive. I look forward to spending more time with them in the future.

Contents

List of Figures

Chapter 1

Introduction

The goal of this research is to outline a viable manufacturing process for thermosetting resins that could be scaled-up for the large-scale production of micro/nano featured components. The outlined manufacturing process applies centrifugal molding technology to the replication of micro/nano featured components using the thermosetting resin polydimethylsiloxane (PDMS). Centrifugal casting by itself is used in a variety of manufacturing settings. Replicating micro/nano featured components using PDMS is also a common practice in academic or research environments. However, no previous work has described how these two technologies might be adapted and merged together for the manufacture and production of useful micro/nano featured devices. This thesis aims to address the synergistic combination of centrifugal casting and micro/nano feature replication.

1.1 Motivation

This thesis is part of a collaborative research program to better understand and improve manufacturing processes for microfluidic device production. At the commencement of this project, the materials of focus were generally thermoplastics such as polycarbonate (PC), acrylic (PMMA), cyclic olefin copolymers (COC), etc. [54, 55, 53, 35, 52, 84, 85, 86, 34, 36]. Later, there was some exploratory work done concerning PDMS, similar to that done by Hum [59], and it became evident that there was room to improve manufacturing processes for "the material most commonly used in academic studies of microfluidics" [114]. This is not to say that thermoplastics are not useful; they may ultimately be the material class of choice. Caliper Technologies (now Caliper Life Sciences) [67] and Agilent Technologies [94] have both

expressed interest in thermoplastic materials for microfluidic chip manufacturing. However, PDMS is still the most commonly used material in lab settings and possesses some uniquely valuable characteristics (e.g. compliance, transparency, some biocompatibility, etc.). PDMS is also easy to mold in device prototyping, but there is a technological gap between building a few lab devices out of PDMS and building millions for consumer use.

When it becomes time to mass-produce millions of microfluidic devices, "there will probably be several such technologies [for microfluidic device manufacturing], but in the early stages the definition of a single set of materials and processes to convert laboratory demonstrations into working commercial devices is an important step [114]." This thesis aims to outline a viable manufacturing process for thermosetting resins that could be scaled-up for the large-scale production of micro/nano featured components.

1.2 Market Background

According to Frost and Sullivan's marketing research, the world annual revenue for microfluidics in 2002 was estimated at approximately $128 million [1]. In 2005, the US microfluidic industry gained an estimated $84.3 million in revenues and will grow to an estimated annual revenue of $200 million in 2012 [3]. While the microfluidic industry may appear to have some impressive gains, these estimated revenue figures are an order of magnitude less than what some of their potential customers, large pharmaceutical companies, individually spend on research and development (e.g. Bristol-Myers Squibb's $3.6 billion [4], Eli Lilly's $3.8 billion [10], Merck's $4.8 billion [12], and Pfizer's $7.9 billion [13] in 2008). There are multiple reasons for the slow emergence of the microfluidics device market, including the paradigm shift associated with the way biochemistry experiments are executed, capital expenses necessary for new microfluidic equipment and sensors, and a lack of confidence in the results obtained. However, microfluidic device revenues are predicted to continue to grow, and this work aims to help that growth by improving the robustness and quality of future devices through establishing guidelines for innovative manufacturing techniques.

A brief examination of the health care industry illustrates the potential importance of the microfluidic device market. The United States and many other nations are currently battling high health care costs. In President Barack Obama's inauguration speech, he stated, "We will restore science to its rightful place and wield technology's wonders to raise health

care's quality and lower its costs [90]." From one perspective, President Obama sounds like a manufacturing engineer trying to lower cost and improve quality. That said, his proposed health care reform may add approximately $104 billion to federal spending in 2010 [74]. "Advances in technology and medical research are making it possible to envision an entirely new health care system that provides more individualized care without necessarily increasing costs [93]." In this newly envisioned health care system, microfluidic devices may play a large role in revolutionizing health care diagnostics. Microfluidic devices were originally targeted to biomedical applications "requiring small amounts of sample, routine operation by untrained personnel, and low cost [114]." Because of the current emphasis on reducing health care costs, health care providers may finally start turning to diagnostic devices based on microfluidic technology. Microfluidic device manufacturing technologies will need to mature to meet the demand that this change in health care diagnostics may create.

1.3 PDMS microfluidic device applications

Researchers have used microfluidic devices in laboratory settings to perform a variety of complex biochemical processes and harvest energy. Some of these biochemical processes include polymerase chain reaction (PCR), DNA sequencing, and flow cytometry. In PCR, DNA molecules are successfully heated and cooled to induce DNA amplification [101]. Kartalov and Quake have demonstrated that small DNA strands can be sequenced using a microfluidic device [63]. In flow cytometry, optical measurements are used to assess particles in a flow; this process can be used for the detection of bioterrorism agents, water-born pathogens, and human disease [109]. Microfluidic device technology has also been adapted to execute cell sorting [43], perform a critical role in microbioreactors [77], culture stem cells [69, 112], and run immunoassays [40]. In addition to biotechnology applications, microfluidic technology has been applied to energy harvesting in fuel cells [99].

All the experiments/procedures in the scientific publications cited above rely on some form of a micro replication process to build the necessary micro channel structures. In addition, the material used for these micro channels is the thermosetting resin PDMS. PDMS is a silicone elastomer, which cures, or cross-links, when its base and curing agent are mixed together. It has been known for years that PDMS is a well-suited material for

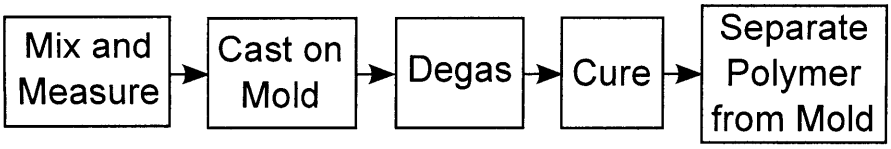

Figure 1-1: Standard prototyping process for PDMS microfluidic devices.

microfluidic device prototyping [88]. PDMS is transparent to light up to 230 nm, is non-toxic to cells, and is easy to bond to other surfaces [102]. It is possible to replicate vertical features less than 2 nm in PDMS [45], and lateral features on the order of 30 nm [118]. In addition, PDMS is being utilized in non-microfluidic type applications such as microcontact printing [119], soft lithography [120], molding scaffolds in tissue engineering [112, 113], and carbon nanotube transfer in solar cell construction [96]. Given the widespread use of PDMS in micro and nano molding at the prototyping level, there may soon be a need for large-scale manufacturing practices of PDMS-based micro and nano featured components.

1.4 Typical PDMS processing

PDMS or silicone manufacturers include Dow Corning, Wacker, Momentive Performance Materials (formerly GE Silicones), Bluestar Silicones, NuSil, Shin-Etsu Silicones, Factor 2, Smooth-On, Silicone Inc, and Applied Silicone Corporation [11]. The most commonly used grade of PDMS or silicone in microfluidic device prototyping is Dow Corning's Sylgard 184. Silicone-based parts (not just microfluidic devices) with micro or nano features in research environments are typically prototyped using the process depicted in Figure 1-1. First, the PDMS base and curing agent are mixed together, which is often done manually. Next, the mixed material is poured onto a mold and placed in a vacuum chamber to remove bubbles introduced during the mixing or pouring steps. The mold and PDMS are then oven cured. After the PDMS has cured, it is typically peeled off the mold by hand.

With respect to mixing, measuring, and dispensing PDMS, most authors in micro/nano device prototyping literature do not detail their methods. Besides stating the ratio of base to curing agent (which can range from 4:1 to 20:1 [20, 82]), the PDMS solution is simply described as "thoroughly mixed" [111, 61]. This is not a criticism of authors in the field, but merely an emphasis on the fact that controlled mixing is not seen as an important step or factor in prototyping small volumes of microfluidic parts; indeed, in producing small

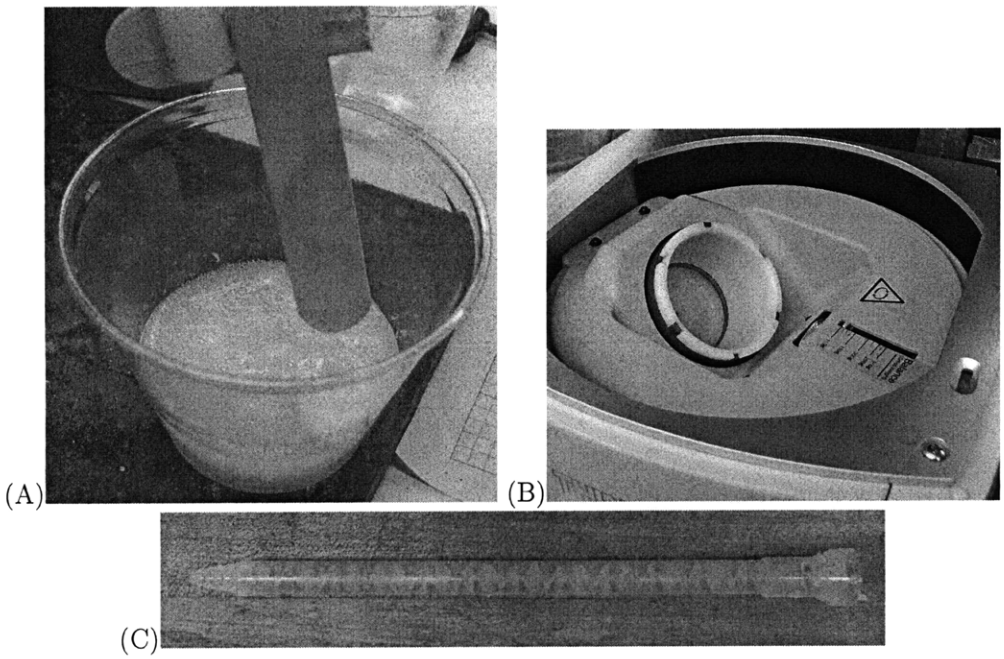

Figure 1-2: (A) PDMS being mixed and stirred using a Popsicle stick mounted to an electric mixer. (B) Thinky mixer with the top cover open showing the cup holder for mixing/degassing a solution. (C) MCX 08-24 static mixer used with the PDMS Sylgard 184 250 ml cartridges from Dow Corning.

quantities of PDMS parts in our lab, a variety of methods have been used, including stirring with a Popsicle stick, running the material through a static mixer nozzle, and using a centrifugal mixer. Once the PDMS has been mixed, it is dispensed on a mold. Often, the PDMS is simply poured onto the mold to make parts a few millimeters thick. If a thin PDMS part ($\sim 25\,\mu$m) is desired, the PDMS can be poured onto a spinning surface (spin coating) [82].

Degassing the PDMS in a vacuum chamber before the curing step is generally mentioned in the PDMS prototyping literature, but authors do not usually state how long or at what vacuum pressure this step is performed. Table 1.1 gives some of the degassing parameters found in the PDMS microfluidic device prototyping literature. As shown in Table 1.1, there appears to be no agreement on the appropriate degassing parameters, which probably reflects the fact that researchers are generally just concerned with making a few parts and keep using the parameters that work for them without searching for optimal values. With small volumes of parts, it is not necessary to measure vacuum pressure or time for degassing. It is apparent whether bubbles are present in the PDMS part or not. One can visually see

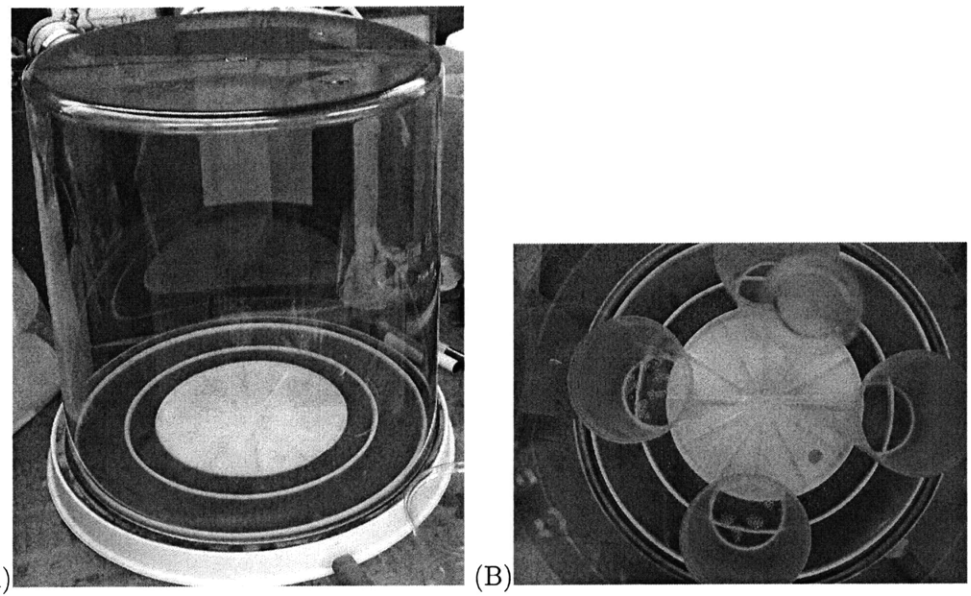

Figure 1-3: (A) Nalgene polyetherimide (PEI) vacuum chamber used for degassing materials. (B) Some cups with PDMS and air bubbles being degassed in the vacuum chamber.

bubbles in a PDMS part during the degassing step in a vacuum chamber and can cycle the vacuum pressure up and down to allow bubbles to grow, coalesce, and burst until all or most of the bubbles have been removed. From a manufacturing perspective, however, there is a need to develop a uniform method for degassing PDMS or use an alternative method to remove unwanted air bubbles.

After the PDMS is cast on a mold and degassed, the PDMS cures at room temperature or is heated to speed up the curing process. For Sylgard 184, Dow Corning suggests allowing the silicone to cure for approximately 48 hours at room temperature, 45 minutes at 100 °C, 25 minutes at 125 °C, or 10 minutes at 150 °C [2]. In the PDMS prototyping literature, researchers have specified a variety of curing temperatures and times as shown in Table 1.2.

In some cases, the PDMS is set to cure overnight out of convenience [42]. In another case, the PDMS was cured in 10 minutes as suggested by Dow Corning [2, 92]. Usually, no reasons are given for the specified curing times or temperature. However, it is known that curing temperature affects the amount of shrinkage the PDMS parts will experience [78]. Researchers likely choose a temperature profile for curing based on their time frame for needing the part and past experience in curing devices. For example, if there is no rush and only a few parts are needed, an overnight or multiple night cure is a simple way to cure a PDMS part. If multiple parts are needed on a regular basis, the lab may

Table 1.1: Degassing parameters for typical PDMS prototype processing.

Grade	Vacuum Pressure (Torr)	Time (min.)	Reference
Sylgard 184 (Dow Corning)	~ 15	15	[70]
GE RTV 615	???	15	[24]
Sylgard 184 (Dow Corning)	$\sim 20 - 30$	Until intermittent popping	[42]
Sylgard 184 (Dow Corning)	???	20	[81]
Silastic J RTV (Dow Corning)	0.005	30	[44]
Sylgard 184	???	35-50	[108]
Silastic J RTV (Dow Corning)	0.03	60	[123]
Sylgard 184 (Dow Corning)	0.02-0.05	60	[60]

Table 1.2: Curing parameters for PDMS prototyping

Grade	Temperature (°C)	Time	Reference
Sylgard 184	150	10 minutes	[92]
Not Specified	90	15 minutes	[20]
Sylgard 184	150	30 minutes	[101]
Sylgard 184	100	1 hour	[78]
Sylgard 184	65	1 – 2 hours	[75]
Sylgard 184	65	2 hours	[69, 113]
Sylgard 184	85	2 hours	[70]
Sylgard 184	85	3 hours	[78]
Sylgard 184	100	3 hours	[60]
Sylgard 184	60	4 hours	[111, 25]
Sylgard 184	65	4 hours	[78]
Not Specified	80	8 hours	[58]
Silastic J RTV (Dow Corning)	65	16 hours	[123]
Sylgard 184	Room Temp.	Overnight	[75, 95]
Sylgard 184	65	Overnight	[42]

have a standard curing temperature protocol with a known amount of shrinkage. In this case, the lab may purposely oversize the molds by a known amount to compensate for the anticipated shrinkage. In a sense, temperature curing profiles have evolved to meet the needs of individual groups without a complete understanding of the trade offs between time, temperature, and shrinkage.

In preliminary investigations, the effect of processing temperatures on the dimensional variation of PDMS has been explored. Micro channel depths and widths (see Appendix B), along with relative distances between fiducial marks on the parts, have been characterized [87, 115]. This thesis does not rigorously analyze the effects of varied temperature profiles on the dimensional stability of cured PDMS products. However, Eehern Wong's thesis work should provide some additional insights to further the understanding of the curing process and its application to large-scale manufacturing of PDMS micro and nano featured components [115].

1.5 Centrifugal casting and fast curing method

One of the goals of this research is to answer the key manufacturing questions that arise in attempting to scale-up micro device production to large part volumes. Another goal is to provide an innovative solution to enable more efficient part production from PDMS or other polymer-based materials. Figure 1-4 outlines the proposed manufacturing process studied in this thesis, which is based on centrifugal casting. This process is capable of producing hundreds of quality, microfluidic parts in a cost effective, flexible, and fast manner.

1.5.1 Mixing and dispensing

In large scale manufacturing of PDMS, the base and curing agent might start in tanks under vacuum. In the system designed for this thesis, the PDMS starts in a Dow Corning 250 ml cartridge with two separate cylinders. One cylinder is filled with the polymer base and the other is filled with the curing agent. The cartridge with its two cylinders is placed in a dispensing gun, which applies pressure and displaces a piston on the back end of the cylinders. The base and curing agent are dispensed in a 10:1 ratio by volume or mass (since the densities are closely matched).

The base and curing agent exit the cartridge and are then brought into a static mixing

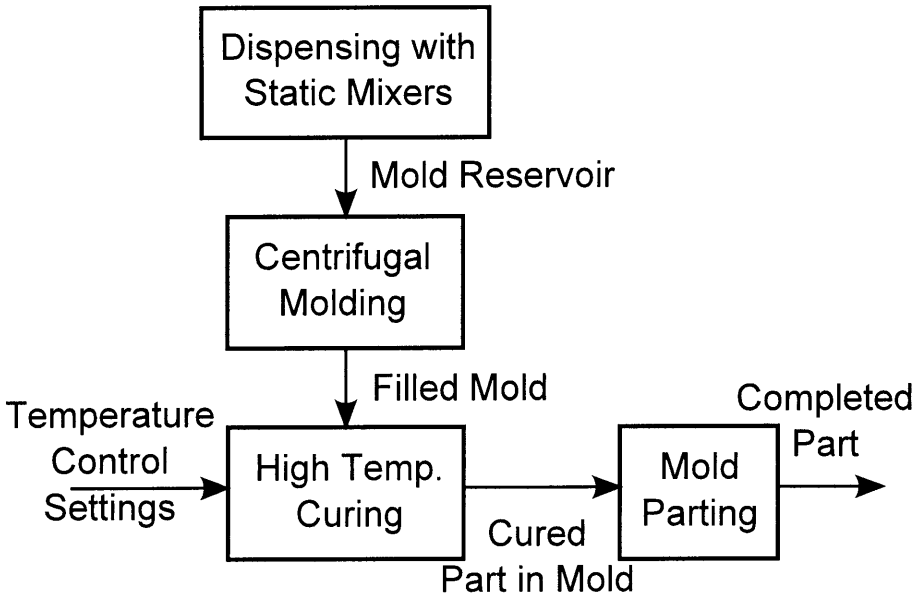

Figure 1-4: Centrifugal casting and fast curing method outlined for the production of micro/nano featured components.

nozzle (see Figure 1-2 C), which splits and recombines laminar flows of the two reagents. By using static mixers, consistent mixing is achieved from part to part, and minimal quantities of bubbles/air are introduced into the polymer because the fluid flow through the mixing nozzle is laminar. The material is then dispensed into a mold with a reservoir section.

1.5.2 Centrifugal casting

Once the polymer is sitting in the reservoir section of the mold as shown in Figure 1-5, the mold is spun about an axis of rotation and the PDMS is forced to the outer edges of the mold, away from the center axis of rotation. While the PDMS is forced to the outer edges of the mold, the PDMS sloshes around and traps air bubbles. Buoyant forces acting against centrifugal acceleration then drive these entrapped bubbles toward the axis of rotation. In addition, the PDMS becomes pressurized during spinning. This pressure compresses bubbles and can promote bubble dissolution. After the polymer is spun fast enough and long enough, the centrifuge is brought to rest. The resulting solution is bubble-free.

Centrifugal casting techniques have been used with a variety of materials including metals, ceramics, thermoplastics, and thermosets. With these various types of materials, the following types of products have been produced by some sort of centrifugal casting: steel

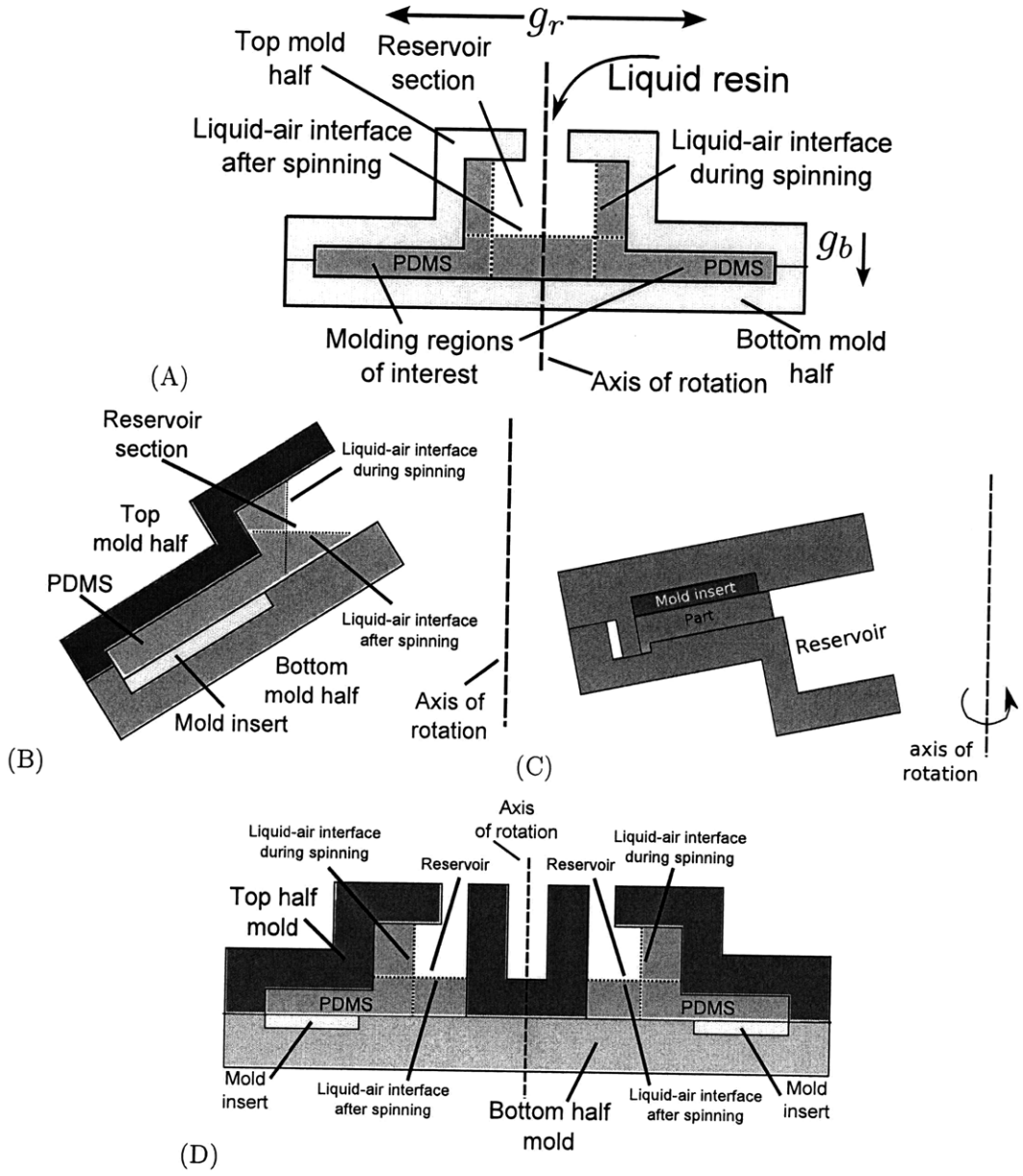

Figure 1-5: (A) Mold cavity for centrifugal casting being spun about an axis of rotation. (B) Centrifugal mold design tilted at an angle with an open end. (C) Another mold design tilted at an angle with an open end. (D) Centrifugal mold design for producing two separate parts.

tubes, optical telecommunication fibers, polyester and polyvinyl pipes, functional gradient metal-ceramic materials, porous ceramic supports for membrane applications, gears, rubber tires, and hollow rubber dolls [22, 106, 76, 27]. In addition to centrifugally molding silicone as demonstrated in this thesis, rubbery, polyurethane materials have also been cast using centrifugal casting techniques [48, 100]. Centrifugal casting can even be used to mold metals with a rubber mold [98].

Centrifugal casting has also been known as a method for removing bubbles from polymer solutions. In some cases, the bubble removal has been described by buoyant transport of the bubbles toward the center axis of rotation [106, 48, 100]. At high enough spin speeds with a polymer with low enough viscosity, buoyant forces aid in removing bubbles. In other cases, the bubble removal is described primarily by diffusion [100, 121, 105, 72, 33, 46]. These are cases in which rotational speeds are not high enough to generate enough gravitational/buoyant forces to overcome the high viscosity of a polymer and significantly move the bubble toward the center of the part. In diffusion-based bubble removal, there is an air concentration gradient between the concentration of air in the bubble wall and the polymer surrounding the bubble. If the concentration of air within the bubble wall is greater than the concentration of air in the surrounding solution, the bubble will lose its air and begin to shrink/dissolve.

In the centrifugal casting that concerns this thesis, the centrifugal accelerations are often on the order of $1000\,\mathrm{g's}$ $\left(10,000\,\mathrm{m/s^2}\right)$ with spinning speeds on the order of thousands of revolutions per minute. The pressure increases within the fluid can be on the order of $100\,\mathrm{psi}$ ($700\,\mathrm{kPa}$). These pressure increases promote bubble dissolution. With a low dynamic viscosity of the polymer on the order of $1\,\mathrm{Pa\ s}$ and high centrifugal accelerations, buoyant forces also play a role in transporting bubbles out of the solution. The theory and physical intuition that govern bubble removal are the main focus of the calculations included in this thesis (Chapter 3 and Chapter 4).

1.5.3 Fast curing

Once the PDMS has been spun in the centrifuge, the mold cavity is then taken over to a hot plate or a specially designed curing station. The hot plate heats the polymer by conduction to speed up the cure. The specially designed curing station heats the polymer and then cools it for the purposes of handling. This step is fairly straightforward, the faster the heating, the

faster the PDMS cures. However, there are a number of issues involved with this heating process (not all of which are completely understood at this point). These issues include questions regarding the amount of time required to completely cure the material, thermal expansion of the part, possible distortion of the part from thermal expansion, varied curing rates within the part, a non-uniform temperature distribution within the part, the possibility of bubbles emerging from the solution or from surfaces with increased temperature, and thermal degradation of the polymer. The answers to all these questions are not answered in this thesis. However, this thesis shows how fast curing of PDMS for bubble-free micro/nano featured components can be performed.

1.6 Manufacturing context

The tenants of manufacturing are quality, flexibility, rate, and cost. Many of the decisions made throughout the development of this work were based on these principles. With an emphasis on manufacturing, the motivation for this work is a little different than the innovation that drives most lab-on-a-chip research. Instead of creating a new, innovative design for a new type of device, innovative thinking has been applied to revolutionize the process of making microfluidic devices.

1.6.1 Quality

In the context of this thesis, quality is synonymous with producing micro/nano featured parts of consistent dimensions without bubbles. Figure 1-6 A, B, and C show a few examples of quality parts produced without any bubbles in the bulk of the device, while Figure 1-6 D shows one part full of bubbles. All of these parts were cast using the centrifugal method. The good quality parts (A-C) may have some bubbles or flash at the edges of the parts, but the main regions of interest (central areas) are bubble free. The example part in Figure 1-6 D was not spun long enough at a high enough speed to remove all of the bubbles in the middle of the part. The samples in Figure 1-6 A,C, and D were all cured in approximately 8 minutes with a maximum temperature of approximately 100 °C.

Figure 1-7 shows run charts for the height and width measurements at a specified channel location on 20 PDMS parts. The height of the specified channel location is approximately 40 μm and the width is approximately 50 μm. These parts were produced by centrifugal

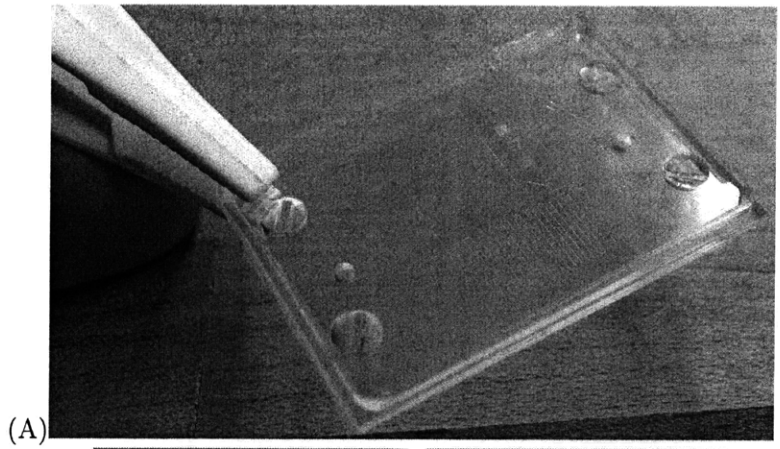
(A)

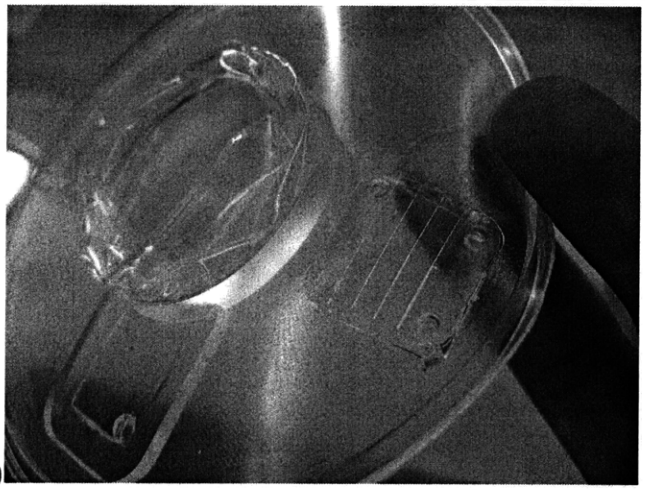
(B)

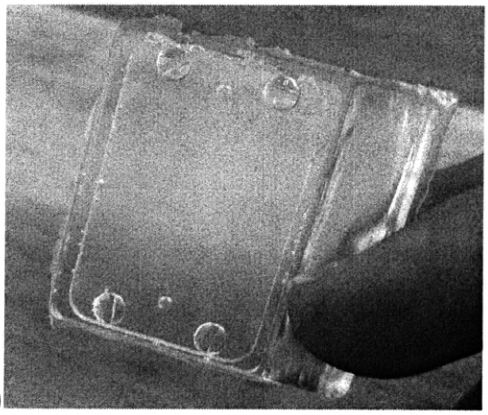
(C)

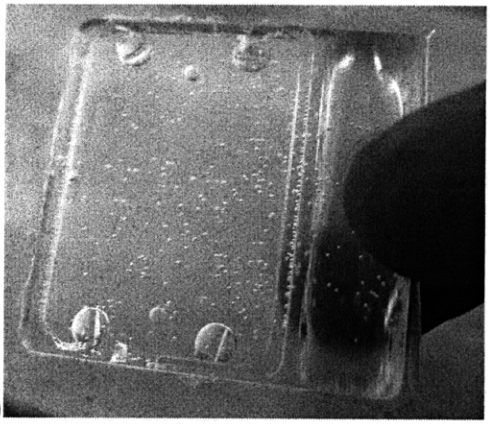
(D)

Figure 1-6: (A) PDMS part with microfluidic channels and fiducials. (B) PDMS part with a diameter of 4 in. (10 cm), which includes some micro channels (bottom left of image), along with some larger ones . (C) Blank PDMS part used for evaluating appropriate spin times and spin speeds. (D) Same as C but not spun long enough and fast enough to remove all the bubbles.

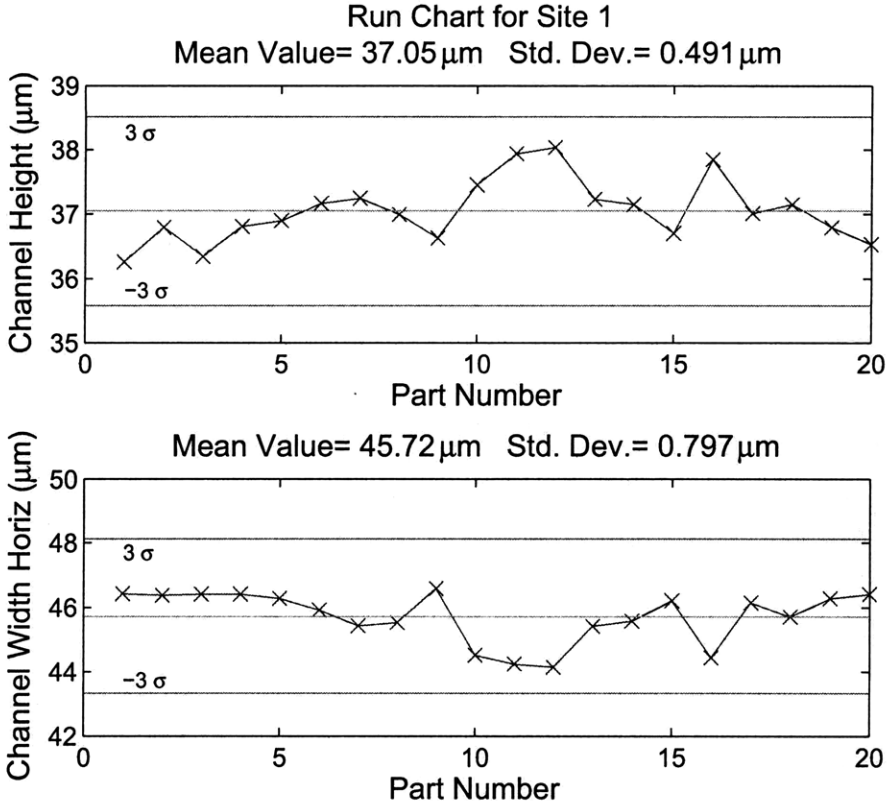

Figure 1-7: Height and width measurements for PDMS parts centrifugally cast and cured quickly. The same, corresponding site on 20 different replicated parts was measured.

casting with a spin time of 1 minute (not including deceleration time) and a specified spin speed of 7000 rpm. The standard deviation for the measured heights and widths of the specified channel location across the 20 PDMS parts is less than a micron.

1.6.2 Rate

Second to only quality for this study, rate is a very important consideration for a PDMS manufacturing system. Based on predictions and experiments, spinning time can be as short as 30 seconds (45 seconds when including the centrifuge's deceleration time) to yield bubble-free parts (no bubbles in the regions of interest around micro/nano features) for PDMS. This spin time may be decreased more with higher speeds, a more powerful centrifuge, or a rotor design with less rotational inertia. The lowest spin speed that yielded a bubble-free part in less than a minute in this study was 4000 rpm.

Proof-of-concept experiments have shown that PDMS can be cured and demolded from a

surface in as few as 30 seconds at approximately 200 °C when the PDMS was poured directly onto a hot plate (see Section 2.4.1). However, this part was very full of bubbles because there was no degassing step and bubbles were easily trapped as the PDMS was poured onto the hot surface. In conjunction with the centrifugal casting system described in Section 2.6, more modest cure times of 8 minutes with a maximum temperature of approximately 100 °C were used. This cure time could be reduced in future designs by either reducing the thermal mass or increasing the amount of power for heating and cooling. The physical limits to cure time are related to the thermal degradation of the polymer, thermal contraction of the material, and potential bubble nucleation at higher temperatures.

Even though the current spinning time can be less than a minute and the curing time as short as 8 minutes, the actual time required for one cycle is approximately 20 minutes. The additional time is spent dispensing the PDMS in the mold reservoir, bolting and unbolting twelve screws, and manually splitting the mold cavity and demolding the cured part. The designed manufacturing system produces two parts per cycle, which leads to a very modest output of 6 parts per hour.

Table 1.1 and Table 1.2 show times for degassing and curing PDMS cited in publications. Summing the shortest times listed, the total time for degassing (15 minutes) and curing (10 minutes) comes to 25 minutes. Summing the shortest, resulting 45 second spin time to produce a bubble-free blank part and the 8 minute cure time shown in this thesis, however, the total time for degassing and curing comes to almost 9 minutes, which is almost three times less than the sum of the shortest reported degassing and curing times. Just considering the degassing times for centrifugal casting in comparison to the best degassing time reported in the literature, the centrifugal degassing is over ten times faster.

Figure 1-8 shows how a cycle can be broken down with respect to time for typical PDMS processing and the new centrifugal casting and fast curing process. This thesis focuses primarily on the reduction of the degassing time t_{dp} and the curing time t_c. That said, as t_{dp} and t_c have been reduced, other processing steps have begun to take more significant percentages of the entire cycle time. For example, the dispensing time t_{dp} was not initially considered as one of the rate limiting steps. However, PDMS dispensing can require a few minutes mainly because the weight of the PDMS accruing in the mold assembly is measured manually and the PDMS inlet into the current mold assembly is a little too narrow, which can result in undesirable spilling.

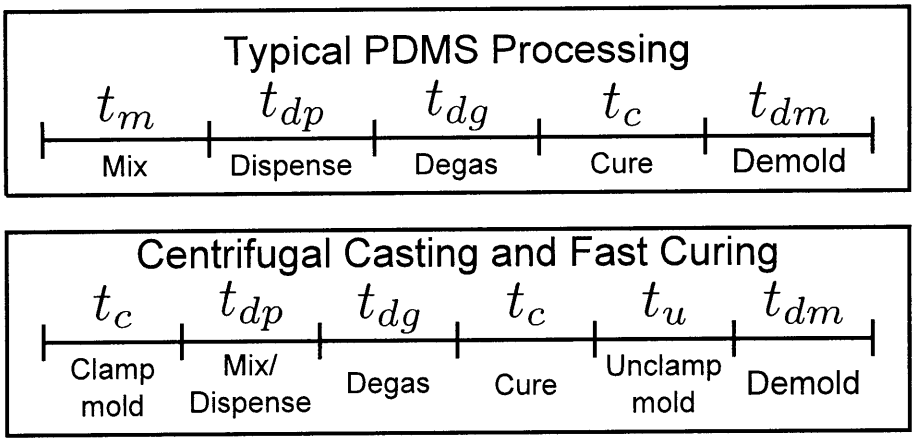

Figure 1-8: Depicted time breakdowns for typical PDMS processing and the new centrifugal casting and fast curing process.

The clamping and unclamping times (t_c and t_u) required to combine or separate the two mold halves for centrifugal casting require approximately 5 minutes. In order to clamp or unclamp the mold assembly, there are 12 bolts that need to be tightened or loosened. Future design modifications should assist in reducing the clamping and dispensing times. Table 1.3 shows some current estimated times, along with some theoretical time limts for the six steps of centrifugal casting and fast curing shown in Figure 1-8.

1.6.3 Flexibility

Flexibility in manufacturing is the simplicity/difficulty associated with suddenly trying to produce a different part using the same core architecture. For micro or nano molding, the flexibility lies in the ease of being able to change mold geometries and processing conditions quickly. While there is a lot of room for improvement with respect to making the current implementation more flexible, the mold cavities for the centrifugal casting system were designed to be capable of interfacing with a variety of mold inserts (see Figure 2-26). Mold inserts have included micromachined aluminum pieces, a bulk metallic glass tool, and blank pieces of sheet metal cut on a water jet machine. With these various mold inserts, microfluidic channels, gratings, fiducial marks such as triangles and squares, and nano sized machining marks have all been replicated in PDMS parts. In a different setup, a 100 mm diameter silicon wafer with SU-8 features was also used as a mold, but the wafer broke during demolding. That said, there is no reason silicon-based, semiconductor mold inserts should not work in the future if properly attached to a substrate that can be bolted into the

Table 1.3: Estimated breakdown for centrifugal casting and fast curing processing steps for current system, along with rough estimates for theoretical limits.

Processing Step	Time (min.)	Comments	Theoretical Limits (min.)
Clamp mold (t_c)	3	12 screws are tightened for mold assembly.	< 1
Mix/dispense (t_{dp})	3	PDMS goes through static mixers into mold assembly.	< 1
Degas (t_{dg})	2	Mold assembly is loaded into centrifuge and spun at 1000s of revolutions per minute for approximately 1.5 minutes.	< 1
Cure (t_c)	8	Thermal management system heats and cools mold assembly.	< 1
Unclamp mold (t_u)	2	12 screws are loosened for mold assembly.	< 1
Demold (t_{dm})	2	Cured part is removed from mold assembly.	< 1
Total	20	Approximate time required for one cycle.	< 6

mold cavity.

1.6.4 Cost

Ultimate cost of a manufacturing process is related to capital equipment costs, labor costs, raw material pricing, energy costs, quality control (what fraction of parts pass inspection), rate, and flexibility (down time associated with switching to a new product). The capital equipment costs with academic pricing were less than $10,000. Purchased equipment includes heaters, thermocouples, a centrifuge, custom-machined parts, mold inserts, electronics, data acquisition equipment, a personal computer, and a protective covering.

A rough estimate for the cost of PDMS Sylgard is USD $50 per kilogram (estimate based on past purchasing from different Dow Corning distributors). Assuming a device consists of approximately 5 g of PDMS (density of 1030 kg/m^3), the resulting cross-sectional area could be 35 mm $\times$ 55 mm with a thickness of 2.5 mm. Some trimming of the final device will also probably be necessary, but a rough estimate would then be USD $0.25 per device just in raw material costs.

Electricity currently costs approximately USD $0.10 per kW hour in the United States (based on DOE report from December 2008) [7]. The manufacturing system in this thesis has power consumption from two NEMA 5-15 outlets, along with a NEMA 5-20 outlet for the chiller. Assuming maximum power consumption from these three outlets, the total electric power consumed can be overestimated as 6000 W $(2 \times (120\,\text{V} \times 15\,\text{A}) + (120\,\text{V} \times 20\,\text{A})) = 6000\,\text{W}$. At the current price of electricity, the cost of running the system for an hour is approximately USD $0.60. With current part production at 6 per hour, that is an estimated USD $0.10 per device.

Current minimum wage in the United States is $6.55 per hour [6]. Estimating a labor cost of USD $20.00 per hour (insurance, pay raises, benefits, etc.) and still assuming only 6 parts per hour, that would result in a labor cost of USD $3.34 per part. So, not including capital equipment costs, repairs, and down time, an estimate cost per part using a system like the one described in this thesis is less than USD $4.00 per part. With such a high percentage of the estimated cost of the part associated with labor costs ($\sim 90\%$), one of the most important ingredients to reducing cost is increasing the rate of production.

1.7 Utility of centrifugal casting and fast curing

In addition to producing PDMS microfluidic devices quickly and efficiently, another research goal is to facilitate the production of features on multiple sides of a part as shown in Figure 1-9. Devices such as those produced by Quake, Thorsen, and others [110, 107] have intricate microfluidic architecture and circuitry, which use multi-layer stacks of PDMS parts with channels on one side of each produced PDMS layer. One layer may have channels that can be pressurized or swelled for blocking channels in an adjacent layer. These channels are known as control channels. The channels being blocked or cut off by the control layer valves are known as flow channels. With this architecture, Quake, Thorsen, and others have developed complex alignment and bonding procedures to build PDMS stacks one layer at a time. By applying centrifugal casting technology to the production of PDMS parts, the need for some or all of the different layers may be eliminated. At this point, the centrifugal casting process has demonstrated the capability of molding multiple sides of a part simultaneously (see Figure 5-7), but further development is required to produce the functioning control-flow valve architecture.

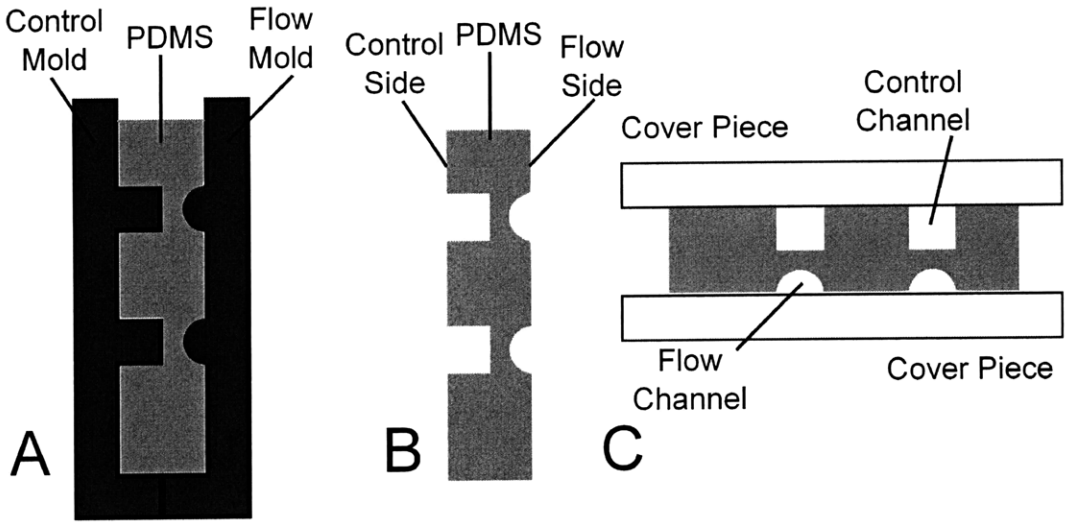

Figure 1-9: (A) PDMS is molded between two mold halves. (B) Molded PDMS part with features on two of its sides. (C) Molded PDMS part bonded to two cover pieces to seal and encapsulate channels.

Chapter 2

System and problem identification

This chapter gives an overview of the developed components and design process for centrifugal casting and fast curing of PDMS parts with micro/nano features. The system was designed to help develop a better understanding of the centrifugal casting process. The entire cost of the system is less than $10,000 (academic pricing) making it a viable option for business ventures wishing to develop curable liquid casting foundries. While there is still room for improvement and adaptation into a large-scale manufacturing process, this prototypical design is robust enough for moderate production.

2.1 Background

One of the initial objectives of this work was to develop possible improvements to the typical PDMS prototyping process as outlined in Figure 1-1. While analyzing the current methods, it became apparent that there were three significant rate-limiting steps in the overall PDMS prototyping steps: mixing, curing, and degassing. The mixing step was resolved using static mixers (an off-the-shelf solution). Curing was improved by increasing the heating temperatures. The degassing step showed the most potential for improvement, partially because it is more tedious than the other two steps. There is also a lack of agreement within the microfluidic device prototyping community concerning the appropriate requirements for removing bubbles from the PDMS in its liquid state. As shown in Table 1.1, many variations of time and vacuum pressure have been used for bubble removal of PDMS parts. In addition to addressing the need for physical explanations to dictate proper procedures for degassing normal microfluidic parts, there was also the hope of improving the degassing step in such

a way that multiple sides of a part might be patterned simultaneously.

The standard method of degassing PDMS parts involves placing the uncured PDMS sitting on its mold in a vacuum chamber. The PDMS part being molded generally requires that almost half of its total surface area be a free surface (open to air) at which bubbles can escape. In other words, it is not generally possible to sandwich the PDMS between two parallel plates as shown in Figure 1-9 without bubble entrapment. That said, injection molding is one way of producing a bubble-free silicone part between two plates. Another potential method for sandwiching PDMS between two plates is described in the work of Kendale and Trumper [64, 65], but it is very slow and involves room temperature curing of the polymer. So, in addition to speeding up the degassing of normal microfluidic parts, a new goal was to introduce a method that could effectively produce parts without requiring almost half of the part's surface area being a free surface. Thus, the degassing objective became two-fold: to reduce the amount of time required for degassing and to degas parts with patterned features on multiple sides in a single step (see Figure 1-9).

The idea for centrifugal casting for the removal of bubbles is not new (see Section 1.5.2), but its application to the production of micro and nano featured components is a new concept. In fact, the author would probably not have arrived at the idea of centrifugal casting if it had not been for AJ Schrauth. AJ had seen quite a bit of struggling with a variety of failed attempts to degas PDMS quickly from sandwiched parts (e. g. vibration, purposeful air injection, and vacuum chamber degassing), when he suggested spinning might work.

2.2 Initial centrifugal casting experiments

After the idea for centrifugal casting was proposed, there was a need for some "lightning empiricism." In other words, some pretty simple experiments were performed before any real understanding of the process had been gained. The following subsections review some of the initial centrifugal casting experiments, which demonstrated that centrifugal casting might work as a manufacturing process for micro and nano featured components.

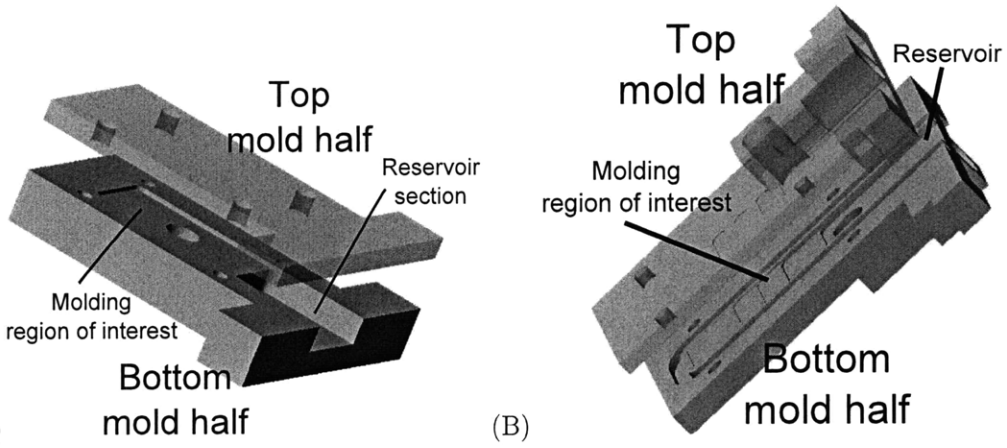

Figure 2-1: (A) Solid model version of two mold halves used for initial Thinky Mixer centrifugal casting. (B) Solid model version of two mold halves used for second version of Thinky Mixer centrifugal casting.

2.2.1 Thinky mixer implementation

The initial proof-of-concept testing of PDMS centrifugal casting was performed using a Thinky Mixer [15] with the open-ended centrifugal mold design shown in Figure 1-5 B. A mold assembly was designed to fit in the Thinky Mixer at a tilt angle relative to the vertical axis of rotation. The Thinky Mixer spun in its non-mixing mode (spinning only about the vertical axis of rotation) at approximately 2000 rpm ($\sim$ 400 g's) for 180 seconds, and the bubbles moved toward the center axis of rotation. Figure 2-1 A shows a solid model of the assembly inserted into the Thinky Mixer. The PDMS starts in the reservoir section and then fills molding region of interest. Figure 2-2 A and Figure 2-2 B show images of the polycarbonate (PC) mold set used for the first centrifugal casting experiment.

After spinning, the mold set filled with PDMS was suspended in boiling water (100 °C) for approximately 30 minutes. The mold assembly was then taken apart, and Figure 2-2 C shows a completed PDMS part. For the most part, the completed PDMS part is bubble-free, although there are a few bubbles near the edge surrounding the part where the PDMS and both mold pieces came in contact with each other.

These initial results showed that the centrifugal spin speed of 2000 rpm ($\sim$ 400 g's) for 180 s was successful at filling the mold. In addition, this experiment shows that many, if not all, bubbles can be removed using a centrifugal mold filling technique. Many of the bubbles appeared to result from trapped air in small crevices of the mold set.

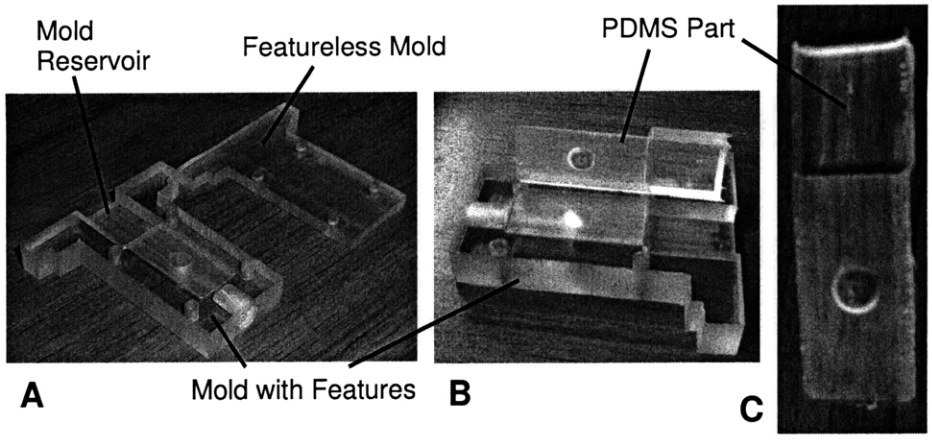

Figure 2-2: (A) Polycarbonate molds for PDMS part molding. (B) Polycarbonate mold with features and resulting PDMS part. (C) PDMS part with an approximate length of 2.5 in., width of 0.75 in., and thickness of 1 mm in its thin region.

After performing the experiment shown in Figure 2-2, another set of experiments was performed using an aluminum mold set. Unfortunately, aluminum is not transparent, so it was not possible to see potential bubble evolution during the curing step. However, aluminum is a good thermal conductor and can be heated to over 200 °C. Using the mold design shown in Figure 2-1 B and Figure 2-3 A, the two mold halves were bolted together with a piece of Viton cord stock (essentially a cut o-ring) placed in a groove between the two halves to keep PDMS from leaking. PDMS was then dispensed into the top section of the mold, and the mold set filled with PDMS was placed in the Thinky Mixer. The Thinky Mixer then spun the mold assembly at 2000 rpm ($\sim$ 400 g's) for 240 s.

After spinning, the aluminum mold set was removed from the Thinky Mixer. The mold assembly was then clamped between two hot aluminum blocks and placed on a hot plate set at approximately 200 °C as shown in Figure 2-4. After approximately 5 to 10 minutes of heating, the mold set was removed and placed under running tap water to quench cool the mold set. The mold set was separated, and the cured PDMS part was removed. Figure 2-3 B shows an example part. Features on both sides were replicated and a region of the part had a thickness of approximately 0.002 in. ($\sim$ 50 μm), demonstrating that thin films may also be cast using centrifugal casting. That said, thin PDMS parts tear easily during demolding, so a better method than just prying the mold assembly apart might be necessary.

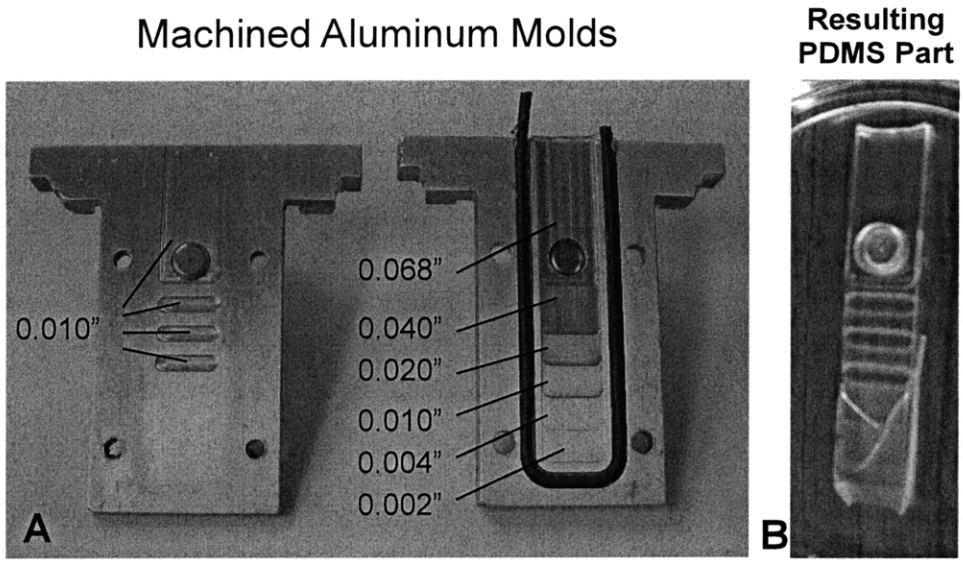

Figure 2-3: (A) Aluminum molds for PDMS part molding with prescribed depths illustrated. (B) PDMS part with an approximate length of 2.6 in. and a width of 0.5 in.

2.2.2 Cylindrical mold sets

After producing the part shown in Figure 2-3 B, another set of centrifugal casting mold designs for larger volume, circular parts were developed. The concept for these designs is shown in Figure 2-5. Figure 2-6 and Figure 2-7 show results of the early attempts at the implementation of the Figure 2-5 concept. Some of the lessons learned can be summarized in the following list and may even be considered design rules for those wishing to implement a centrifugal casting system in the future:

1. Water from cool quenching a mold can seep into the o-ring groove and cause water vapor to get trapped in the PDMS part as shown in Figure 2-6 A and Figure 2-6 C.

2. If a silicon wafer or a silicon-based mold is to be used, it needs to be securely fixtured in the centrifugal mold assembly. Otherwise, it can break during demolding (see Figure 2-6 B), even if the wafer or silicon-based mold survives the spinning.

3. Thin films of PDMS on the order of 100 μm can be centrifugally cast (see Figure 2-6 C), but demolding them may be very challenging.

4. If there are deep grooves or trenches around a mold insert, bubbles may appear in those regions. A part may be bubble-free in the regions of interest around micro and nano

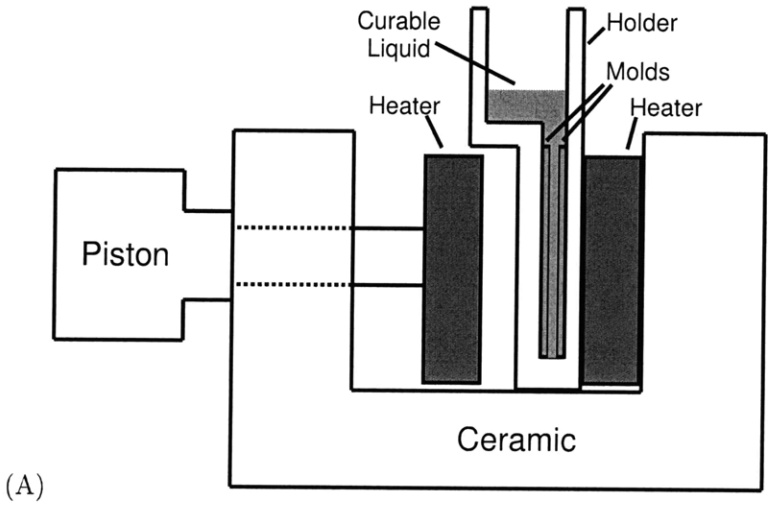

(A)

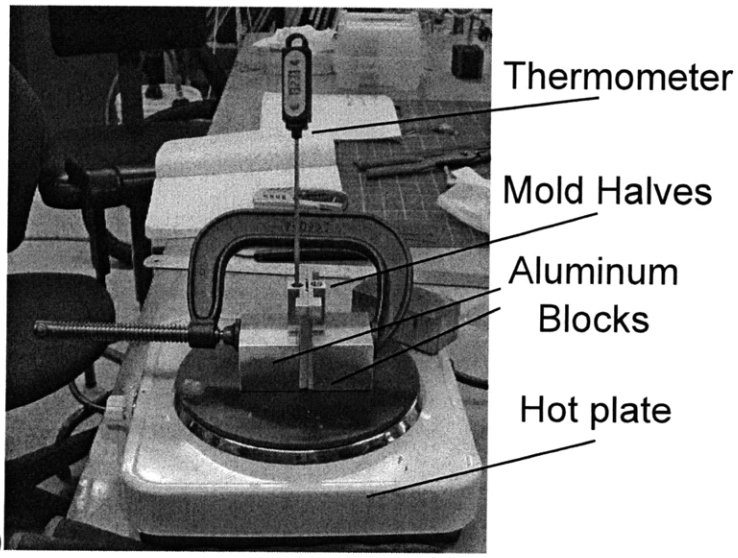

(B)

Figure 2-4: (A) Concept for heating open-ended centrifugal mold. (B) Aluminum mold set being heated clamped between two blocks and sitting on a hot plate.

features but have bubbles caused by deep trenches surrounding the mold insert (see Figure 2-6 D). However, longer spin times may eliminate the bubbles by dissolution.

5. A rubber o-ring can prevent some PDMS from leaking (see Section 2.2.3), but there is generally some PDMS that escapes the mold assembly.

6. The reservoir section needs some type of overhang as depicted in Figure 2-5. The reservoir sections shown in Figure 2-7 A and Figure 2-7 B without any overhang in the reservoir section lead to excessive loss of PDMS during spinning. The additional cover with a hole in it (Figure 2-7 D) corrected the problem. There is a simple technique to determining the size of the overhang. This technique first requires looking at a cross-section of the mold set and rotating the cross-section 90° or the appropriate amount to have a radial acceleration vector pointing downward like gravity. Then, it is necessary to visualize whether or not water or a liquid would spill out of the rotated cross-section. In other words, one needs to imagine where the liquid-air interface would be and how much volume of PDMS would need to be stored in the reservoir section during spinning. This visualization helps determine whether or not there will be enough retained PDMS in the reservoir during spinning for their to be enough PDMS to completely cover the entrance to the molding section when the centrifuge stops spinning. If there is not enough PDMS left in the reservoir when the centrifuge stop spinning to completely cover the entrance to the molding section, the PDMS may not make complete contact with the top mold half. Without the molding section being completely filled, height control and replication of potential features on the top mold half are lost. Well-designed liquid-air interface lines are depicted back in Figure 2-5.

7. A rubber stopper without any restraint (see Figure 2-7 C) was not sufficient to compensate for a missing overhang. The pressure buildup was too great and the PDMS-rubber stopper interface was too slippery to hold it in place during spinning.

8. Pressure builds up in the PDMS fluid as shown in Figure 4-6 A and requires sufficient clamping to keep the mold set together. Figure 4-6 E shows a portion of the rubber o-ring that came out during spinning. While the mold set was spinning, there was essentially a small explosion, in which the plates separated enough for the rubber o-ring to come out. This problem was solved by decreasing the lateral separation

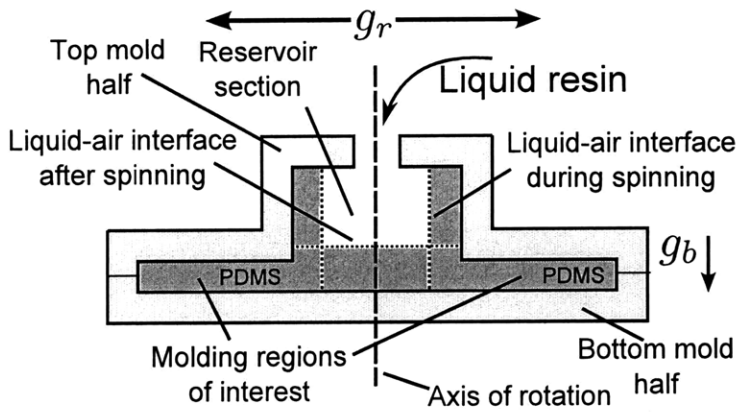

Figure 2-5: Mold cavity for centrifugal casting being spun about an axis of rotation.

between clamping bolts and thickening the top mold half.

Standard PDMS microfluidic devices have overall dimensions on the meso scale with functional features on the micro or nano scale. As already shown in various figures, the centrifugal processing technique replicates meso scale features on the order of a millimeter without difficulty. In order to repetitively produce PDMS parts with consistent overall dimensions and micro/nano features, the mold assembly should be specially designed to work with special mold inserts with the micro/nano features.

The two aluminum components of the last designed version of the cylindrical mold set and its associated aluminum inserts are shown in Figure 2-8. These aluminum parts were machined using standard CNC milling and turning techniques by Preliminary Machine Inc., in Minnesota. Figure 2-8 B shows a control channel mold insert with protruding channels of 1.2 mm width and 2.0 mm height. Figure 2-8 C shows a flow channel mold insert with protruding channels 0.1 mm width and 0.1 mm height in the regions that would overlap the control channels. The gap between the two mold halves or thickness of the PDMS part is 2.5 mm.

2.2.3 O-ring usage

As shown in Figure 4-6 E, one of the design requirements is maintaining the mold halves together and preventing fluid leakage from the mold cavity. In reality, sealing is an issue for any medium/high pressure polymer processing application. Injection molding generally has some type of metal-metal seal with very large clamping pressures to keep the polymer from leaking. A variety of sealing materials were qualitatively tested for use in centrifugal casting.

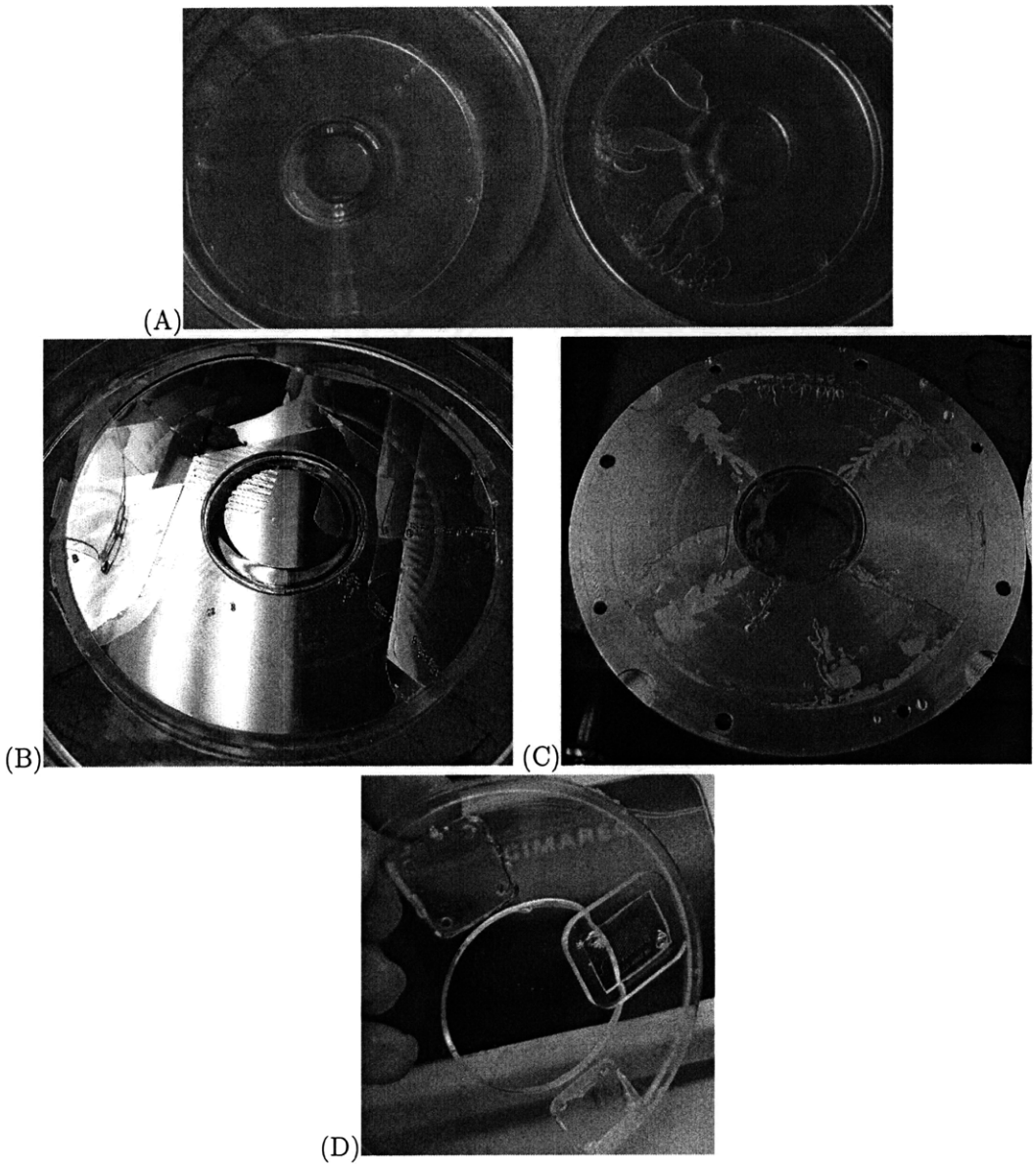

Figure 2-6: (A) Left PDMS disc (100 mm diameter) was cured without water boiling in the mold cavity, while the right part had water vapor bubbles form in the PDMS. (B) Poor attempt to centrifugally cast PDMS on 100 mm silicon wafer with SU-8 features. (C) Thin film ($\sim 250\,\mu$m thick) with water vapor bubble issues is stuck to an aluminum mold half. The aluminum piece shown has an outer diameter of 133 mm. (D) PDMS annulus (outer diameter of 100 mm) part with a few meso and micro features.

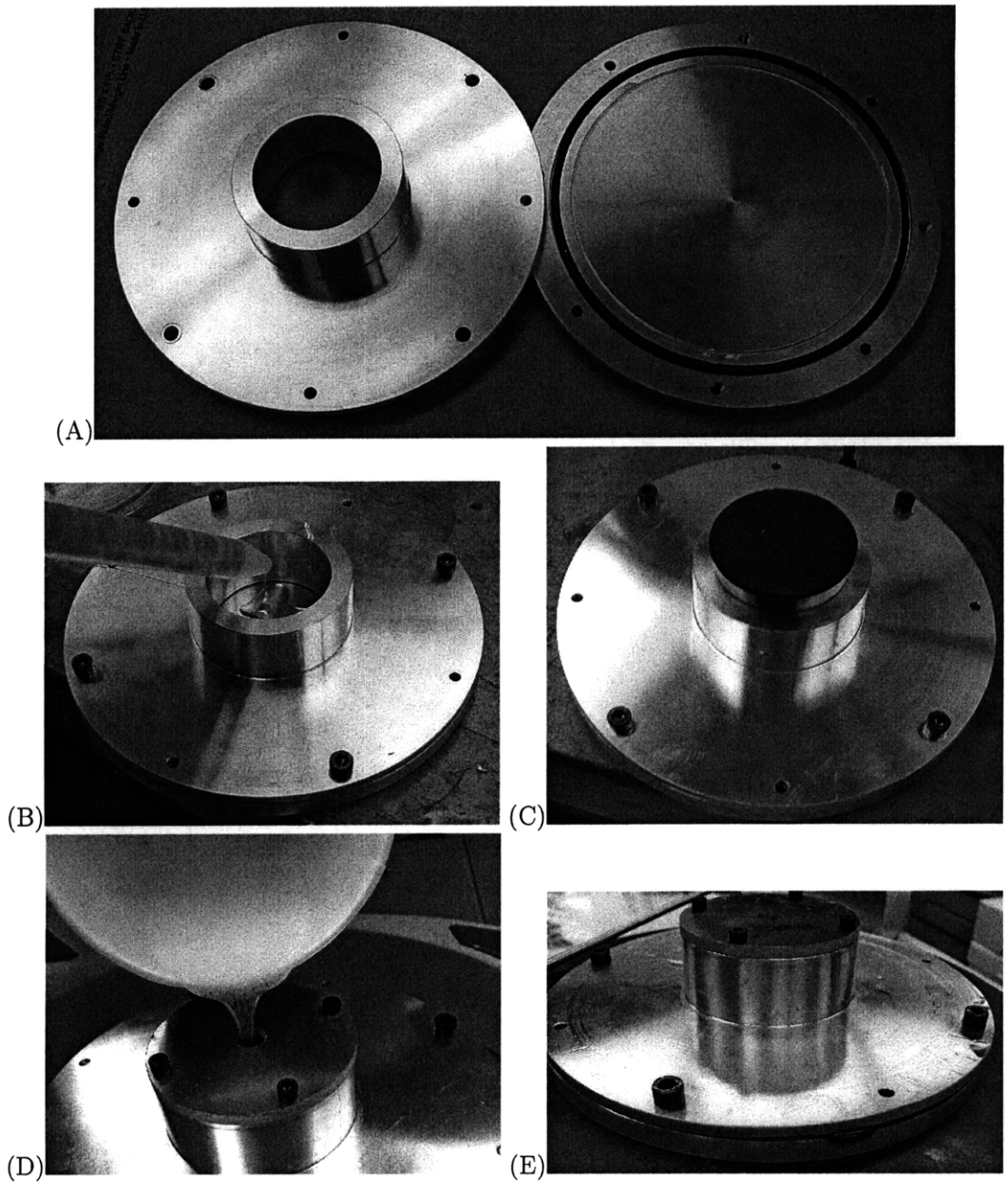

Figure 2-7: (A) First version of circular discs made for centrifugal casting. (B) Static mixer dispensing PDMS into mold assembly. (C) Rubber stopper inserted into rotor assembly. (D) PDMS being poured into modified assembly with cap. (E) Mold assembly with protruding o-ring.

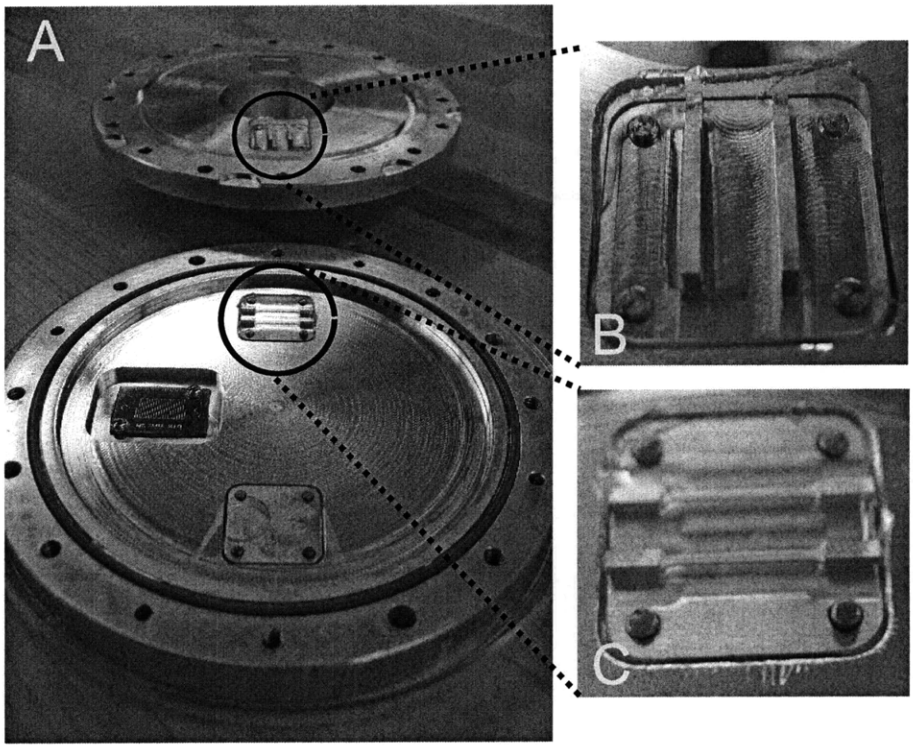

Figure 2-8: (A) Two mold halves used to mold multiple PDMS surfaces simultaneously. (B) Mold insert for control channels with some torn PDMS still attached. (C) Mold insert for flow channels.

The initial molds were two pieces of plastic (polycarbonate), which sealed well enough at low spin speeds/centripetal accelerations (2000 rpm or 4000 m/s^2). At higher spin speeds, an aluminum-aluminum seal with bolts also seemed to work. When approaching speeds of 13,000 rpm for the 5.25 in. (133 mm) diameter mold set, however, the bolts and metal-metal seal did not provide enough clamping pressure to keep the fluid from seeping between the two mold halves. To ensure better leaking protection, o-rings provided a seal between the two mold halves.

To produce the o-ring grooves, a CNC milling machine and a lathe were used in different cases to remove material from the bottom half of the mold halves used. Grooves with a width of 0.125 in. (3.18 mm) and depth of 0.077 in. (1.96 mm) worked well with rubber AS568A o-rings with a width of 3/32 in. (2.38 mm). From a design perspective, the radius around corners was kept larger than 0.07 in. (1.78 mm), and the minimum possible radius around corners can be determined by reviewing the minimum available overall/ring diameter of an o-ring with a given material and width. Tested o-ring materials, which prevented leaking for more than one use, include Viton, silicone, and Aflas. In particular, silicone o-rings with a Shore A hardness of 70 have been resilient for more than forty uses. PTFE material-based o-rings were not as effective because they deformed plastically after a single use. Before purchasing o-rings, it is also wise to look at the temperature specifications of the material being used. The silicone o-rings used in this work were rated from −65 °F to 450 °F (−54 °C to 232 °C). All the o-rings were purchased through McMaster-Carr.

2.3 High density liquid demolding

To assist in the demolding of the PDMS from the mold halves, liquid parting [65, 64] is a viable method to release the PDMS without tearing. Experiments using a modified form of liquid parting have been performed, and this modified form of liquid parting may hold promise for the future of the demolding of liquid thermosets. The modified form uses a parting fluid with a higher specific density than the curable liquid resin being cast. The curable liquid resin is cast on a mold and one or more inlet ports filled with a higher density parting fluid. The inlet port(s) may be incorporated into the desired feature set or surround the features. Figure 2-9 A shows a mold upon which a curable resin may be cast, along with inlets for the introduction of a parting fluid. In Figure 2-9 B, the higher density (HD) fluid

fills the inlet ports and the resin is then poured onto the mold. Because the parting fluid has a higher density than the resin being cast and gravity is acting in the downward direction as shown in 2-9, there will be minimal mixing of the resin and the parting fluid at their interface provided the two fluids do not react with each other. After the resin has cured, the HD fluid can be pressurized to release the cured part from the mold as shown in Figure 2-9 C. Factors that influence the separation of the cured part from the resin include but are not limited to the rigidity of the cured resin, the adhesion between the mold material and the cured resin, the aspect ratio and number of the features being replicated, and the roughness of the mold surface.

The liquid parting method using a high density fluid has been reduced to practice as shown in Figure 2-10 A. A machined aluminum mold is prepared by cleaning it and filling the inlet hole with Karo corn syrup, after which, mixed PDMS is cast on the mold. The corn syrup in the inlet hole has a higher density than the PDMS, so the PDMS does not sink into the inlet hole. The PDMS cures, and the corn syrup is then pressurized. A blister forms, and then the PDMS part is easily removed from the mold. The resulting PDMS part is shown in Figure 2-10 B.

2.4 Fast curing/high temperature experiments

Before a well-designed PDMS curing system was built, centrifugally cast PDMS was cured on a hot plate. Using a hot plate to heat a mold with PDMS inside of it allowed the author to quickly evaluate the effectiveness of the centrifugal casting process without building a more complicated curing system. The following subsections detail some of the initial PDMS curing experiments executed on a hot plate within or without a mold set PDMS container.

2.4.1 Initial proof-of-concept

Liquid PDMS was poured directly onto a thin piece of sheet metal ($\sim 200\,\mu$m thick) resting on a hot plate at temperatures greater than 200 °C. Within 30 seconds of pouring the PDMS onto the hot plate, the PDMS cured or hardened enough so that it could be peeled off the hot plate. This hot plate experiment suggests that PDMS parts can be cured in less time than the 10 minutes suggested by O'Neill et. al. [92], and that the quick curing property of PDMS should be conducive to manufacturing if the bubbles can be properly eliminated.

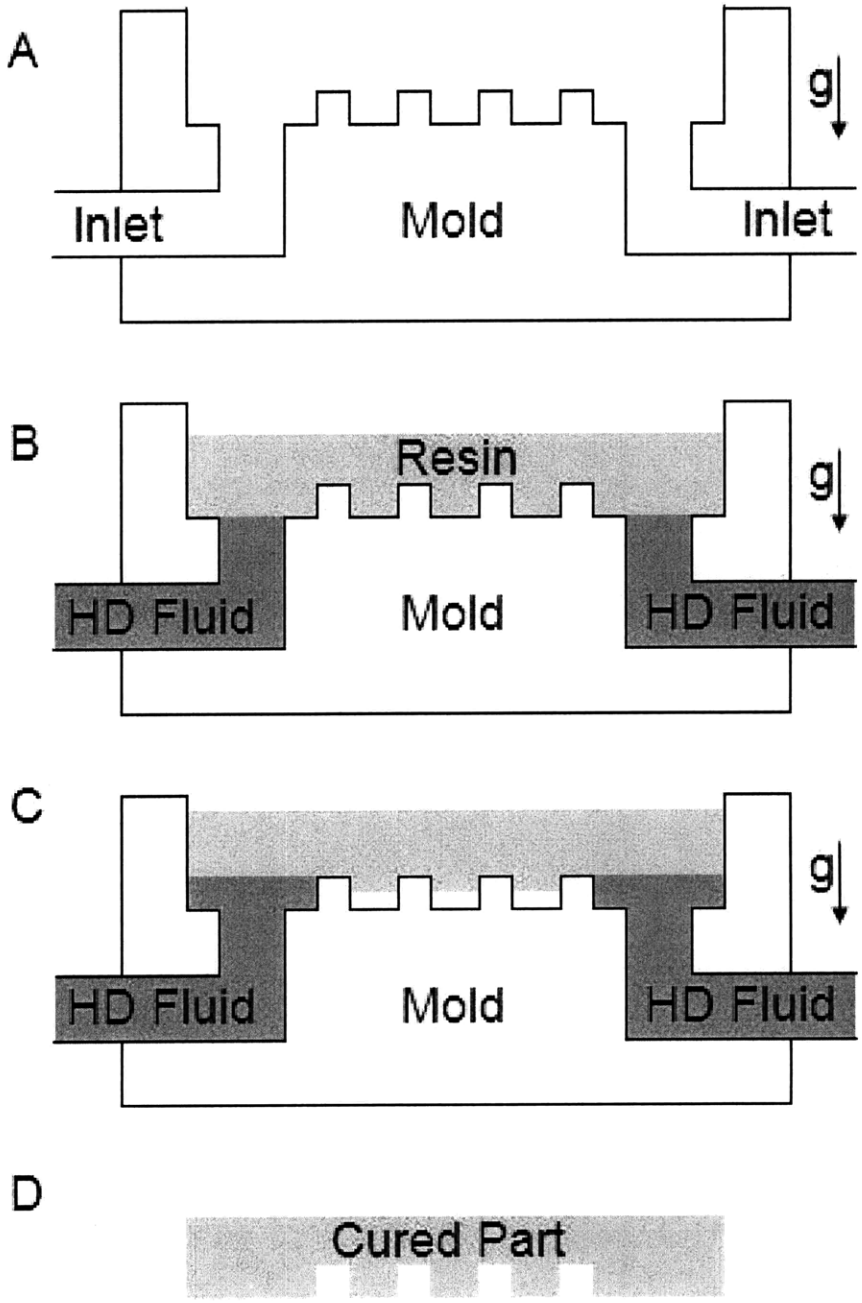

Figure 2-9: The steps to liquid parting of a thermosetting fluid with a lower density than the parting fluid.

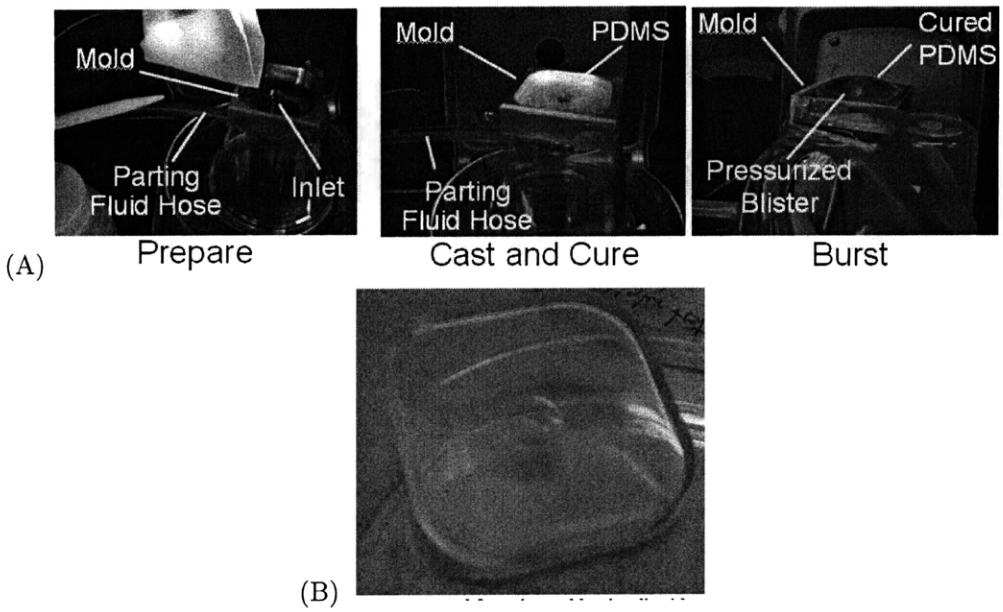

Figure 2-10: (A) The steps to liquid parting of a thermosetting fluid with a lower density than the parting fluid. (B) An example part, which was demolded using corn syrup.

This observation is in agreement with material provided by Dow Corning. In the Q&A section of Dow Corning's website, the following quote can be found referring to adhesion issues and the fast curing of their silicone products: "If the part can withstand it, another method that has been used is a short (1 minute) bake cycle at >200°C [14]."

2.4.2 Degradation concerns with fast curing

The physical limit to the maximum temperature or rate at which one might cure PDMS or any polymer is related to the physical degradation of the polymer. By exposing PDMS Sylgard 184 to varied curing temperatures for differing periods of time, qualitative results indicating differing degrees of polymer degradation have been observed. A few centrifugally cast PDMS samples (spun at 13,000 rpm for 3 minutes) were cured with the temperature profiles shown in Figure 2-12. The temperature was measured within the bottom mold half with an Omega TJ C36-CASS-032U-6 thermocouple in a 0.035 in. (0.89 mm) hole drilled with a non-metric size 65 drill bit. The center of the drilled hole was 1.32 mm away from the polymer-metal interface.

For the parts heated for 21.5, 10, and 5 minutes, some yellowish tint or discoloration of the polymer was observed. For the samples cured for 2 and 3 minutes, no yellow discoloration

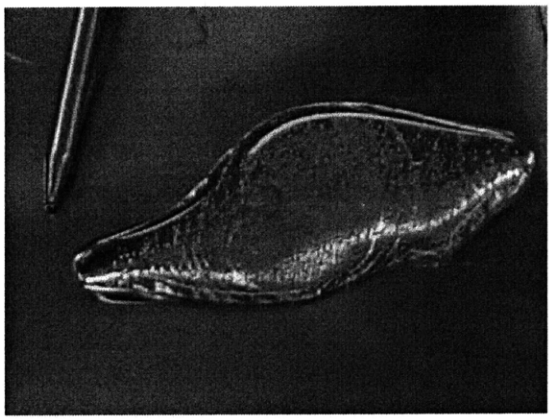

Figure 2-11: PDMS puddle cured quickly by pouring it onto a thin metal sheet resting on a hot plate.

of the polymer was observed. Yellow discoloration of a polymer is often a sign of degradation, where the material breaks down because it was exposed to too high a temperature for too long a period of time.

For the sample cured for 1 minute (Figure 2-12 F), the polymer was not completely solidified. The sample was slightly gooey when it was removed from the mold cavity. During the one minute attempted cure shown in Figure 2-12 F, the maximum temperature recorded was 130.4 °C. With the maximum temperature recorded below 200 °C during the attempted 1 minute cure, it is not surprising that the part did not cure completely given Dow Corning's statement included in Section 2.4.1 of this thesis. To fully cure the PDMS in one minute for this mold configuration, it would be necessary to apply more heat or reduce the thermal mass of the mold set surrounding the polymer. Speeding up the PDMS cure might result in additional thermal shrinkage, warpage, or possibly even distortion. That said, the meso scale parts produced in this subsection have not shown any geometric deformations that might hinder PDMS bonding or prevent their use in microfluidic applications. Eehern Wong's current work and future thesis should illuminate how molds could be designed to compensate for thermal distortion or shrinkage with high temperature curing [115].

2.5 High speed video image acquisition

Using a Vision Research Phantom v7.3 camera, bubble behavior during centrifugal casting was recorded. The hardware setup for the video acquisition is shown in Figure 2-13. Figure

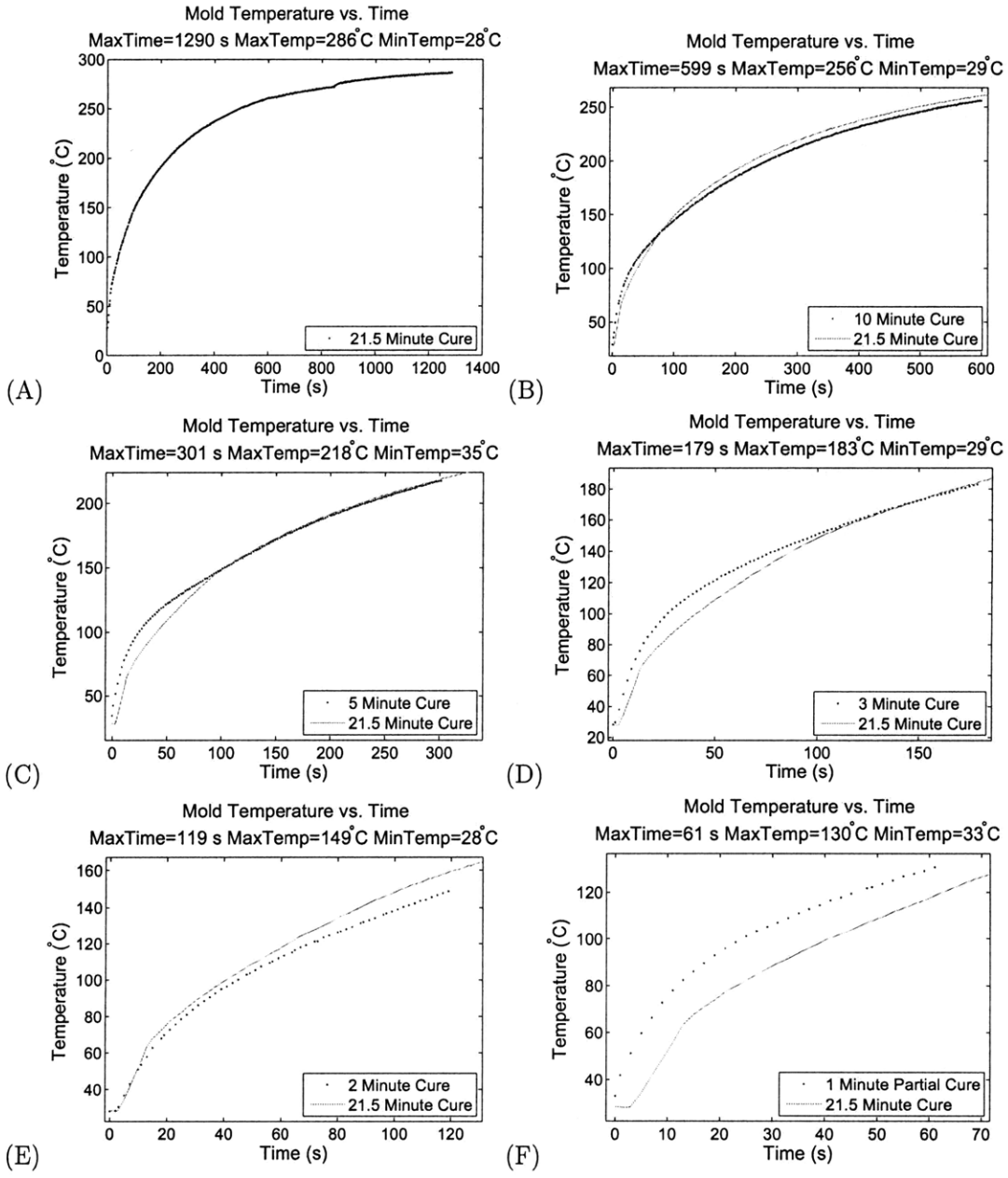

Figure 2-12: Temperature profiles for cured disks of PDMS.

2-13 B shows a mold set with a clear polycarbonate top half. Figure 2-13 A shows the high speed camera on a tripod aimed at the centrifuge.

The high speed camera was operated in two modes: fixed sample rate and synchronized. In the fixed sample rate mode, the camera took images at fixed time intervals ignoring the speed of the centrifuge. For the centrifugal casting experiments, the maximum rate for image acquisition was 1000 Hz for 800 pixel x 600 pixel resolution. The fixed sample rate mode was useful for observing the startup portion of the centrifugal process, which showed the liquid PDMS filling the mold cavity. In the synchronized mode, the camera took an image every time it received a "high" TTL signal from a Monarch PLT200 tachometer. Using the tachometer allowed an image to be taken once per revolution. In this way, the bubbles' progression in velocity and position toward the center axis of rotation was monitored.

Images taken at a fixed sample rate (500 Hz) of a centrifuge in the process of accelerating up to 5000 rpm are shown in Figure 2-14. The PDMS initially starts in the reservoir section as shown in Figure 2-14 A. The PDMS then begins to fill the molding region and some liquid fingers are observed in Figure 2-14 B. As the centrifuge continues to accelerate, the PDMS fills the entire molding area and the large bubbles are removed. In Figure 2-14 D, some bubbles remain within the PDMS, but the molding area is completely filled and bubbles migrate toward the center axis of rotation.

In Figure 4-22, the images were taken in the synchronized mode (one image per revolution). These images are just a portion of the entire video taken and show the migration of bubbles moving toward the center axis of rotation. The images show the startup of the centrifuge and a solution with fewer, smaller bubbles after approximately 10 seconds. The centrifuge accelerated up to its set spin speed of 2000 rpm within a few seconds and then maintained the desired spin speed.

Images also had to be calibrated to convert pixels to metric distances or displacements. Figure 2-16 demonstrates this calibration using two different image features. A penny was placed in the field of view and a circle was fit to 20 selected points on the edge of the penny. Using a circle fitting technique with the image of the penny, the penny's radius in pixels was calculated [28]. A penny is nominally 19.05 mm in diameter, and we measured the radius of the penny to be 312.41 pixels. Therefore, the conversion factor using the penny is 30.05 μm per pixel.

The second feature analyzed is the outer edge of a circular feature embedded in the clear

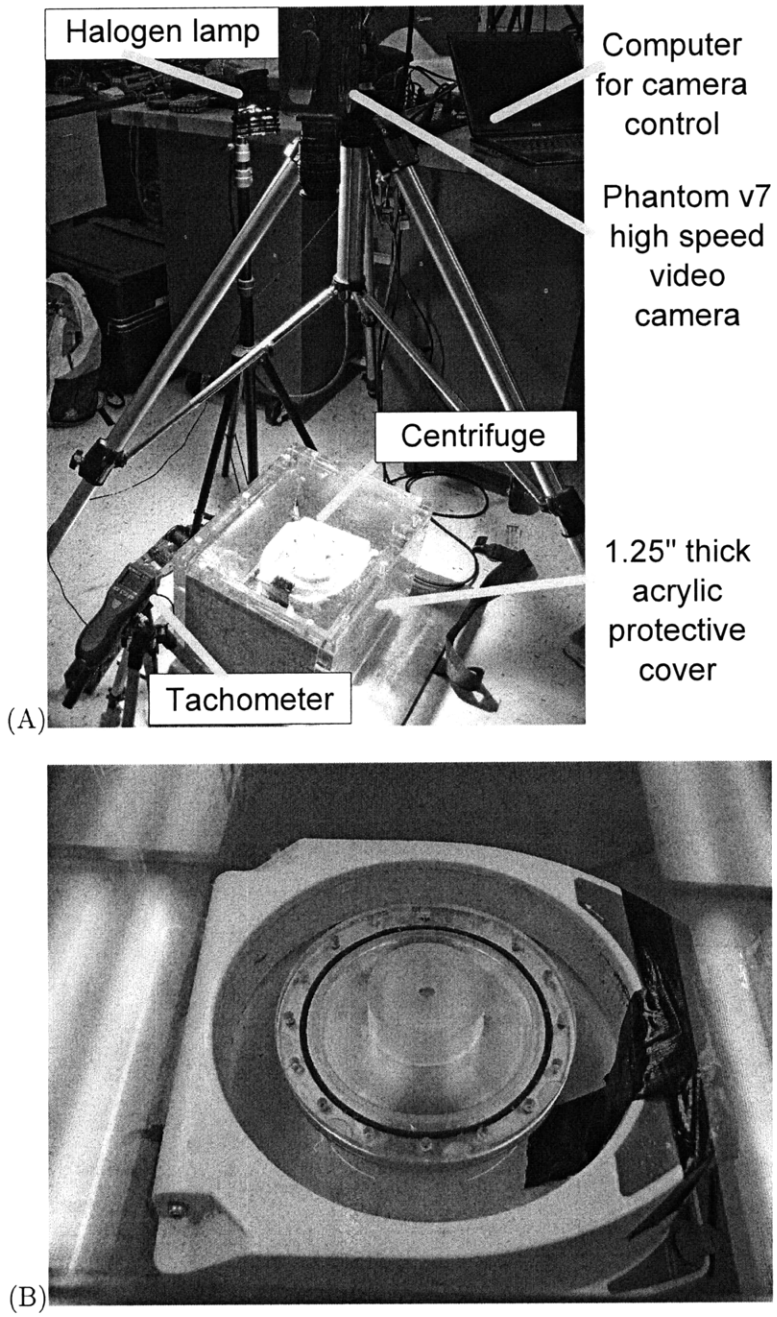

Figure 2-13: (A) High speed video setup for monitoring bubble behavior during centrifugal spinning. (B) Mold with clear polycarbonate top cover sitting in the centrifuge. The centrifuge and the mold are sitting under an acrylic protective cover.

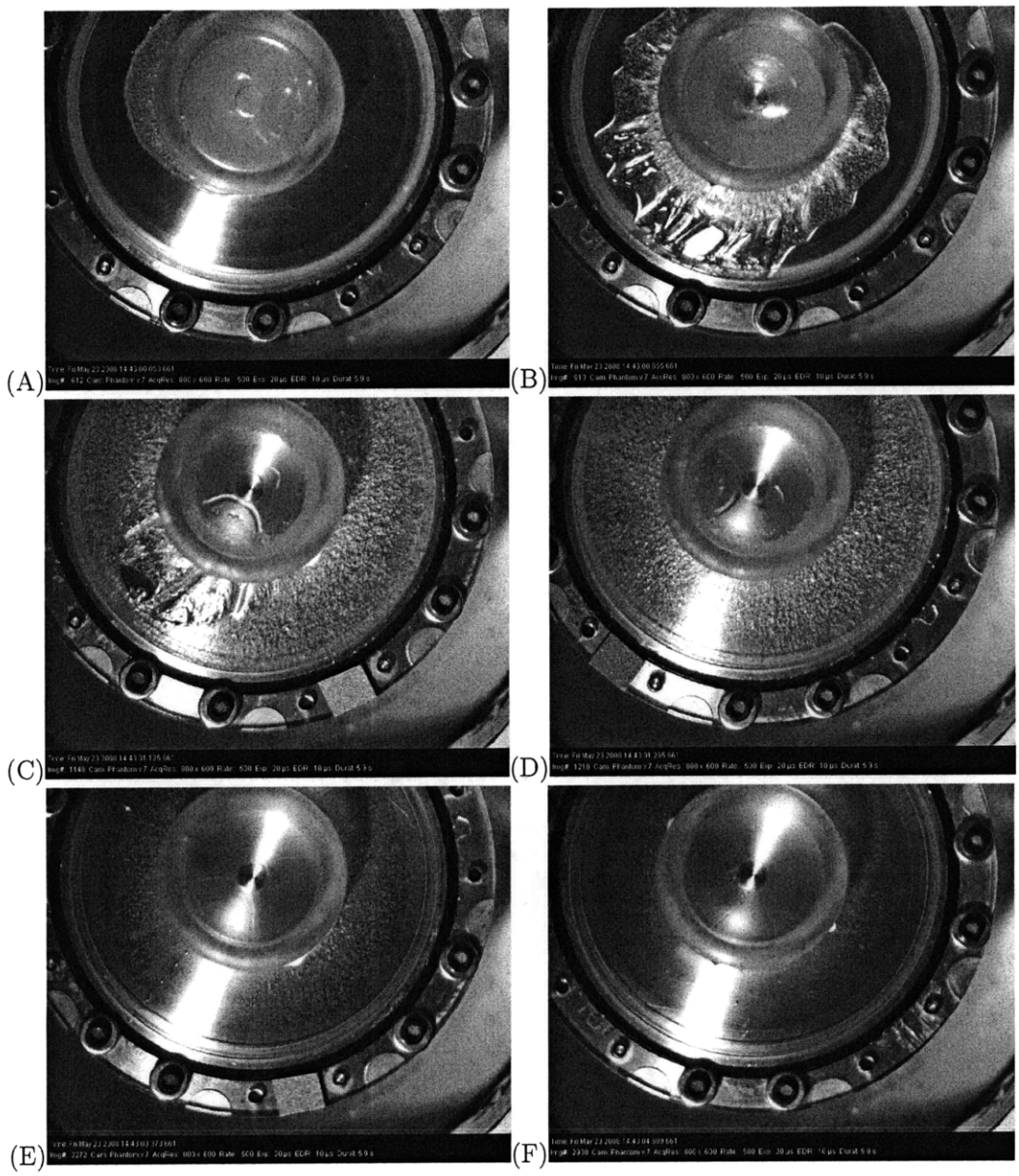

Figure 2-14: (A) Fixed frame rate image #612: 1.224 seconds from video start. (B) Fixed frame rate image #913: 1.826 seconds from video start. (C) Fixed frame rate image #1148: 2.296 seconds from video start. (D) Fixed frame rate image #1219: 2.438 seconds from video start. (E) Fixed frame rate image #2272: 4.544 seconds from video start. (F) Fixed frame rate image #2931: 5.860 seconds from video start.

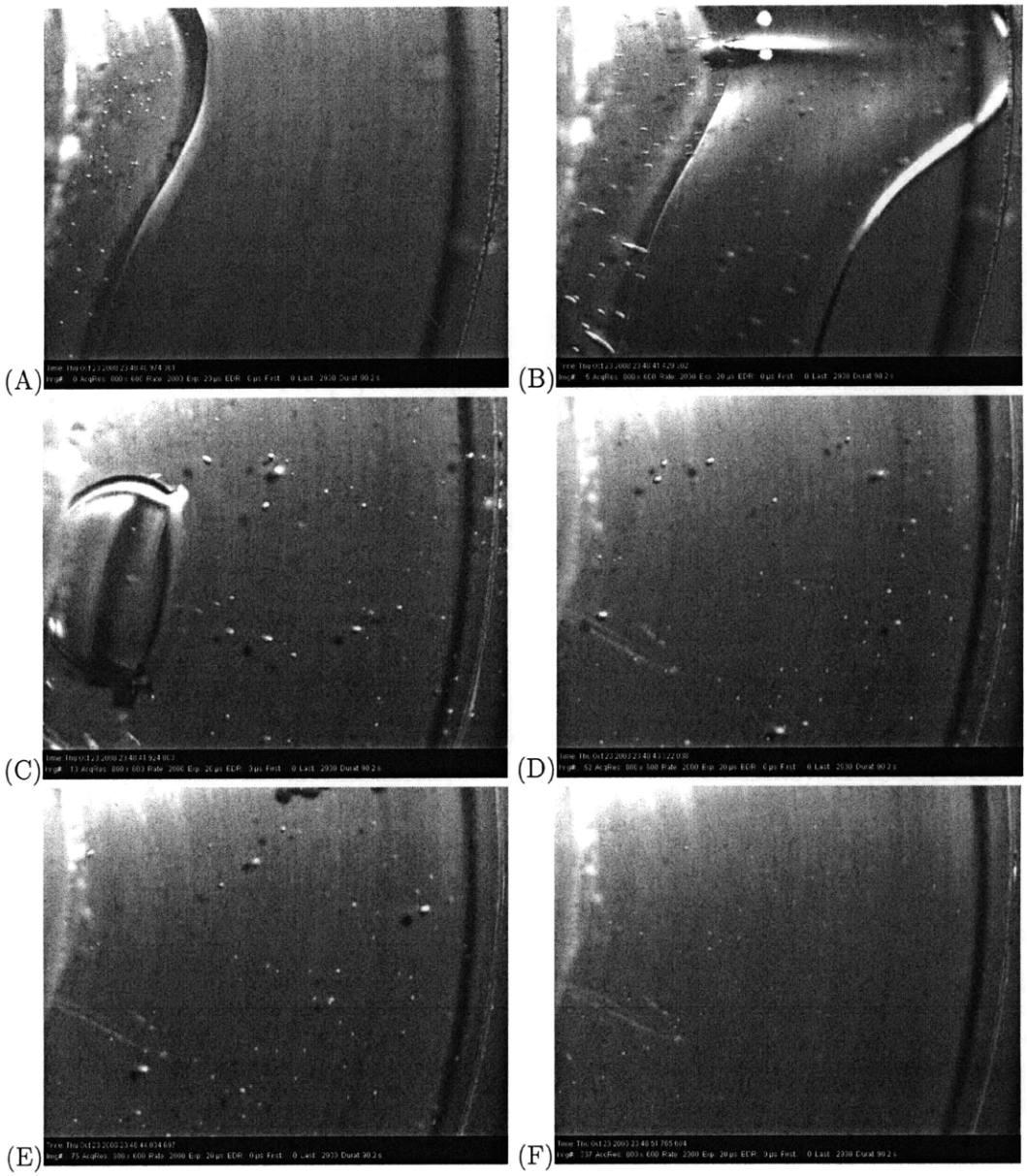

Figure 2-15: (A) First synchronized video frame: frame 0. (B) Synchronized video frame after 0.455 seconds: frame 5. (C) Synchronized video frame after 0.950 seconds: frame 13. (D) Synchronized video frame after 2.348 seconds: frame 52. (E) Synchronized video frame after 3.060 seconds: frame 75. (F) Synchronized video frame after 10.791 seconds: frame 337.

top half of the mold (see Figure 2-16 B). This circular feature, a bubble trap, is analyzed with the same circle fitting method and has a diameter of approximately 2 in. (50.8 mm). Using the circle fitting, this feature was found to have a pixel radius of 1538.54 pixels. Therefore, the conversion factor using this circular mold feature is 33.0 μm per pixel. Averaging the value for the calibration with the penny (30.05 μm per pixel) and the value for the calibration with the circular mold feature (33.0 μm per pixel), the calibration value is 31.5 μm per pixel. This calibration factor of 31.5 μm was used for bubble tracking in the set of experiments described in Figure 2-15 and Chapter 4.

Calibrating from the circular feature embedded in the mold set is also useful for calculating the position of the centrifuge's center axis of rotation. The circle fitting technique estimates a position for the center of the circular object being measured. Using the fitted center position, which corresponds to the center axis of rotation outside of the field of view of the images taken, it was possible to estimate a bubble's distance from the center axis of rotation in any given image. Being able to calculate an object's relative position to the center axis of rotation was very important for the bubble speed prediction models included in Chapter 4.

2.6 Centrifugal Casting and Manufacturing System

After performing a number of proof-of-concept experiments using a centrifuge and a hot plate for curing, designs for a more robust PDMS production system were implemented. The current implementation is similar to a work cell that might be used in a production facility. Figure 2-17 shows a potential work flow based on the centrifugal curing and fast curing techniques described in this thesis.

2.6.1 Centrifugal casting

For the most part, there were not significant changes in the centrifugal casting portion of the system from what was used in the proof-of-concept phase. The Labnet Spectrafuge 24D continued to be the workhorse for the experiments. However, a larger rotor assembly was designed and utilized for producing two parts simultaneously as shown in Figure 2-18 A. With the larger rotor assembly and wind resistance of the protruding features, the rotor assembly was no longer capable of reaching the centrifuge's maximum speed of 13,300 rpm.

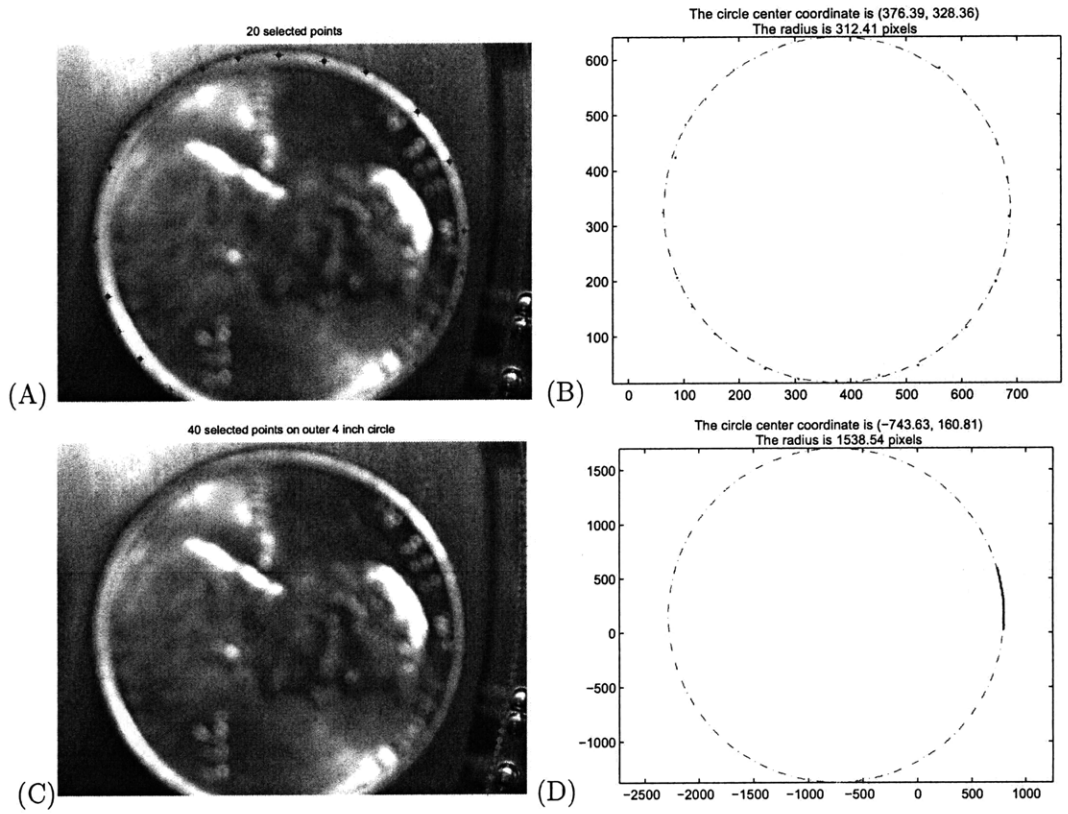

Figure 2-16: (A) Image of selected points on edge of penny for circle fitting algorithm and calibration. (B) Graphical depiction of fitted circle to selected points from A, along with calculated center position and radius. (C) Image of selected points on circular edge of a defined feature in the clear polycarbonate piece of the mold set. (D) Graphical depiction of fitted circle to selected points from B, along with calculated center position and radius.

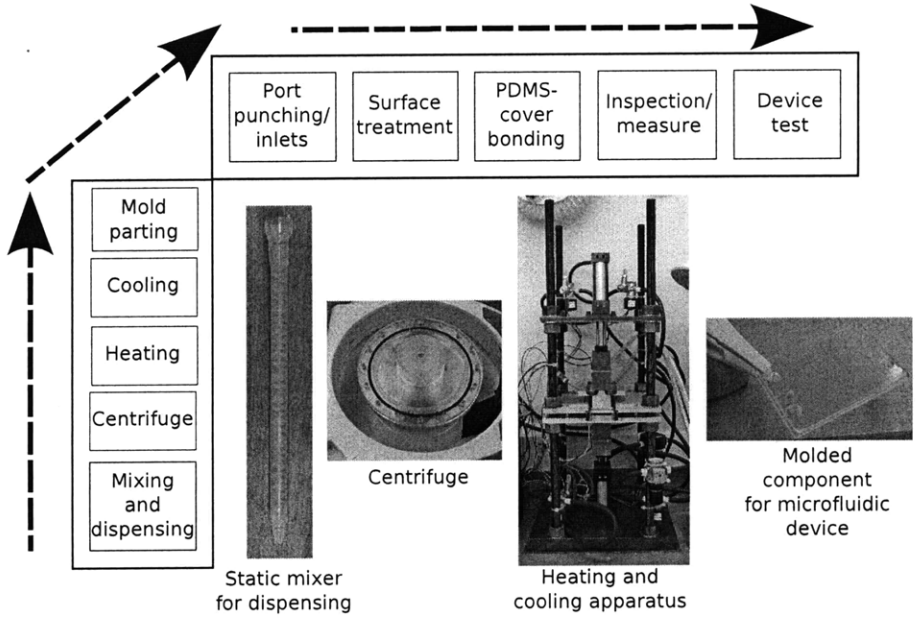

Figure 2-17: PDMS manufacturing work flow with centrifugal casting and fast curing depicted in the left column, along with the photos. The top row indicates additional processing steps that may be necessary for completing the manufacturing process.

Figure 2-18 B shows a spin speed profile with a maximum speed close to 12,000 rpm.

2.6.2 Heating and Cooling System

In order to repetitively cure PDMS parts, a heating and cooling station was designed and built. Figure 2-19 shows a schematic drawing of the system. The mold set holding the PDMS part is retained in the middle of the frame. During the heating portion of the process, a heated block/plate bolted to an air cylinder rises up and makes contact with the bottom side of the mold set. After a set amount of time, the heated plate retracts, and a set of cold blocks come down and makes contact with portions of the top side of the mold set containing the PDMS. By cooling the mold set immediately following heating, the mold set becomes easier to handle and disassemble for the removal of the PDMS part. Cooling the mold set also permits the next PDMS part to be centrifugally cast with the mold set starting near room temperature. In attempting to mold the next PDMS part, if the mold set were still at an elevated temperature ($\sim 100\,^{\circ}\mathrm{C}$), it would be possible for portions of the newly dispensed PDMS in the hot mold cavity to cure before completing the centrifugal bubble removal.

Figure 2-20 shows the completed heating and curing station. The air cylinders, which

(A)

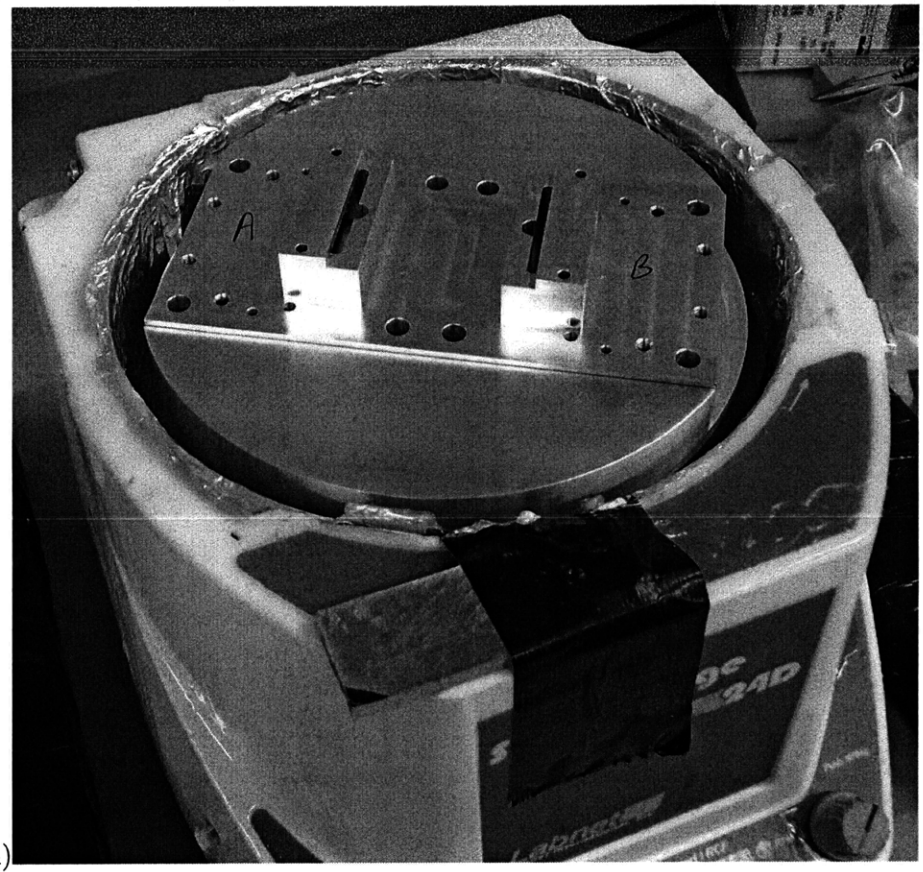

(B)

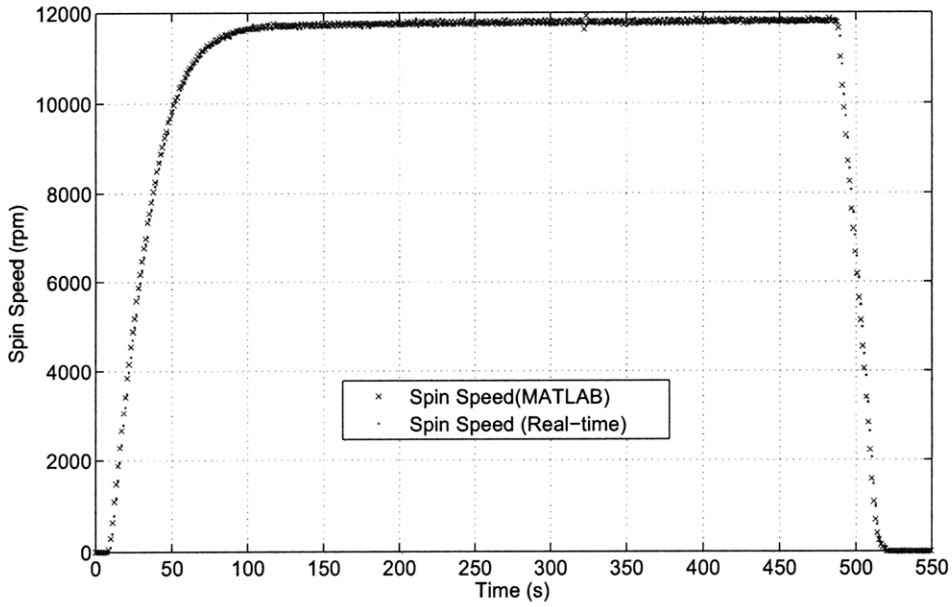

Figure 2-18: (A) Modified centrifuge rotor for creating two parts simultaneously. The rotor diameter is 6.75 in. (171 mm). (B) Measured/calculated spin speed profile of centrifuge rotor assembly in A.

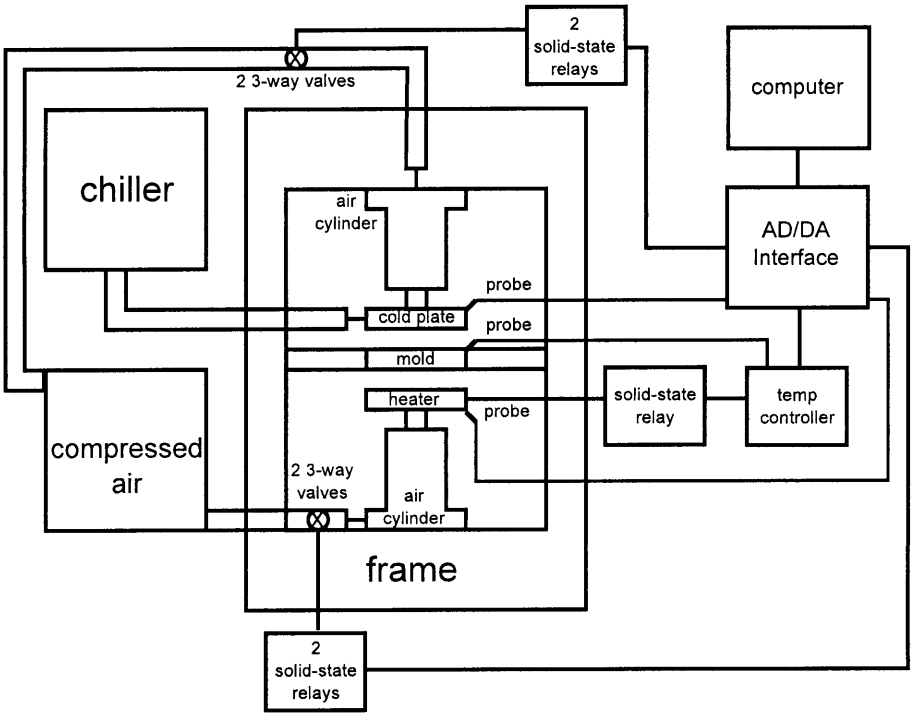

Figure 2-19: The layout for the heating and cooling system, which relies on the basic principle that the cooling and heating of the mold set are performed primarily on the top and bottom surfaces respectively.

bring the heated plate and cold blocks in contact with the mold set, have a diameter of 1.5 in. (38.1 mm). With a pressure of 60 psi (4 atm), there is approximately 100 lbf. (440 N) of force being exerted on the mold set during the heating and cooling portions of the curing cycle.

To insulate the air cylinders from the hot and cold temperatures of the heaters and cold plate, a piece of alumina silicate (ceramic insulation) was placed in between the air cylinder and the hot and cold elements. The alumina silicate as shown in Figure 2-20 has a height of 4 in. (102 mm), a width of 2 in. (50.8 mm), and a depth of 4 in. (102 mm). Within the pieces of alumina silicate, bolts keep the air cylinder, alumina silicate, and heating or cooling element assemblies together. However, there are two sets of bolts in each piece of ceramic which come from the bottom and top, never providing a potential heat path directly from the metal components of the air cylinder to the metal components of the heating or cooling elements.

Figure 2-21 A shows a set of three cooling blocks mounted to a Lytron CP12G02 cold plate. The cooling blocks are cooled down to approximately 5 °C and come down to make contact with the mold set after the heating portion of the cycle is completed. Figure 2-21 A also shows how the mold assembly fits into the mold support. The mold support consists of two plates linked to each other with bolts and spacers. In the middle of the mold support, there is an open region with lips and insulation to support the mold assembly as it gets pushed up from the bottom during heating or pushed down from the top during cooling. The mold support system also allows for easy insertion and removal of the mold assembly. There are spacers in the back of the mold support, which keep the mold assembly in the right location relative to the descending cooling blocks from above.

Figure 2-21 B shows the thin heating plate with two Watlow Ultramic 600 aluminum nitride (ceramic) heaters. Each of these heaters is 50 mm × 50 mm with a thickness of 2.5 mm. These heaters are mounted in between two pieces of aluminum. The heaters have an internal thermocouple, but there is also an Omega thermocouple placed in between the two of them to monitor the temperature of the heating plate assembly. When the mold assembly needs to be heated, the heating plate assembly is pushed up by the bottom air cylinder and makes contact with the bottom of the mold assembly.

To monitor the temperature of the PDMS during curing, two custom-built thermocouple devices were built to be inserted directly into the PDMS fluid. Figure 2-22 shows images

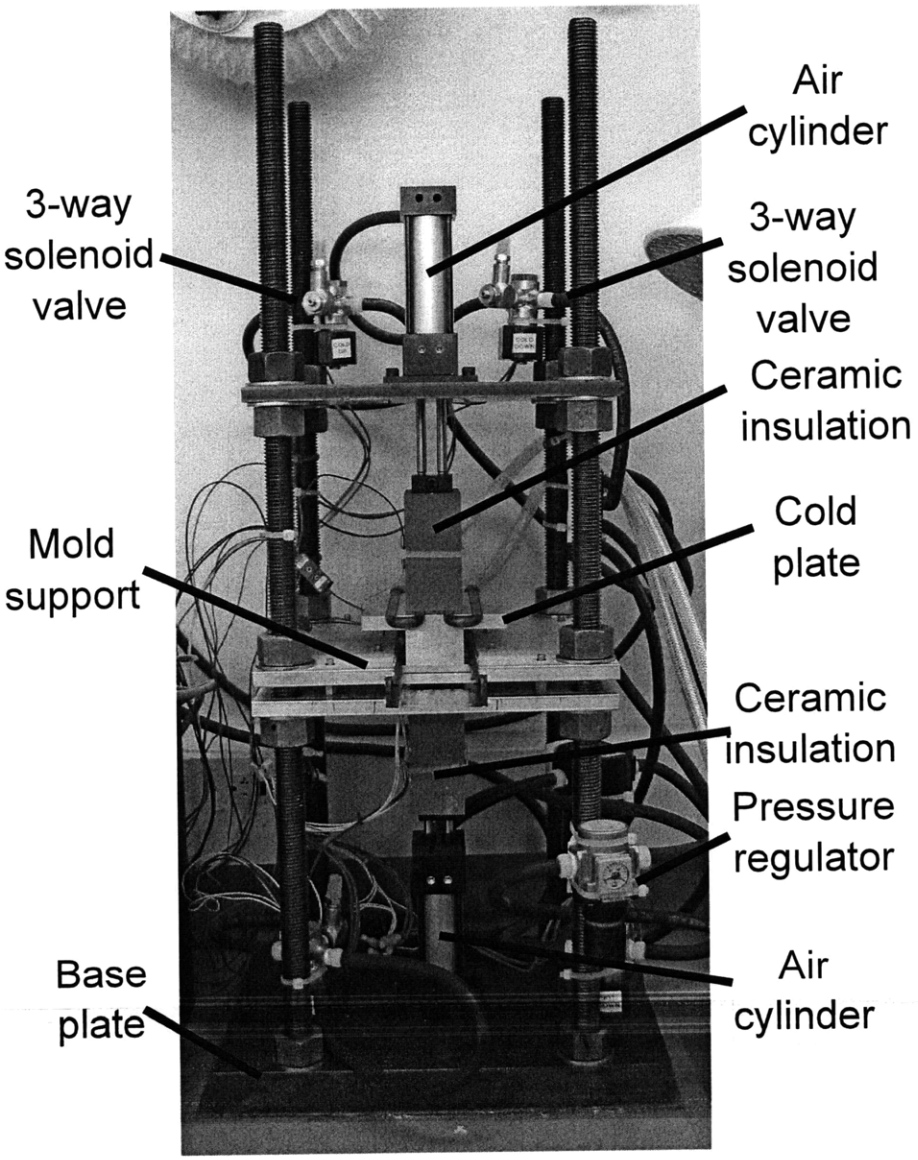

Figure 2-20: Heating and cooling station for curing PDMS. The total height of the system is 3 ft. (91 cm).

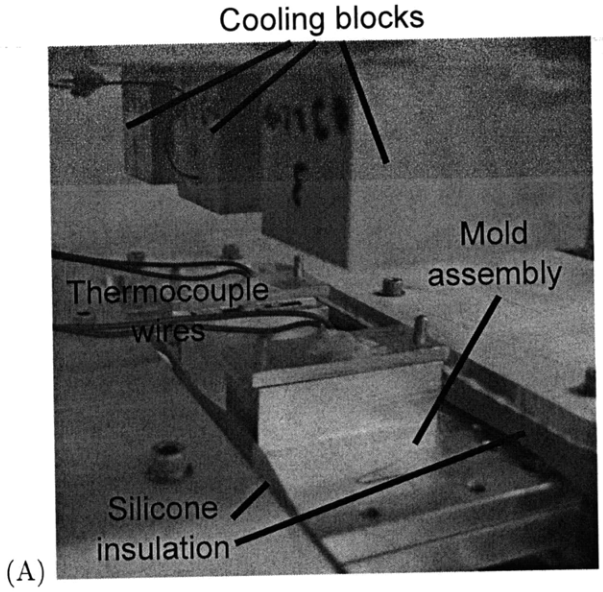

(A)

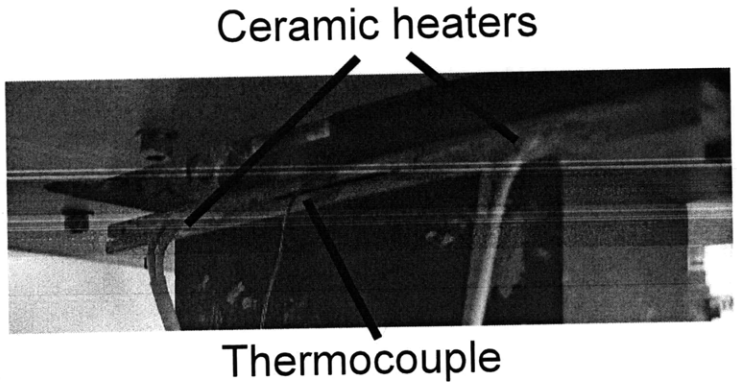

(B)

Figure 2-21: (A) This image shows the mold assembly inserted into the machine with the cooling blocks in the upper, non-contact position. (B) This image shows the heaters and heating assembly, which makes contact with the bottom surface of the mold assembly.

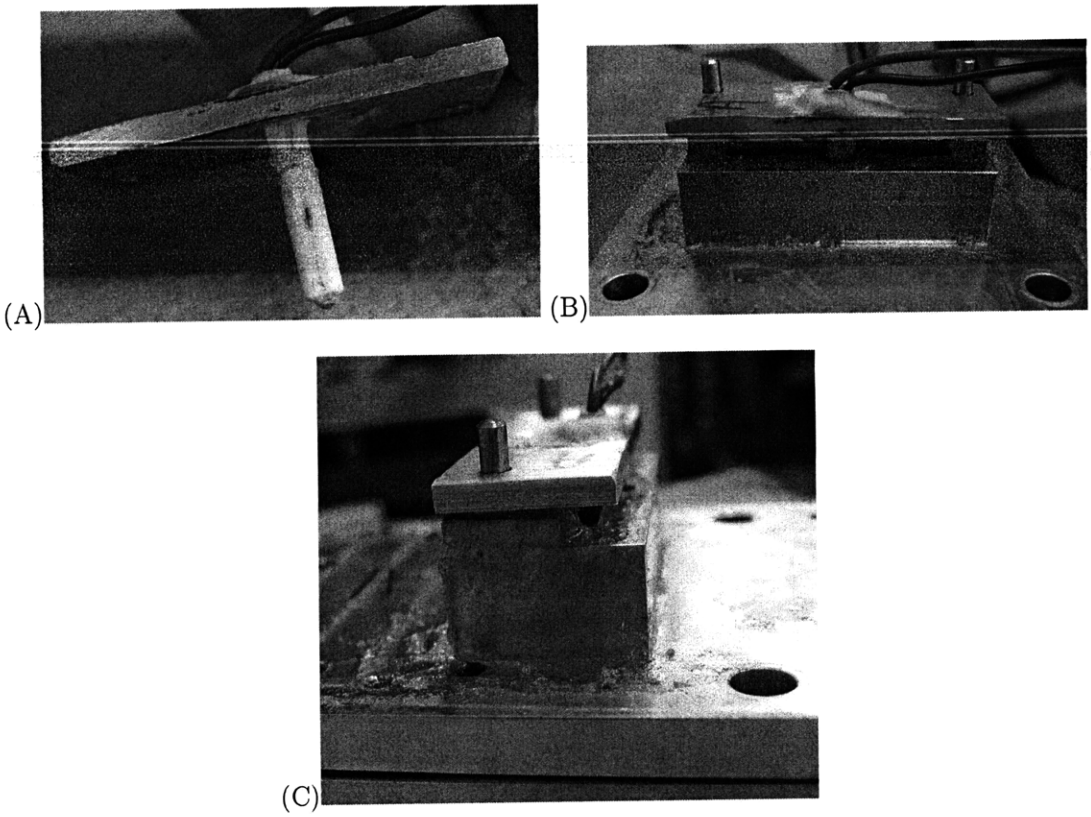

Figure 2-22: (A) Image showing the thermocouple assembly for measuring the temperature of PDMS. (B) Image showing thermocouple assembly inserted into top half of centrifugal mold assembly. (C) Side view image of thermocouple assembly inserted into top half of centrifugal mold assembly.

of the PDMS temperature monitoring assembly. Figure 2-22 shows an Omega T-type thermocouple (COCO-032) run through a trimmed Omega double hole oval piece of ceramic (OV-1-20-100) bonded to a piece of aluminum with Omega OB 400 cement. A little bit of Omega OB 400 cement was also applied at the tip of the thermocouple. The assembly in Figure 2-22 A could then be inserted into the mold set assembly as shown in 2-22 B and C. Dowel pins are used to keep the thermocouple assembly from coming loose during the heating and cooling portions of the curing cycle.

The heaters shown in 2-21 B are activated using Watlow SD series controllers; use of ceramic heaters was inspired by Melinda Hale [49]. The temperature of the PDMS being heated is monitored by the thermocouple assembly in Figure 2-22. The temperature readout from the thermocouple assembly is fed back into the Watlow SD series controllers via a custom-designed LabView PID controller. The transfer function for the LabView PID

controller is given by

$$C = 22\frac{(s+0.1)\,(s+0.004)}{s}, \tag{2.1}$$

which relates the temperature of the measured thermocouple readings within the PDMS in degrees Celsius to the commanded set temperature values to the Watlow SD series controllers in degrees Celsius. The s parameter is a complex conjugate associated with the Laplace transform of the time-based PID controller. The controller given by Equation 2.1 is obviously only implemented during the heating portion of the curing cycle.

During the cooling portion of the curing cycle, the only active controller is the automatic controller built into the VWR 1175 MD Signature Refrigerated Recirculating Chiller used to cool the Lytron cold plate. As shown in Figure 2-21 A, there are a set of cold blocks mounted to the Lytron cold plate. The temperature of these cold blocks will vary by tens of degrees Celsius when cooling the mold set assembly down from 100 °C. However, because of the height and thermal mass associated with the cooling system, the VWR chiller will only show the temperature of the working fluid (combination of water and ethylene glycol) changing by a few degrees Celsius.

Figure 2-23 shows measured temperature profiles of PDMS parts during the heating and cooling of 14 different parts. Ideally, the temperature profiles would overlap each other exactly, but the temperature profiles can vary by approximately 10 °C from one cured PDMS part to anther. The temperature profiles also indicate that the PDMS part toward the front of the heating and curing station (closer to the photographer in Figure 2-20) is heated and cooled a little more rapidly than the PDMS part in the back. This slight difference in heating and cooling rates might be attributed to a larger amount of thermal mass near the rear portion of the machine.

2.6.3 Electronics for curing station

The configuration of the electronics for the curing station was inspired by Melinda Hale [49]. She uses a similar setup in her hot micro-embossing machine. Figure 2-24 A shows a photo taken of the front panel with a couple of emergency stop switches, the thermocontrollers, some switches, and ports for power cables. Figure 2-24 B shows the backside of the same box of electronics without all of the wires installed.

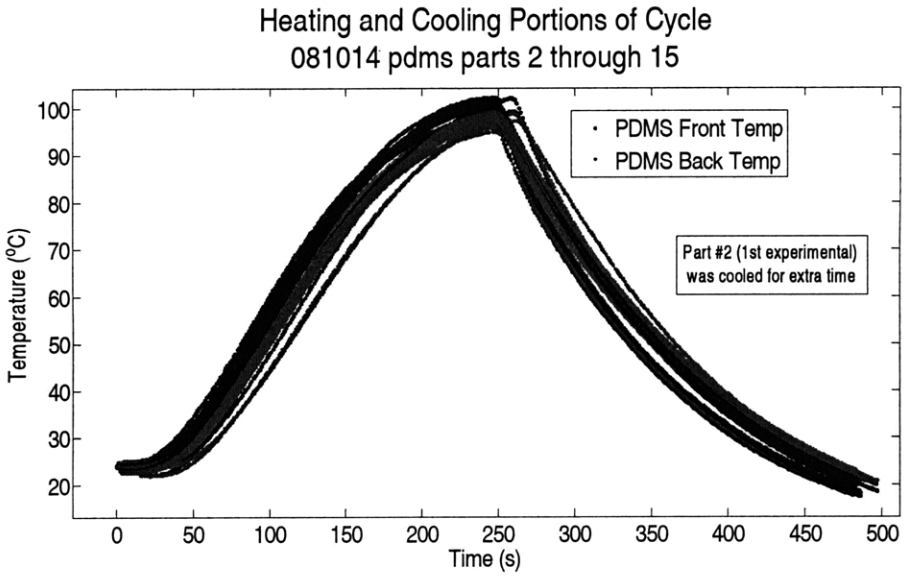

Figure 2-23: Superimposed temperature profiles of the heating and cooling system for the front and back heaters for 14 runs (28 lines shown).

2.6.4 Safety concerns and stress calculations

With high speed machinery, hot surfaces, and pneumatic cylinders, the designed apparatus had to be safe. For the heating and cooling stations, two emergency switches cut off electric power to the system. One switch cuts off power to the heater controllers, and the other cuts power to the air cylinders' valve relays. When the air cylinders' valve relays are not powered, the the valves to both sides of the pistons used in the pneumatic cylinders are open to the room/atmospheric pressure through orifices.

With respect to protection from the fast moving objects associated with the centrifuge, one precaution is the use of a Plexiglas (PMMA) cover purchased from Pacific Bulletproof [5]. The cover has a wall thickness of 1.25 in. (31.8 mm), and the Plexiglas is thick enough to stop a 0.22 caliber round and is a UL listed 752 bullet-resistant material. The cover is placed over the centrifuge, and a strap is run around the cover and the centrifuge. The strap is designed to keep the cover from being largely displaced in the case of an explosion or a flying object coming loose within the enclosure.

From a centrifuge rotor design perspective, the rotor assembly must be able to handle the radial and circumferential stresses that build up during spinning. Often the centrifuge assembly can be approximated as either a solid cylinder with a hole in the middle or a solid

(A)

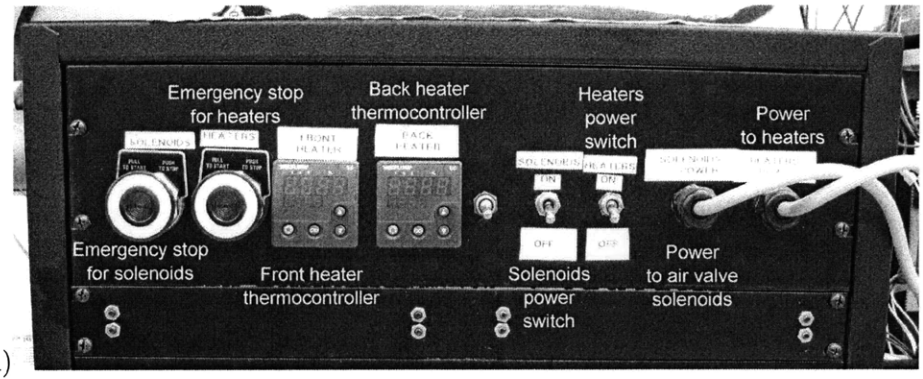

(B)

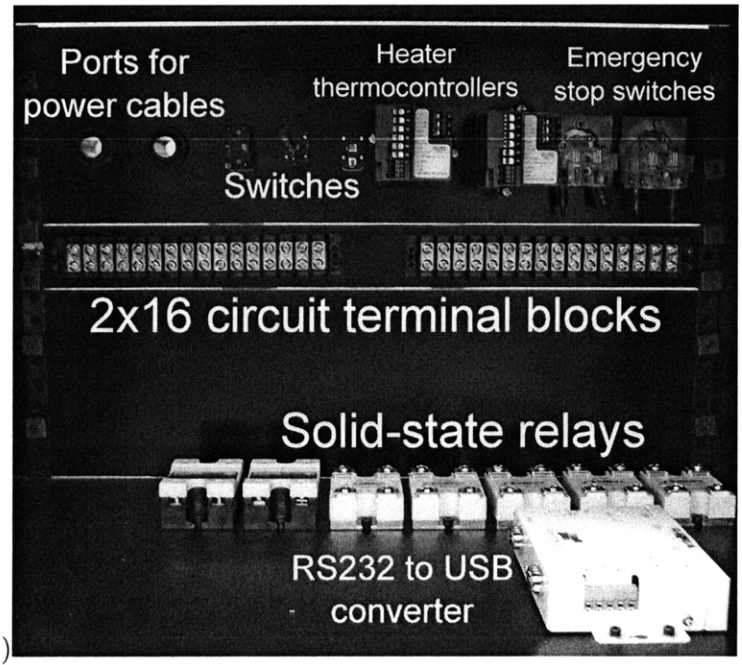

Figure 2-24: (A) Front panel of electronics box for curing station. (B) Backside of the box of electronics before wiring.

disc. For a cylindrical disc with a central hole, the circumferential stresses (T_θ) and radial stresses (T_r) are given by the following [50]:

$$T_\theta = \frac{3+\nu}{8}\rho\omega^2\left(r_i^2 + r_o^2 + \frac{r_i^2 r_o^2}{r^2} - \frac{1+3\nu}{3+\nu}r^2\right) \tag{2.2}$$

$$T_r = \frac{3+\nu}{8}\rho\omega^2\left(r_i^2 + r_o^2 - \frac{r_i^2 r_o^2}{r^2} - r^2\right), \tag{2.3}$$

where ρ is the density of the material of the disc, ω is the spin speed (rad/s), r_i is the radius of the central hole, r_o is the outer radius of the cylinder, ν is the Poisson ratio of the material of the disc, and r is the radial distance from the center of the disc. The maximum circumferential stress occurs at $r = r_i$ and is given by

$$T_{\theta,max} = \frac{3+\nu}{4}\rho\omega^2\left[r_o^2 + \frac{r_i^2(1-\nu)}{3+\nu}\right]. \tag{2.4}$$

The maximum radial stress occurs at $r = \sqrt{r_i r_o}$ and is given by

$$T_{r,max} = \frac{3+\nu}{8}\rho\omega^2(r_i - r_o)^2. \tag{2.5}$$

For a solid cylindrical disc without a hole, the circumferential stresses (σ_θ) and radial stresses (σ_r) are given by the following [50]:

$$T_\theta = \frac{3+\nu}{8}\rho\omega^2\left(r_o^2 - \frac{1+3\nu}{3+\nu}r^2\right) \tag{2.6}$$

$$T_r = \frac{3+\nu}{8}\rho\omega^2(r_o^2 - r^2). \tag{2.7}$$

The maximum stresses occur at $r = 0$ and are given by

$$T_{\theta,max} = T_{r,max} = \frac{3+\nu}{8}\rho(r_o\omega^2). \tag{2.8}$$

Equations 2.2 through 2.8 can be used to estimate the stresses a rotor design may need to withstand. Finite element packages such as ADINA and ALGOR allow for stress analysis with centrifugal loading on more complicated designs.

Finally, within the mold cavity itself, there is significant hydrostatic pressure buildup during spinning as shown in Figure 4-6 A. More than once, the mold cavity assembly failed during attempts to go to higher spin speeds. One reason for failure was not having enough bolts around the outer circumference to keep the two mold halves together as the pressure increased during startup (see Figure 2-7 E). Another was not having a long enough steel bolt-aluminum thread interaction to keep the force on the bolt from ripping the bolt and a few threads of contact right out of the material. When designing a centrifugal casting system, it is necessary to have enough clamping force to keep the mold halves together. The mold halves themselves also need to be strong enough to resist the hydrostatic pressure and maintain a good seal with the o-rings. The hydrostatic pressure adds extra stress to the rotor assembly not accounted for in Equations 2.2 through 2.8.

2.6.5 Mold designs

Micro machined aluminum molds and bulk metallic glass were used as mold inserts for micro or nano feature replication in PDMS. The micro machined aluminum mold shown in Figure 2-25 B was produced by Micro Manufacturing of Northern Illinois. The Vitreloy-1 (bulk metallic glass) mold fabricated by MIT collaborators Hayden Taylor, Lallit Anand and David Henann [57] is shown in Figure 2-25 A. Similar bulk metallic glass molds have also been used for injection molding and hot embossing of thermoplastic-based microfluidic devices for a polymer microfabrication project [51]. Both of these molds are more expensive and time consuming to produce than molds with SU-8 photoresist features patterned on a silicon wafer, but they have the benefit of being more durable for repetitive production of polymer parts.

For the centrifugal casting manufacturing setup, the mold inserts are held in place with screws, as shown in Figure 2-26. The design shown in Figure 2-26 is a physical implementation of the design concept shown in Figure 1-5 D. Two PDMS parts are produced simultaneously from each spinning and curing cycle. After the PDMS parts have been cured, the mold is disassembled, and the parts are removed.

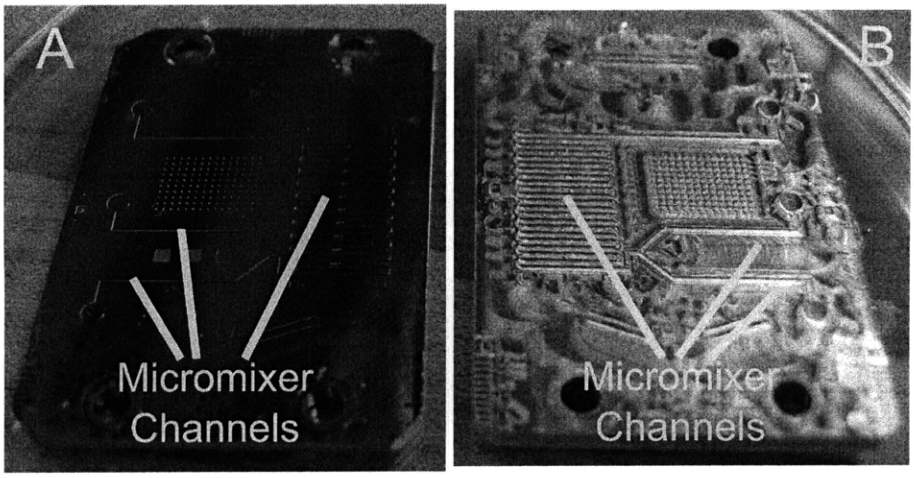

Figure 2-25: (A) Bulk metallic glass mold insert with micro features. (B) Micromachined aluminum insert with micro features and nano surface machining marks.

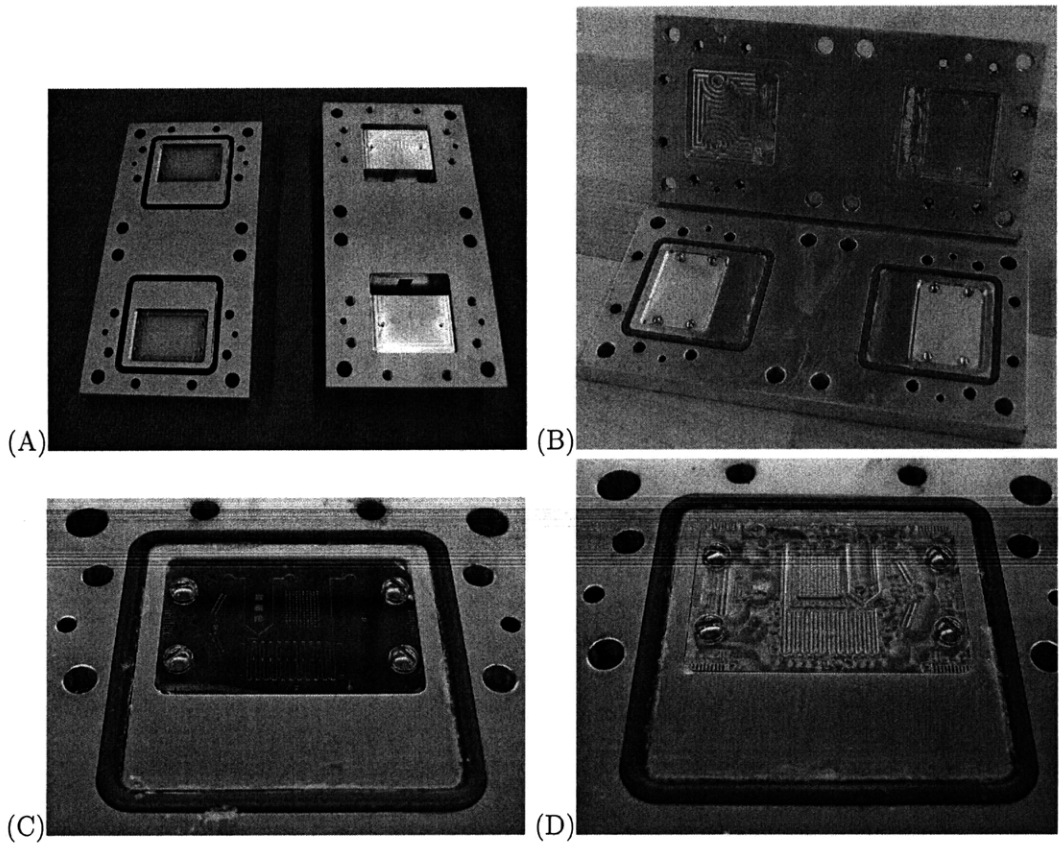

Figure 2-26: (A) Photo showing the empty mold cavities used in the manufacturing system. Inserts can be bolted into tapped holes on the mold half shown on the left. (B) Blank inserts bolted into mold cavities are shown. (C) Bulk metallic glass insert bolted into bottom half of mold assembly. (D) Micro machined, aluminum insert bolted into bottom half of mold assembly.

Chapter 3

Bubble growth, dissolution, and stability

In Chapter 2, degassing or bubble removal from PDMS was identified as one of the rate limiting steps for PDMS component production. For a centrifugally cast part to be free of bubbles, the part needs to be spun long enough for bubbles to disolve or be carried out of solution by buoyancy. This chapter focuses on the necessary conditions for dissolving an air bubble in a liquid. The following subsections focus on the physics of determining a critical bubble size for dissolution, solubility of gases in liquids, diffusion, bubble nucleation, and bubble stability.

3.1 Air bubble stability in centrifugal casting

In centrifugal casting, the PDMS is poured into a reservoir, which is then spun to fill the mold cavity. Some air from the mold cavity gets trapped in the PDMS solution, causing it to be slightly more saturated with air relative to the PDMS's initial state. Two things then happen during spinning: (1) the PDMS tries to return to a normal saturated state via diffusion and the pressure-based, air concentration bondary conditions at all liquid-air interfaces and (2) bubbles move toward the center of the centrifuge (larger ones more quickly than the smaller ones). Diffusion attempts to get air to dissolve into solution from wherever it might be available: trapped bubbles within the bulk of the PDMS and the liquid-air interface near the center of the centrifuge. The movement of bubbles toward the center leaves a distribution of smaller and smaller bubbles in the PDMS as time progresses. Our

objective is to produce PDMS parts, which are bubble free, by either removing the bubbles physically or causing them to shrink and dissolve.

Bubbles shrink or grow depending on the difference between the air concentration inside the bubble wall and the air concentration in the PDMS solution surrounding the bubble. If the concentration of air inside the bubble wall is less than the concentration of air in the solution surrounding the bubble, the bubble will grow as air diffuses into the bubble through the bubble wall. If the concentration of air in the bubble wall is greater than the concentration of air in the solution surrounding the bubble, the bubble will shrink.

The concentration of air in the bulk of the PDMS solution is initially slightly supersaturated from the centrifugal startup. During the spinning process, the air concentration in the bulk of the PDMS solution remains fairly constant. However, the air concentration in a PDMS bubble wall is dependent on the bubble's internal pressure according to Henry's Law. Higher internal bubble pressures will correspond to higher concentrations of air in the bubble walls. The Laplace-Young bubble equilibrium equation, which relates the internal bubble pressure and the pressure in the surrounding solution to surface tension and the bubble diameter, states that the internal bubble pressure will be greater for bubbles with smaller diameters and also increases when the pressure of the surrounding fluid increases.

During the centrifugal process, smaller and smaller bubbles are left in the solution as time progresses. Smaller bubbles in PDMS have higher internal pressures than larger bubbles. Since the air concentration in PDMS scales linearly with increases in pressure according to Henry's Law, the air concentration in the bubble wall will be larger for smaller bubbles. If the air concentration in the bubble wall is larger than the air concentration of the surrounding PDMS fluid, the bubble will shrink and eventually dissolve completely.

3.2 Gas solubility in liquids

Solubility describes the quantity of solute/penetrant that can be supported or maintained in a solvent. In this study, the concern is the amount of dissolved air PDMS can support at a specified pressure in the bulk of the fluid or inside the bubble wall. Two theories for describing the solubility of a gas in a liquid are embodied in Henry's Law and the Flory-Huggins treatment.

Table 3.1: Henry's coefficients for selected gases in liquid PDMS. [62, 80]

Gas	k_D (cm^3 gas STP) / (cm^3 polymer atm)	k_D (kg gas)/ (m^3 polymer Pa)	Gas Molecular Weight (kg/kmol)
N_2	0.127	$1.567x10^{-6}$	28.01
O_2	0.224	$3.158x10^{-6}$	32.00
Ar	0.256	$4.506x10^{-6}$	39.95
CH_4	0.528	$3.731x10^{-6}$	16.04

3.2.1 Henry's Law

Henry's Law is often utilized to describe the concentration of gas in a fluid. This law states the following:

$$c = k_D p, \tag{3.1}$$

where c is the concentration of gas in the solution (units of mass per volume), k_D is Henry's coefficient (units of mass per volume per pressure), and p is the penetrant pressure [41]. Henry's law can be used to calculate the concentration of air in PDMS. The air in our atmosphere at sea level is composed of 78.08% nitrogen gas, 20.95% oxygen gas, and 0.93% argon gas by volume [80]. The Henry's constant for these gases in liquid PDMS are given in Table 3.1. The conversion factor for nitrogen gas for the table value listed is $1.234x10^{-5}$ (kg gas/ (m^3 polymer Pa)) /(cm^3 air STP/ (cm^3 polymer atm))with a standard temperature of 273 K, a standard pressure of $101.3x10^3$ Pa, and the molecular weight of the specified gas. The conversion factors for the other gases are different because the gases have different molecular weights.

3.2.2 Flory-Huggins treatment

For some gases at high pressures, the linear relationship described by Henry's law is not adequate for describing the concentration of a gas in the solution. These departures from linearity are described by the Flory-Huggins treatment. One extended form of the Flory-Huggins treatment for vapor sorption in a cross-linked rubber developed by Flory and used by Fleming and Koros [41] is

$$\ln(p/p_o) = \ln(1 - v_p) + v_p + \chi v_p^2 + V_1(v_e/V_o)(v_p^{1/3} - v_p/2), \tag{3.2}$$

where p is the penetrant pressure, p_o is the vapor pressure of the penetrant, χ is the Flory-Huggins parameter, V_1 is the molar volume of the penetrant, v_e is the effective number of cross-links expressed in moles, V_o is the volume of the dry polymer, and v_p is the volume fraction of the polymer. Using Equation 3.2 at 35°C with CO_2 dissolved in silicone rubber and Equation 3.3 relating sorption or concentration of gas in the rubber c to v_p, they were able to get good agreement with deviations from Henry's law at pressures greater than 300 psi.

$$v_p = 1 - \frac{cV_1/22415\text{cm}^3}{cV_1/22415\text{cm}^3 + 1} \tag{3.3}$$

Their values for p_o, χ, V_1, and v_e/V_owere 78 atm, 0.75, 46 cm^3/mol, 1.24x10^{-4} gmol/cm^3 respectively. For pressures less than 300 psi, their data was in good agreement with a Henry's law coefficient of 1.385 cm^3 STP/(cm^3polymer atm).

A simpler Flory-Huggins treatment used by Kamiya et. al. [62] to model their sorption experimental results in liquid PDMS is given by

$$c = \frac{k_D p}{1 - \sigma k_D p}, \tag{3.4}$$

where σ is a constant relating polymer and gas interaction. For CO_2 dissolved in liquid PDMS, Kamiya et. al. found a Henry's coefficient of 1.39 cm^3 STP/(cm^3polymer atm) and a σ of 0.0073. When σ goes to zero, Equation 3.4 reduces to Equation 3.1 or Henry's Law. Table 3.1 again shows results from their study with nitrogen, oxygen, argon, and methane gases. In their work, they state that these four gases have negligible σ terms to match their experimental results. Thus, the solubility of nitrogen, oxygen, and argon (the three primary components in air) in PDMS can be adequately described using the linear relationship of Henry's Law without need for the more elaborate Flory-Huggins treatment.

3.2.3 Solubility's temperature dependence

Henry's coefficient is often termed Henry's constant, but in reality Henry's coefficient is not a constant and has a non-linear relationship with temperature [104]. In general, a solution can support a higher concentration of a given gas solute at higher temperatures. However, that is not always the case as described in Section 4.7.3.

3.3 Growing or dissolving bubbles

In 1950, Epstein and Plesset published a seminal work describing diffusional growth or dissolution of an air bubble in water. In one case, they ignored surface tension. In the more realistic case, they included surface tension. Their results are applicable to air bubbles in PDMS as well.

3.3.1 Epstein-Plesset bubble with no surface tension

Epstein and Plesset [39] start their derivation of diffusional bubble growth or shrinkage with the diffusion equation and no advective term:

$$\frac{\partial c}{\partial t} = \kappa \frac{\partial^2 c}{\partial r^2}, \tag{3.5}$$

where c is the concentration of gas at a distance r from the center of the bubble, t is time, and κ is the diffusion coefficient. The center of the bubble is placed at the origin of spherical coordinates with r describing a point's distance away from the origin. The boundary conditions for this bubble are

$$\begin{aligned} &c(r,0) = c_i \text{ for } r > R \\ &\lim_{r\to\infty} c(r,t) = c_i \text{ for } \quad t > 0 \\ &c(R,t) = c_s \text{ for } t > 0, \end{aligned} \tag{3.6}$$

where R is the bubble radius, c_i is the initial air concentration of dissolved air in the surrounding solution, and c_s is the concentration of dissolved gas in the bubble wall.

In their initial derivation, they assume no surface tension, and the resulting differential equation from their derivation describes the change of the bubble's radius with respect to time:

$$\frac{dR}{dt} = \frac{\kappa\delta}{\rho}\left\{\frac{1}{R} + \frac{1}{(\pi\kappa t)^{1/2}}\right\}, \tag{3.7}$$

where ρ is the density of the air (assumed to be constant) and $\delta = c_i - c_s$. From this derivation for a bubble without surface tension and for $t > 0$, it becomes apparent that if $c_i > c_s$, then dR/dt will be positive and the bubble will grow. If $c_i < c_s$, then dR/dt will be negative and the bubble will shrink. Figure 3-1 depicts the shrinking or growing behavior

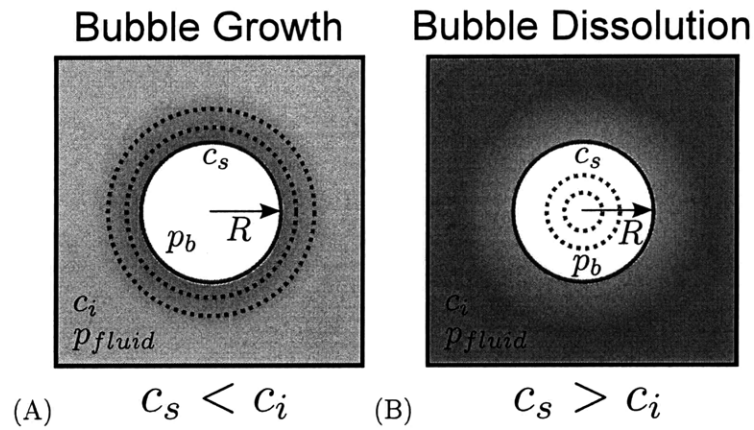

Figure 3-1: (A) Bubble growing by diffusion due to higher concentration of air in the solution surrounding the bubble than in the bubble wall. (B) Bubble shrinking by diffusion due to lower concentration of air in the solution surrounding the bubble than in the bubble wall. Figure inspired by [72].

depending on the direction of the concentration gradient. Epstein and Plesset also express Equation 3.7 in the following form:

$$\frac{dR}{dt} = \alpha \left\{ \frac{1}{R} + \frac{1}{(\pi \kappa t)^{1/2}} \right\}, \tag{3.8}$$

where $\alpha = \kappa (c_i - c_s) / \rho = \kappa d (f - 1)$. The d term becomes c_s/ρ, and the f term becomes c_i/c_s.

They derive parametric expressions for the growth of a bubble without surface tension in a supersaturated solution to avoid the need of numerical integration:

$$R = R_o e^{\gamma z} \left\{ \cosh \left[\left(1+\gamma^2\right)^{1/2} z \right] + \gamma \left(1+\gamma^2\right)^{-1/2} \sinh \left[\left(1+\gamma^2\right)^{1/2} z \right] \right\} \tag{3.9}$$

$$t = \left\{ \frac{R_o}{\sqrt{2\alpha}} e^{\gamma z} \left(1+\gamma^2\right)^{-1/2} \sinh \left[\left(1+\gamma^2\right)^{1/2} z \right] \right\}^2. \tag{3.10}$$

The above expressions for a growing bubble are accompanied with the following additional relationships:

$$\gamma = \left(\frac{c_i - c_s}{2\pi\rho}\right)^{1/2} \tag{3.11}$$

$$\alpha = \kappa\left(c_i - c_s\right)/\rho \tag{3.12}$$

$$= \kappa d\left(f - 1\right) \tag{3.13}$$

$$d = c_s/\rho. \tag{3.14}$$

where R is the radius of the growing bubble, R_o is the initial size of the bubble, t is time, c_i is the uniform concentration of gas dissolved in the fluid, c_s is the dissolved gas concentration of a saturated fluid at the given temperature and pressure, κ is the coefficient of diffusivity, and ρ is the density of the gas.

For a dissolving or shrinking bubble, they derived the following parametric expressions:

$$R = R_o e^{-\gamma z}\left\{\cos\left[\left(1-\gamma^2\right)^{1/2} z\right] - \gamma\left(1-\gamma^2\right)^{-1/2}\sin\left[\left(1-\gamma^2\right)^{1/2} z\right]\right\} \tag{3.15}$$

$$t = \left\{\frac{R_o}{\sqrt{2\alpha}} e^{-\gamma z}\left(1-\gamma^2\right)^{-1/2}\sin\left[\left(1-\gamma^2\right)^{1/2} z\right]\right\}^2. \tag{3.16}$$

The above expressions for a dissolving bubble are accompanied with the following additional relationships:

$$\gamma = \left(\frac{c_s - c_i}{2\pi\rho}\right)^{1/2} \tag{3.17}$$

$$\alpha = \kappa\left(c_s - c_i\right)/\rho \tag{3.18}$$

$$= \kappa d\left(1 - f\right) \tag{3.19}$$

$$d = c_s/\rho. \tag{3.20}$$

3.3.2 Epstein-Plesset bubble with surface tension

Epstein and Plesset also derived an analytical differential equation to describe the bubble growth or shrinkage in time including the effects of surface tension. They start using the Young-Laplace relationship and the Ideal Gas Law to describe the pressure within the bubble. The Young-Laplace relationship can be expressed as

$$P_b - p = \frac{4\sigma}{d}, \tag{3.21}$$

and they derived the following:

$$\begin{aligned} P_b &= p + \frac{2\sigma}{R} && (3.22) \\ &= \frac{BT\rho(R)}{M}, && (3.23) \end{aligned}$$

where P_b is the pressure within the bubble, p is the liquid pressure, σ is the surface tension, B is the universal gas constant 8.314 J/(mol K), M is the molecular weight of the gas, and $\rho(R)$ is the density of the gas within the bubble. They describe the density of the gas within the bubble with the following:

$$\begin{aligned} \rho(R) &= \frac{M}{BT}p + \frac{2M\sigma}{BT}\frac{1}{R} && (3.24) \\ &= \rho_\infty + \tau/R, && (3.25) \end{aligned}$$

where ρ_∞ is the density of the air at the pressure and temperature of the liquid surrounding the fluid and $\tau = 2M\sigma/(BT)$.

The mass of gas in the bubble is given by

$$m = \frac{4\pi}{3}R^3\rho(R) \tag{3.26}$$

and the rate of change of mass is

$$\frac{dm}{dt} = 4\pi R^2 \frac{dR}{dt}\left\{\rho_\infty + \frac{2\tau}{3R}\right\}. \tag{3.27}$$

Using the principle of diffusion (Equation 3.5) and the appropriate boundary conditions (Equation 3.6), Plesset and Epstein also express the rate of change of mass as

$$\frac{dm}{dt} = 4\pi R^2 \kappa \left(c_i - c_s\right)\left\{\frac{1}{R} + \frac{1}{(\pi\kappa t)^{1/2}}\right\}. \tag{3.28}$$

By equating Equations 3.27 and 4.31, they arrive at the following:

$$\frac{dR}{dt} = \frac{\kappa\left(c_i - c_s\right)}{\rho_\infty + 2\tau/(3R)} \left\{ \frac{1}{R} + \frac{1}{(\pi\kappa t)^{1/2}} \right\}. \tag{3.29}$$

As in Equation 3.7 for $t > 0$, it becomes apparent that if $c_i > c_s$, then dR/dt will be positive and the bubble will grow. If $c_i < c_s$, then dR/dt will be negative and the bubble will shrink. However, in this case, the c_s term is dependent on the radius of the bubble, and Epstein and Plesset give the following expression:

$$c_s = \left[\rho_\infty + \tau/R\right] d, \tag{3.30}$$

stating "the value of d is the same as that used in the previous formulation since it may be shown that d is not affected by surface tension effects." The previous formulation they refer to is the formulation given in Section 3.3.1, where in Equation 3.19, $d = c_s/\rho(R)$.

Epstein and Plesset make no mention of Henry's coefficient in their paper, but using Equation 3.1 in Section 3.2.1 gives us a relationship for the concentration of air/gas in the bubble wall:

$$c_s = k_D p_b, \tag{3.31}$$

where p_b is the internal bubble pressure. Another expression for the density of the air within the bubble follows using Equation 3.24 with Equation 3.21:

$$\begin{aligned}
\rho(R) &= \frac{M}{BT} p + \frac{2M\sigma}{BT} \frac{1}{R} && (3.32)\\
&= \frac{M}{BT} \left[p + \frac{2\sigma}{R} \right] && (3.33)\\
&= \frac{M}{BT} \left[p + p_b - p \right] && (3.34)\\
&= \frac{M}{BT} p_b. && (3.35)
\end{aligned}$$

Rearranging this final expression in Equation 3.35 and using it with Equation 3.31, the following expressions result:

$$c_s = k_D\left(\frac{BT\rho(R)}{M}\right) \tag{3.36}$$

$$c_s/\rho(R) = \frac{k_D BT}{M}, \tag{3.37}$$

which agree with Epstein and Plesset's comments about their expression for d having no dependence on surface tension. However, the $c_s/\rho\,(R)$ has a dependence on temperature and the Henry's coefficient.

Epstein and Plesset's work includes the following ordinary differential equation:

$$\frac{dR}{dt} = -\kappa d\frac{1-f+\tau/\left(R\rho_\infty\right)}{1+2\tau/\left(3R\rho_\infty\right)}\left\{\frac{1}{R}+\frac{1}{\left(\pi\kappa t\right)^{1/2}}\right\} \tag{3.38}$$

with the accompanying relationships:

$$\tau = \frac{2M\sigma}{BT} \tag{3.39}$$

$$\rho_\infty = \frac{M}{BT}p \tag{3.40}$$

$$\rho = \rho_\infty + \tau/R \tag{3.41}$$

$$d = c_i/\left(\rho_\infty f\right), \tag{3.42}$$

where R is the radius of the growing bubble, M is molecular weight of the gas (28.97 kg/1000 mol), t is time, c_i is the initial concentration of gas dissolved in the fluid, c_s is the dissolved gas concentration in the bubble wall, κ is the coefficient of diffusivity, and ρ_∞ is the density of the gas in the bulk solution or in a bubble with zero curvature (infinite radius).

For the sake of clarity, the parameter f has a slightly different meaning in Equations 3.38 and 3.39 than in Section 3.3.1. Using the relationships in Equation 3.39, the following can be shown:

$$
\begin{aligned}
f &= \frac{c_i}{\rho_\infty}\frac{\rho(R)}{c_s} && (3.43)\\
&= \frac{c_i\left(\rho_\infty + \tau/R\right)}{\rho_\infty c_s} && (3.44)\\
&= \frac{c_i}{c_s}\left(1 + \frac{\tau}{R\rho_\infty}\right) && (3.45)\\
&= \frac{c_i}{c_s}\left(1 + \frac{2\sigma}{Rp}\right) && (3.46)\\
&= \frac{c_i}{c_s}\left(\frac{p_b}{p}\right). && (3.47)
\end{aligned}
$$

If a bubble has no curvature (infinite radius), then f becomes c_i/c_s, which is the same value used in Section 3.3.1. Otherwise, f is dependent on the radius of curvature of the bubble. In reality, however, the p_b/p term is very nearly 1 for large bubbles. For example, if the bubble size is 10 microns and the surface tension is 0.02 N/m (surface tension for air-PDMS at room temperature) [116, 117, 97, 38, 88, 91], then $p_b/p = 1.04$. For their study, Epstein and Plesset generally kept f constant when calculating bubble growth or dissolution times.

Epstein and Plesset did not have the same computational power in 1950 as currently available, so they developed parametric relationships to analytically calculate values for their model without surface tension (Section 3.3.1) and estimates to calculate values for their model with surface tension. Given the current relative ease and access to basic numerical solvers for first order ordinary differential equations, this work implements the Epstein and Plesset model with surface tension numerically. To verify this numerical implementation of Equation 3.38, the following table is included showing Epstein and Plesset's estimate values and the numerically determined values using the MATLAB **ode45** function, which implements a Runge-Kutta solver. This implementation is similar to that performed by Kloek et. al [71].

Even though our numerical implementation of Equation 3.38 matches Epstein and Plesset's results for air bubbles in water, there seems to be a simpler form of their differential equation, which is more intuitive for the bubbles of concern in this work. In Equation 3.48, the derivative of the bubble radius with respect to time is dependent on the difference between the concentration of dissolved air is the bubble wall and in the surrounding liquid.

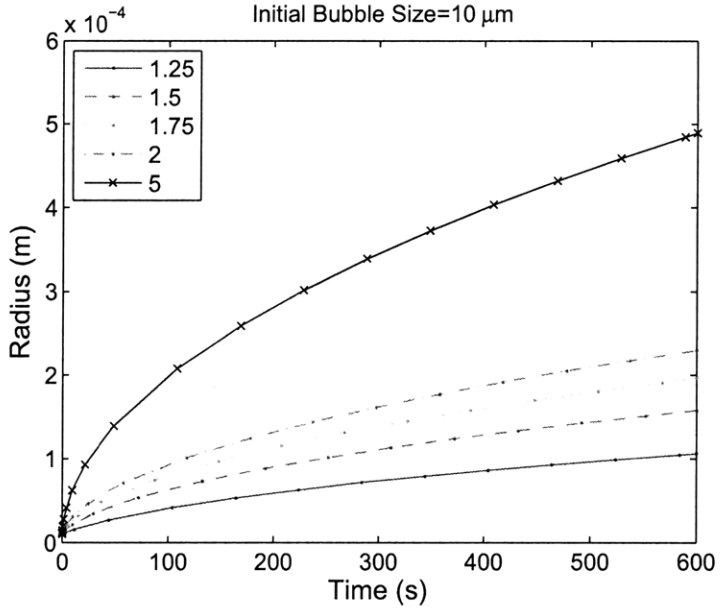

(A)

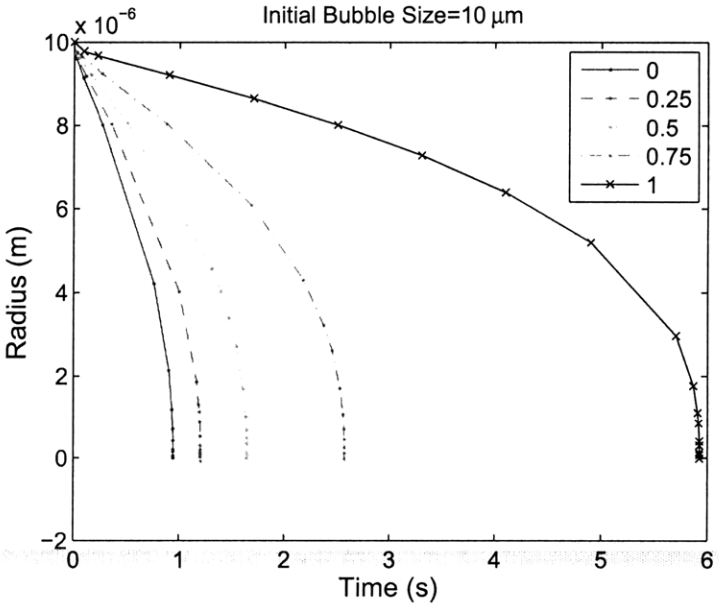

(B)

Figure 3-2: Numerical implementation of Epstein-Plesset bubble growth and dissolution model for air bubbles in water. Initial bubble radius is 10 μm, and the legends show diferent values for the f parameter as described by Epstein and Plesset.

Table 3.2: Numerical Implementation of Epstein-Plesset Bubble Growth or Dissolution with Surface Tension

f	Plesset $R_o = 10\ \mu$m Time(s)	Numerical $R_o = 10\ \mu$m Time(s)	Plesset $R_o = 100\ \mu$m Time(s)	Numerical $R_o = 100\ \mu$m Time(s)	Comments
0	1.17	0.95	124	101	Dissolution
0.25	1.46	1.21	164	136	Dissolution
0.50	1.96	1.65	241	206	Dissolution
0.75	2.99	2.58	460	406	Dissolution
1.00	6.63	5.93	588	550	Dissolution
1.25	567	537	50,100	47,301	$10R_o$ Growth
1.50	266	246	24,900	22,996	$10R_o$ Growth
1.75	174	159	16,600	15,134	$10R_o$ Growth
2.00	129	116	12,400	11,166	$10R_o$ Growth
5.00	31.7	26	3,100	2,548	$10R_o$ Growth

Thinking of the c_s term with respect to Henry's Law (Equation 3.31) and the Laplace-Young relationship (Equation 3.21), the following results:

$$\frac{dR}{dt} = \frac{\kappa\left(c_i - k_D p_b\right)}{\rho_\infty + 2\tau/(3R)}\left\{\frac{1}{R} + \frac{1}{(\pi\kappa t)^{1/2}}\right\} \tag{3.48}$$

$$= \frac{\kappa\left(c_i - k_D\left(p_{fluid} + 2\sigma/R\right)\right)}{\rho_\infty + 2\tau/(3R)}\left\{\frac{1}{R} + \frac{1}{(\pi\kappa t)^{1/2}}\right\} \tag{3.49}$$

In order for a bubble to grow, the $c_i - k_D\left(p_{fluid} + 2\sigma/R\right)$ expression must be greater than zero. Likewise, the bubble will shrink if $c_i - k_D\left(p_{fluid} + 2\sigma/R\right)$ is less than zero. The form in Equation 3.40 shows whether or not a bubble will grow or shrink. Another parameter $c_{s\infty}$ can be defined as follows:

$$c_{s\infty} = k_D p_{fluid}. \tag{3.50}$$

Equation 3.50 is essentially the same parameter as c_s (concentration of dissolved air in the bubble wall) used in Section 3.3.1 where the radius of the bubble is infinite. Defining another term $c_f = c_i/c_{s\infty}$, Equation 3.48 can be rewritten as

$$\frac{dR}{dt} = \frac{\kappa\left(c_f c_{s\infty} - k_D\left(p_{fluid} + 2\sigma/R\right)\right)}{\rho_\infty + 2\tau/(3R)}\left\{\frac{1}{R} + \frac{1}{(\pi\kappa t)^{1/2}}\right\} \tag{3.51}$$

$$= \frac{\kappa\left(c_f c_{s\infty} - k_D p_{fluid} - 2k_D\sigma/R\right)}{\rho_\infty + 2\tau/(3R)}\left\{\frac{1}{R} + \frac{1}{(\pi\kappa t)^{1/2}}\right\} \tag{3.52}$$

$$= \frac{\kappa\left(c_f c_{s\infty} - c_{s\infty} - 2k_D\sigma/R\right)}{\rho_\infty + 2\tau/(3R)}\left\{\frac{1}{R} + \frac{1}{(\pi\kappa t)^{1/2}}\right\} \tag{3.53}$$

$$= \frac{\kappa\left(c_{s\infty}\left(c_f - 1\right) - \frac{2k_D\sigma}{R}\right)}{\rho_\infty + 2\tau/(3R)}\left\{\frac{1}{R} + \frac{1}{(\pi\kappa t)^{1/2}}\right\}. \tag{3.54}$$

Now, if $c_f \leq 1$, the bubble will always shrink regardless of its radius. However, if $c_f > 1$, the bubble may or may not shrink depending on its radius R. For the case when $c_f > 1$, the following condition must hold for the bubble to shrink:

$$R < \frac{2k_D\sigma}{c_{s\infty}\left(c_f - 1\right)} \tag{3.55}$$

$$< \frac{2\sigma}{p_{fluid}\left(c_f - 1\right)} \tag{3.56}$$

Conversely, if $R > 2\sigma/\left[p_{fluid}\left(c_f - 1\right)\right]$ for a $c_f > 1$, then the bubble will grow. Using the Epstein-Plesset model and Equation 3.51, growth or dissolution times have been compiled in Table 3.3 and Table 3.4. These tables provide some insight into the time requirements for bubbles to grow or shrink. The Henry's coefficient was estimated using the values in Table 3.1, along with the concentration of these gases in the atmosphere at sea level. The diffusivity of nitrogen gas in PDMS was estimated by using the diffusivity of nitrogen gas in PDMS ($1.47\text{x}10^{-5}\text{cm}^2/\text{s}$) reported by Singh, et. al. [103].

3.3.3 Bubble dissolution with viscosity

Viscosity can retard shrinkage but not prevent dissolution, while elasticity can stop growth [71]. In its uncured state, liquid PDMS does not have any elasticity to it. So, once the bubble shrinking process has begun in uncured, liquid PDMS, it should end with dissolution.

Kloek et. al. [71], Zana and Leal [122], Kim, et. al. [68], and others have derived relationships for diffusional bubble growth or dissolution including the viscosity of the fluid. Kon-

Table 3.3: Dissolution or diameter growth to 100 μm using the Epstein-Plesset model in the form of Equation 3.51. G indicates growth; D indicates dissolution. Table contains time values in seconds. A pressure of 101.3 kPa (1 atm), a Henry's Coefficient of $1.927\text{x}10^{-6}$kg (air)/m^3 (PDMS)/Pa, and a diffusion coefficient of $1.47\text{x}10^{-9}$ m^2/s were used for these calculations.

Bubble Diameter (μm)	c_f 0.995	c_f 1.00	c_f 1.005	c_f 1.010	c_f 1.015	c_f 1.020	c_f 1.025	c_f 1.03	c_f 1.035	c_f 1.040
10	D	D	D	D	D	D	D	D	D	D
	0.38	0.40	0.42	0.44	0.47	0.50	0.53	0.57	0.62	0.67
25	D	D	D	D	D	D	D	D	G	G
	5.5	6.2	7.1	8.3	10	13	18	36	240	187
50	D	D	D	D	D	G	G	G	G	G
	40	50	66	101	283	422	268	193	150	123
75	D	D	D	D	G	G	G	G	G	G
	124	168	271	950	341	182	123	93	74	62
100	D	D	D	G	G	G	G	G	G	G
	270	399	819	0	0	0	0	0	0	0
125	D	D	D	G	G	G	G	G	G	G
	490	781	2212	N/A	N/A	N/A	N/A	N/A	N/A	N/A

Table 3.4: Dissolution or diameter growth to 100 μm using the Epstein-Plesset model in the form of Equation 3.51. G indicates growth; D indicates dissolution. Table contains time values in seconds. A pressure of 506.5 kPa (5 atm), a Henry's Coefficient of $1.927\text{x}10^{-6}$kg (air)/m^3 (PDMS)/Pa, and a diffusion coefficient of $1.47\text{x}10^{-9}$ m^2/s were used for these calculations.

Bubble Diameter (μm)	c_f 0.90	c_f 0.975	c_f 0.985	c_f 0.995	c_f 1.00	c_f 1.005	c_f 1.010	c_f 1.015	c_f 1.020	c_f 1.03	c_f 1.040
10	D	D	D	D	D	D	D	D	G	G	G
	0.3	0.9	1.6	1.6	2.0	2.7	4.1	11.7	292	180	130
25	D	D	D	D	D	D	G	G	G	G	G
	2.4	8.2	12	20	32	92	643	375	265	166	120
50	D	D	D	D	D	G	G	G	G	G	G
	10	39	59	121	263	1335	470	283	202	127	92
75	D	D	D	D	D	G	G	G	G	G	G
	24	92	145	326	892	676	256	156	111	70	50
100	D	D	D	D	D	G	G	G	G	G	G
	43	170	270	644	2123	0	0	0	0	0	0
125	D	D	D	D	D	G	G	G	G	G	G
	67	271	436	1079	4157	N/A	N/A	N/A	N/A	N/A	N/A

topoulou and Vlachopoulos [72] applied diffusional bubble dissolution models with viscosity to rotational molding. They modeled bubble dissolution in polyethylene using viscosity values of 500 Pa s, 5000 Pa s, and 10000 Pa s (all of which are at least two orders of magnitude greater than the viscosity of PDMS) and determined that for these values "the effect of viscosity is marginal and is more prominent at longer times, when bubble diameter becomes small." Gogos [46] also addresses bubble dissolution in rotational molding, cites the work of Kontopoulou and Vlachopoulos [72], and ignores the effects of viscosity in his calculations. In both works by Kontopoulou and Gogos, the authors assume the bubble is stationary. They also model the case of a single bubble in an infinite medium. Given the effect of the material's viscosity has only "marginal effects" on bubble growth/dissolution and in order to maintain the simplicity of solving the first order differential equation, viscosity is ignored in modeling bubble dissolution for this work.

3.4 Bubble growth experiments

Section 3.3 covered models for predicting bubble growth or dissolution. Bubble dissolution will be revisited in the context of centrifugal casting in Chapter 4. This section focuses on a method to estimate the initial c_f parameter, the ratio of air concentration dissolved within the bulk of the PDMS after centrifugal startup to the air concentration within a bubble of infinite radius at atmospheric pressure. This initial air concentration parameter is difficult to measure directly but can be estimated based on the rate a bubble grows if the fluid pressure, diffusion coefficient, and surface tension of the fluid are known. Using these three values, along with recorded bubble growth data, the c_f parameter was adjusted to fit the bubble growth model to the observed results. Videos of bubbles growing in PDMS were taken after spinning the PDMS for 30 seconds with a set spin speed of 1000 rpm. Parts were purposely spun for an inadequate amount time at an insufficient speed for complete bubble removal, thus purposely producing bubble-filled parts. After spinning, the growth of the trapped bubbles was then observed and recorded.

3.4.1 Image acquisition and calibration

The setup for image acquisition is very similar to that described in Section 2.5. The Vision Research Phantom v7.3 high speed camera is mounted on a tripod and is focused on a

portion of a mold assembly with a clear top like the one shown in Figure 2-13 B. The mold assembly is filled with PDMS and bubbles within the PDMS are monitored. To focus on the bubbles, a Tamron SP AF 90 mm F/2.8 Di 1:1 Macro lens is used.

The video field of view is calibrated using the Pratt circle fitting MATLAB script provided by Nikolai Chernov [28]; the field of view can be calibrated with a penny as shown in Figure 3-3 (A) and (B). The calibration factor is 22 μm per pixel in the original image.

3.4.2 Bubble growth movies

After the field of view was calibrated and the mold was spun for a set time of 30 seconds and a set speed of 1000 rpm, a thermocouple was inserted into the PDMS. Then, the mold assembly filled with PDMS was placed on a hot plate or left to cure at room temperature depending on the desired temperature conditions for an experimental trial. While the PDMS or mold assembly was sitting, bubbles were observed to grow in the PDMS solution. The bubbles' growth was monitored with the high speed video camera. However, the high speed camera was triggered to take images at a very slow image acquisition rate (0.042 Hz for the room temperature sample). The frame rate acquisition was slower than what we could set using the camera's own software/hardware, so a separate function generator was used to deliver a high TTL signal for each image acquired. Some acquired images are shown in Figure 3-4.

3.4.3 Measured bubble growth at room temperature

Using the video acquired and demonstrated in Figure 3-4, regions of interest have been selected for bubble image processing in MATLAB. Figure 3-5 (A) shows the selected areas for image processing. Figure 3-5 (B) shows the processed pixel diameters of the bubbles within each region of interest plotted against time.

While the bubbles were growing, a thermocouple was placed in the PDMS to measure its temperature. The bottom portion of Figure 3-5 (B) shows the measured temperature of the PDMS plotted against time. Unfortunately, synchronization between temperature data and bubble growth data was not exact with respect to start time. The start times of the temperature recording and bubble growth are within 30 seconds of each other. In addition, the internal clock on the Phantom high speed camera seemed to consistently get ahead of the computer clock being used to log the temperature data. Over a period of about

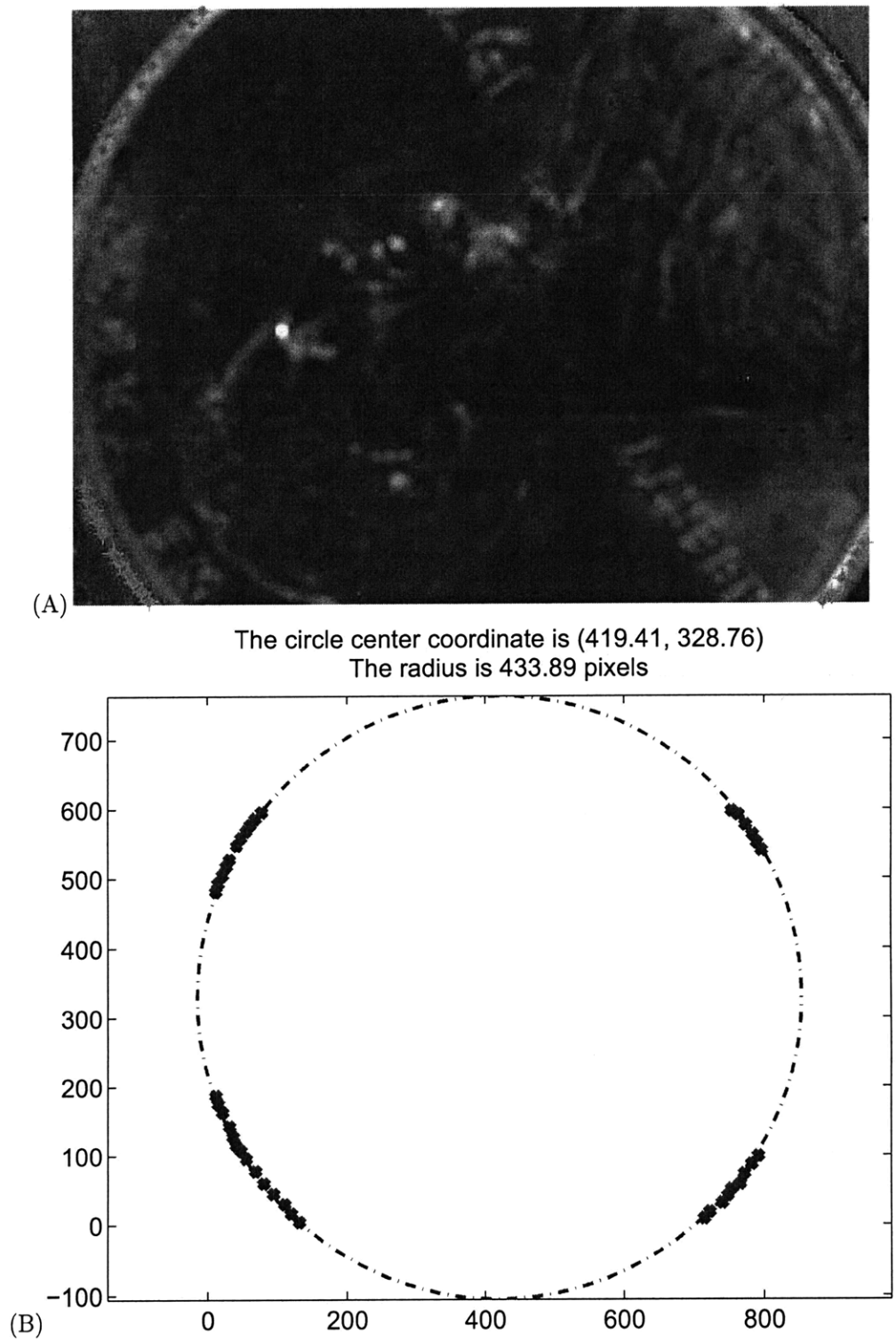

Figure 3-3: Calibration images with estimated penny diameter of 19.05 mm. Calibration factor is 22 μm per pixel in the original image.

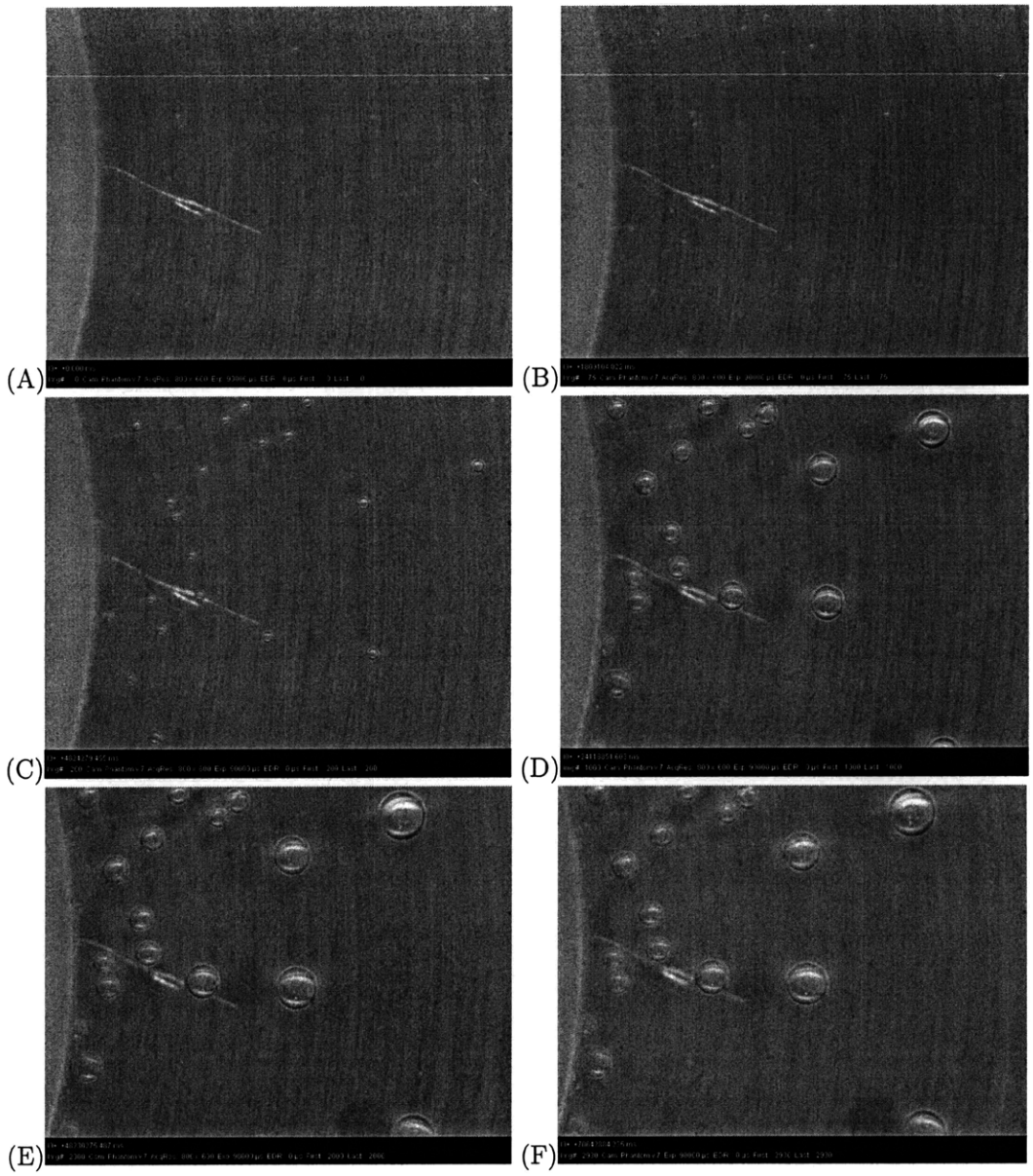

Figure 3-4: (A) First frame image of bubbles: image 0. (B) Image of bubbles after 1,809 seconds (approx. 30 minutes): frame 75. (C) Image of bubbles after 4,824 seconds (approx. 1 hour 20 minutes): frame 200. (D) Image of bubbles after 24,119 seconds (approx. 6 hours 42 minutes): frame 1000. (E) Image of bubbles after 48,230 seconds (approx. 13 hours 24 minutes): frame 2000. (F) Image of bubbles after 70,643 seconds (approx. 19 hours 37 minutes): frame 2930.

12 minutes, the clocks would be out of synchronization by approximately 6 seconds. Over a period of about 55 minutes, the clocks would be out of synchronization by approximately 20 seconds. In spite of these limitations, given the accuracy and variation that we expect in our experiments, it is still possible to form estimates for bubble growth behavior with respect to time.

In order to reduce the noise seen in the individual readings for the bubble diameters shown in Figure 3-5 (B), the measured diameters were averaged. Figure 3-6 (A) shows the average pixel diameter of the six bubbles plotted against time. In addition to calculating an average bubble diameter at each time step, the MATLAB Curve Fitting Toolbox was used to fit a first order step response function to the data. The fitted solution has the form:

$$D = A\left(1 - e^{-t/\tau}\right) + B, \tag{3.57}$$

where t is time, τ is the time constant of the response, D is the diameter of the bubble, A is the amplitude of the response, and B is an offset or diameter value when $t = 0$. For the bubble diameter growth measured at room temperature, the fitted amplitude A had a value of 57.8 pixels, the fitted time constant τ had a value of 12,930 seconds (3 hours 36 minutes), and the fitted offset B had a value of 8.6 pixels. For this fit, the R-square and adjusted R-square values are both 0.991.

In Figure 3-6 (B), the Epstein-Plesset bubble growth is numerically calculated for an initial bubble radius of 94.78 μm , a c_f value of 1.038, an initial time of 1×10^{-5} seconds, a Henry's coefficient of 1.927×10^{-6} kg(air)/m^3(polymer)/Pa, and a temperature of 25 °C. The c_f value indicates a supersaturation of 3.8% for the liquid PDMS surrounding the bubble. Based on this fitted value for c_f, future calculations in this work generally assume an initial c_f value of 5% supersaturation. Notice that the Epstein-Plesset model agrees well for the first 5 hours, but then the experimental data and model begin to diverge because the Epstein-Plesset model does not capture the curing kinetics. In these growth experiments, the PDMS is curing over time and develops some elasticity or has an exponential increase in viscosity, which stunts bubble growth.

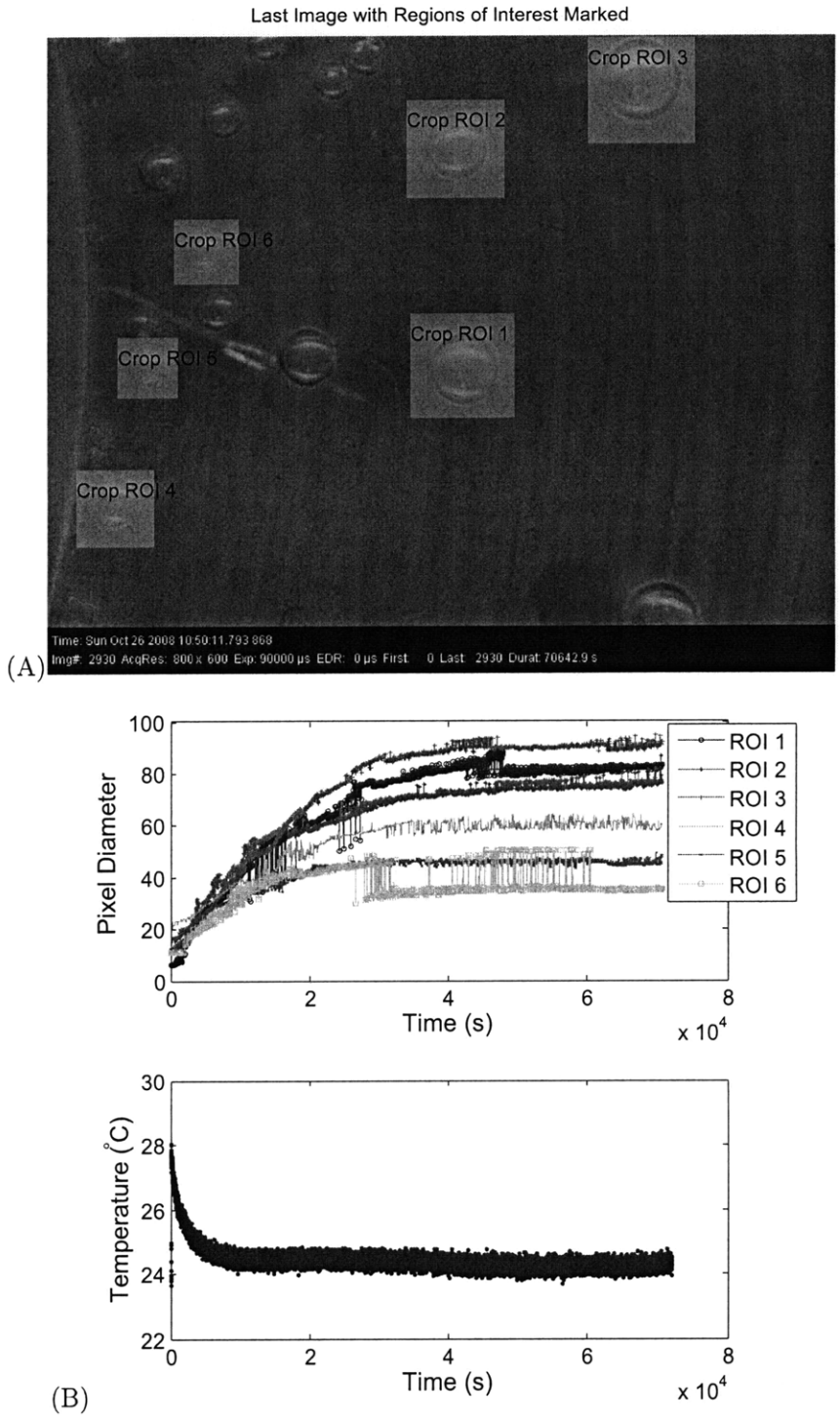

Figure 3-5: (A) Regions of interest for 6 growing bubbles. (B) Growth data for bubbles in regions of interest shown in A.

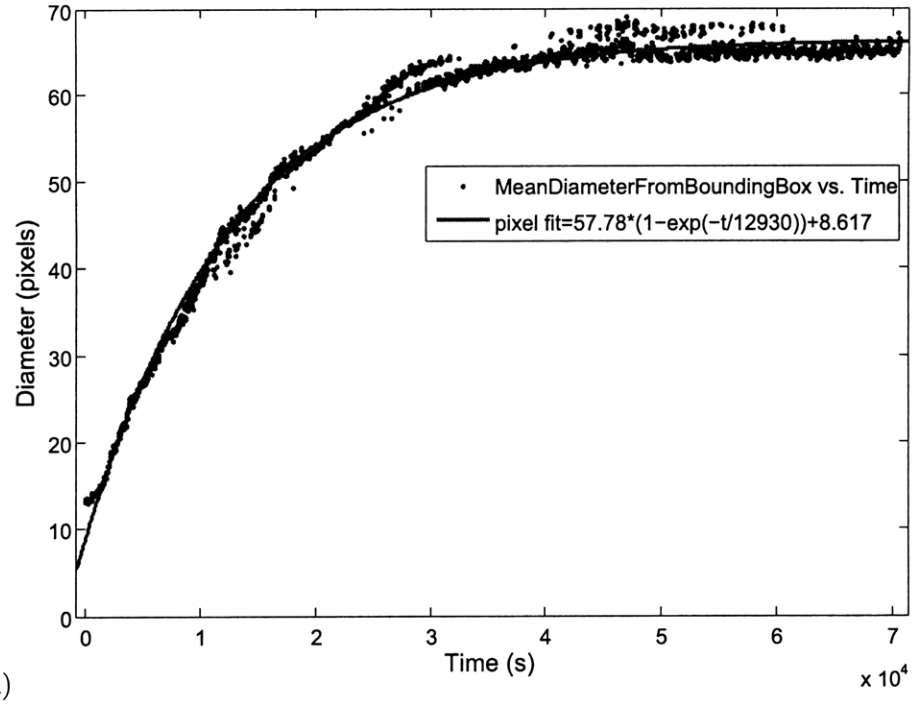

(A)

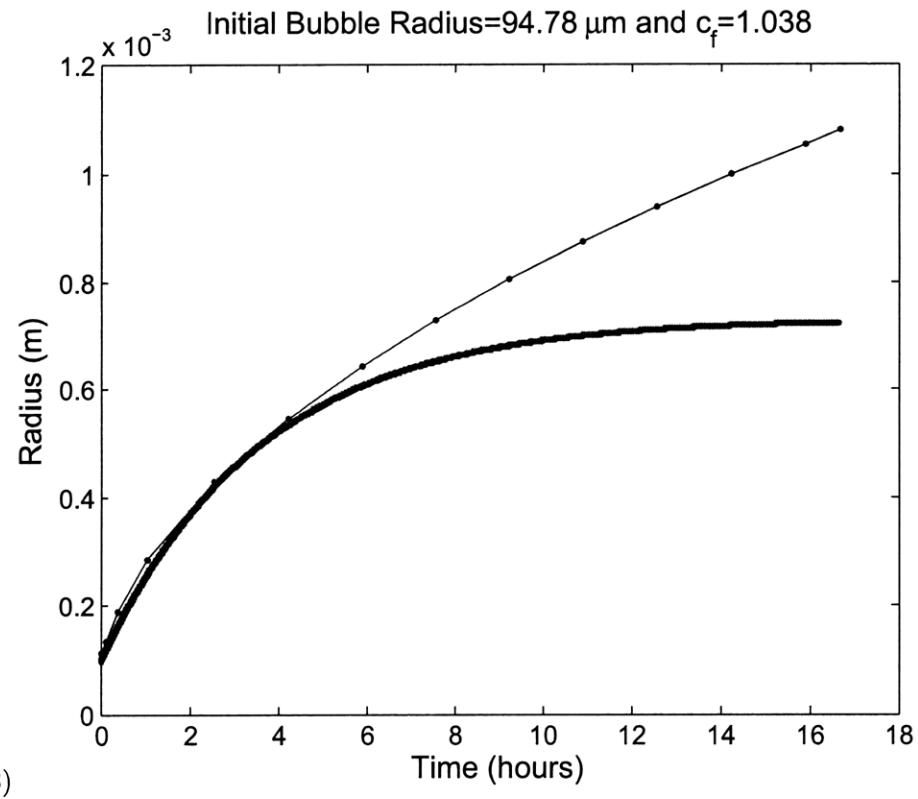

(B)

Figure 3-6: (A) Bubble growth data from room temperature experiment with appropriate curve fit. (B) The thin, blue line with dots is the numerical implementation of Epstein-Plesset bubble growth using Equation 3.51. The thicker, red line is the curve fit to the data from A.

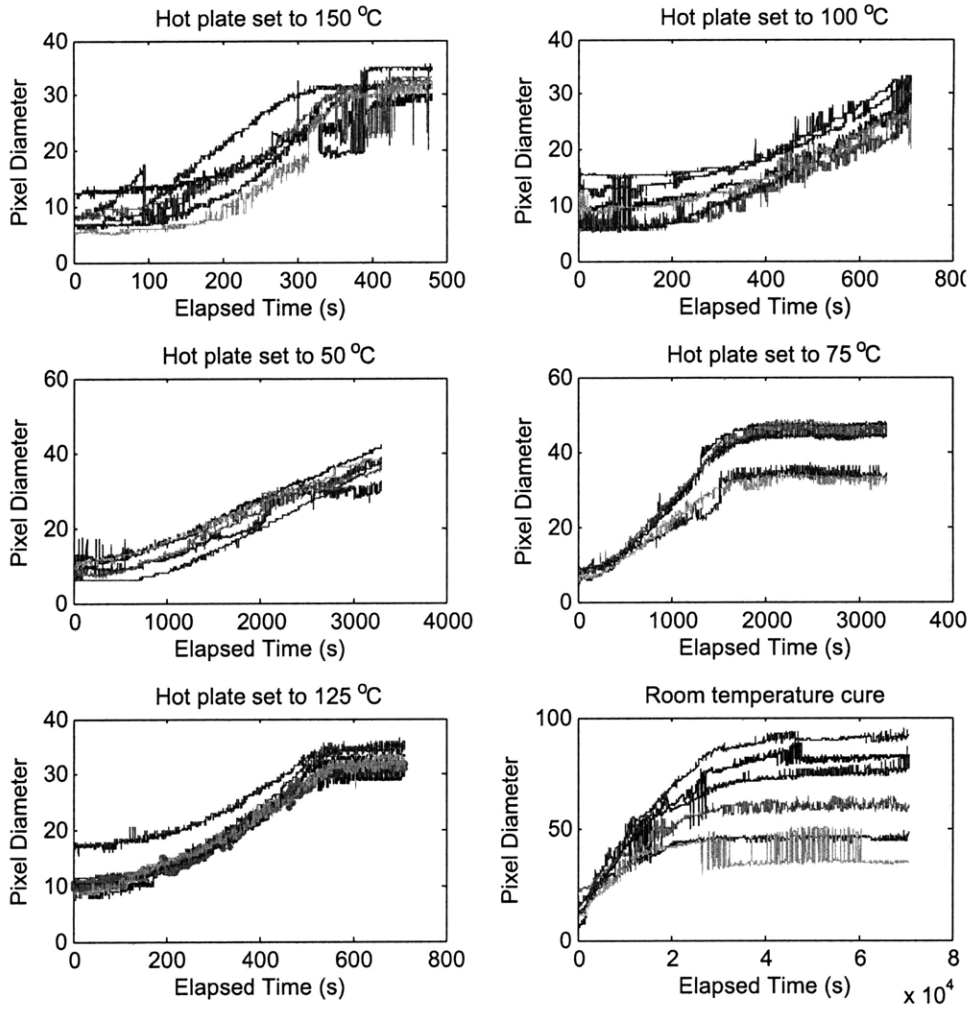

Figure 3-7: The measured bubble growth of six bubbles/regions of interest in each sample.

3.4.4 Temperature dependence of measured bubble growth

Section 3.4.3 has shown the fitting of bubble growth models to growing bubbles in PDMS at room temperature. Additional experiments were performed showing the dependence of bubble growth rate on temperature. As demonstrated in Figure 3-5 (A), six bubbles/regions of interest were selected for each experiment performed. The raw data for these measured diameters are shown in Figure 3-7. The bottom, right graph in Figure 3-7 contains the same data shown in Figure 3-5 (B). The conversion between pixels and units of length for the original 800 x 600 images is again 22 μm per pixel.

As shown in Figure 3-8, the average diameter of the six bubbles at each temperature

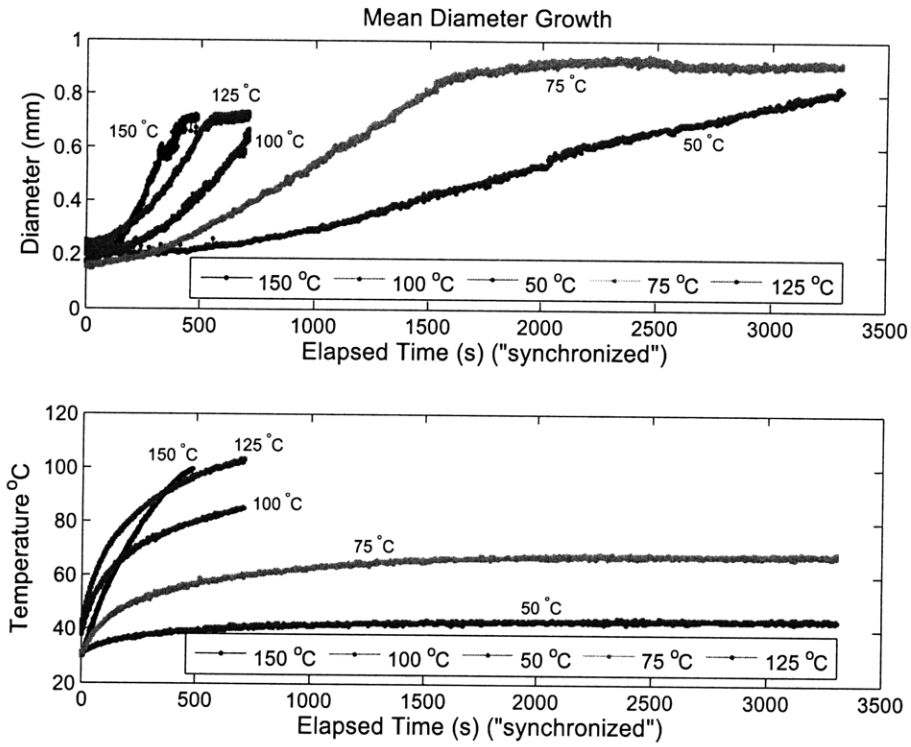

Figure 3-8: The average bubble growth of the six bubbles of interest depicted in Figure 3-7.

can be calculated to reduce the noise in the image processing. Figure 3-8 also shows the measured temperature of the PDMS against time. Figure 3-7 and Figure 3-8 definitely show that the bubble growth rate is dependent on temperature. In addition, increases in temperature correspond to a more rapid stunting of bubble growth. Bubbles tend to grow faster at higher temperatures, but their growth is stunted more quickly because of the faster curing of PDMS at higher temperatures.

Chapter 4

Centrifugal casting and fast curing bubble behavior

The primary objective of the centrifugal casting process is to eliminate bubbles from specified regions of a liquid resin-filled mold. In the implemented system described in this work, there are two modes of bubble elimination. The first mode of elimination is that the bubbles are transported out of the regions of interest by the buoyant forces associated with the centrifugal acceleration of the centrifuge. The bubbles are carried from the molding region to the exit near the center axis of rotation. The second mode of elimination is by dissolution. In dissolution, the bubbles dissolve into solution in less time than it takes for the bubbles to be moved out of the regions of interest by the buoyant forces and centrifugal acceleration.

4.1 Bubble speed with a given diameter

Balancing buoyant and drag forces acting on a bubble, it is possible to estimate terminal velocities for bubbles based on their size, liquid properties, goemetry, and spin speed. These calculated terminal velocities can then be integrated to estimate the time necessary to move bubbles a set distance. Figure 4-1 shows the forces acting on an air bubble of diameter d in a mold cavity fluid. The components of the buoyant force acting in the r and z-directions on the bubble are given by F_{Br} and F_{Bz}. The components of the drag force acting in the r and z-directions on the bubble are given by F_{Dr} and F_{Dz}. The two components of the gravitational/buoyant forces acting on the bubble are given by F_{gr} and F_{gz}. Acceleration due to centrifugal spinning is given by g_r, and acceleration due to the earth's gravity is given

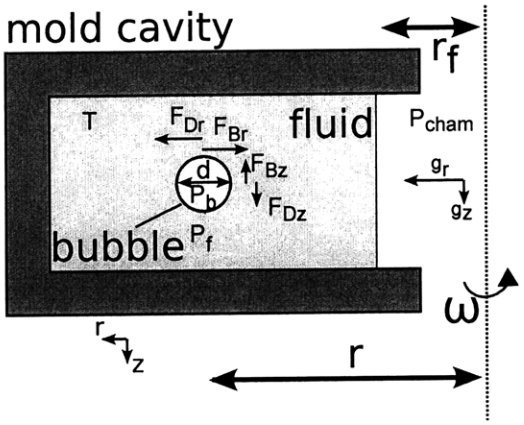

Figure 4-1: Air bubble in a mold cavity fluid being spun in a centrifuge.

by g_z. The pressure of the fluid surrounding the bubble is given by P_{fluid}, and the pressure of the air chamber is given by P_{cham}. Uniform temperature T is assumed throughout the system. The angular velocity of the bubble and the system are given by ω, and the distance of the bubble from the axis of rotation is given by r.

The accelerations due to rotation and gravity are given by the following:

$$g_r = r\omega^2 \tag{4.1}$$

$$g_z = 9.8\,\mathrm{m/s^2}. \tag{4.2}$$

Given the density of the fluid ρ_f and the density of the air ρ_a, we have the following for the components of buoyant force acting on the bubble in the r and z-directions follow:

$$F_{gr} = (\rho_f - \rho_a)V_r g_r \tag{4.3}$$

$$F_{gz} = (\rho_f - \rho_a)V_b g_b. \tag{4.4}$$

The drag force components in the r and z-directions on the bubble are given by the Hadamard-Rybczynski relationship [46, 29, 39]:

$$F_{Dr} = 3\pi\mu_f dv_r \frac{2\mu_f + 3\mu_b}{3\mu_f + 3\mu_b} \tag{4.5}$$

$$F_{Dz} = 3\pi\mu_f dv_z \frac{2\mu_f + 3\mu_b}{3\mu_f + 3\mu_b}, \tag{4.6}$$

where μ_f is the dynamic viscosity of the fluid surrounding the bubble and μ_b is the dynamic viscosity of the fluid within the bubble. The bubbles in this study are filled with air, and the viscosity of air is on the order of 10^{-5} Pa s. For PDMS Sylgard 184, the fluid viscosity is on the order of 1 Pa s. Therefore, for an air bubble in PDMS, Equation 4.7 and Equation 4.8 would reduce to

$$F_{Dr} \approx 2\pi\mu_f dv_r \tag{4.7}$$

$$F_{Dz} \approx 2\pi\mu_f dv_z. \tag{4.8}$$

If the viscosity of the material within the bubble were much greater than the viscosity of the fluid, then Equation 4.7 and Equation 4.8 reduce to the Stokes' flow solution for the drag force on a hard sphere in laminar flow:

$$F_{Dr} = 3\pi\mu_f dv_r \tag{4.9}$$

$$F_{Dz} = 3\pi\mu_f dv_z. \tag{4.10}$$

For this work, we will define a parameter D_c as follows:

$$D_c = \frac{F_{Dz}}{\pi\mu_f dv_z}. \tag{4.11}$$

For the gas bubble case depicted by Equation 4.7, D_c would have a value of 2. In the hard sphere case of Equation 4.9, D_c would have a value of 3. Citing Clift, et. al. [29], "the Hadamard-Rybczynski theory predicts that the terminal velocity of a fluid sphere should be up to 50% higher than that of a rigid sphere of the same size and density. However, it is commonly observed that small bubbles and drops tend to obey Stokes's law, rather than the corresponding Hadamard-Rybczynski result." Therefore, in the experiments performed

in this thesis, the bubbles might be expected to have D_c values between 2 and 3. That said, a D_c value of 2 seems more appropriate based on the experimental results described in Section 4.2.

Summing the forces and using Newton's second law,

$$m_{virtual}a_r = -F_{Br} + F_{Dr} \tag{4.12}$$

$$m_{virtual}a_z = -F_{Bz} + F_{Dz}, \tag{4.13}$$

where $m_{virtual}$ is the virtual mass of the bubble, and a is the acceleration of the bubble. The classical virtual mass of the bubble is half the mass of the displaced volume of fluid [66]. For the purposes of our analysis, we assume the bubble has reached a steady-state velocity meaning the acceleration terms on the left-hand side of Equation 4.12 go to zero. Therefore, equating the drag force and buoyant force terms using Equations 4.3 through 4.12, along with the volume-diameter relationship for a sphere $\left(V_b = \pi d^3/6\right)$, the following holds:

$$0 = (\rho_a - \rho_f)V_b g_r - 2D_c\pi\mu_f \left(\frac{3V_b}{4\pi}\right)^{(1/3)} v_r \tag{4.14}$$

$$0 = (\rho_a - \rho_f)V_b g_z - 2D_c\pi\mu_f \left(\frac{3V_b}{4\pi}\right)^{(1/3)} v_z. \tag{4.15}$$

Solving for the steady-state velocities,

$$v_{r_{ss}} = \frac{(\rho_a - \rho_f)g_r}{2D_c\pi\mu_f}\left(\frac{4\pi V_b^2}{3}\right)^{(1/3)} \tag{4.16}$$

$$v_{z_{ss}} = \frac{(\rho_a - \rho_f)g_z}{2D_c\pi\mu_f}\left(\frac{4\pi V_b^2}{3}\right)^{(1/3)}. \tag{4.17}$$

Another way to express these terminal velocities using the volume-diameter relationship for a sphere is given by

$$v_{r_{ss}} = \frac{(\rho_a - \rho_f) g_r}{6 D_c \mu_f} d^2 \tag{4.18}$$

$$v_{z_{ss}} = \frac{(\rho_a - \rho_f) g_z}{6 D_c \mu_f} d^2. \tag{4.19}$$

According to Equation 4.18, the bubble speed toward the center axis of rotation scales linearly with the distance away from the center axis of rotation, with the square of the diameter, and the square of the spin speed. The bubble speed will also decrease linearly with increases in viscosity or decreases of the D_c parameter.

4.2 Drag coefficient verification

Using the high speed video setup described in Section 2.5, experiments were performed to track bubbles moving toward the center axis of rotation in a centrifuge. An example subset of the images used to track a bubble are shown in Figure 4-2. Each bubble was manually selected by drawing a box around it in the MATLAB rendered image. By taking the square root of the pixel area of this box, it was possible to calculate the bubble pixel diameter. The pixel diameter was then converted into metric units and the measured diameters are included in Figure 4-3. The resolution/conversion factor for the acquired images is 31.5 μm per pixel. This calibration is described in Section 3.4.1 and Section 2.5.

Overall, six bubbles with differing average diameters were selected in approximately 470 video images collected while the centrifuge was spinning at approximately 2000 rpm. Data from these images are included in Figure 4-3. There is some noise in the measured diameters, and the calculated statistics for this noise are included in Table 4.1. The distance from center measurement values were determined by calculating the distance between the centrifuge's center axis of rotation and the bubble position in each frame.

Using the data shown in Figure 4-3, a D_c parameter of 2 (Hadamard-Rybczynski relationship), a viscosity of 3.9 Pa s as specified by Dow Corning [2], a density of 1030 kg/m^3, Figure 4-4 was generated from Equation 4.18 and Equation 4.1. The ω parameter in Equation 4.1 is determined by taking the first difference/approximate derivative of the time values shown in Figure 4-3. By taking this first difference of the data, the lengths of the arrays were all reduced by one element. In plotting the resulting arrays of predicted/calculated

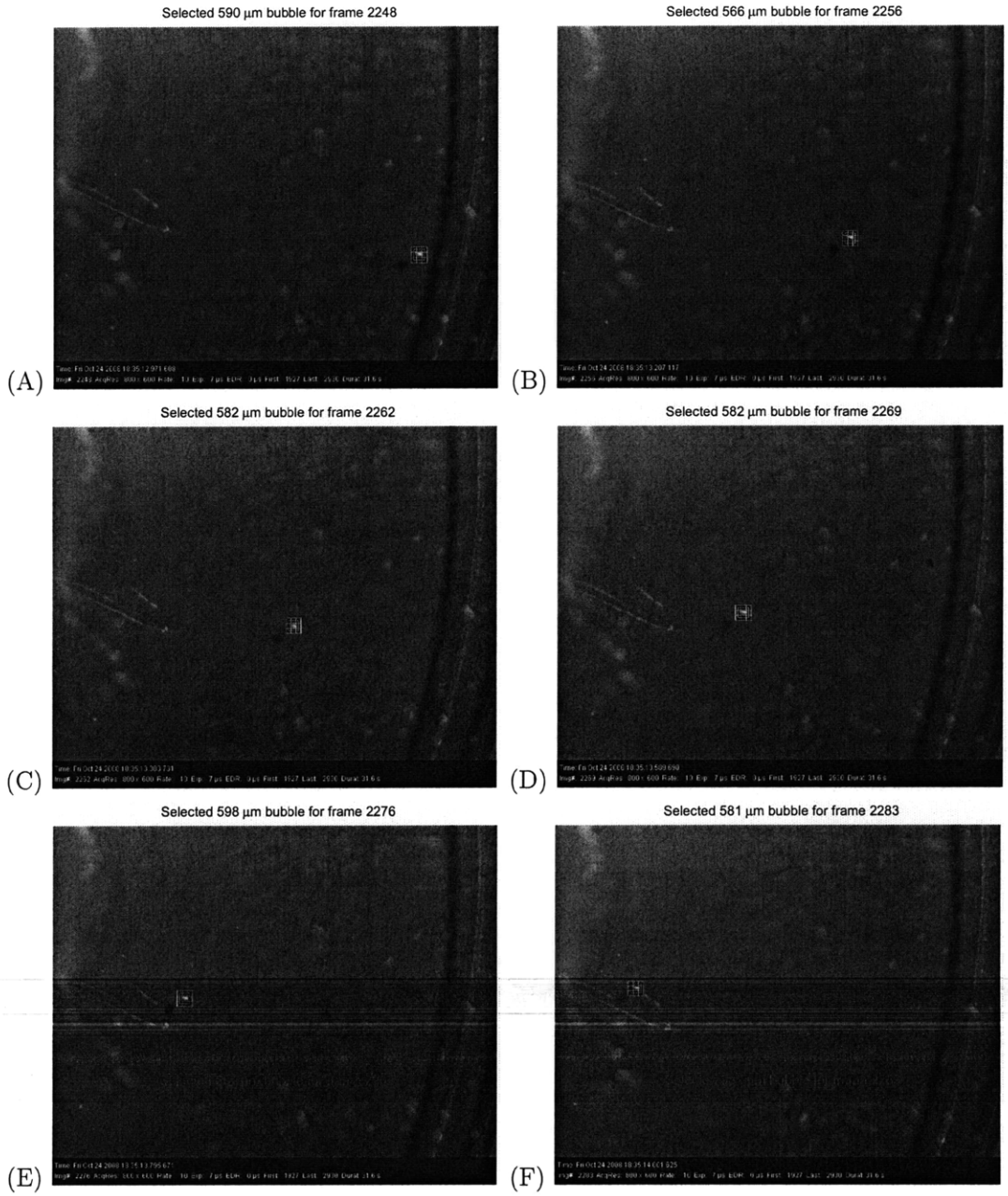

Figure 4-2: A subset of images used to track the selected bubble as it progresses toward the center. (A) Frame 2248 at time 10.45 s (B) Frame 2256 at time 10.65 s (C) Frame 2263 at time 10.89 s (D) Frame 2270 at time 11.09 s (E) Frame 2277 at time 11.30 s (F) Frame 2283 at time 11.48 s.

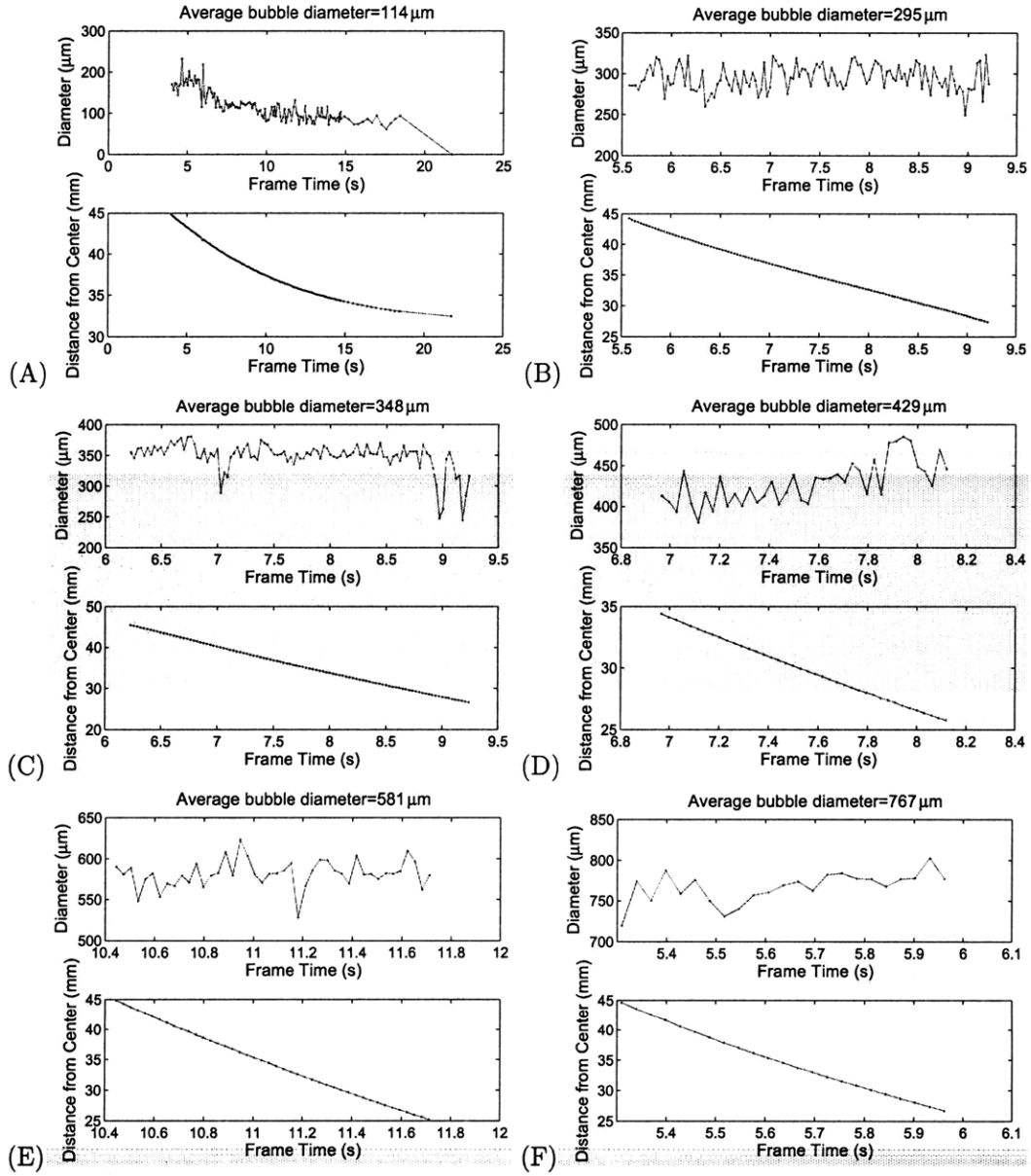

Figure 4-3: Diameter and position data manually extracted from video captured with the centrifuge spinning at approximately 2000 rpm. (A) 114 μm average measured bubble diameter. (B) 295 μm average measured bubble diameter. (C) 348 μm average measured bubble diameter. (D) 429 μm average measured bubble diameter. (E) 581 μm average measured bubble diameter. (F) 767 μm average measured bubble diameter.

values with one less element, the first element of the data (the distance value farthest away from center axis of rotation) was removed, and the last element of the data (distance value closest to the center axis of rotation) was included. For large arrays of collected data, the removal of one data point is generally not noticeable.

The bottom graph of each lettered item in Figure 4-4 shows the difference between the measured diameter and the predicted diameter using the derived relationships of Section 4.1. A negative value indicates that the predicted bubble size is greater than the measured value. Generally speaking, the measured bubble speeds are greater than expected given the measured bubble diameter using a D_c value of 2 with the specified viscosity of 3.9 Pa s.

The discrepancies between the expected and measured values for the bubble velocities/diameters may be related to inaccuracies in spatial measurements for the centrifugal casting experiments. The resolution of the images taken is 31.5 μm per pixel, and the bubbles were selected manually using MATLAB image tools. As shown in Table 4.1, the root mean square deviation (RMSD) value for the diameter difference in the measurements is approximately 90 μm, which is less than 3 pixels. RMS deviation is given by the following equation:

$$RMSD = \sqrt{\frac{1}{n}\sum_{i=1}^{n}(d_{meas_i} - d_{calc_i})^2}, \tag{4.20}$$

where d_{meas_i} is an individual manually measured diameter, d_{calc_i} is an individual calculated diameter, and n is the total number of measurements/calculated diameters.

However, the most likely source of deviation from the model is because the viscosity of the PDMS is lower than its specified value as a result of an increase in temperature. During the high speed image recording, a Lowel Light-pro lamp was used to illuminate the PDMS liquid and the bubbles. This lamp radiated enough heat to cause physical discomfort to its user. In one instance, the lamp even melted some plastic on the macro lens used with the Phantom high speed camera. Given its heat-radiating nature, the lamp could definitely elevate the temperature of the PDMS fluid being used in an experiment, thus affecting the viscosity.

The acceptable viscosity range for Sylgard 184 is from 4000 cSt. to 6500 cSt. at 25°C when mixed (3900 centiPoise to 6300 centiPoise with a specific density of 1.03) [32]. That said, all fluids exhibit some viscosity-temperature dependence. Dow Corning was not able to

provide viscosity-temperature dependence data, but specification sheets from Clearco Products (www.clearcoproducts.com) share applicable information. Clearco Products carries a number of siloxane/silicone oils with viscosities ranging from 0.65 cSt. to 2.5 million cSt. In one of their specification sheets [18], they include the following relationship:

$$\log_{10} h_{T_C} = \frac{763.1}{273 + T_C} - 2.559 + \log_{10} h_{25°\mathrm{C}}, \tag{4.21}$$

where h_{T_C} is the kinematic viscosity in mm^2/s or cSt. of the silicone oil at the desired temperature, T_C is the desired temperature in degrees Celsius, and $h_{25°\mathrm{C}}$ is the kinematic viscosity of the silicone at 25°C. The silicone oil from Clearco Products is not the same as the PDMS from Dow Corning, but Equation 4.21 can be used to estimate a change in viscosity of the PDMS based on temperature. Using a kinematic viscosity of 4000 cSt. at 25 °C with a temperature increase to 45 °C, an estimate for the lowered viscosity of the PDMS solution is 2770 cSt. (2.69 Pa s with a specific density of 1.03). This value of 2.69 Pa s is an estimate for a 20 °C increase in temperature, which represents an approximate 30% decrease in the viscosity of the PDMS.

To explore whether or not adjusting the fluid viscosity would provide a better data fit, the MATLAB optimization toolbox was used to minimize the root mean square deviation (RMSD) between the predicted bubble diameters and the manually measured diameters. The resulting D_c value from this optimization is 1.326 with the dynamic viscosity at 3.9 Pa s. The resulting diameter RMSD value is 36 μm, which is almost within 1 pixel of error given the image resolution of 31.5 μm per pixel. The resulting calculated values, along with the measured values, are shown in Figure 4-5. Equation 4.20 has also been applied to calculate an RMS value for the deviation of measured diameters against the average of the measured diameters. In this case, the d_{calc_i} term becomes the mean of the measured diameters. As shown in Table 4.1, these RMS values for diameter measurements range from 15.2 μm to 35.4 μm.

The velocity results in Figure 4-5 overlap better and the diameter differences are smaller than those shown in Figure 4-4. However, a D_c value of 1.326 is not between 2 and 3, the expected range between the Hadamard-Rybczynski and Stokes' flow regimes. Again, this could be a result of calibration errors in the experimentation, but a more likely explanation is that the viscosity of the PDMS has been lowered because of a temperature increase caused

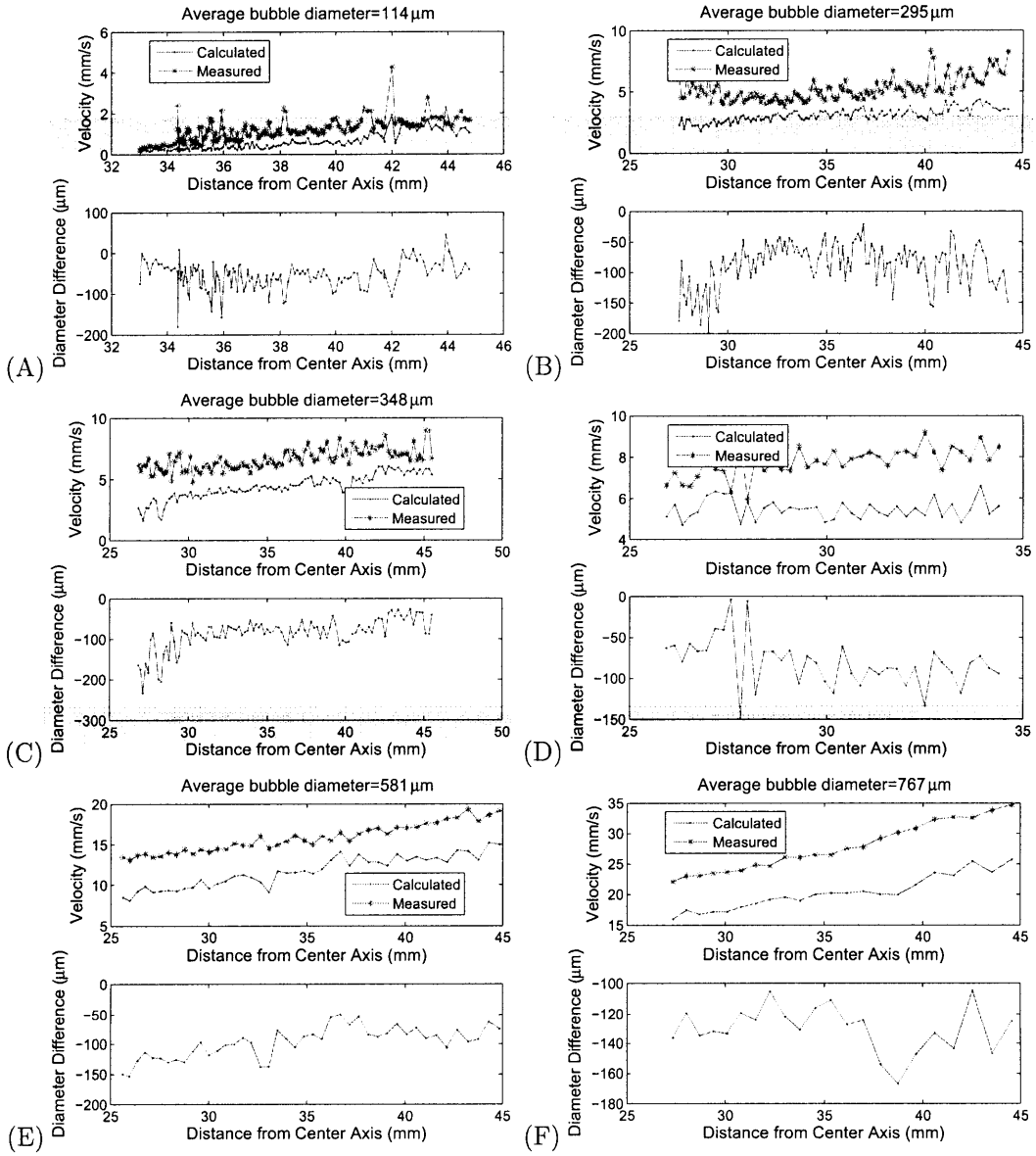

Figure 4-4: Speed and bubble diameter differences between measured and predicted values for the data included in Figure 4-3. The value for the D_c parameter is 2 and the viscosity used is 3.9 Pa s. (A) 114 μm average measured bubble diameter. (B) 295 μm average measured bubble diameter. (C) 348 μm average measured bubble diameter. (D) 429 μm average measured bubble diameter. (E) 581 μm average measured bubble diameter. (F) 767 μm average measured bubble diameter.

Table 4.1: Statistics for bubble measurements shown in Figure 4-3 and Figure 4-5.

Mean measured bubble diameter (μm)	RMS for diameters (μm)	Std. Dev. for diameters (μm)	RMSD $D_c = 2$@3.9 Pa s (μm)	RMSD $D_c = 1.326$@3.9 Pa s $D_c = 2$@2.59 Pa s (μm)
767	18.5	18.9	130.9	39.8
581	16.5	16.7	101.3	35.9
429	25.8	26.1	86.3	31.0
348	23.6	23.7	94.1	35.0
295	15.2	15.3	94.2	34.4
114	35.4	35.5	65.0	38.8
Average/ Total Values	22.5 (Ave.)	22.7 (Ave.)	88.8 (Tot.)	36.0 (Tot.)

by the halogen lamp illumination used with the experimental apparatus. Increasing the D_c value to 2 from 1.326 corresponds to a decrease in dynamic viscosity to 2.59 Pa s, which is within 5% of the 2.69 Pa s estimate corresponding to the 20 °C increase in temperature of the PDMS. Thus, the temperature increase of the PDMS is likely the reason for a discrepancy between the specified kinematic viscosity value of 3.9 Pa s and the fitted/measured viscosity value of 2.59 Pa s. For the rest of this thesis, the value $D_c = 2$ will be used to describe the drag on a bubble. For the data set collected using the halogen lamp, the dynamic viscosity will be reduced to 2.59 Pa s. For bubble speed and time estimates without the use of the halogen lamp, the dynamic viscosity will be set to Dow Corning's specified value of 3.9 Pa s.

4.3 Bubble speed calculations without diffusion

4.3.1 Numerical implementation

Using Equation 4.18, it is possible to calculate the steady-state velocity of the bubble if the density of the air ρ_a and the displaced fluid volume V_b are known. To calculate these two quantities, the pressure of the spinning fluid needs to be determined. The pressure of the spinning fluid is dependent on the distance of the air-fluid interface from the center. In Figure 4-1, this distance is given by r_f. The pressure in the fluid is then given by

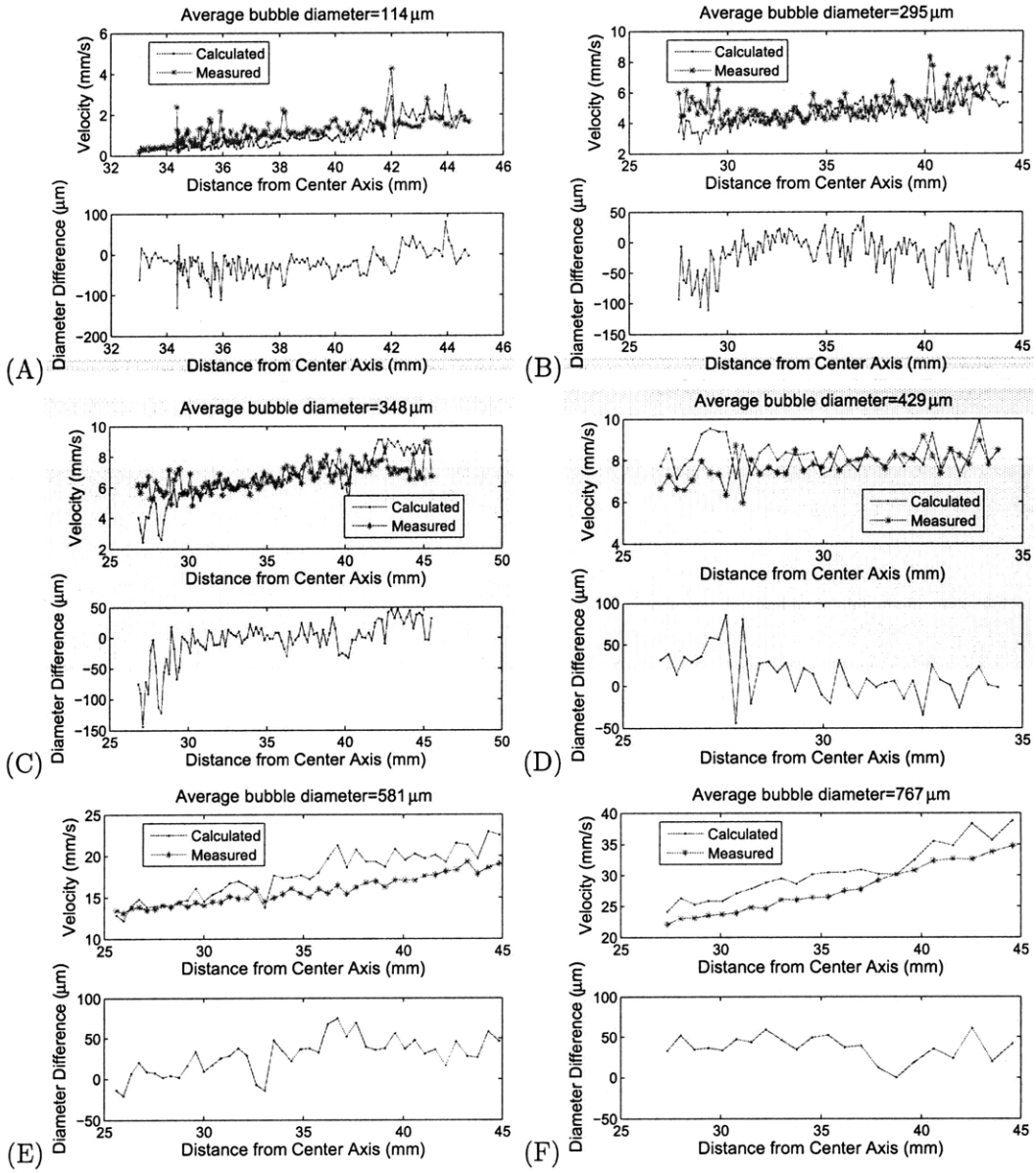

Figure 4-5: Speed and bubble diameter differences between measured and predicted values for the data included in Figure 4-3. The value for the D_c parameter is 1.326 with a dynamic viscosity of 3.9 Pa s or 2 with a dynamic viscosity of 2.59 Pa s. (A) 114 μm average measured bubble diameter. (B) 295 μm average measured bubble diameter. (C) 348 μm average measured bubble diameter. (D) 429 μm average measured bubble diameter. (E) 581 μm average measured bubble diameter. (F) 767 μm average measured bubble diameter.

$$P_{fluid} = P_{cham} + P_{gz} + \frac{1}{2}\rho_a \omega^2 r_f^2 + \frac{1}{2}\rho_f \omega^2 \left(r^2 - r_f^2\right), \tag{4.22}$$

where P_{cham} is the air pressure surrounding the mold assembly (useful for calculations in a pressure chamber) and P_{gz} is the pressure on the bubble from earth's gravity. In our case, the P_{gz} and the $1/2\rho_a\omega^2 r_f$ terms are negligible. Using the Young-Laplace equation, the pressure difference between the fluid and the air in the bubble is given by

$$P_b - P_{fluid} = \frac{4\sigma}{d}. \tag{4.23}$$

Using the ideal gas law and the relationship between the diameter and the volume of a sphere, the following is derived:

$$P_b - P_{fluid} = 2\sigma \left(\frac{4\pi P_b}{3nBT}\right)^{1/3}, \tag{4.24}$$

where n is the number of moles of gas in the bubble and B is the universal gas constant of 8.314 J/(mol K). Using the symbolic solver in MATLAB, an expression for Equation 4.24 for P_b was obtained. That expression can be found in the MATLAB scripts included in Appendix A.2.3 and Appendix A.3.3. The value for the bubble diameter d is also calculated with P_b using Equation 4.23.

$$d = \frac{4\sigma}{P_b - P_{fluid}} \tag{4.25}$$

Once P_b is obtained, the density of the air within the bubble can then also be calculated using the following relationship:

$$\rho_a = \frac{P_b}{B_s T}, \tag{4.26}$$

where B_s is the specific gas constant of 287.05 J/(kg K). With values for r, ω, μ, P_b, d, and ρ_a, the components of the bubble velocity can be calculated using Equations 4.18 and 4.19.

Assuming there is no mass transfer or diffusion between the bubble and the liquid, we can relate n (number of moles of gas) to an initial bubble diameter parameter d_o. This bubble diameter d_o is given by

$$d_0 = \left(\frac{6\pi nBT}{P_{cham}}\right)^{1/3} \tag{4.27}$$

and can be thought of as the bubble diameter before the centrifuge starts spinning. The parameter d_o can be thought of as the bubble diameter of a bubble when the bubble is at the chamber pressure, which for our experiments is atmospheric pressure. The parameter d_o is also the diameter for the bubble when the bubble reaches the liquid-air interface. Once the centrifuge begins to spin, the bubble diameter will decrease from initial diameter d_o. Assuming no diffusion, the shrinking diameter of a bubble is because the pressure in the PDMS fluid surrounding the bubble increases as spin speeds increase or the bubble is placed farther from the axis of rotation. As the bubble travels, the number of moles of gas contained in the bubble will not change, assuming gas from the bubble does not diffuse into the surrounding solution. However, the bubble diameter will grow as the bubble moves toward the center and the fluid pressure decreases.

Figure 4-6 A shows how the fluid pressure scales with the square of both the distance from the center axis of rotation and the spin speed. The pressure increases compress the bubbles. Figure 4-6 B shows how the diameter of a bubble sitting 61.5 mm away from the center axis of rotation is affected by a set spin speed. Figure 4-6 C shows how the bubble diameter will change at a given distance from the center axis of rotation and a given spin speed. All these calculations were performed with a liquid-air interface 34.3 mm away from the center axis of rotation.

Figure 4-7 shows predicted bubble speeds, which make use of the relationships between Equation 4.22 and Equation 4.27. These relationships predict changes in the bubble diameter as the bubble is moving from the outside edge to the liquid-air interface at the middle as described in Figure 4-6. Once the diameter of the bubble d, the air density of the bubble ρ_a, the spin speed ω, and the bubble's distance relative to the center axis of rotation r are known, the steady-state speed can be computed from Equation 4.18.

The model for bubble speed calculations was developed independent of previous work on centrifugal casting predictions for bubble speed. However, once the model in this thesis was completed and while it was being numerically implemented, similar work performed by Spencer [106] in the 1960s on thermoplastics was found to be in very close agreement. Spencer developed his model accounting for pressure increases in the fluid, but he ignored

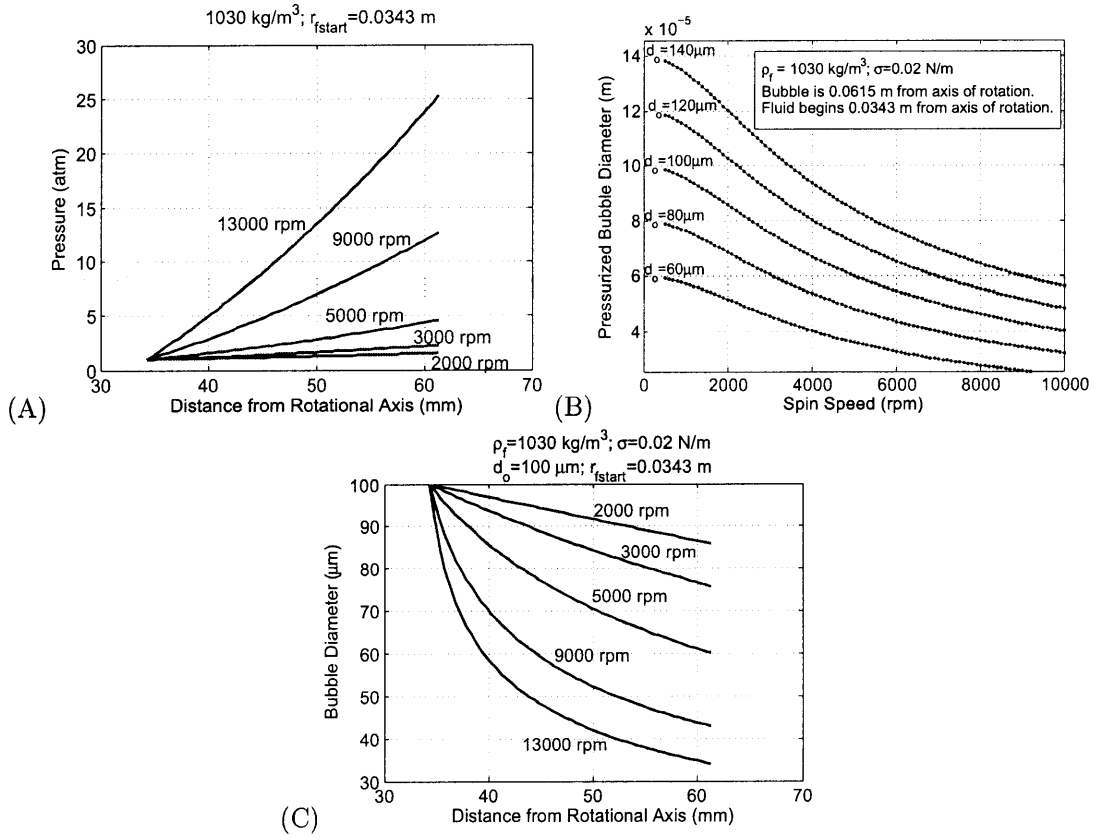

Figure 4-6: (A) Fluid pressure for a given spin speed at a given distance from the rotational axis. (B) Pressurized bubble size versus steady-state spin speed at a given distance from the axis of rotation. (C) Bubble diameter as a function of centrifugal spin speed and distance from the axis of rotation.

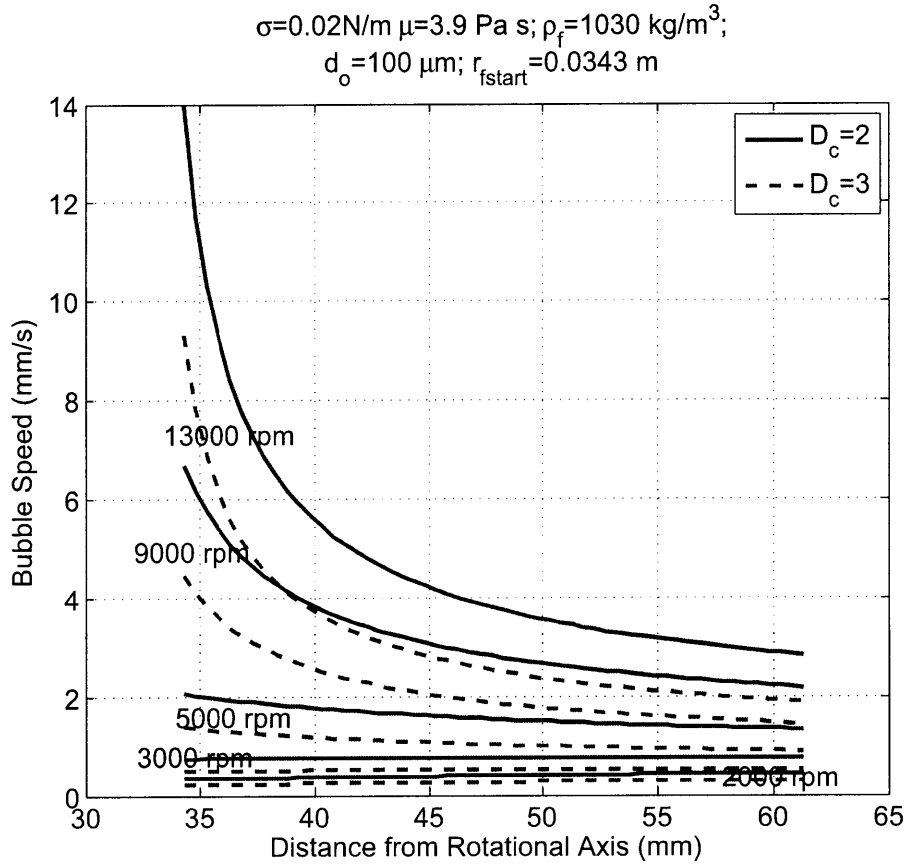

Figure 4-7: Bubble speed as a function of centrifugal spin speed (rpm) and distance from the axis of rotation. The dashed lines also show the predicted velocities with a D_c value of 3.

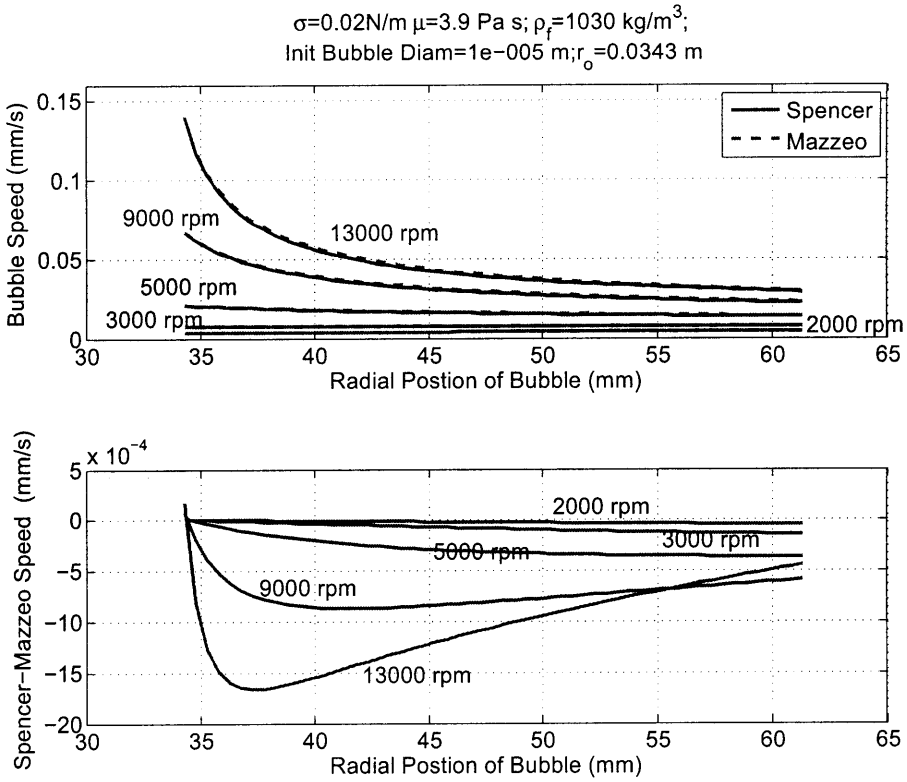

Figure 4-8: Comparison of bubble speeds as predicted by Spencer [106] and the current work.

the effects of surface tension and neglected the density of the air within the bubble. Figure 4-8 shows the comparison of these two models. In reality, for the bubble sizes, spin speeds, and surface tension concerning this work, there are minor differences in the predicted velocities for the two models. However, the slightly modified model is used throughout this work for describing bubble travel without mass transfer/diffusion because the numerical implementation does not pose much additional difficulty. Because the current work subtracts the air density from the PDMS density in the determination of the buoyant force (Equation 4.16), the bubble speeds predicted by Spencer are generally slightly higher.

The bubble speed model derived in this section can also be used to make predictions concerning the bubble's position as time progresses and the centrifuge continues to spin. A simple relationship for integrating velocity in time to get position is given by

$$r_{i+1} = r_i + v_i \Delta t, \tag{4.28}$$

where r_i represents the current bubble distance from the center axis of rotation, r_{i+1} represents the next bubble position/distance from the center axis of rotation, v_i represents the current bubble velocity, and Δt is the time step. Using this simple integration scheme, Figure 4-9 shows bubble position (distance from the center axis of rotation) relative to time for three different d_o values and four different spin speeds. In addition, this numerical implementation accounts for the startup portion of the centrifugal spinning with a linear acceleration of 300 rpm/s. Upon startup, the spin speed of the centrifuge continues to increase until reaching its set spin speed. Based on a number of experiments, the Labnet Spectrafuge 24D's rate of acceleration varies depending on the rotational inertia of the assembly being spun. Typical acceleration/slew rates for our experiments range from 300 rpm/s to almost 900 rpm/s. The D_c value is 2 with a viscosity of 3.9 Pa s.

4.3.2 High speed video and numerical implementation comparisons

Returning to the measured bubble position tracking against time (Figure 4-3), it is possible to compare the bubble speed model without diffusion to the measured data. In this case, the objective is to minimize the difference between the measured positions/distance from the center axis and the predicted position by selecting the most appropriate value for d_o. Table 4.2 shows the resulting optimized d_o values, along with the corresponding minimized RMSD position difference. The RMSD diameter difference is also included to show that the measured diameters and the predicted diameters using the model without diffusion are close to the resolution of the captured images (31.5 μm per pixel). The D_c value of 2 with a viscosity of 2.59 Pa s was fixed during the optimization routine.

Figure 4-10 shows comparisons between the bubble model without diffusion to the measured bubble diameters and positions from the high speed video images. The values of d_o for the plots come from Table 4.2 and represent optimized values for best matching the predicted and measured bubble positions. In other words, the bottom plot of each lettered subfigure in Figure 4-10 should be matched as closely as possible. Upon reviewing the bottom subplots and the RMSD position difference values for these six different bubbles, the plot with the greatest error is Figure 4-10 A. The RMSD position difference value is over 5 times as large as any of the other corresponding RMSD position difference values. The reason for this large RMSD position difference value is related to the apparent dissolution of the bubble in Figure 4-10 A. In the captured video, the bubble essentially disappears into

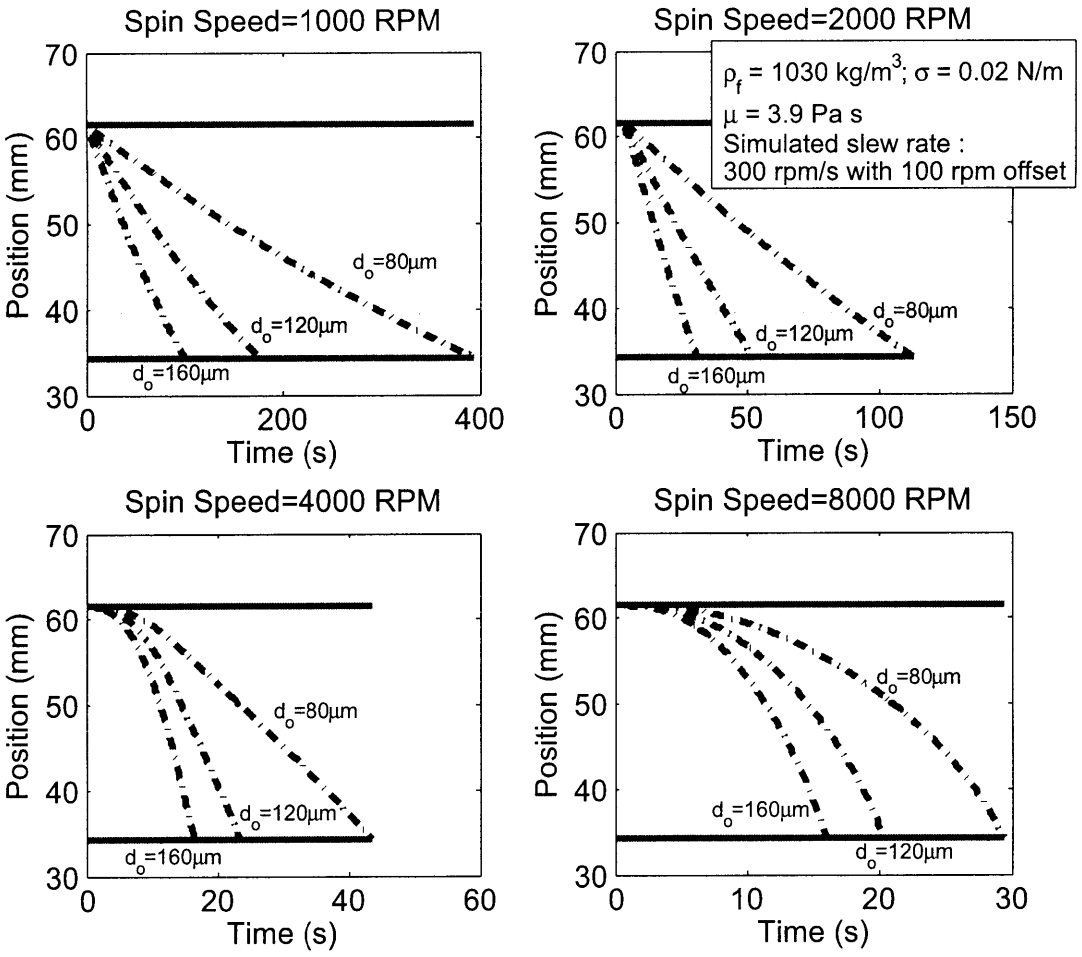

Figure 4-9: Bubble position plotted against time as a function of spin speed and initial bubble diameter.

Table 4.2: Optimized $d_o$values to minimize RMSD Position Difference (3rd column) for bubble position model without diffusion.

Mean measured bubble diameter (μm)	d_o (μm)	RMSD Position Difference (mm)	RMSD Diameter Difference (μm)
767	781.3	0.171	43.7
581	583.1	0.046	41.1
429	427.8	0.014	31.6
348	366.9	0.088	28.8
295	316.9	0.200	16.3
114	145.0	1.008	42.2
Average		0.25	34.0
Standard Deviation		0.38	10.6

the solution before making it to the liquid-air interface. While the video resolution does not completely guarantee the bubble has dissolved completely into solution, it does suggest that the bubble shrinks significantly. The next section will address combining the bubble velocity model and the bubble diffusion model described in Chapter 3 to add the possibility of a bubble dissolving into solution during centrifugal casting.

4.4 Bubble behavior with diffusion

4.4.1 Numerical implementation

Chapter 3 describes the dissolution or growth of bubbles in a quiescent stationary fluid. Surface tension and diffusion were shown to play dominant roles in describing the rate of growth or shrinkage of a bubble. Viscosity, inertia, and elasticity also affect bubble growth or shrinkage, but to a lesser extent. For the sake of simplicity, surface tension and diffusion effects are included in this section with respect to bubble growth or shrinkage, while viscosity, inertia, and elasticity are ignored. That said, the viscosity of the material is essential for calculating the bubble speed given the bubble size, spin speed, and position using the bubble velocity modeling described in Section 4.3. One of the objectives of this thesis is to develop a model that will simultaneously predict bubble speed and bubble growth based on the theoretical work that has been described up to this point in the thesis.

Conceptually, it is helpful to think about the series of events that transpire in the centrifugal casting of PDMS in order to better understand the bubble behavior within the PDMS. The PDMS is mixed and poured into the mold reservoir before the centrifuge is started. While sitting in the mold reservoir, the PDMS has a set concentration of air dissolved within it. Since the resin components are not stored in vacuum chambers before mixing, the PDMS is assumed to be saturated according to Henry's Law at atmospheric pressure. When the centrifuge starts up, the PDMS rapidly spreads into the molding region and additional air bubbles are trapped. The PDMS material spreads out in a finger-like fashion, folds into itself, and collects additional air bubbles[1]. Because the mold cavity is filled with air initially and the air has to pass by the PDMS to escape, the concentration of dissolved air in the PDMS has the potential to increase slightly during the centrifugal casting startup.

[1]Video observations of this behavior are shown in Figure 2-14

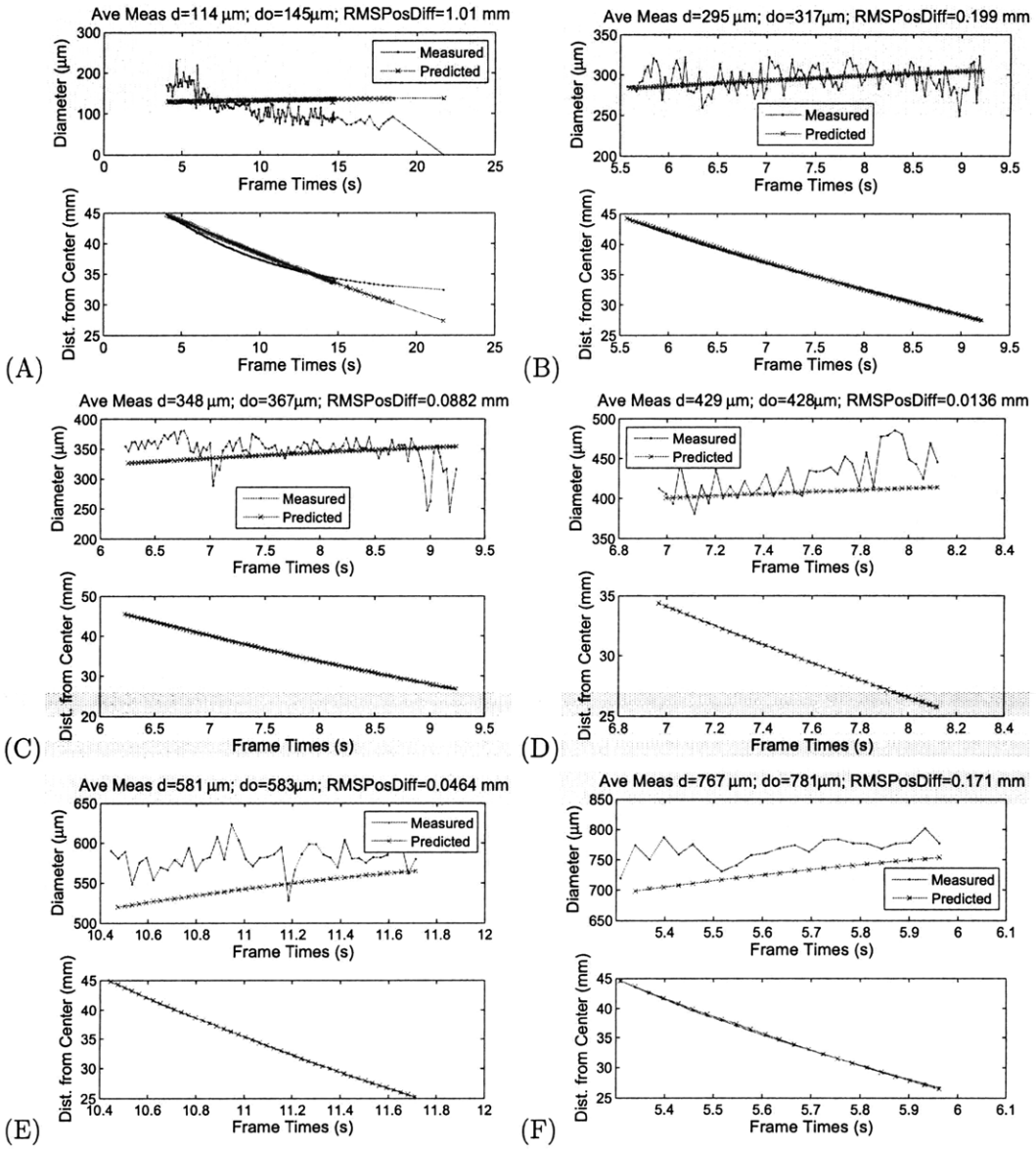

Figure 4-10: Speed and bubble diameter differences between measured and predicted values for the data included in Figure 4-3 using the bubble speed model without diffusion. The value for the D_c parameter is 2 with a dynamic viscosity of 2.59 Pa s. (A) 114 μm average measured bubble diameter. (B) 295 μm average measured bubble diameter. (C) 348 μm average measured bubble diameter. (D) 429 μm average measured bubble diameter. (E) 581 μm average measured bubble diameter. (F) 767 μm average measured bubble diameter.

After the initial centrifugal startup, the PDMS stops sloshing around in the mold cavity and reaches a state of rigid body rotation. Within the rigidly rotating PDMS, many bubbles have been trapped, and they begin to migrate toward the center axis of rotation. Another more subtle point is that the air concentration in the PDMS has to remain nearly constant, because the only surface in contact with air is the liquid-air interface near the center of the centrifuge. In other words, the only way for the air concentration to increase is by air diffusing into the solution through the liquid-air interface. However, with the time scale of the spinning process on the order of a minute, a diffusion coefficient on the order of $10^{-9}\,\mathrm{m}^2/\mathrm{s}$, and pressures on the order of 10 atm, air diffusing through the liquid-air interface near the center of the centrifuge does not likely change the concentration of air within the bulk of the PDMS.

The pressure within the PDMS eventually reaches steady-state and has a distribution shown in Figure 4-6 A. The increased pressure in the bulk of the solution signifies that the PDMS could support a higher concentration of air according to Henry's Law (Equation 3.1) if there were an adequate supply of air in contact with the fluid. An adequate supply of air does not exist for the bulk of the PDMS, but an adequate supply of air exists for the wall interfaces of the air bubbles in solution. Therefore, the bubble walls will have increases in air concentration according to Henry's Law because the internal bubble pressure is even greater than the pressure of the surrounding fluid. This increase in air concentration within the bubble walls will create a concentration gradient at the interface between the bubble wall and the PDMS in the bulk of the fluid. According to Equation 3.48, this concentration gradient with respect to the concentration of air within the bubble wall being greater than the concentration of air in the surrounding fluid will favor dissolution.

If the PDMS solution is not supersaturated before the spinning begins, all the bubbles in solution will begin to dissolve. With the possibility of bubbles dissolving in the solution, the rate at which they dissolve or the time required for them to dissolve is an important concern. Assuming the radius of the spinning part is on the order of a few centimeters, a large bubble (1 mm in diameter for example) will be removed from a solution spinning at thousands of revolutions per minute by buoyant forces before the bubble has sufficient time to dissolve completely. Smaller bubbles ($10\,\mu$m in diameter for example) will dissolve into solution before enough time passes for them to be transported out of the solution. Thus, a numerical implementation of a combined diffusion and bubble speed model would prove

useful in making additional predictions for the amount of spin time required to remove bubbles from a part being centrifugally cast.

The bubble velocity model of Section 4.3 and the Epstein-Plesset diffusion model with surface tension in Section 3.3.2 can be combined using the simple numerical integration scheme described by Equation 4.28. The major simplification/assumption in using the Epstein-Plesset model, which was developed for a bubble in a quiescent fluid, is that the bubble velocity will not alter the rate of gas diffusion. For very small bubbles in centrifugal spinning, the bubbles are almost stationary, which condition is closer to the assumption made by Epstein and Plesset. However, moving bubbles will encounter "fresh" PDMS in each step along the way toward the center axis of rotation. The idea that a moving bubble would grow or shrink at a different rate than that predicted by the Epstein-Plesset model was known by the authors. Epstein and Plesset actually start off their work [39] mentioning a rising bubble in motion with a Hadamard-Rybczynski drag coefficient. They also state that "even this slow motion through the diffusion atmosphere around the bubble is sufficient to produce some slight acceleration of the diffusion process. Hence, the diffusion rates deduced here will be somewhat low." Therefore, while the implementation in this thesis may sufficiently describe the overall bubble behavior in the centrifuge, there is still room to improve the model by including the effects of bubble velocity in the diffusion calculations.

The numerical implementation of the combined model can be described with the following steps and the actual code is given in Appendix A.3:

1. Centrifugal casting parameters are set.

   A. Outer edge of part being cast or bubble starting point is specified.

   B. Distance of liquid-air interface near the center is specified.

   C. Fluid properties include viscosity, density, surface tension, Henry's coefficient, diffusion coefficient, molecular weight of the gas, and the initial concentration of air within the liquid as given by

$$c_i = c_{f\_init} k_D p_{init}, \tag{4.29}$$

   where c_{f_init} is the initial amount of fractional supersaturation (i.e. $c_{f\_init} = 1.05$ would indicate a supersaturation of 5%) caused by

pouring, mixing, or the sloshing of fluid during the spinning startup. The parameter p_{init} is the initial pressure (atmospheric for this work).

D. Additional parameters include chamber pressure, temperature, max spin speed, slew rate (centrifuge's angular acceleration), and time step for the numerical integration.

2. Bubble diameter d_o at atmospheric pressure is set, and the first time step iteration begins.

3. Given the value of d_o, the initial molar mass of the bubble is calculated.

4. The liquid pressure at the bubble's location with the given spin speed is calculated. The bubble's internal pressure and diameter are also calculated.

5. Given the diameter, the bubble speed is calculated. Using that bubble speed with Equation 4.28, a new bubble position is calculated. The next iteration begins.

6. The fluid pressure is calculated using the new spin speed and bubble location. Using the fluid pressure and the Henry's coefficient, the c_f parameter is also calculated using the following:

$$c_f = \frac{c_i}{k_D p_{fluid}}. \tag{4.30}$$

7. Using the current molar mass and molecular weight of the gas, the bubble mass is calculated. Using a form of Equation 4.31, the change in mass of the bubble is calculated:

$$\frac{dm}{dt} = 4\pi R^2 \kappa k_D \left[p_{fluid} (c_f - 1) - \frac{2\sigma}{R} \right] \left\{ \frac{1}{R} + \frac{1}{(\pi \kappa t)^{1/2}} \right\}. \tag{4.31}$$

8. Using this change in mass of air within the bubble, a new molar mass is calculated using the molecular weight of the gas.

9. Using the new molar mass of the bubble, along with the fluid pressure at the current bubble location, a new internal bubble pressure is calculated. With this new internal bubble pressure, the new diameter is calculated.

Table 4.3: Parameter values used in simulating combined bubble speed and diffusion behavior.

Parameter	Value	Description
bubble_start_pos	0.0615 m	Bubble start distance from center axis of rotation
bubble_end_pos	0.0343 m	Bubble ending distance from center axis of rotation
r_{fstart}	0.0343 m	Liquid-air interface distance from center axis of rotation
T	298 K	Temperature during spinning
σ	0.02 N/m	Liquid-gas surface tension
μ	3.9 Pa s	Liquid viscosity
ρ_f	1030 kg/m^3	Liquid density
P_{cham}	101.3 kPa	Chamber pressure
ϕ	0°	Mold tilt angle
spin_speed	1000 – 8000 rpm	Set spin speed
slew rate	300 rpm/s	Spin speed acceleration (slew rate)
offset	100 rpm	Spin speed at start
κ	1.47×10^{-9} m^2/s	Diffusion coefficient
k_D	1.927×10^{-6} kg (gas) / m^3(polymer)/Pa	Henry's coefficient
M	0.02897 kg/mol	Molecular weight of gas
dt	0.01 s	Time step
c_{f_init}	1.05	Initial supersaturation fraction
D_c	2	Drag force coefficient (used in this work)

10. Steps 5 through 9 are then repeated until the bubble diameter goes to zero or the bubble position reaches the desired end point. Throughout this process keep track of time, bubble position, and any other parameters of interest.

Using this combined centrifugal bubble velocity and diffusion numerical implementation, it is possible to simulate or predict bubble behavior given a set of centrifugal spinning parameters . The following three figures show a variety of outputs for simulations using the parameter values in Table 4.3. The termination point of a line signifies that the bubble has either reached the desired end position (the liquid-air interface in this case) or dissolved into solution ($d \leq 0$). These selected parameter values are representative of the designed and tested system described in Section 2.6.

Figure 4-11 shows the value of c_f plotted against time for different spin speed profiles and initial bubble diameters. The initial value of c_f starts at 1.05 and then decreases. This

decrease is due to the acceleration of the centrifuge. As the centrifuge accelerates, the fluid pressure builds up causing a decrease in c_f as described by Equation 4.30. The centrifuge then reaches steady-state speed, and the bubble continues moving toward the liquid-air interface near the center of the centrifuge. As the bubble moves closer to the center of the centrifuge, the fluid pressure surrounding the bubble decreases as described by Equation 4.1. This decrease in fluid pressure leads to an increase in the c_f parameter, and if the bubble makes it all the way to the liquid-air interface before dissolving, the c_f parameter returns to 1.05.

As shown in Figure 4-6 C, in a situation with no diffusion, a bubble will grow as it gets closer to the center due to the decreasing fluid pressure. The bubble starts at the right of each graph (0.0615 m from the axis of rotation) and moves toward the center/left of the graph (0.0343 m from the axis of rotation). Figure 4-12 shows the bubble diameter as a function of the bubble position and includes diffusion behavior in the numerical implementation. By adding diffusion behavior into the model, it is possible for bubbles to shrink and dissolve into solution as time progresses. All four charts in Figure 4-12 show bubbles with $d_o = 75\,\mu$m or $d_o = 100\,\mu$m dissolving into solution within 5 mm of of the starting point. It is also possible for a bubble to shrink by diffusion and then reach a region where the change in pressure causes the concentration gradient between the bubble wall and the PDMS surrounding the bubble to flip directions (assuming solution is originally slightly supersaturated) leading to bubble growth as the bubble gets closer to the center of the centrifuge. Figure 4-12 A shows an interesting example of a bubble ($d_o = 132.1\,\mu$m) actually growing after reaching a region less than 5 mm away from the liquid-air interface in a solution that has an initial c_f parameter of 1.05 at atmospheric pressure.

Figure 4-13 is similar to Figure 4-9 in that it shows the trajectory of bubbles with different diameters. The bubbles start at the green line/top horizontal line and progress toward the red line. The bubbles either dissolve into solution or have buoyancy carry them to the red line/bottom horizontal line. Each one of the graphs shown in Figure 4-13 has an initial bubble diameter ($d_o = 132.1\,\mu$m for a spin speed of 1000 rpm, $d_o = 157.2\,\mu$m for a spin speed of 2000 rpm, $d_o = 165.3\,\mu$m for a spin speed of 4000 rpm, and $d_o = 166.2\,\mu$m for a spin speed of 8000 rpm) that results in a maximum amount of time required for a given centrifugal spinning profile. These values of d_o that result in the maximum amount of time required were obtained by the MATLAB optimization function **fminsearch** with the

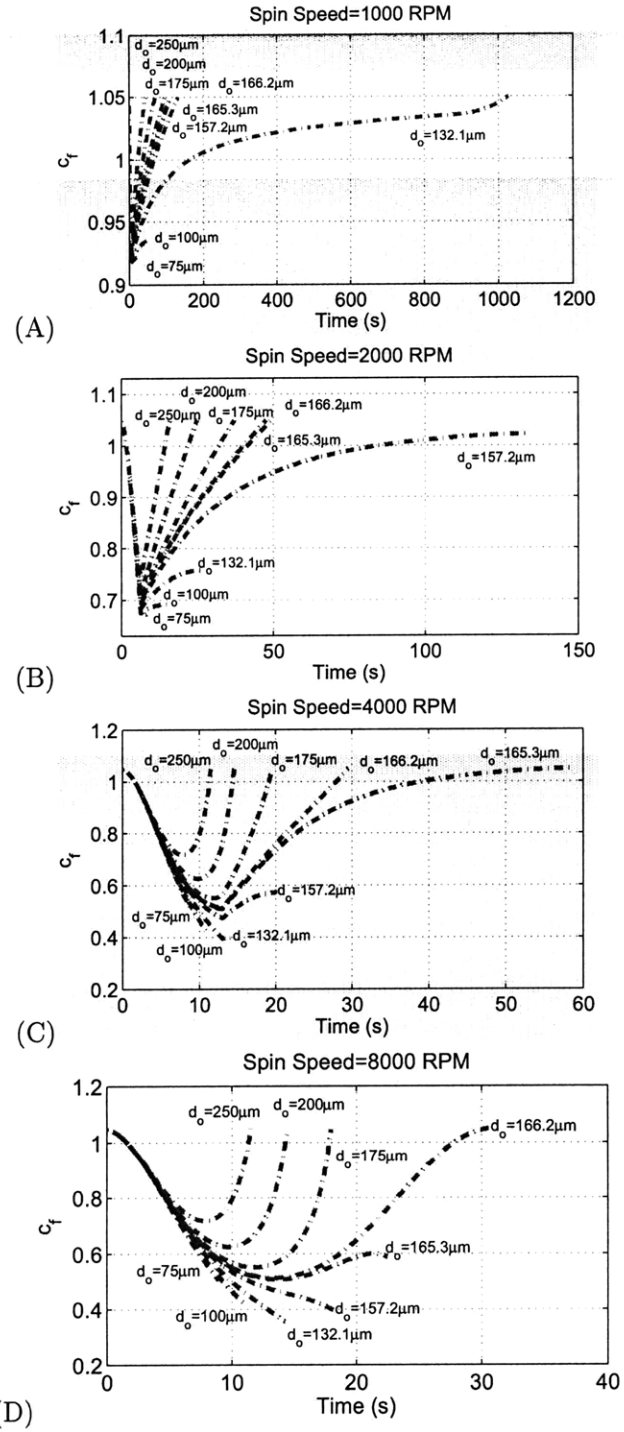

Figure 4-11: The c_f parameter plotted against time for a variety of initial bubble diameters and set spin speeds with slew rates of 300 rpm/s. The D_c value is 2 with a viscosity of 3.9 Pa s, density of 1030 kg/m^3, surface tension of 0.02 N/m, and a time step of 0.01 second. The bubble starts 61.5 mm away from the center of rotation, and the liquid-air interface is 34.3 mm from the center of rotation. (A) Set spin speed of 1000 rpm. (B) Set spin speed of 2000 rpm. (C) Set spin speed of 4000 rpm. (D) Set spin speed of 8000 rpm.

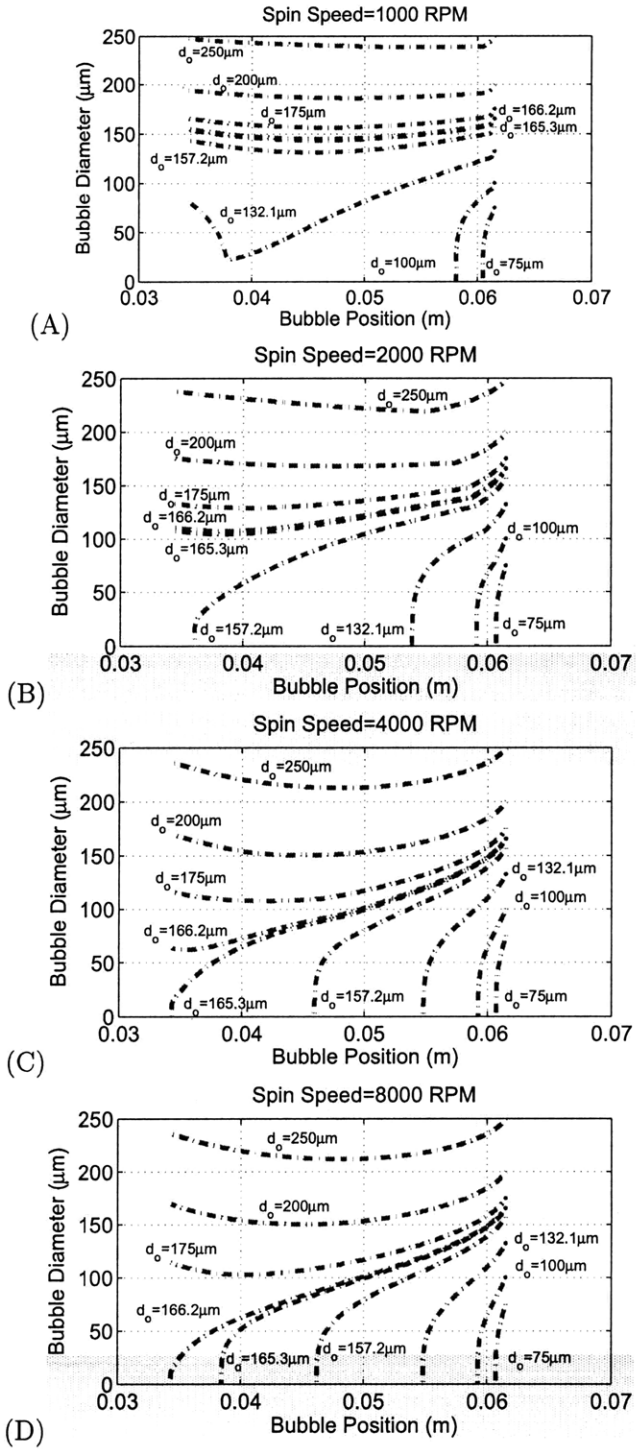

Figure 4-12: The bubble diameter plotted against position for a variety of initial bubble diameters and set spin speeds with slew rates of 300 rpm/s. The D_c value is 2 with a viscosity of 3.9 Pa s, density of 1030 kg/m^3, surface tension of 0.02 N/m, and a time step of 0.01 second. The bubble starts 61.5 mm away from the center of rotation, and the liquid-air interface is 34.3 mm from the center of rotation. (A) Set spin speed of 1000 rpm. (B) Set spin speed of 2000 rpm. (C) Set spin speed of 4000 rpm. (D) Set spin speed of 8000 rpm.

negative of the time output for the numerical implementation of the combined bubble speed and diffusion model. The maximum time values for these optimizations plotted against spin speed are shown in Figure 4-14.

The numerical implementation is very sensitive to changes or perturbations to initial diameter d_o in the domain[2] very close to the optimized value of d_o, which yields the maximum time required for a bubble to exit. This sensitivity is illustrated in Figure 4-15 A. The actual maximum[3] occurs at $d_o = 132.118527930570\,\mu$m with a time value of 1027 s. Using the numerical implementation with $d_o = 132.11852793\,\mu$m, the resulting time value is 774 s. Using the numerical implementation with $d_o = 132.118527931\,\mu$m, the resulting time value is 925 s. A change of $1 \times 10^{-9}\,\mu$m corresponds to an exit time difference of 151 seconds. To get around these issues with sensitivity for the maximum exit time, a fairly straightforward probabilistic approach is applied to determining a realistic exit time.

Assuming a random distribution of d_o values (equal probability of any particular bubble diameter occurring) between $0\,\mu$m and 1 mm, domains of d_o values can be associated with a probability of existence. For example, if a specified domain includes $d_o = 100\,\mu$m to 1 mm, there is a 90% chance of a bubble existing within the specified domain over the master domain between $0\,\mu$m and 1 mm. Likewise, if one is interested in removing 99% of all the bubbles in the master domain between $0\,\mu$m and 1 mm, only a domain length of $10\,\mu$m is permissible. This domain length could be from $d_o = 100\,\mu$m to $110\,\mu$m or it might be from $d_o = 500\,\mu$m to $510\,\mu$m.

Applying this probability of domain lengths to the relationship between exit times and initial bubble diameters as shown in Figure 4-15, it is possible to estimate the time required to remove a certain fraction of the total bubbles, given a master domain. Figure 4-15 B and Figure 4-15 C show the exit times for a bubble to be removed from the outer edge of the spinning mold plotted against initial bubble diameters given a spin speed of 1000 rpm and 8000 rpm. In addition, these plots show a cutoff line with a length of $100\,\mu$m. A cutoff line with a length of $100\,\mu$m over a master domain with a length of 1 mm corresponds to 10% of its total length. The cutoff line with a length of $100\,\mu$m in Figure 4-15 B at an exit time value of 65 seconds suggests that 90% of the bubbles that started at the outer edge of the mold would be removed from the part in 65 seconds with a set spin speed of 1000 rpm. The

[2]The term domain represents a set of input values for a given function.

[3]The number of significant digits for d_o may initally appear absurd. The point is to show that the numerical implementation can be extemely sensitive to changes in d_o.

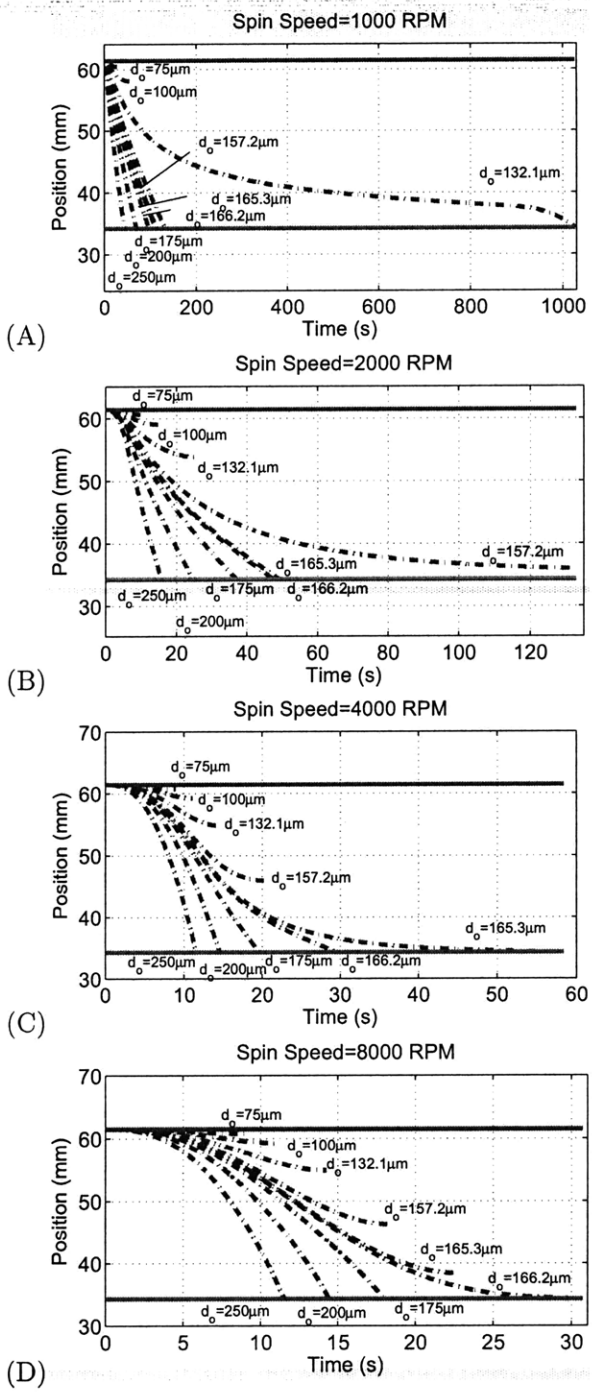

Figure 4-13: The bubble position plotted against time for a variety of initial bubble diameters and set spin speeds with slew rates of 300 rpm/s. The D_c value is 2 with a viscosity of 3.9 Pa s, density of 1030 kg/m^3, surface tension of 0.02 N/m, and a time step of 0.01 s. The bubble starts 61.5 mm away from the center of rotation, and the liquid-air interface is 34.3 mm from the center of rotation. (A) Set spin speed of 1000 rpm. (B) Set spin speed of 2000 rpm. (C) Set spin speed of 4000 rpm. (D) Set spin speed of 8000 rpm.

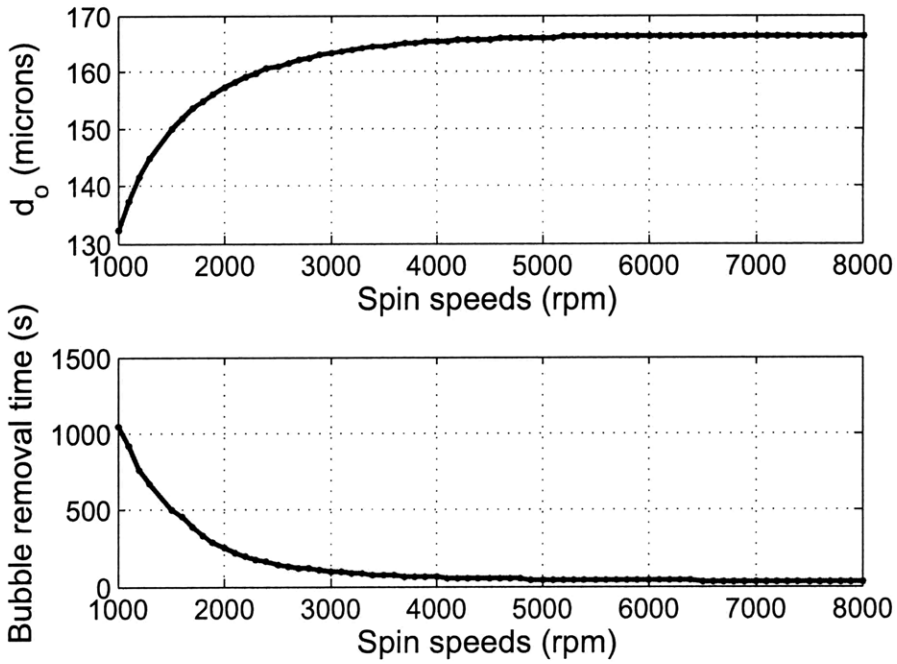

Figure 4-14: Top graph shows initial bubble diameter values (d_o) found by MATLAB's **fminsearch** optimization to take the longest time to exit the solution. Bottom graph shows the optimized times for the bubble to exit.

cutoff line in Figure 4-15 B suggests that 90% of the bubbles that started at the outer edge of the mold would be removed from the part in 13 seconds.

Given the unrealistic sensitivity of maximum time in the numerical simulations as shown in Figure 4-15 A, the line width calculating method described in Figure 4-15 B and Figure 4-15 C can be used to estimate the amount of time required to remove a desired percentage/fraction of bubbles that may have started at a given location with a given spin speed profile. Figure 4-16 shows different predictions for exit time based on the numerical implementation of the combined bubble speed and diffusion model, along with the probability of removing a specified fraction of all the bubbles with an initial diameter between 0 μm and 1 mm.

In Figure 4-16, the time for bubble removal was calculated by optimizing d_o to yield the maximum time with the MATLAB function **fminsearch**. The resulting optimized values do show the longest times to exit, but changes in the optimized d_o values of less than an Angstrom lead to significant variation of the time to exit value. Therefore, using the maximum exit time associated with the optimized value of d_o alone will likely overpredict

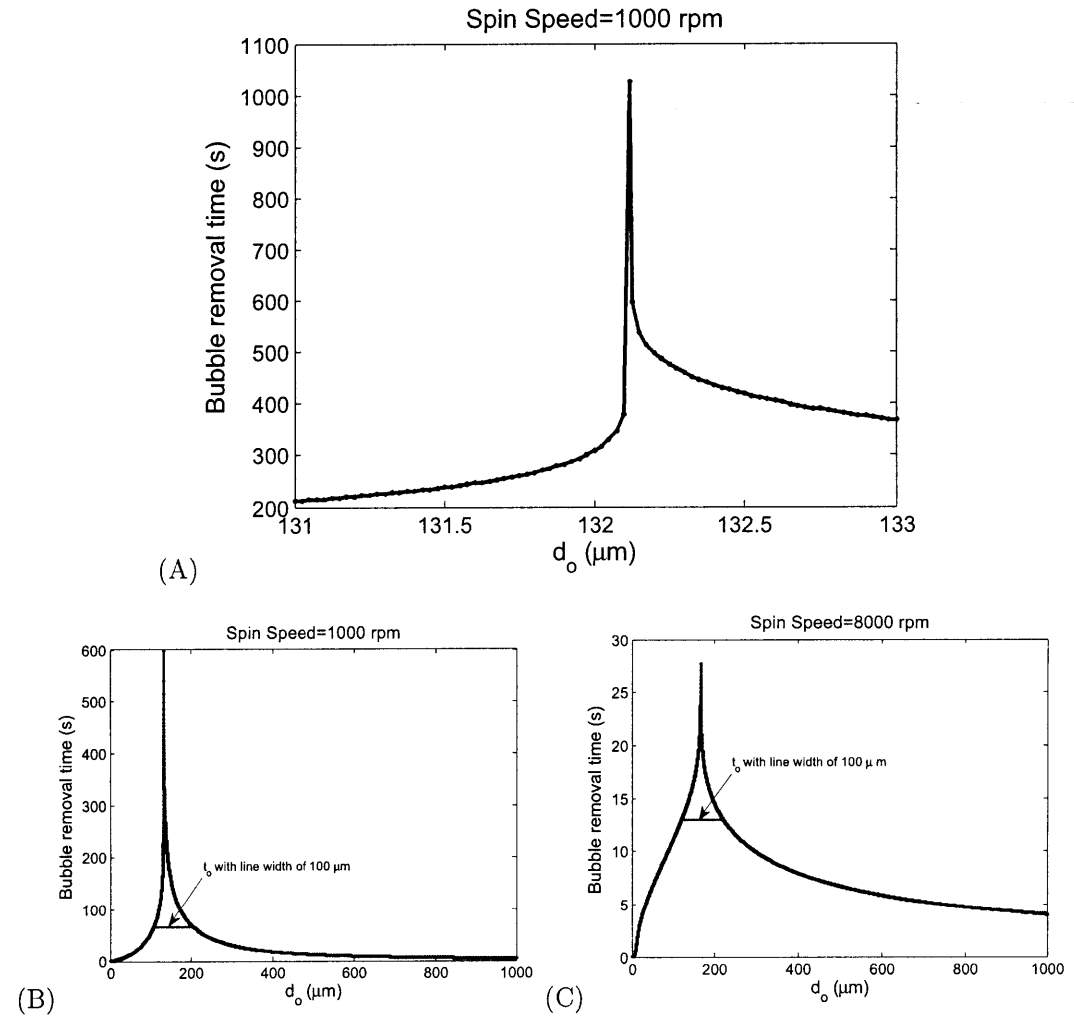

Figure 4-15: (A) The time to exit in the region near the maximum for a spin speed of 1000 rpm. (B) Calculated time to exit for a spin speed of 1000 rpm with d_o step of 25 nm. (C) Calculated time to exit for a spin speed of 8000 rpm with d_o step of 25 nm.

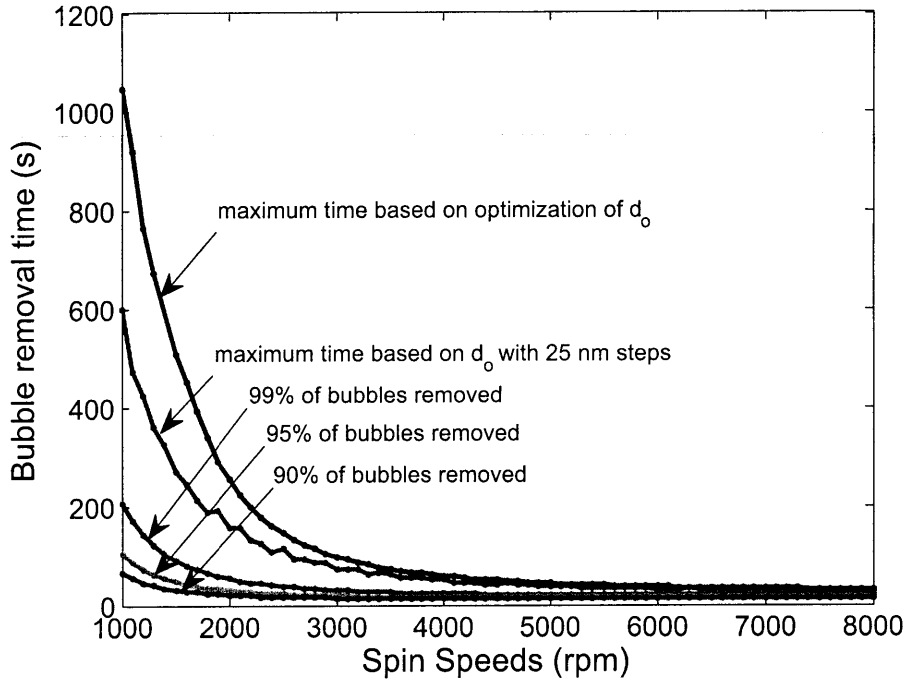

Figure 4-16: Times for bubbles to exit based on optimization of d_o and fractional number of bubbles removed. The bubbles are assumed to have started at the outer edge of the molding region.

the amount of time necessary to remove bubbles from solution at a given spin speed.

To use the line width method to calculate the exit time associated with a percentage of bubbles removed after a specified amount of time, exit times were calculated over the domain of $0\,\mu$m to 1 mm for d_o with a spacing of 25 nm. The maximum of the time values over the specified d_o domains with varied spin speed are shown in Figure 4-16. These values are depicted by the jagged curve just inside the curve showing the maximum exit times. Using the line width calculation methods to estimate the fraction/percentage of bubbles removed at a specified amount of time, the lower three lines of Figure 4-16 indicate the amount of spin time required to remove approximately 90% (line width of $100\,\mu$m), 95% (line width of $50\,\mu$m), and 99% (line width of $10\,\mu$m) of the bubbles that may have initially existed at the outer edge of the mold.

In calculating the maximum amount of time required to remove a bubble from solution, it has been implied that this maximum time is associated with a bubble that moves from the outer edge of the mold to the center. In reality, the most time consuming bubbles for removal do not necessarily start at the outer edge of the mold. There is a balance between

the speed at which a bubble travels due to buoyancy and the speed at which it dissolves into solution. It is possible that the bubbles, which would take the longest time to exit could exist somewhere in the middle of the part. In a case study of different geometries (Section 5.3), it is numerically shown that the most time-consuming bubbles for removal may start in the middle of the part and not necessarily at the outer edge of the mold geometry.

Going back to the current scenario, Figure 4-18 shows the maximum time required for removal plotted against set spin speed and bubble starting position. The set spin speed parameter refers to the maximum spin speed attained by the centrifuge using the spin speed profile with a slew rate of 300 rpm/s. The bubble start position is with respect to the axis of rotation. As shown in both the plots of Figure 4-18 but especially Figure 4-18 B, the maximum time for a set spin speed of 1000 rpm actually occurs with a bubble starting approximately 4.5 cm from the center axis of rotation. However, at higher spin speeds, the maximum time occurs with a bubble starting at the outer edge of the mold. For example, the bubble removal time is $\sim$ 20 seconds for bubbles that start at the outer edge with a set spin speed of 5000 rpm, but less than 20 seconds for bubbles that start at 4 cm from the center axis of rotation with a set spin speed of 5000 rpm. Because the differences in maximum times for bubble removal are not too much greater at low spin speeds ($\sim$ 1000 rpm) for bubbles starting in the middle of the part versus the outer edge of the part, it is simpler to use the outer edge as the starting position associated with the maximum bubble removal time for the calculations in this section.

4.4.2 High speed video and numerical implementation comparisons

In measured bubble behavior from high speed video footage (Figure 4-3), it is possible to compare the bubble speed model with diffusion to the measured data. In this case, the objective is to minimize the difference between the measured positions/distance from the center axis and the predicted position by selecting the most appropriate value for d_o. Table 4.4 shows the resulting optimized d_o values, along with the corresponding minimized RMSD position difference. The RMSD diameter difference is also included to show that the measured diameters and the predicted diameters using the model without diffusion are close to the resolution of the captured images (31.5 μm per pixel). The D_c value of 2 with a viscosity of 2.59 Pa s was fixed during the optimization routine.

In comparing the RMSD values in Table 4.2 to Table 4.4, the RMSD position differ-

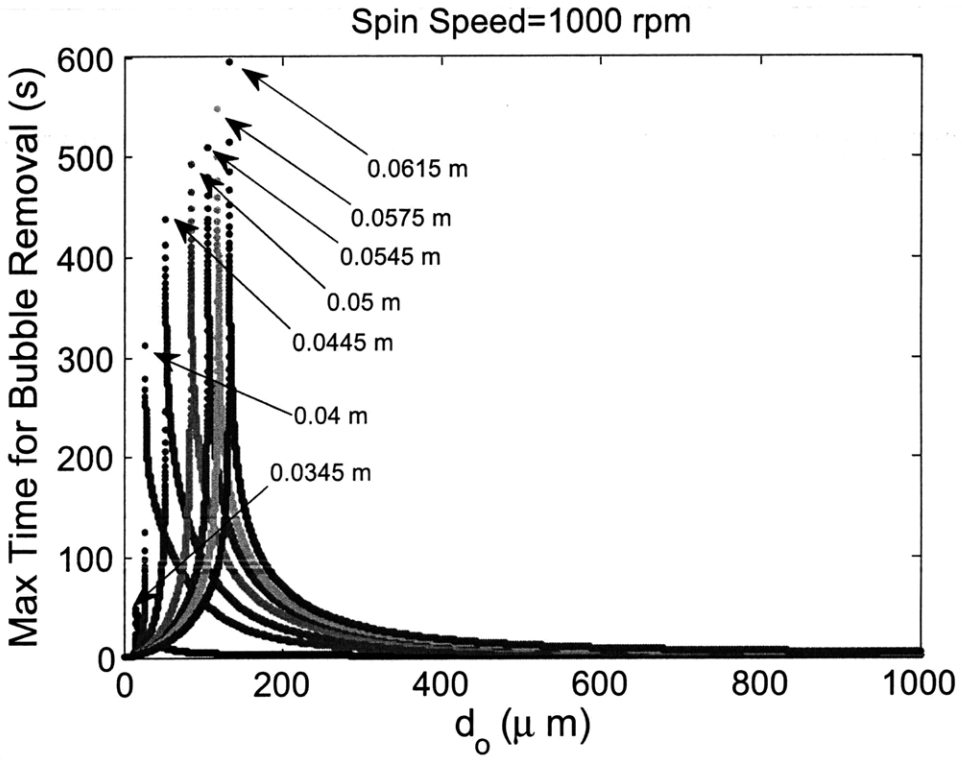

(A)

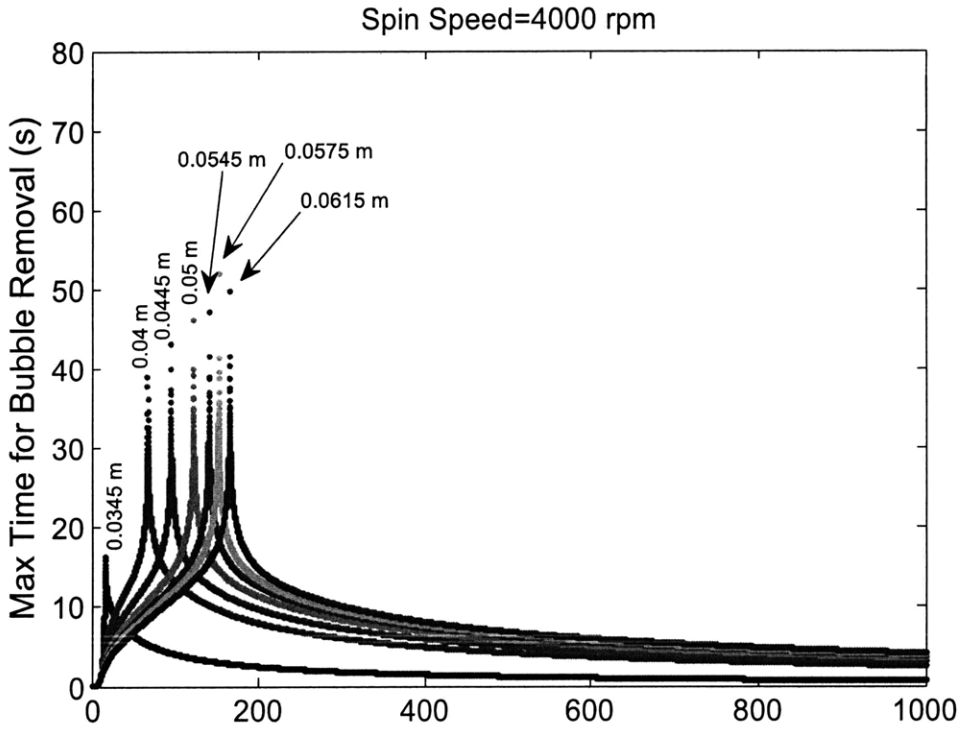

(B)

Figure 4-17: Simulated times for bubbles to be removed from PDMS plotted against a domain of initial bubble diameters. The lengths indicated at the various peaks indicate the bubble starting position. (A) Set spin speed of 1000 rpm. (B) Set spin speed of 4000 rpm.

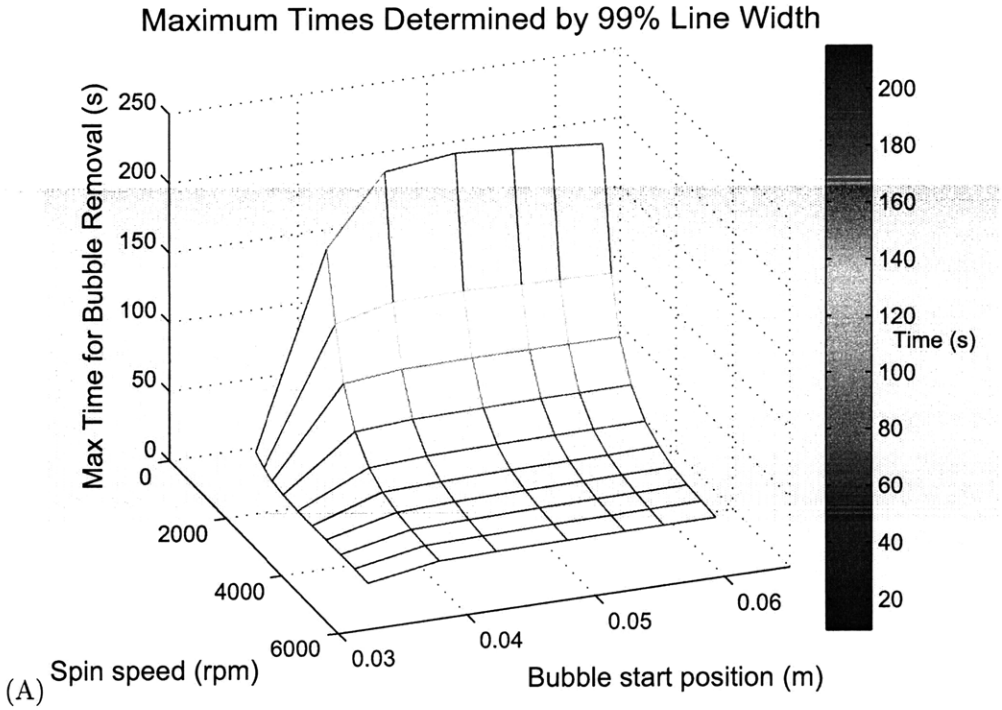

(A)

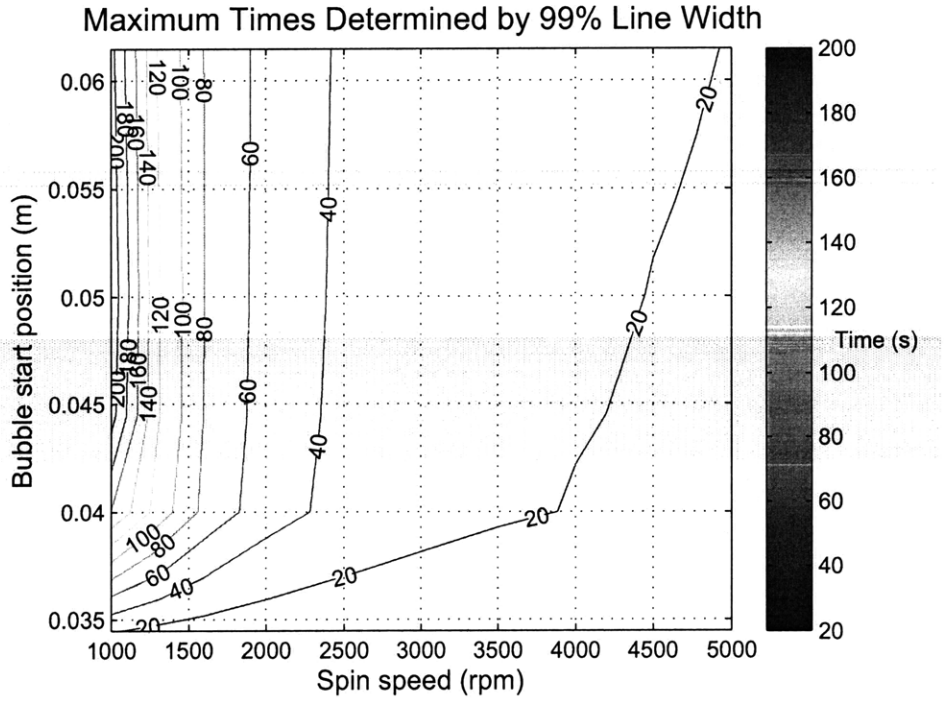

(B)

Figure 4-18: Simulated times for bubbles to be removed from PDMS plotted against set spin speeds and bubble starting positions. (A) 3-D depiction of simulated results. (B) Contour representation of the same numerical results.

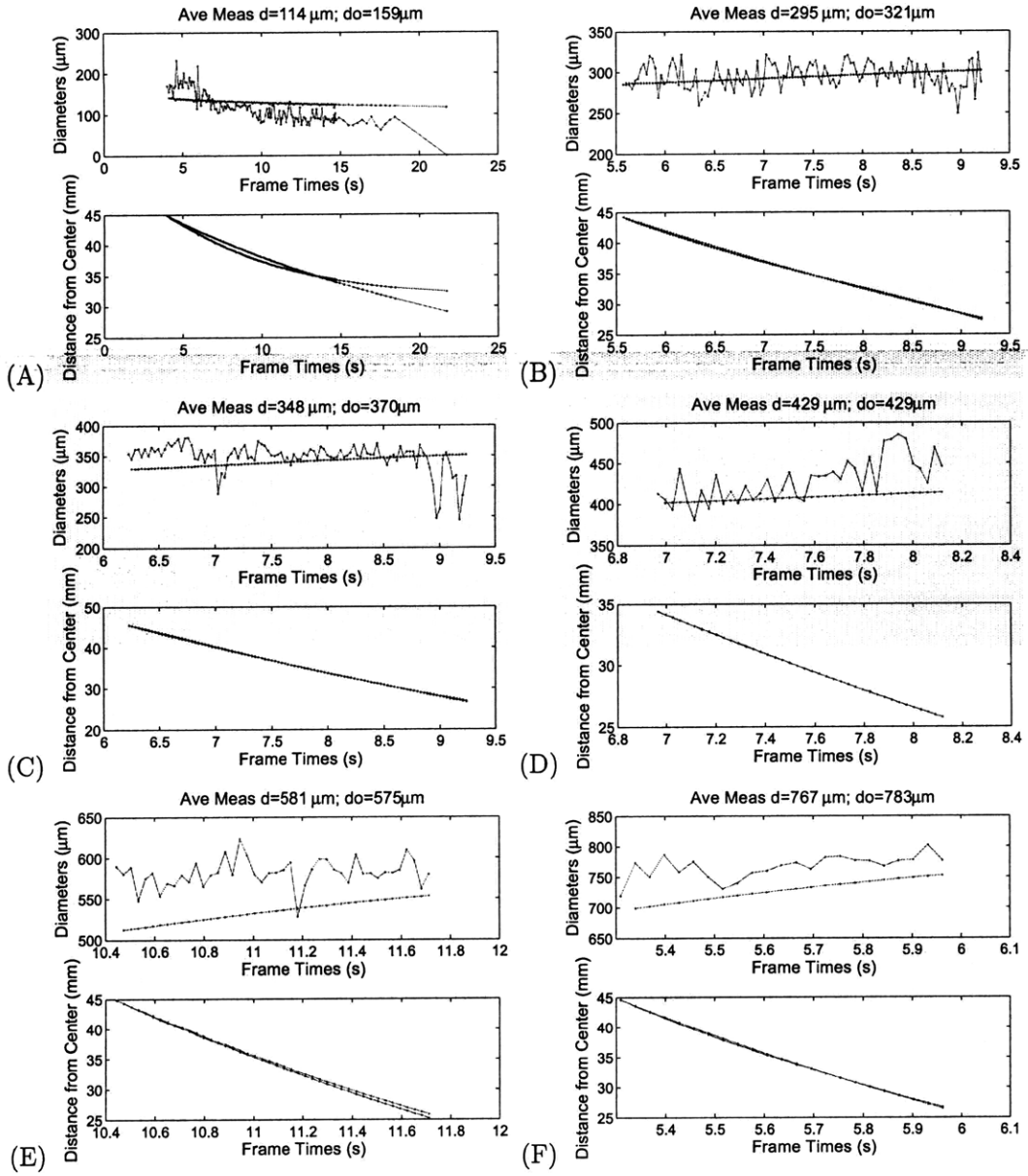

Figure 4-19: Speed and bubble diameter differences between measured and predicted values for the data included in Figure 4-3. The value for the D_c parameter is 2 with a dynamic viscosity of 2.59 Pa s. (A) 114 μm average measured bubble diameter. (B) 295 μm average measured bubble diameter. (C) 348 μm average measured bubble diameter. (D) 429 μm average measured bubble diameter. (E) 581 μm average measured bubble diameter. (F) 767 μm average measured bubble diameter.

Table 4.4: Optimized $d_o$values to minimize RMSD Position Difference (3rd column) for combined bubble velocity/position and Epstein-Plesset diffusion model.

Mean measured bubble diameter (μm)	d_o (μm)	RMSD Position Difference (mm)	RMSD Diameter Difference (μm)
767	781.3	0.166	43.7
581	583.1	0.355	50.2
429	427.8	0.016	31.7
348	366.9	0.117	28.2
295	316.9	0.172	15.8
114	145.0	0.681	34.8
Average		0.25	34.1
Standard Deviation		0.24	12.1

ence value for the smallest bubble (mean diameter of 114 μm) is reduced to 0.681 mm from 1.008 mm. That said, the average RMSD value for the rest of the measured bubble diameters goes up because the overall RMSD average value for the position differences are the same. So, using the new combined diffusion and bubble velocity model does not negatively affect the overall mean value of the RMSD position differences, but it does seem to introduce greater errors into predictions for the tracking of the bubbles with a mean diameter greater than 114 μm. This observation is also reflected in the the standard deviation of the RMSD differences decreasing from 0.38 mm for the fitting to the model without diffusion to 0.24 mm for fitting to the model including diffusion. Running an F-test comparing the RMSD position differences for the model without diffusion and the model with diffusion in OpenOffice Calc, the probability that these two data sets could have come from the same distribution is only 34%. The reduction of the standard deviation combined with the same overall average values and major reduction of the RMSD position difference from 1.008 μm to 0.681 μm signifies that the newer fit is better at capturing the bubble behavior for a broader domain of bubble diameters. However, the data fit is not as good for bubbles with a mean diameter greater than 114 μm.

Given all this work on attempting to fit the model and measured data results, it is important to come back and realize that the objective of this work is to build a model capable of predicting the amount of time required to remove bubbles from solution given a particular geometry configuration and spin speed profile. The true test of the modeling comes when looking at the quantity of bubbles remaining in centrifugally cast parts with

varied spinning parameters.

4.5 Validation of bubble speed models

To test the predictive capabilities of the models proposed and developed in this chapter, a set of designed experiments were performed varying two parameters: spin time and spin speed. The spin speeds and spin times were carefully chosen to produce approximately half of the resulting parts with bubbles and half without bubbles. The varied spin times were 0.5, 1, 2, 3, and 5 minutes, and the varied spin speeds were 1000, 1600, 2500, and 4000 minutes. With five discrete spin times and four discrete spin speeds, there are 20 possible combinations. The spin time refers to the total amount of time the centrifuge motor was energized and does not include the time for the centrifuge to decelerate and stop. The centrifuge accelerated to the desired spin speed with an acceleration (slew rate) of 300 rpm/s. The rest of the important geometry and fluid properties are given by Table 4.3.

The temperature profile for curing was not purposefully varied from part to part, and it was set to be similar to the temperature profiles included in Figure 2-23. Keeping the number of varied parameters to two (spin time and spin speed) makes for simpler analysis. Given the work and hypotheses in Section 4.7, variation of the temperature profile should not have as large an effect on whether or not a PDMS part has bubbles in it as compared to the effects of varying spin time or spin speed. If the part has been spun for the right combination of speed and time to remove all the bubbles from solution, the temperature profiles for curing should not cause bubbles to form. That said, it might be possible for a bubble to get caught in a surface cavity and not completely dissolve during spinning. In that case, it would be possible for the bubble to grow or come out of the cavity with a temperature increase. The temperature profile for curing might have a larger effect on the number of bubbles or their size distribution, if the part is not spun long enough to remove all of the bubbles before curing. However, the temperature profile will probably not affect the binary question of whether or not a PDMS part has any bubbles at all in the regions of interest given the features being replicated in this thesis.

Two parts were produced per trial (see balanced mold design shown in Figure 2-26 C) and each set of parameters was run twice. With 20 possible combinations and each combination run twice, there were 40 trials. Since each trial yielded two parts, there were a total of

80 parts produced. The number of bubbles in each part were counted, and the number of bubbles observed for a given combination of spin time and spin speed was calculated by averaging the number of bubbles in four parts. For example, if the number of bubbles found in the four parts that were spun at 1000 rpm for 1 minute were 49, 192, 2, and 8, then the average number of bubbles found for this combination of spin time and spin speed would be 62.8.

To measure the number of bubbles in each part, the parts were scanned using a Canon CanoScan LiDE 600F scanner at a resolution of 1200 dpi. Figure 4-20 A shows an example image of parts (trial #37) scanned without any bubbles in the regions of interest (outlined rectangular regions of images). Figure 4-20 B shows an example image of parts (trial #31) scanned with a number of bubbles left in them. Once the images were acquired with the scanner, the images were processed using a custom designed graphical user interface shown in Figure 4-20 A and Figure 4-20 B. The graphical user interface used the following algorithm to detect bubbles, which was inspired by numerous examples in the MATLAB help documentation:

1. Load image and adjust contrast using the MATLAB **imadjust** command. For the images shown in Figure 4-20, the command was essentially the following: **imadjust**(handles.AI, [38/255 233/255]).

2. Apply the MATLAB **imopen** command, which performs morphological opening on the image. For the images shown in Figure 4-20, the command was essentially the following: **imopen**(AIadj,strel('square',3)).

3. Threshold the image to black and white using the MATLAB **im2bw** command and then invert the image. For the images shown in Figure 4-20, a threshold value of 0.74 was used.

4. Label and identify regions that satisfy the black and white thresholding by using the MATLAB command **bwlabel**.

5. Calculate a diameter for every labeled area based on the square root of the area of the found regions.

6. Keep all areas with an estimated diameter greater than a diameter threshold value. For the images in Figure 4-20, the diameter threshold value is 0.2 mm.

Table 4.5: Centrifugal casting trials in randomized order.

Trial	Spin Speed (rpm)	Spin Time (min.)	Bubbles in A	Bubbles in B
1	2500	5	0	0
2	1600	2	0	0
3	1600	3	0*	0
4	2500	3	0	0
5	1000	5	0	0
6	4000	1	2	0
7	4000	5	0	0
8	2500	3	0	0
9	4000	2	0	0
10	2500	1	1	0
11	1000	1	2	8
12	1600	5	0	0
13	2500	0.5	0	0
14	4000	2	0	0
15	4000	0.5	0	0
16	1000	1	49	192
17	1000	0.5	84	26
18	1600	1	8	0
19	4000	5	0	0
20	1600	0.5	4	12
21	4000	0.5	0	0
22	1000	2	6	1
23	1600	1	0	0
24	4000	3	0	0
25	4000	3	0	1
26	1600	2	0	0
27	2500	2	0	0
28	2500	1	0	0
29	1000	3	0	0
30	1600	3	0	0
31	1000	0.5	144	21
32	1600	5	0	0
33	1000	2	7	3
34	1000	3	0	0
35	2500	2	0	0
36	2500	0.5	5	0
37	1000	5	0	0
38	2500	5	0	0
39	1600	0.5	46	11
40	4000	1	0	0

*sample tore during demolding; 0 bubbles counted by eye.

7. Show images of the regions of interest with the bubbles highlighted. For the images in Figure 4-20, the bottom images are the cropped regions of interest with the found bubbles highlighted in grey.

The bubble finding algorithm is not perfect, as can be seen in Figure 4-20 B; not all the bubbles are identified, and some of the groupings of the bubbles that are very close to each other get counted only as one bubble. That said, the algorithm has enough accuracy to compare quantities of bubbles in the given regions of interest. Using the outlined image processing technique with the same settings shown in the GUI of Figure 4-20, the bubble counting data in Table 4.5 were generated, and Figure 4-21 presents the average number of bubbles found in four parts at each combination of spinning parameters. The numbers next to the dots are the average number of bubbles measured in four samples.

4.5.1 Bubble speed model without diffusion

Before understanding that concentration gradients could lead to diffusive growth or shrinkage of a bubble in solution, a thought process associated more with classical bubble nucleation theory was followed. This thought process suggests that there is a critical bubble radius that determines whether a bubble will continue to exist or not. In other words, if the bubble is below the critical radius as described by Equation 4.38, the energy arguments suggest the bubble will dissolve into solution. If the bubble is above this critical radius, then the bubble will continue to exist. This hypothesis removes the aspect of time associated with how long bubbles below a critical radius might take to dissolve into solution, but it captures the idea that a critical diameter might exist and that there is a binary stability condition. Bubbles below a certain cutoff cannot exist in the solution, and bubbles above a certain cutoff radius will continue to exist. Thus, the effort was to identify what this critical bubble size might be by experimentation.

At any given time during spinning, all bubbles above a certain size should no longer exist in solution because they have been moved to the liquid-air interface by buoyancy. As the speed or time of spinning is increased, the maximum size of bubbles that should still exist in the solution will continue to decrease. By calculating the amount of time bubbles with different initial diameters (varying values of d_o) might take to move from the outer edge of the mold cavity to the liquid-air interface near the center of rotation, it is possible to estimate what the maximum bubble size left in a solution should be for a given spin profile.

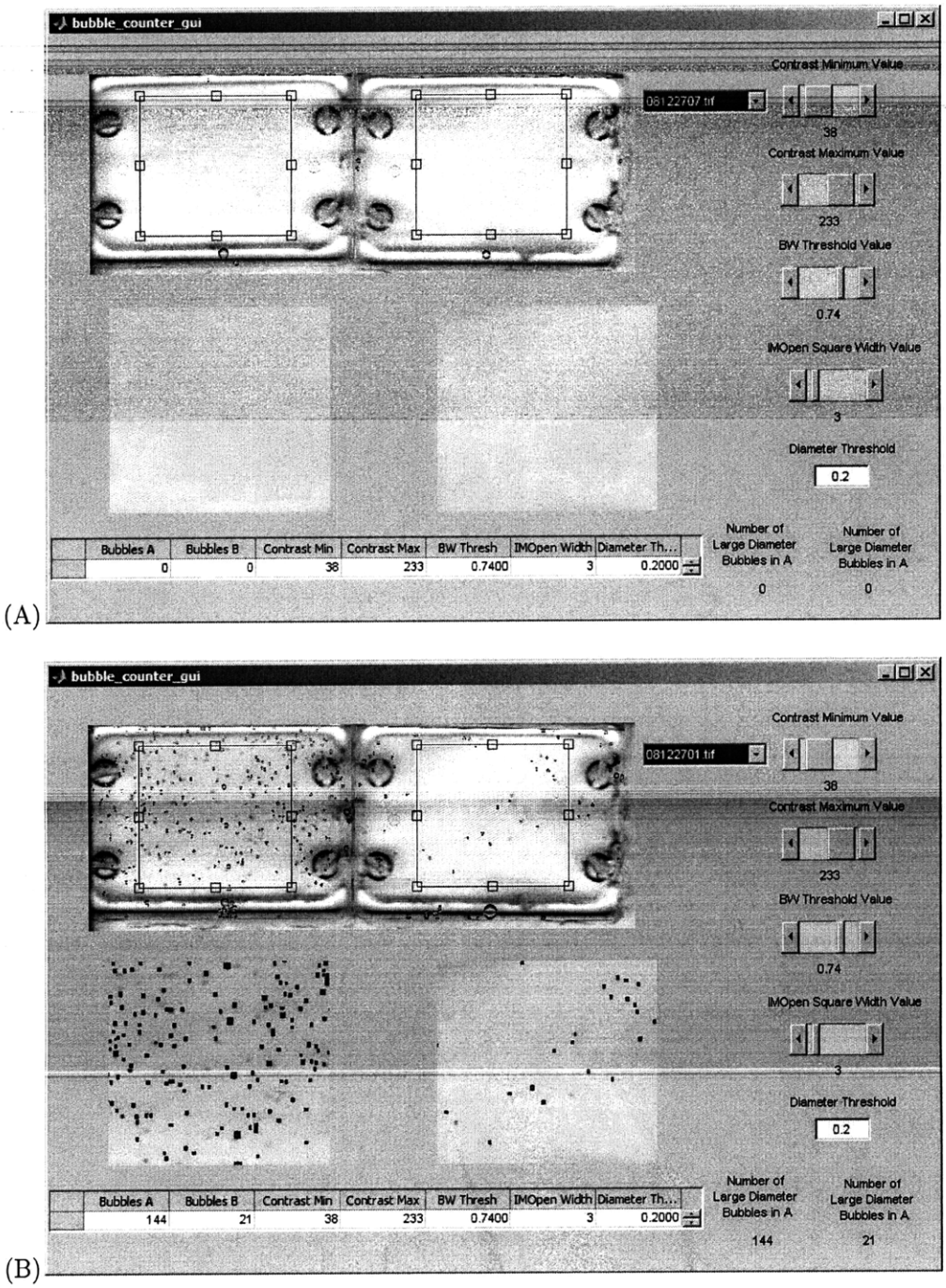

Figure 4-20: (A) Scanned image of parts produced in trial #37 (1000 rpm and 5 minutes) with no counted bubbles in the regions of interest. (B) Scanned image of parts produced in trial #31 (1000 rpm and 0.5 minutes) with 144 bubbles counted within the region of interest in the part on the left (part A) and 21 bubbles counted within the region of interest in the part on the right (part B)

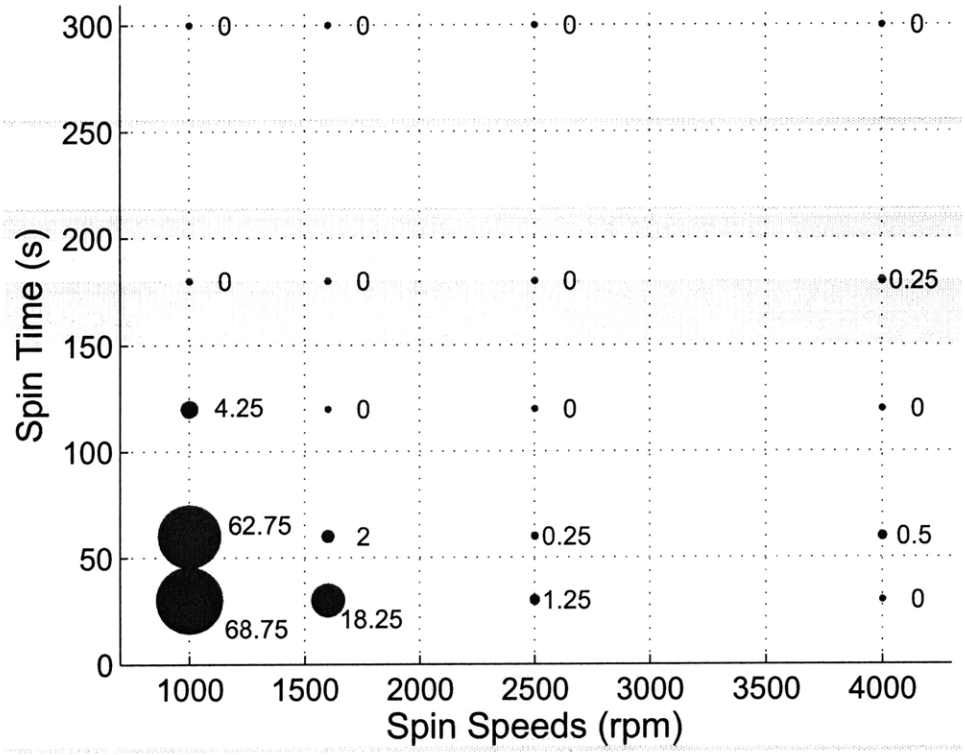

Figure 4-21: Average number of bubbles found at each combination of spinning parameters. The size of the dot corresponds to the average number of bubbles measured.

Combining this principle that bubble sizes in a solution are gradually decreasing over longer spin times with the idea that bubble diameters below a certain critical size should not exist, it becomes possible to identify the critical bubble size that needs to be removed in order for a solution to be bubble-free. Of course, the time required for a bubble to exit is dependent not only on the initial diameter but the spin speed profile, the PDMS fluid properties, and the mold cavity with its specific geometries.

Based on observations of the time required for the centrifuge to spin up to desired speeds, the centrifuge spin speed is estimated by the following equation for set spin speeds up to 8000 rpm:

$$\text{Spin Speed} = \begin{cases} 300\,\text{rpm/s} \times \text{time} + 100\,\text{rpm} & \text{for } 300\,\text{rpm/s} \times \text{time} + 100\,\text{rpm} \\ & < \text{Set Spin Speed} \\ \text{Set Spin Speed} & \text{for } 300\,\text{rpm/s} \times \text{time} + 100\,\text{rpm} \\ & \geq \text{Set Spin Speed} \end{cases}, \quad (4.32)$$

where the spin speed is in units of revolutions per minute and time is in seconds. Figure 4-22 shows the simulated spin speed profiles of the centrifuge for set spin speeds of 1000 rpm, 1600 rpm, 2500 rpm, and 4000 rpm. The lines for each of the profiles shown terminate when the bubble with an initial diameter of 100 μm has successfully reached the liquid-air interface 34.3 mm from the center axis of rotation after traveling from a position 61.5 mm from the center axis of rotation.

Using the spin speed profiles for the spinning centrifuge described by Equation 4.32, along with the fluid and geometric properties described in Figure 4-22, it is possible to simulate the amount of time necessary for bubbles of varied initial diameters to move from the outer edge of the part to the liquid-air interface near the center axis of rotation. Using the relationships described in Section 4.1 and Section 4.3, Figure 4-23 shows the simulated amount of time required for bubbles to exit at the liquid-air interface. Figure 4-23 B shows the same simulated curves from Figure 4-23 A but also includes the experimental results shown in Figure 4-21 rounded to the nearest bubble. No number next to one of the experimental data points signifies zero bubbles.

By plotting the simulated spin time versus spin speed curves for various bubbles of

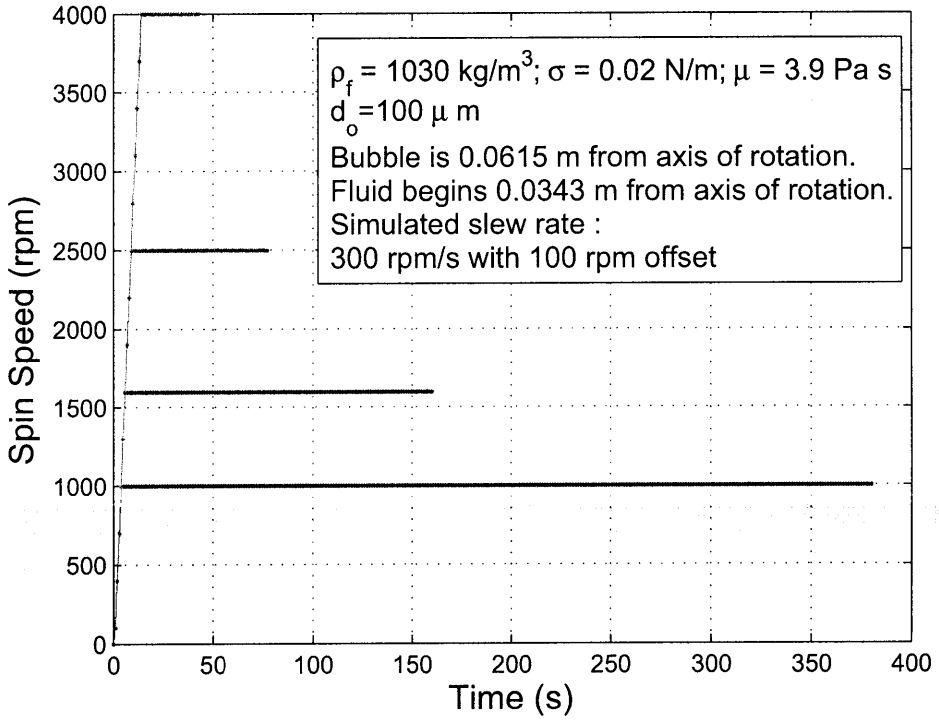

Figure 4-22: Spin speed vs time with slew rate.

different initial diameters, it becomes possible to estimate a critical bubble size using the hypothesis that for a given amount of spin time, all bubbles above a certain size should have been removed by buoyant forces. For example, imagine that the set spin speed were 2000 rpm. After a period of 100 s (see Figure 4-23 A), all bubbles larger than those that started out with a diameter of 100 μm should have exited from solution. However, the bubbles that started out with diameters of 60 – 80 μm have not yet exited from solution after 100 s. That said, if a part is bubble free after being spun for 100 s with a set speed of 2000 rpm, then it is possible to conclude that the solution is not capable of supporting bubble sizes less than 80 μm because the bubbles would otherwise be present in the completed PDMS part. It might be said that the critical bubble size for this particular solution and geometry is 100 μm.

To better visualize the relationship between the experimental data and the simulated results, the data and curves shown in Figure 4-23 can be plotted on a log-log plot as shown in Figure 4-24. In Figure 4-24, the values for d_o are set in 20 μm increments over the domain from 80 μm to 160 μm, and the highlighted line with pentagram markers corresponds to the spin times and set spin speeds associated with a bubble of an initial diameter of 160 μm. This highlighted line roughly divides the parts containing multiple bubbles in the regions of interest from the parts averaging less than a single bubble.

With this dividing line based on a d_o value of 160 μm, it is possible to use this critical bubble diameter with the buoyancy model to predict whether or not parts will have bubbles with a given spin profile. Because of the buoyancy model's simplicity, it has the potential to be quite powerful and similar work in the past has been used to describe centrifugal casting processes [106, 48, 100]. That said, the buoyancy model does not capture the potential for bubbles to dissolve into solution. The buoyancy model also does not predict the critical bubble size itself but depends on a set of experiments for its determination.

4.5.2 Bubble speed model with diffusion

Using the bubble speed model with diffusion and the implementation described in Section 4.4, it is possible to make predictions for the amount of time required for a bubble to move from a given starting position to a predetermined location. Figure 4-25 shows the same predictive simulated times for exit data included in Figure 4-16 with the bubble starting position at the outer edge of the mold. In addition, the experimental bubble data are also

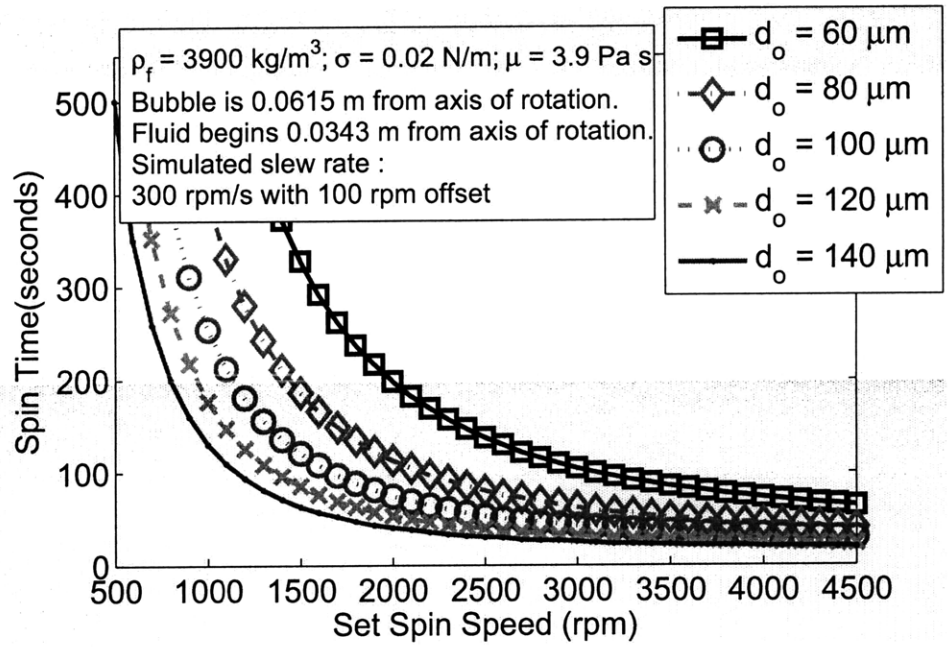

(A)

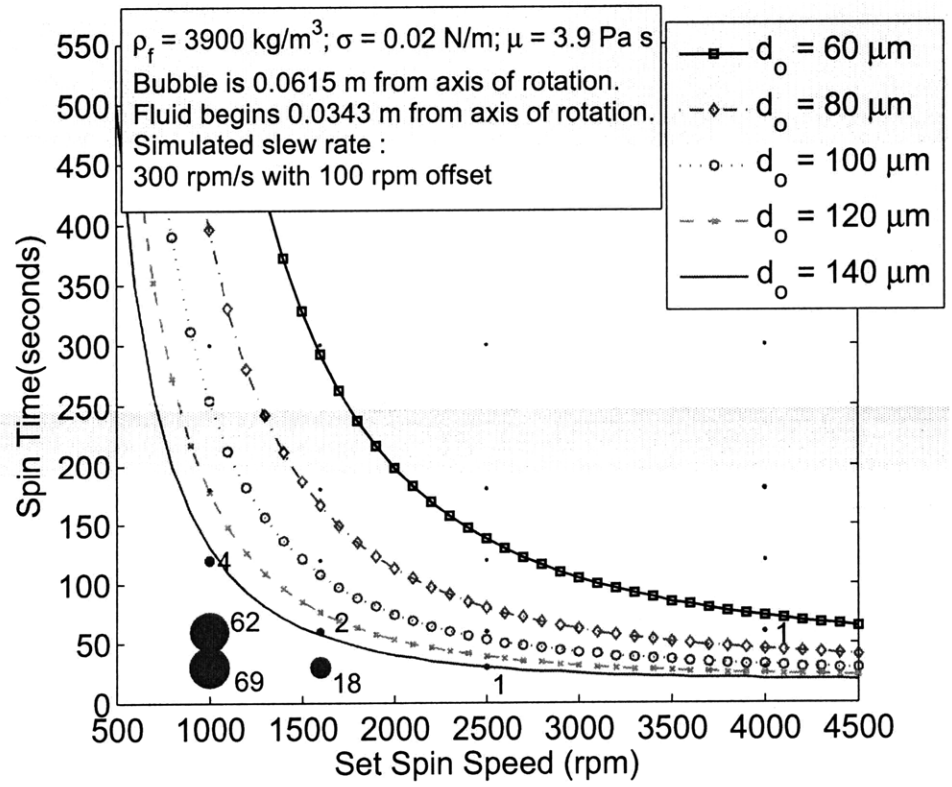

(B)

Figure 4-23: (A) Required amount of spin time for a bubble to move from the outside edge of the mold to the liquid-air interface near the center axis of rotation plotted against the set spin speed using the buoyancy model without diffusion. (B) Same predictive lines as in A but the additional data from experiments are included.

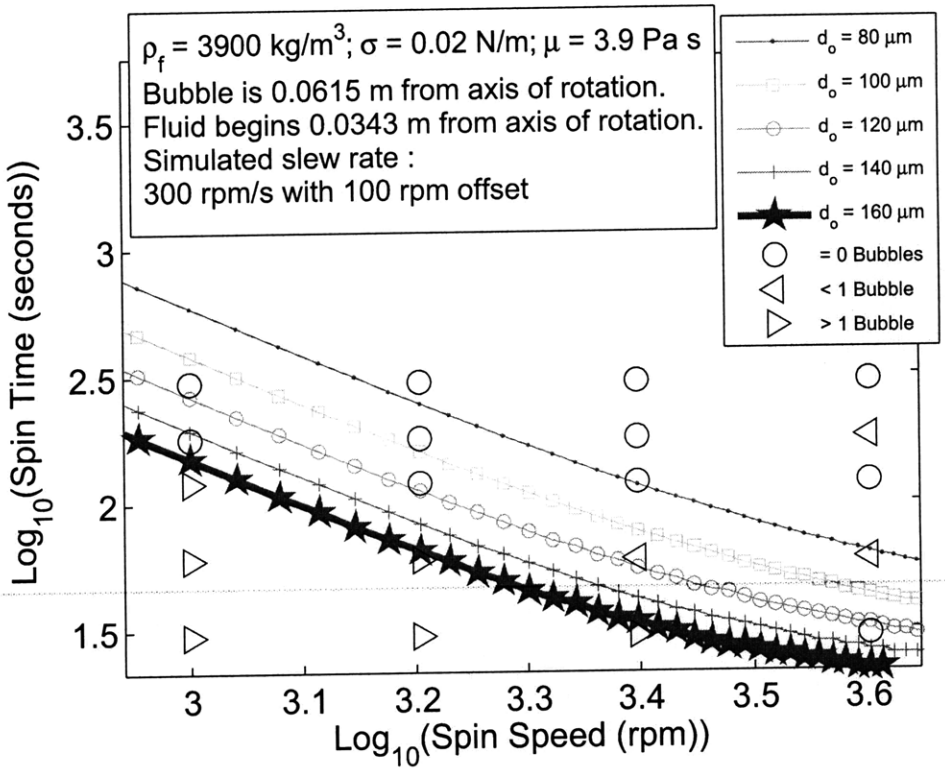

Figure 4-24: Log-log plot of the experimental spinning-bubble data and the buoyancy model curves shown in Figure 4-23.

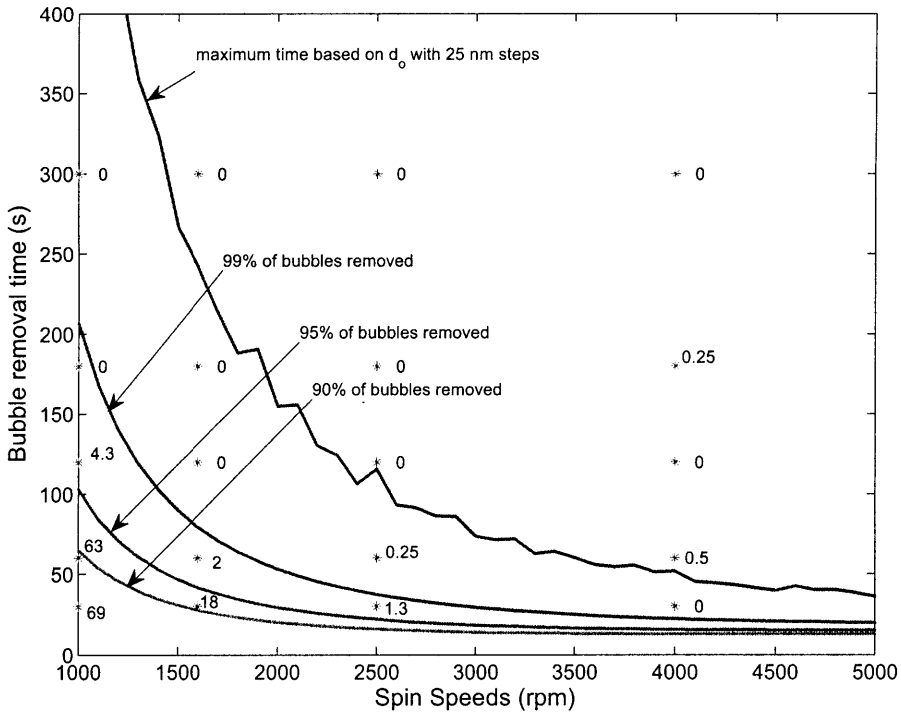

Figure 4-25: Experimental data plotted against predictions from combined bubble velocity and diffusion model.

included with the asterisk marks representing the combination of spin times and set spin speeds. Each number is the average number of bubbles counted in four measured parts using the technique described in Figure 4-20, and these experimental data are the same shown in Figure 4-21.

Placing the lines and data from Figure 4-25 on a log-log plot as shown in Figure 4-26, the simulated curves become straight lines. The line with pentagrams (time required to remove 99% of the bubbles) roughly separates the parts with more than one bubble from those which averaged less than one bubble. This dividing line represents a good match between the experimental data and the bubble speed model including diffusion. Unlike in Figure 4-24, there is not just one critical bubble size representing the bubble that takes the longest time to either exit the fluid or dissolve into the fluid, but a domain of critical sizes, which are dependent on the starting position and the spin speed profile. The dependence of the critical bubble size (bubble size corresponding to the longest required amount of time for removal) on spin speed is shown in Figure 4-14. The dependence of the critical bubble

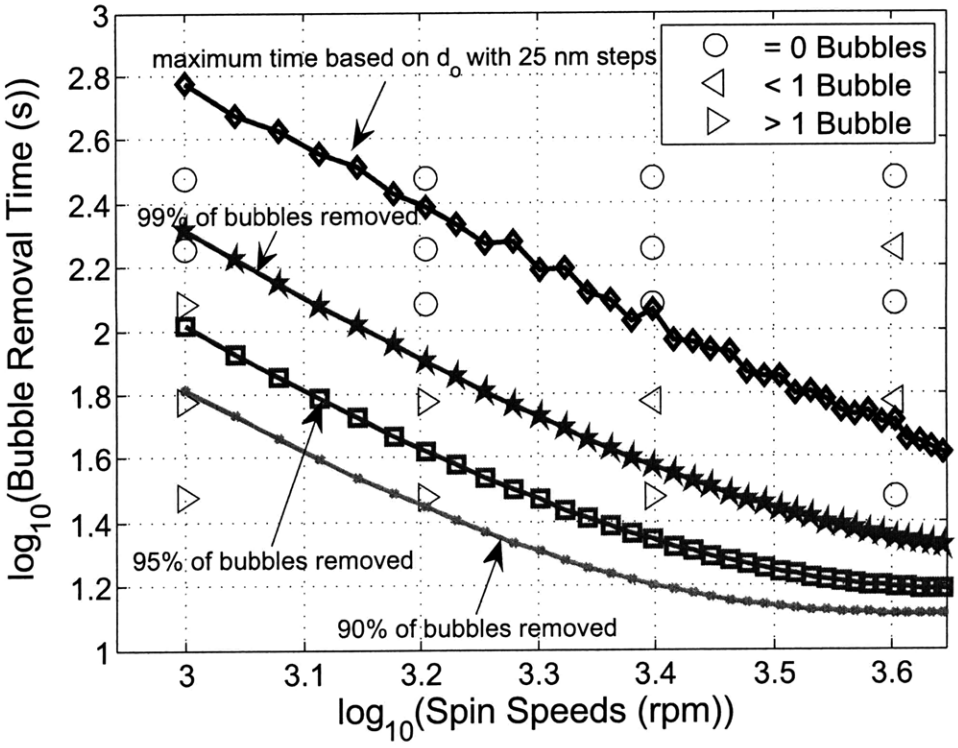

Figure 4-26: Log-log plot showing experimental data and predictions from combined bubble velocity and diffusion model.

size/maximum time on bubble starting position is shown in Figure 4-18 and will be further explored in Section 5.3.

4.6 Bubble cavity experiments

Bubbles can get caught in pockets or trenches within a centrifugal mold assembly as illustrated in Figure 4-27. In some of the initial experiments, it was common to see a few bubbles that appeared to have come from the the outer edge of the mold. Air appeared to get trapped in the o-ring assembly or between the top and bottom mold halves. To prevent these bubbles from affecting the molded regions of interest, an intentional bubble trap (recessed ring or channel) was milled into the top half of the mold. Figure 4-28 shows photos of bubble traps milled in polycarbonate and aluminum. The mold assembly in Figure 4-28 B has an outer diameter of 133 mm.

In addition to designing intentional bubble traps to keep bubbles out of the regions of interest during molding or curing, mold designs often lend themselves to including uninten-

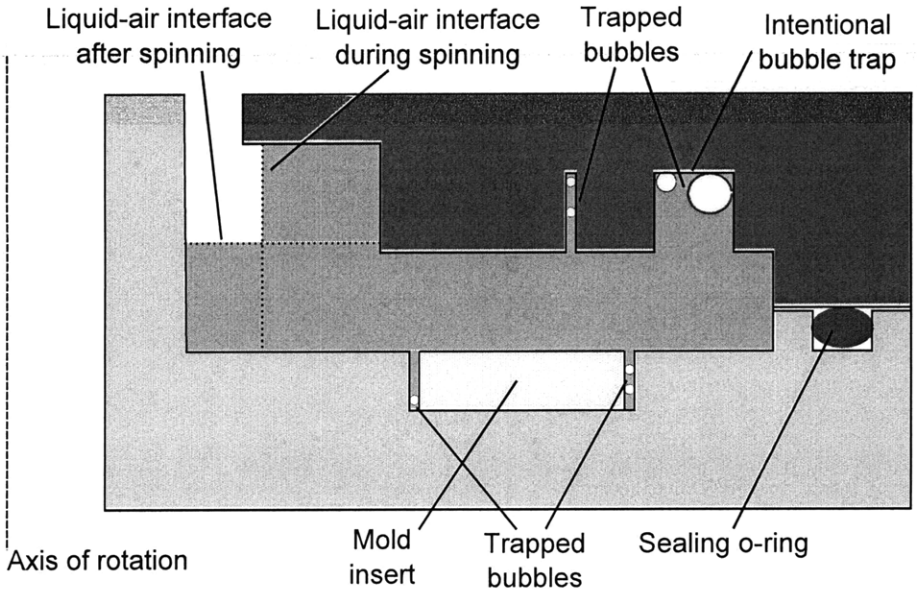

Figure 4-27: Cavities or trenches in a centrifugal mold assembly that can catch bubbles.

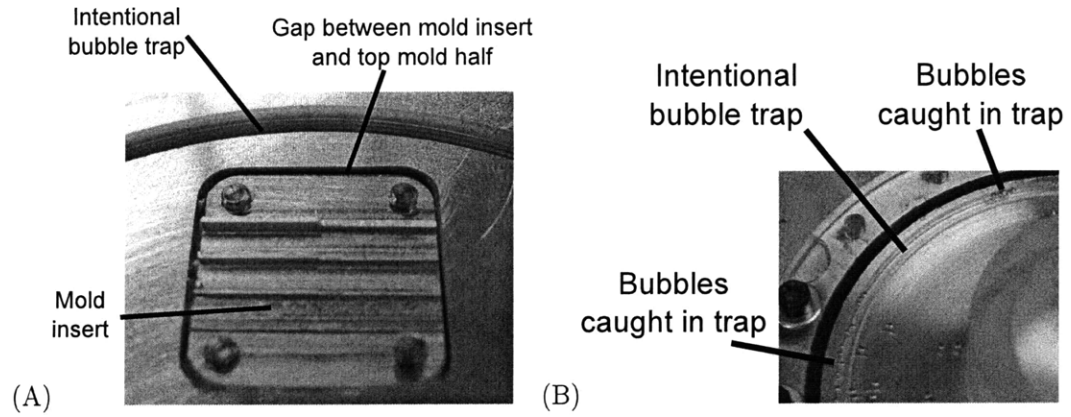

Figure 4-28: Intentional bubble traps can help eliminate bubbles that get caught at the interface between the two molds. Gaps between mold inserts and the rest of the assembly can serve as unintentional bubble traps.

tional bubble traps or trenches. These unintentional bubble traps are commonly found at the interface between two distinct mold components that are adjacent to each other. One example is shown in Figure 4-28 A. There is a noticeable gap around the mold insert. The mold insert's lateral dimensions are 19 mm × 19 mm.

Another couple of examples are shown in Figure 4-29. Figure 4-29 A shows a machined aluminum insert (lateral dimensions of 35 mm x 25 mm) bolted into the bottom half of a mold assembly. Because both the mold insert and bottom half mold were machined in aluminum, the clearance between the mold insert and the surrounding aluminum mold assembly was specified to be 0.0025 in. (64 μm). This slight clearance of 64 μm goes down approximately 5.6 mm, forming a narrow trench. Figure 4-29 B shows a metallic mold insert bolted in the same fashion as Figure 4-29 A, but the clearance is much greater surrounding the mold insert because the outer dimensions of the bulk metallic glass mold were not as easily controlled. Therefore, the surrounding trench in B is much wider.

Based on experimental results and images such as the one shown in Figure 4-29 C, the narrow deep trench appears to be a source of bubbles in molded parts. The PDMS parts in Figure 4-29 C were spun simultaneously in the same mold assembly shown in Figure 2-26 with a set spin speed of 7000 rpm for 4.5 minutes (not including the time required for spin down). The PDMS was then cured using one of the temperature profiles shown in Figure 2-23.

The single experiment shown in Figure 4-29 C was part of a series of experiments performed by only varying the spin time, while keeping the set spin speed constant at 7000 rpm. The varied spin times ranged from half a minute to 7 minutes (not including the time required for spin down) in 30 second intervals. In every case, no bubbles were found in the regions of interest for the parts molded on the metallic glass. For the PDMS parts molded on the aluminum tool, the resulting numbers of bubbles counted are shown in Figure 4-30. For spin times of 1, 2, 3, 4, 5, 6, and 6.5 minutes, no bubbles were observed in the regions of interest.

When the initial results shown in Figure 4-30 were combined with the results of the parts molded off the metallic glass, the initial conclusion was that the surface roughness of the metallic glass tool was the cause of the additional bubbles being trapped in the PDMS parts. However, upon further review of the images similar to the one shown in Figure 4-29 C, the disparity between the PDMS parts molded off of metallic glass and the aluminum

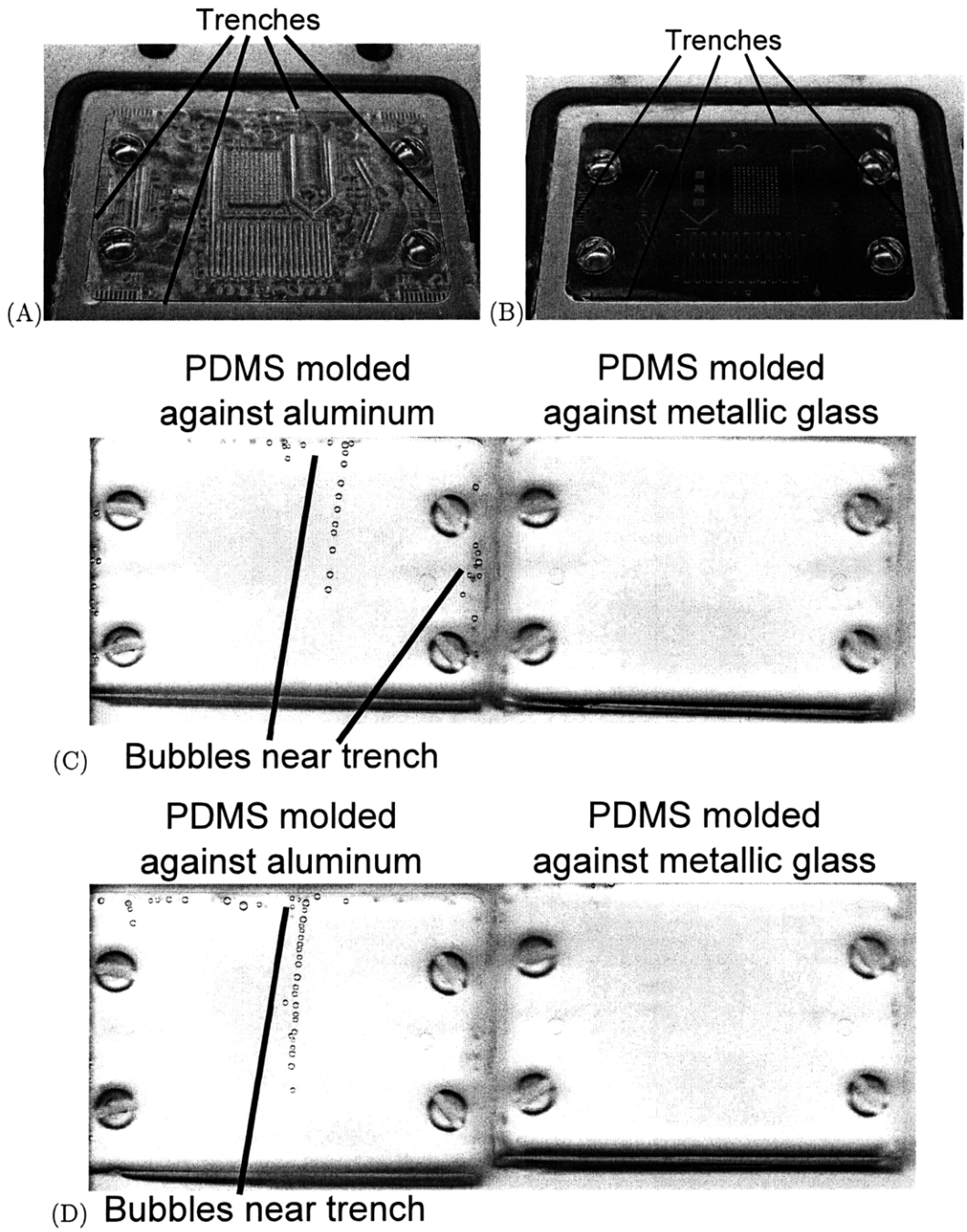

Figure 4-29: (A) Micromachined aluminum tool with very narrow trenches between the mold insert and the surrounding mold assembly. (B) Bulk metallic glass tool with larger trenches than those shown in A. (C) PDMS parts cast against the molds shown in A and B with a spin time of 4.5 minutes. (D) PDMS parts cast against the molds shown in A and B with a spin time of 30 seconds.

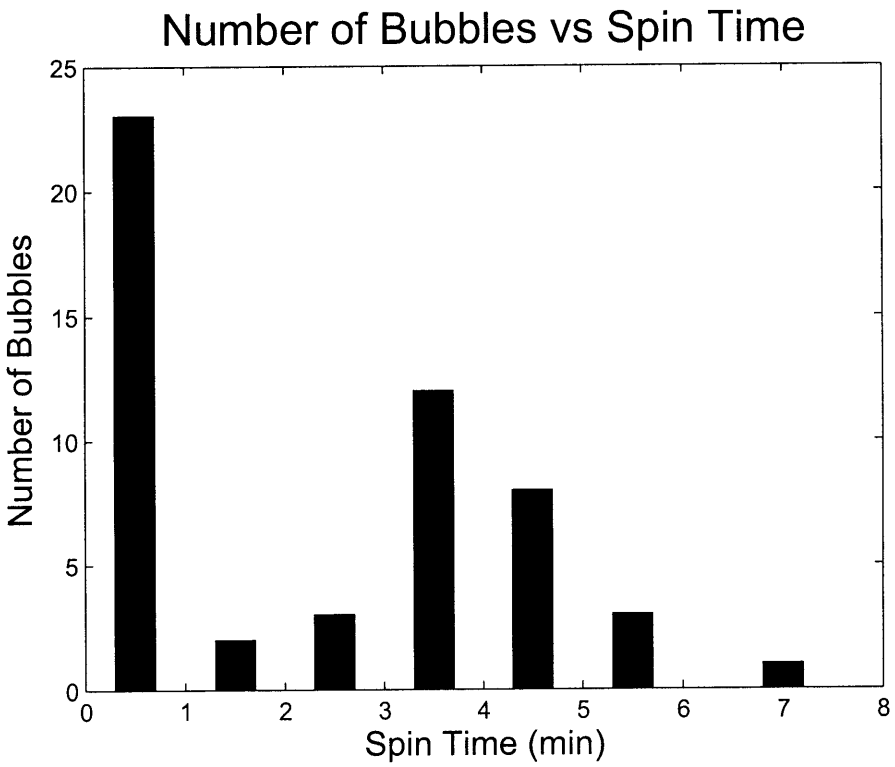

Figure 4-30: Histogram showing the number of bubbles counted in PDMS parts molded off a micromachined aluminum tool with a set spin speed of 7000 rpm and spin times varying from half a minute to 7 minutes in 30 second intervals.

insert appears to be more related to the size of the trenches surrounding the parts.

In the left half of the image in Figure 4-29 C, there appears to be a trail of bubbles progressing down the part. This trail commences at the top edge and the line progresses toward the axis of rotation for this part. The hypothesis for this behavior is that undissolved air was trapped in the trench near the top during spinning. While the centrifuge was spinning, the pressure above the trench increased tremendously, and the undissolved air did gradually begin to dissolve into the PDMS solution. However, the undissolved air did not completely dissolve into the PDMS. As the centrifuge slowed down, the pressure over the trench was reduced, and the remaining undissolved air expanded and came free. If the undissolved air came free during the spin down time, buoyant forces could have caused the bubbles to migrate toward the middle of the part but not make the complete journey to the liquid-air interface near the center axis of rotation. The resulting PDMS part ended up having bubbles caught in the regions of interest.

To provide some rough calculations for the volume of undissolved air that may have been trapped near the outer edge, the bubble speed model with diffusion was applied to the problem of a bubble fixed (no velocity) at a given distance away from the center axis of rotation. Using this modified bubble with no velocity, diffusion is the only mechanism for bubble removal. Figure 4-31 shows the simulated results for bubbles with various initial diameters. In this simulation, the input parameters were the same as those shown in Table 4.3 with the exception of the bubble starting position, which was changed slightly to 60.8 mm reflecting the distance of the trench from the center axis of rotation.

Looking at these simulations results in Figure 4-31, there is an initial sharp decrease in the bubble diameter. This sharp decrease is caused by the PDMS pressure buildup over the trench associated with the acceleration of the centrifuge startup (300 rpm/s). This pressure buildup essentially decreases the initial volume/diameter of the bubble according to the Ideal Gas Law. Then, once the centrifuge has reached its steady-state speed, bubble diameter decrease is completely caused by diffusion.

The experimental results in Figure 4-30 suggest that bubbles may or may not be left in the PDMS part in the vicinity of the trench after spinning is complete. However, there were a significant number of bubbles left in the trial that ran for 4.5 minutes as shown in Figure 4-29 C. Looking at the simulated results in Figure 4-31, notice that bubbles with a diameter larger than 1700 μm could still exist and not be completely dissolved. A bubble

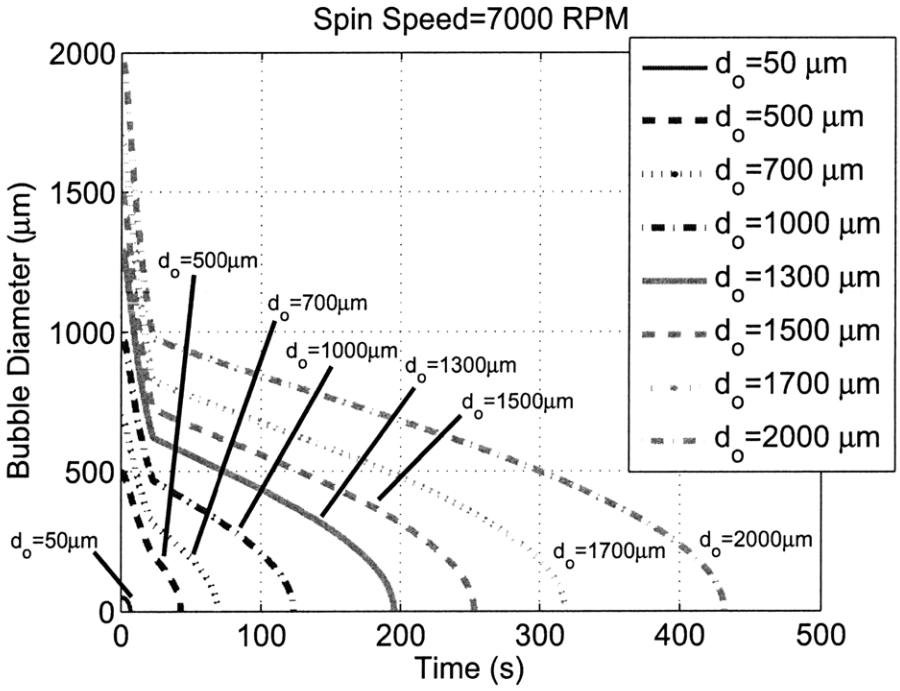

Figure 4-31: Plot showing shrinking bubbles which are fixed 60.8 mm away from the center axis of rotation. The set spin speed is 7000 rpm, and there is a slew rate of approximately 300 rpm/s up to the set spin speed.

with an initial diameter of 1700 μm has a volume of 2.57 mm^3. By conservation of volume, undissolved air with a width of 64 μm (width of trench) and depth of 5 mm would need to have a length of 8 mm. Given the lateral dimensions of the mold inserts (35 mm x 25 mm), it is feasible that this quantity of air could be trapped in the trench between the mold insert and the surrounding aluminum portion of the mold assembly.

One major assumption of the bubble diffusion model employed in this example is that the bubble is a complete sphere. In reality, the quantity of undissolved air assumed to be trapped in the trench cannot exist in the form of a complete sphere. Air bubbles that form against metal surfaces (heterogeneous bubbles) will not diffuse air through the metal. In a metal trench with undissolved air present, there might only be a small fraction of the total surface area surrounding the air pocket that makes contact with the liquid. It is only through this small liquid-air interface that the bubble can diffuse air. An air pocket with a small liquid-air surface area to volume ratio will require much longer times to dissolve. With the estimates for the time for dissolution of bubbles possibly being too long, the above simulation likely overpredicts the volume of air trapped in the trenches.

4.7 Potential bubble growth after spinning

In centrifugal casting, if the bubbles are not completely removed by dissolution or buoyancy, there is the possibility for bubble growth after spinning is completed. A bubble in a supersaturated solution with a diameter larger than the critical diameter given by Equation 3.55 and Equation 3.56 will grow[4]. If the diameter of the remaining bubbles is less than this critical diameter and the temperature remains constant, then they will dissolve into solution. To avoid problems with bubbles growing because they are not completely dissolved or have not been removed by buoyant forces, it is desirable to spin fast enough and long enough to have a solution devoid of any bubbles before moving to the curing step.

In the case of complete bubble removal, all the bubbles in the bulk of the material have either dissolved into the solution or have been removed by buoyant forces. However, one

[4]A bubble in an undersaturated solution will always shrink. If a bubble in a supersaturated solution has a diameter less than the specified critical diameter, it will shrink. As the diameter of a bubble decreases, the pressure within a bubble increases by the Young-Laplace relationship (Equation 4.23). With increases in internal bubble pressure, the bubble wall becomes more saturated with air by Henry's Law (Equation 3.1). At a small enough bubble diameter (critical size), the air concentration within the wall becomes greater than the air concentration in the surrounding solution. When the air concentration within the bubble wall is greater than the air concentration in the surrounding PDMS, the bubble loses air and shrinks.

might argue that small bubbles could be trapped in pits or cavities of the surfaces of the molds. While this is possible, it is not likely because bubbles in small cavities (on the order of 100 μm or smaller) would have diffused into solution because of pressure build up in the mold and a lowering of the c_f parameter (see Section 4.4). For example, with the lowering of the c_f parameter to a value of 0.9 at a pressure of 5 atm, a 25 μm diameter bubble would dissolve in 2.4 seconds (see Table 3.4). Once all of these bubbles are completely removed from the solution, it is undesirable for them to return during later phases of the production cycle.

For bubbles to emerge from a solution devoid of bubbles, there are a few potential phase separation phenomena [79]: boiling, foaming, cavitation, devolatilization, or wave foaming. In addition, mechanical entrapment of air bubbles is a potential method of forming air bubbles in PDMS. The following subsections will describe three of the most likely bubbling phenomena that could occur after centrifugal spinning: mechanical entrapment, bubble formation by boiling, and bubble nucleation from dissolved air in the PDMS.

4.7.1 Bubble formation by mechanical entrapment

If one starts with a bubble-free solution, bubbles can be introduced by mechanical means. For example, shaking a bottle of water will lead to bubble entrapment. Mechanical stirring with a rod can also lead to bubble entrapment (see Figure 1-2 A). Even pouring a solution or transferring a material from one container to another can lead to bubble entrapment. In mold-filling applications for polyurethanes, careful planning may be used to minimize mechanical folding of the material and air entrapment [89]. Thus, it is important to not mechanically disturb the material between the centrifugal spinning and curing steps in a way that introduces air bubbles into the solution.

4.7.2 Bubble formation by boiling

In boiling, liquid goes through a phase change into its vapor form. One useful intrinsic property of a liquid for determining whether or not boiling will occur is vapor pressure. Vapor pressure can be defined as "the pressure of a gas in equilibrium with a liquid (or, in some usage, a solid) at a specified temperature [80]." If, at a specified temperature, the vapor pressure is greater than the ambient pressure, boiling can occur.

For PDMS Sylgard 184, the vapor pressures at varied temperatures are not listed by

Dow Corning. However, Clearco Products (www.clearcoproducts.com) lists vapor pressures for some of their PDMS solutions. Based on their data sheets [17, 16], the vapor pressure decreases as viscosity increases. The highest viscosity grade of PDMS that they list vapor pressure values for is 1000 cSt., and the PDMS Sylgard 184 has a viscosity of approximately 4000 cSt. Thus, their vapor pressure values listed for PDMS with a viscosity of 1000 cSt. will likely be greater than the vapor pressure values of the PDMS Sylgard 184 used in this thesis. At 350 °C, Clearco lists the vapor pressure for their 1000 cSt. grade PDMS with a value of 53 mm Hg (7066 Pa). Since the vapor pressure of the Clearco Products PDMS is so low at the high temperature of 350 °C, the Sylgard 184 should not approach boiling at ambient pressure (101.3 kPa) with the processing temperatures used in this thesis, which are less than 300 °C. In fact, if the polymer were allowed to get to such a high temperature at such a low pressure, the Sylgard 184 material would probably cure and degrade before boiling.

4.7.3 Bubble formation by nucleation of dissolved air

After spinning the PDMS for a period of time on the order of a minute at thousands of revolutions per minute to remove all bubbles from solution, the concentration of air within the bulk of the PDMS is approximately the same as it was before being spun (saturated or slightly supersaturated). According to the diffusion and centrifugal casting theories described up to this point, it is possible to remove all bubbles from the regions of interest within the PDMS either by diffusion or buoyancy. Now, when the PDMS moves to the curing step, it is important to know whether or not the dissolved air within the PDMS might form air clusters leading to phase-separated bubbles [68].

At this current stage of the manufacturing process between spinning and curing, it is assumed that there are no bubbles in the solution. However, if there were, the following condition:

$$c_i - k_D \left(p_{fluid} + 2\sigma/R\right) > 0 \tag{4.33}$$

from Equation 3.49 would have to hold true for a bubble to grow by diffusion. It is possible to write the following expression:

$$R_{cd} > \frac{2k_D\sigma}{c_i - k_D P_{fluid}}, \tag{4.34}$$

which is the condition for a critical radius for diffusion (R_{cd}) so that growth occurs. Using this expression, it is possible to estimate what the bubble size would need to be for growth to occur if the solution were supersaturated. For example, if the assumption were $c_f = 1.05$ ($c_i = 0.205\,\text{kg(air)/m}^3\text{(PDMS)}$) with a Henry's coefficient of $1.927 \times 10^{-6}\,\text{kg(air)/m}^3\text{(PDMS)/Pa}$ at a pressure of 101.3 kPa, then a bubble would need to have a diameter greater than 15.8 μm to grow.

If the temperature were increased from 25 °C to 200 °C to cure the part while keeping the pressure constant, the concentration of dissolved air in the bulk of the PDMS would again stay nearly constant because the bulk of the PDMS has a very small liquid-air interface for air transfer to/from the surrounding environment. In other words c_i and p_{fluid} in Equation 4.33 would remain unchanged. However, the values of the Henry's coefficient k_D, the PDMS-air surface tension σ, and the PDMS viscosity are generally dependent on temperature and might be expected to change. While visocity may have some effect on bubble nucleation, surface tension and the Henry's coefficient appear to be more dominating factors.

Based on nitrogen solubility data in octamethylcyclotetrasiloxane in [21] and a brochure chart for oxygen and nitrogen solubility in Wacker AK 100 (similar properties to the Clearco product with a viscosity of 5000 cSt.) [19], it is possible to infer that the Henry's coefficient k_D is not significantly affected by the 175 °C increase in temperature. Battino et. al. [21] include a fitted relationship to nitrogen solubility in octamethylcyclotetrasiloxane at 101.3 kPa:

$$\ln x = -5.823 - 0.423/\tau, \tag{4.35}$$

where x is the mole fraction of nitrogen in the polymer and τ is the temperature in Kelvin divided by 100. Thus, at 25 °C, the mole fraction of nitrogen to polymer is 2.55×10^{-3}. Using the same relationship and extrapolating out to 200 °C (fitted data only went up to 40 °C), the mole fraction of nitrogen to polymer only increases to 2.69×10^{-3}. The value of k_D corresponds to an increase by a factor of 1.06. This increase may appear counterintuitive because solubility often goes down with increases in temperature as in the case of CO_2 in aqueous solution [26, 37, 30]. However, the chart in the Wacker information

[19] agrees with this information showing a slight increase in the solubility of nitrogen in silicone, while showing a very slight decrease in the solubility of oxygen in silicone. This same chart from Wacker also shows almost a factor of 4 decrease in the CO_2 solubility of silicone going from 25 °C to 200 °C. In the current example, if k_D were to be reduced by a factor of 4, the new critical diameter would be 0.25 μm. However, the Henry's coefficients for nitrogen and oxygen gas (the primary components of air) in silicone do not seem to be significantly reduced. Thus, the slight changes in the Henry's coefficient for air in PDMS do not significantly reduce the critical diameter for bubble growth by diffusion.

With respect to surface tension σ, there will be a reduction from 0.02 N/m to approximately 0.012 N/m based on data by Sauer and Dee [97] and Wu [117]. As a side note, Wu gives a simple simple linear coefficient of -0.048 mN/m/K for approximating the surface tension for increasing temperatures for poly(oxydimethylsilylene) with a molecular weight of 7500 and 3900. Going back to Equation 4.34 and using the updated value for surface tension of 0.012 N/m at 200 °C, the new critical diameter would be approximately 9.5 μm for bubble growth to occur by diffusion. Going even further and using the ideal gas law to state that the volume of a bubble would increase by a factor of 1.6 (no mass loss) with a temperature increase from 25 °C to 200 °C, it follows that the diameter would increase by only a factor of 1.2. Therefore, the diameter of a bubble would need to be greater than 7.9 μm at 25 °C to have the possibility of growth for PDMS originally 5% supersaturated ($c_f = 1.05$) with air. This new critical diameter for no bubble growth by diffusion is half of the original critical diameter for no bubble growth without the temperature increase. Based on this factor of 2 change in critical diameter for diffusive bubble growth, bubble growth would only be expected if a nucleation site or a gas pocket of approximately this size existed. Without such a site, no bubble growth is expected during the curing cycle. Thus, it is possible to conclude that diffusive bubble growth during the curing cycle is not likely to occur solely due to changes in the solubility or surface tension of PDMS with temperature.

To take this hypothetical analysis one step further in justifying the lack of bubble formation after complete bubble removal via centrifugal casting, it is useful to look at classical nucleation theory and its application to the manufacture of polymer-based foams. The classical nucleation theory starts out looking at the energy required (W) to create a bubble in a liquid with the assumption that chemical potential of the gas within the liquid is the same as the gas within the bubble [23, 31, 79]:

$$W = 4\pi R^2\sigma - \frac{4}{3}\pi R^3 \left(P_b - P_{fluid}\right). \tag{4.36}$$

By differentiating this expression with respect to R and setting the new expression equal to zero, it is possible to find a local maximum for work, which is actually the minimum work (activation energy) required to create a bubble that would thermodynamically favor growth. The expression for this minimum work (activation energy) is given by

$$W_{min} = \frac{16\pi\sigma^3}{3(P_b - P_{fluid})^2}. \tag{4.37}$$

With this minimum work, there is a critical bubble radius for nucleation given by

$$R_{cn} = \frac{2\sigma}{(P_b - P_{fluid})}. \tag{4.38}$$

This is when the arguments can become circular without additional assumptions or experiments for making bubble nucleation predictions. There are essentially three unknowns: the minimum work W_{min}, the critical bubble radius R_{cn} and the pressure difference $P_b - P_{fluid}$ in two equations derived from Equation 4.36. For bubble foaming in polymers, there is usually a large amount of pressure (greater than 20 atm) applied to a gas-polymer mixer to fully saturate the polymer. In the foaming literature [31, 79], it is often assumed that

$$P_b - P_{fluid} \approx P_{app} - P_{rel}, \tag{4.39}$$

where P_{app} is the pressure applied to saturate the polymer and P_{rel} is the pressure at which foaming occurs, usually atmospheric pressure. In order to make relative comparisons with respect to the amount of foaming a particular set of parameters yields, some form of the following rate of nucleation is used [23, 79]:

$$J = N\left(\frac{2\sigma}{\pi m}\right)^{1/2} e^{\left(\frac{-W_{min}}{kT}\right)}, \tag{4.40}$$

where N is the number of molecules per unit volume, k is the Boltzmann constant, m is the mass of a gas molecule, and T is the temperature in Kelvin. Looking at the terms that make up the exponential term of Equation 4.40, it becomes evident that the overall exponent becomes closer to zero (less negative) with the square of the pressure difference. Temperature

by itself affects the exponential term, but the exponential term is only inversely proportional to temperature increases. That said, the temperature effect on the surface tension may have a great impact on the rate of nucleation because the exponential term goes with the cube of the surface tension, and the surface tension of a polymer is temperature dependent.

In general, it is much easier to affect the nucleation rate of bubbles (Equation 4.40) by increasing the pressure difference than by solely increasing the temperature, because the polymer is a poor thermal conductor and will degrade at high temperatures [79]. Usually some combination of pressure and temperature are varied in polymer foam processing. For example, when opening a bottle/can of soda, there is some temperature dependence on foaming [30]. However, the majority of the bubble nucleation in opening a bottle of soda occurs because of the pressure supersaturation of the carbon dioxide and the subsequent pressure release.

In the fast curing process described and proposed in this thesis, only the temperature of the part being cured is increased, while the pressure is left constant. The solubility of the solution remains nearly constant for PDMS, and the surface tension can decrease. While one may argue that the increase in temperature combined with the decrease in surface tension could lead to bubble nucleation, experimental results have not indicated that bubble formation occurs during curing for adequately degassed PDMS via centrifugal casting. In Figure 4-32, the temperature profile for the heating portion of a curing process and a photo of the completed part are shown. The part was heated for over 20 minutes, reached a temperature close to 300 °C, and actually began to degrade slightly. Based on observations in Section 2.4.2, the PDMS was probably cured within 2 minutes by the time the material reached a temperature of approximately 150 °C. So, it is possible that a higher temperature cure might introduce some bubbles, but based on the hypotheses in this section regarding solubility, requirements for diffusional bubble growth, classical nucleation theory, lack of a high pressure saturation step, and the material's fast cure at high temperatures, it is unlikely that bubbles not already present in the PDMS appear during high-temperature curing.

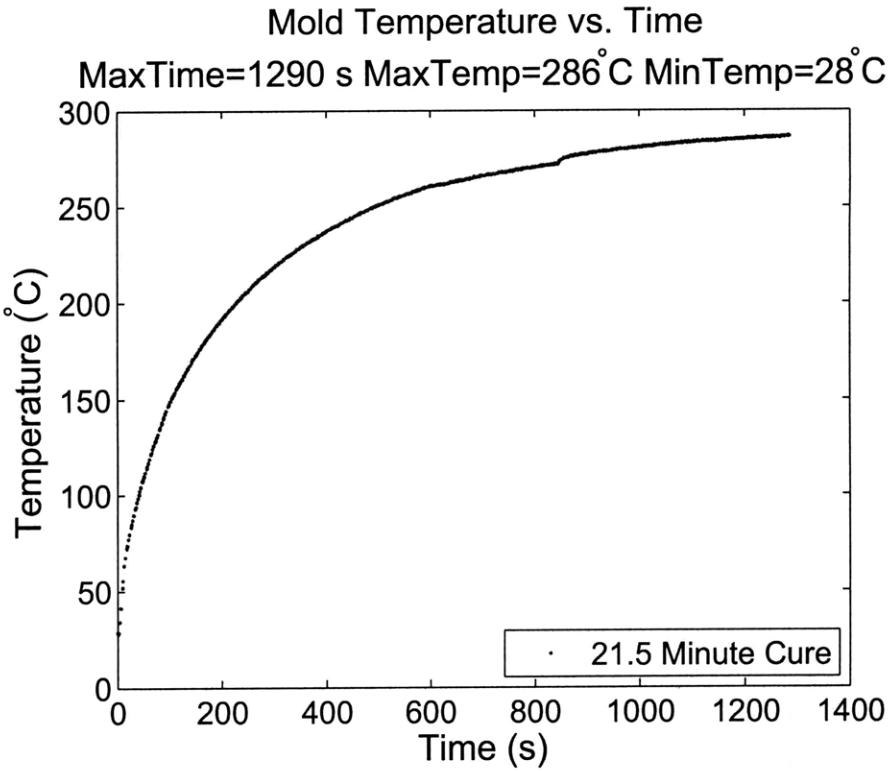

(A)

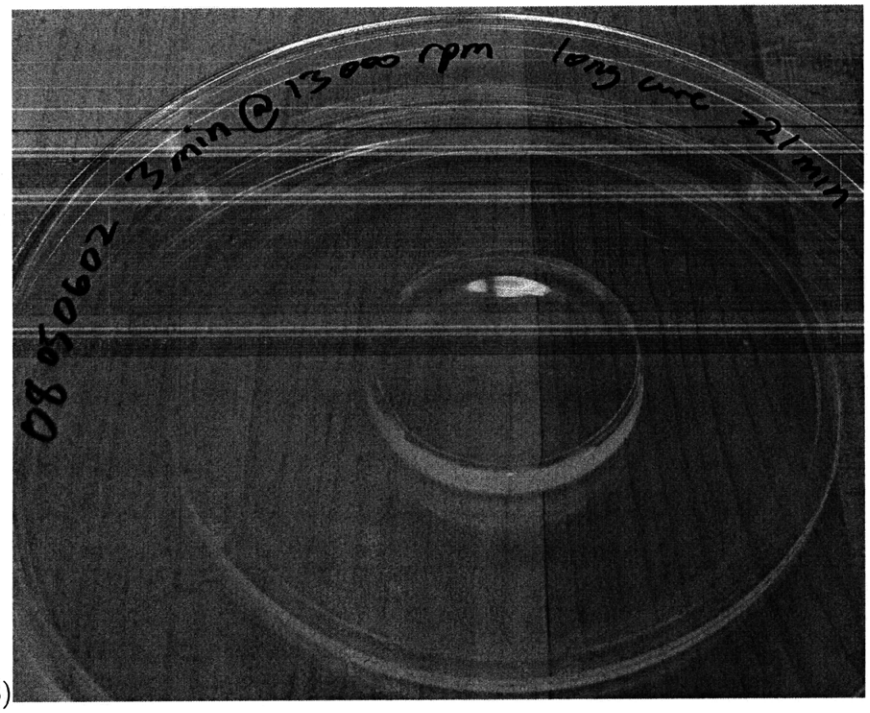

(B)

Figure 4-32: (A) Temperature profile of the heating portion of a PDMS Sylgard 184 part cured after centrifugal spinning at 13000 rpm for 3 minutes. (B) Photo of cured bubble-free part corresponding to the profile in A.

Chapter 5

Results

The past few chapters have outlined the theory of bubble diffusion, estimates for bubble diffusion combined with centrifugal casting, and the apparatus necessary to carry out experiments and create devices. This chapter focuses on how the theory and designed apparatus can be merged together to both produce micro/nano featured components and make predictions for the amount of time required to centrifugally cast components. The photos, images, and experiments included in this chapter demonstrate the potential centrifugal casting and fast curing have for the manufacture of micro/nano featured components.

5.1 Fabricated Parts

Over a hundred PDMS parts have been produced in an effort to understand the limits of centrifugal casting and fast curing methods outlined in this thesis. Many have had bubbles and others have not depending on the mold design and processing parameters. This section shares some bubble-free example parts.

5.1.1 Micro features

PDMS is widely used in microfluidics for its ability to replicate micro features. With the introduction of a novel method for PDMS processing, it is important to verify that micro feature replication is still possible. This section reviews some images and measurements to show that centrifugal casting does not appear to negatively impact micro feature replication. The primary tool for measuring and characterizing the quality of parts is a Zygo NewView 5000 optical profilometer (see Appendix B).

Figure 5-1 shows images of the Y-mixer portions of the bulk metallic glass and micromachined aluminum molds shown in Figure 2-25. These features were used for molding PDMS. Figure 5-1 B and Figure 5-1 F show corresponding PDMS features that were molded against the bulk metallic glass and aluminum micro machined molds using centrifugal casting. The PDMS parts were spun up to 7000 rpm with an approximate slew rate of 300 rpm/s for 7 minutes of spinning (not including deceleration time) in the mold configuration shown in Figure 2-26. After being centrifugally cast, they were cured in a period of approximately 8 minutes with one of the temperature profiles shown in Figure 5-4. The channel widths of the bulk metallic glass images shown and the corresponding PDMS part are approximately 50 μm. The channel heights are approximately 40 μm. For the micro machined Y-mixer, the channel width for the upper-left portion of the Y is approximately 70 μm, the upper-right portion of the Y is approximately 50 μm, and the lower,vertical portion of the Y is approximately 60 μm. The height of these channels is approximately 50 μm.

Figure 5-2 shows images of a bulk metallic glass channel and its corresponding PDMS replicate. These channels are actually continuations of the bottom, vertical portions of the Y-mixers shown in Figure 5-1. Images A and B were taken with the Zygo profilometer, and the plots shown in C and D are the results of post-processing the Zygo height measurements in MATLAB using the algorithm outlined in Appendix B. The measured height for the bulk metallic glass channel is 37.9 μm, and the measured height of the PDMS channel is 36.8 μm. The measured width of the bulk metallic glass channel is 49.3 μm, and the measured width of the PDMS channel is 44.9 μm. These measurements are within a few microns of each other, and differences in the measurements may be due to a variety of reasons: thermal contraction of the PDMS part, lack of sidewall data in the Zygo measurements, feature deformation during demolding, etc.

Figure 5-3 A shows some grating features from a different section of the bulk metallic glass mold used in Figure 5-1 and Figure 5-2. Figure 5-3 B shows corresponding features replicated in a centrifugally cast PDMS part. The pitch of the gratings is approximately 20 μm, and their height is approximately 30 μm. The centrifugally cast PDMS part was spun up to 7000 rpm with a slew rate of approximately 300 rpm/s for a total spin time of 30 seconds (not including deceleration time). The part was then cured with one of the temperature profiles shown in Figure 5-4.

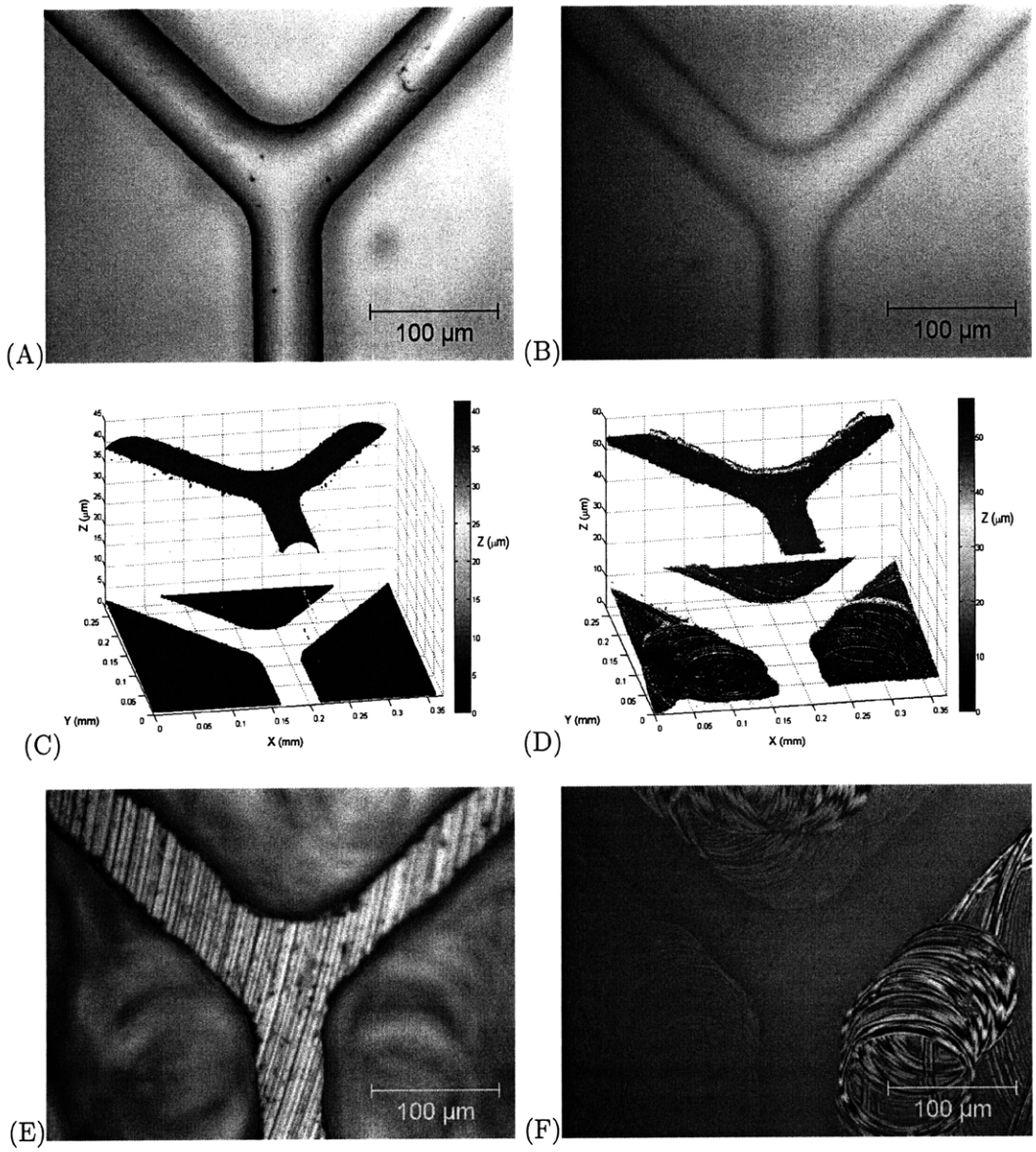

Figure 5-1: (A) Y-mixer protruding channels in bulk metallic glass mold. (B) Y-mixer channels in PDMS part produced by centrifugal casting off of bulk metallic glass features shown in A and C. (C) Same as A in bulk metallic glass mold with heights included. (D) Y-mixer protruding channels in micro-machined aluminum. (E) Same as D without height information. (F) Y-mixer channels in PDMS part produced by centrifugal casting off of micro-machined features shown in D and E.

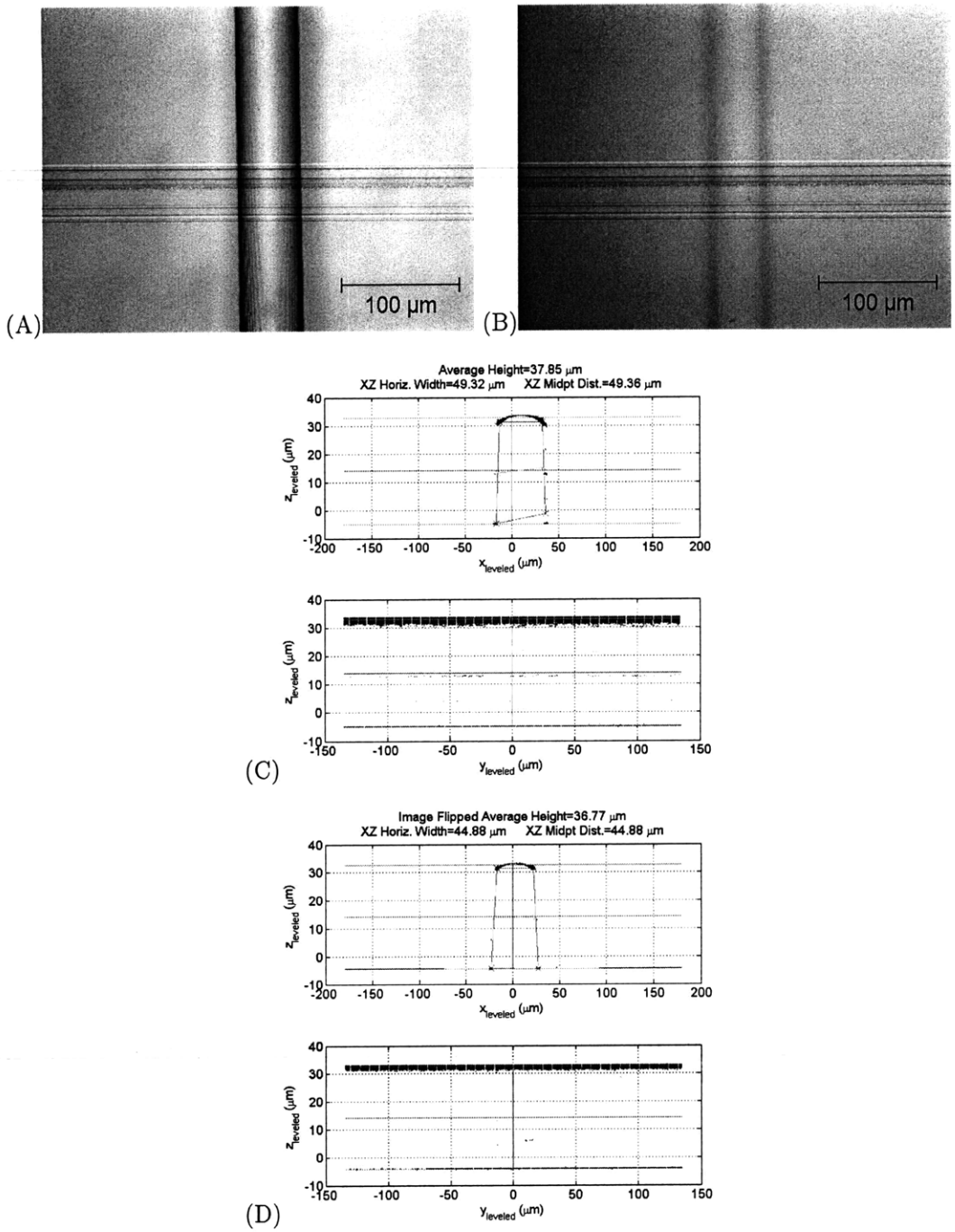

Figure 5-2: (A) Section of bulk metallic glass tool right below Y-mixer shown in Figure 5-1 A. (B) Corresponding portion of PDMS part to A molded off of bulk metallic glass tool. (C) Leveled and measured image of A. (D) Leveled and measured image of B.

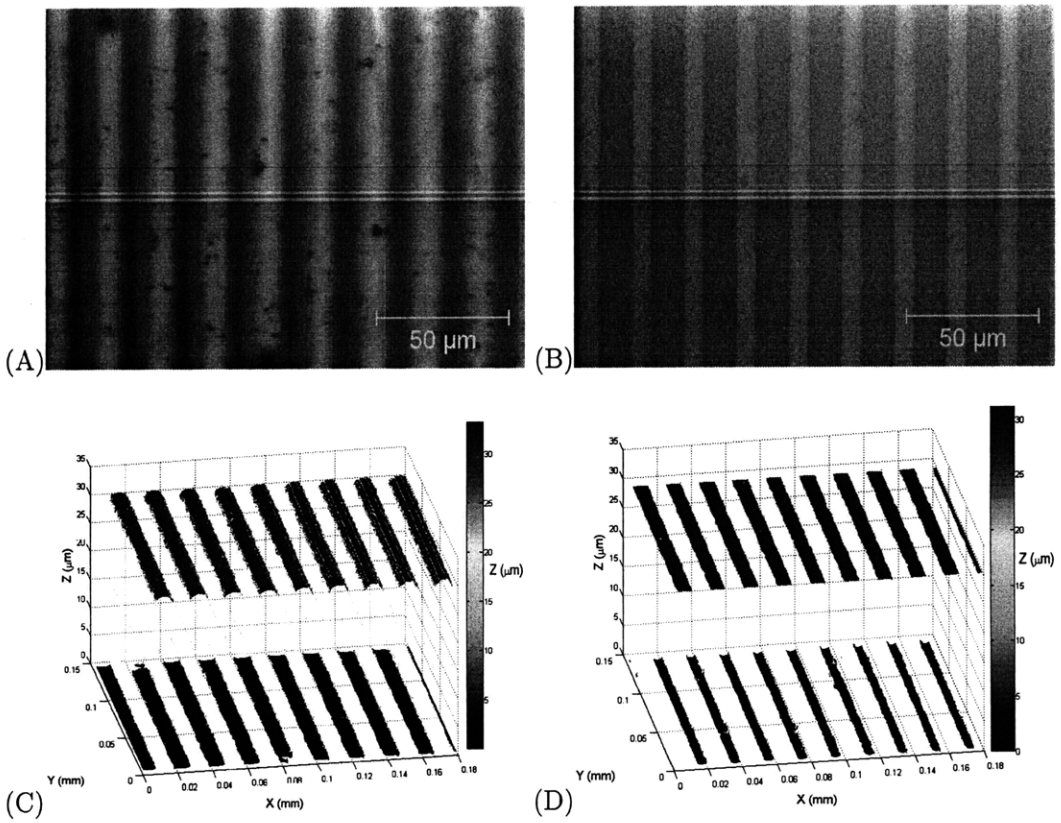

Figure 5-3: (A) Section of grating features on a bulk metallic glass mold with a pitch of approximately 20 μm and a height of approximately 30 μm. (B) Corresponding portion of PDMS part to A molded off of bulk metallic glass tool. (C) 3-D Zygo measurements of image A. (D) 3-D Zygo measurements of image B.

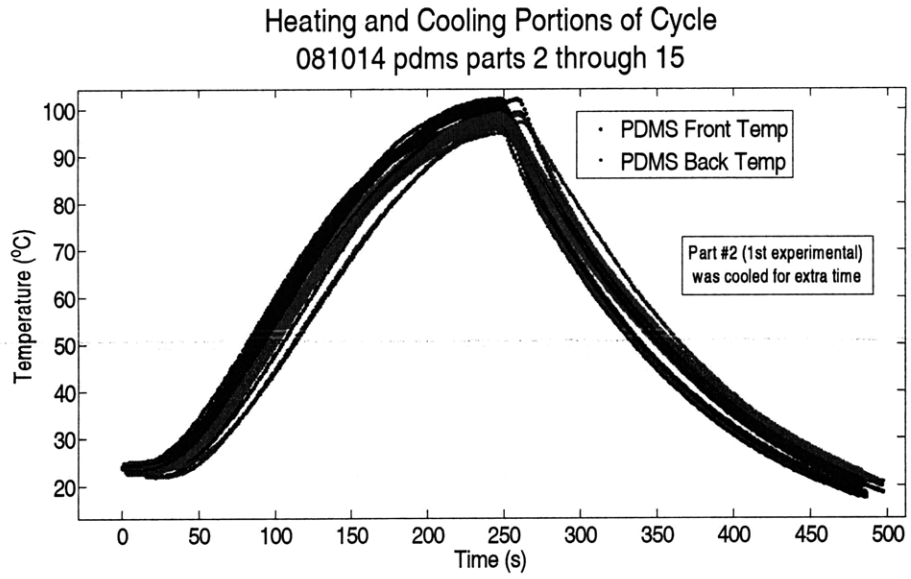

Figure 5-4: Superimposed temperature profiles of the heating and cooling system for the front and back heaters for 14 runs (28 lines shown). The temperature profiles were measured with a probe in contact with PDMS.

5.1.2 Nano features

As mentioned in Section 1.4, PDMS casting has been shown to replicate nano features as small as 2 nm in the vertical direction and as small as 30 nm in the lateral direction. Using a Zygo optical profilometer (see Appendix B), it is possible to characterize part dimensions with nanometer accuracy in the vertical direction. Figure 5-5 A shows some images of milling marks previously shown in Figure 5-1 E but at higher magnification. Figure 5-5 B shows the corresponding milling marks replicated in a centrifugally cast PDMS part, which was spun up to 7000 rpm at a slew rate of 300 rpm/s for a total spin time of 6.5 minutes (not including deceleration time). The temperature curing profile was one of those shown in Figure 5-4. The minimum resolution in the lateral direction is 275 nm based on the original images having 73 pixels over a length of 20 μm.

Figure 5-5 C and Figure 5-5 D show the same images as Figure 5-5 A and Figure 5-5 B, but the greyscale level is now associated with the height at a given pixel location. The highest to lowest point in these images is approximately 11 μm. Figure 5-5 C and Figure 5-5 D also show regions to be cropped from the original images for further analysis. Figure 5-6 A and Figure 5-6 B show the cropped regions at higher magnification (no change in optical resolution though), and pixelation is evident. The highest to lowest point in these images

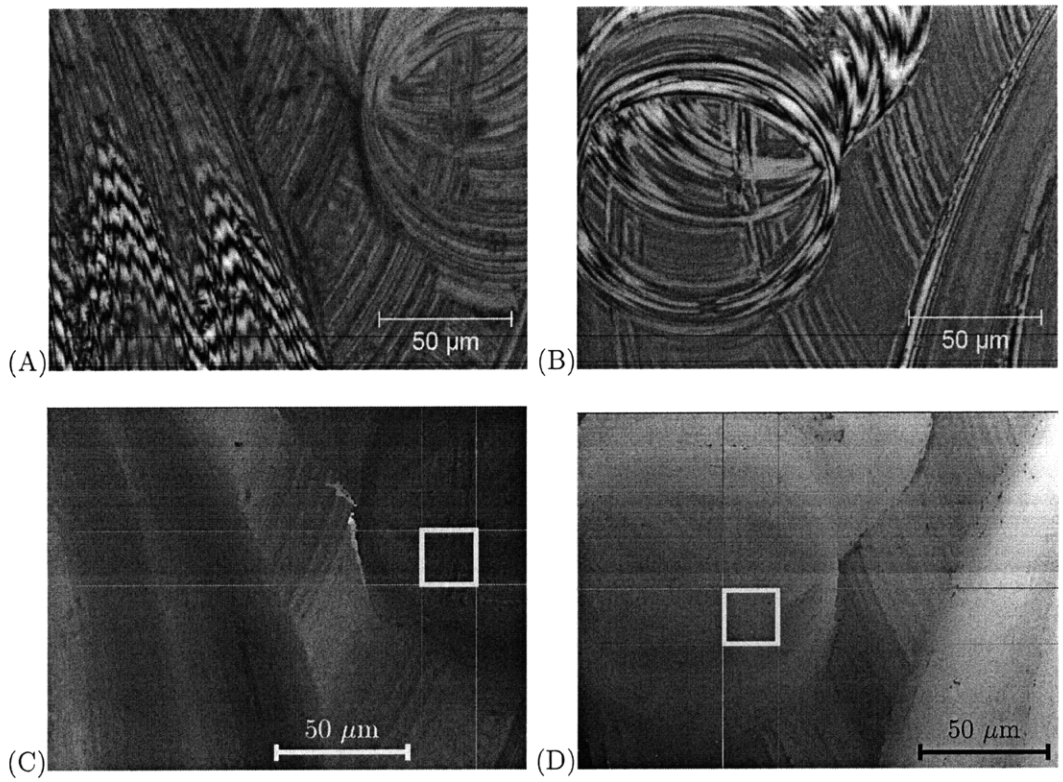

Figure 5-5: (A) Section of micro machined aluminum tool near the Y-mixer areas shown in Figure 5-1 E and F. (B) Corresponding portion of PDMS part to A molded off of micromachined aluminum. (C) Contour plot showing a 20μm x 20μm region to be cropped, which starts 139.1 μm from the left and 45.1 μm from the top. (D) Contour plot showing a 20μm x 20μm region to be cropped, which starts 53.0 μm from the left and 63.5 μm from the top.

is approximately 2 μm. These images look flipped right to left and inverted with respect to their greyscale fill, meaning the high points are now low points and the low points are now high points. This behavior in replication is expected and has also been demonstrated with the previous images shown in Section 5.1.

Corresponding profile lines are selected from the images in the circled regions of Figure 5-6 A and Figure 5-6 B. The associated line profiles are included in Figure 5-6 C and Figure 5-6 D. The line profile in Figure 5-6 C shows a depth of less than 300 nm, and the corresponding line profile in Figure 5-6 D shows a height between 200 nm and 300 nm. Thus, it is possible to conclude that nano-sized features can be replicated in PDMS using the centrifugal casting and fast curing processes outlined in this thesis.

5.1.3 Overlapping Features

As shown in Figure 1-9, one of the objectives of our research is the single-step production of parts with features on multiples faces. There is a desire to produce the microfluidic control and flow channel architecture in a single molding step. In order to have a functioning control valve that successfully closes down on the corresponding flow channel, the membrane separating the two layers from each other must be sufficiently compliant and thin enough to obstruct flow when pressurized.

In an attempt to produce the control and flow channel architecture in a single piece of PDMS, we have centrifugally molded the part shown in Figure 5-7. This part was spun at 5000 rpm for 3 minutes and then cured on a hot plate set to 300°C for 3 minutes. After the part was cured and cooled, it was removed from the two halves of the molds shown in Figure 2-8.

In order to produce control channels with widths closer to the standard sizes (10s to 100s of microns) used in microfluidic devices with the centrifugal casting process, it would be necessary to either produce higher aspect ratio control channels (thin and tall) or thinner parts on the order of 100s of microns in thickness. In order to produce thinner parts, the two mold halves would need to be closer to each other. If the mold halves are brought closer to each other, the overall thickness of the PDMS device will decrease and separating the mold halves from the PDMS will become more difficult. To assist in the demolding of the PDMS from the mold halves, liquid parting [65, 64] or possibly some modified version of the demolding method described in Section 2.3 should be a viable method to release the PDMS

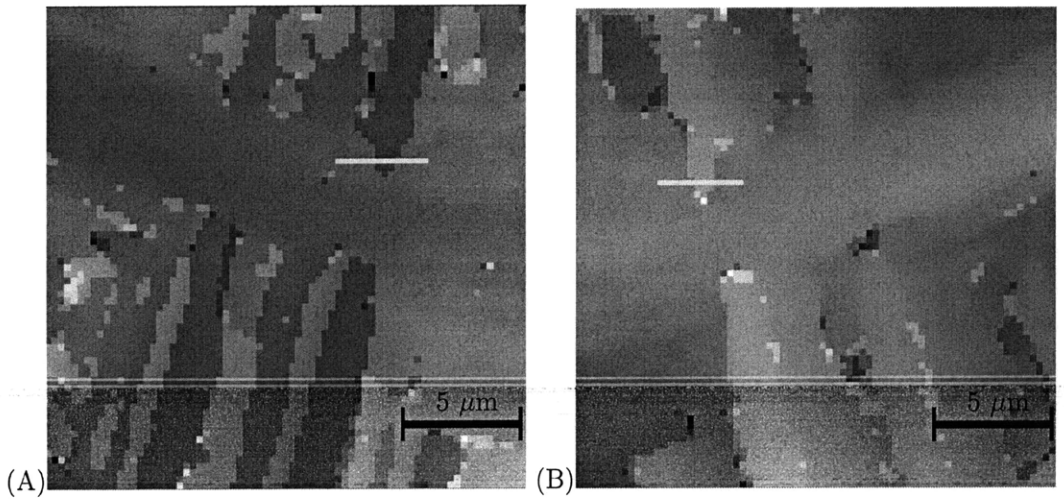

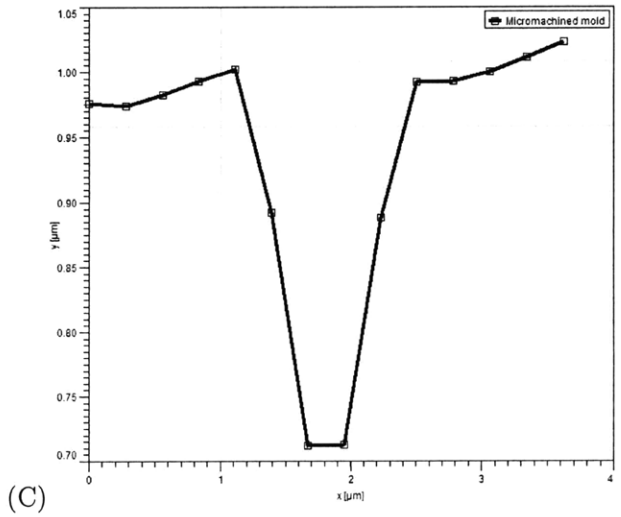

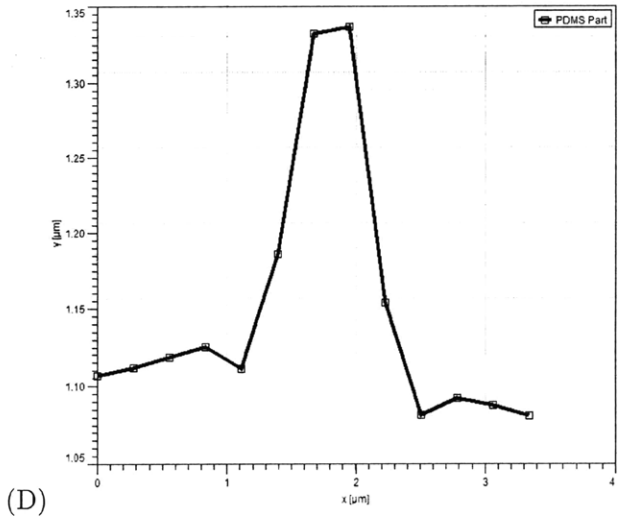

Figure 5-6: (A) 20 μm x 20 μm cropped region of Figure 5-5 C. (B) 20 μm x 20 μm cropped region of Figure 5-5 D. (C) Profile of selected line in A. (D) Profile of selected line in B.

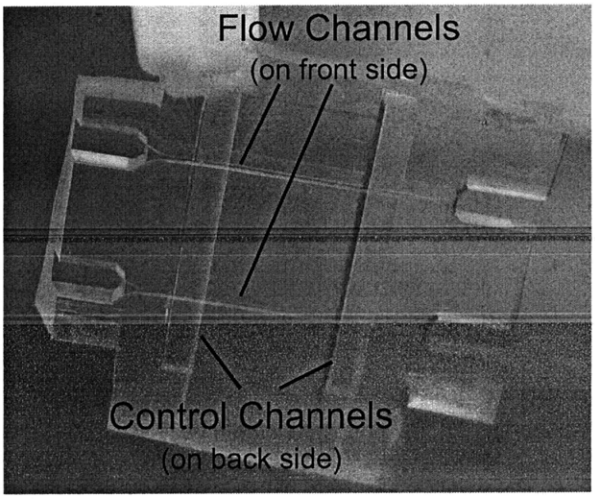

Figure 5-7: Control and flow channels molded simultaneously by centrifugal casting. This PDMS part has been trimmed down to approximately 16 mm X 16 mm and has a thickness of approximately 2.5 mm.

without tearing. Further work and testing are required to complete the control and flow layer architecture in a single step using centrifugal casting.

5.1.4 Functioning devices

Up to this point in this section, images have been shown depicting the replication of micro and nano features by centrifugal casting and fast curing. Using PDMS parts produced by centrifugal casting and fast curing, working devices have been assembled. PDMS components created through the centrifugal casting and fast curing methods have been plasma treated and bonded to glass. The ability to bond PDMS to glass by dry plasma treatment is an important reason for using PDMS in microfluidic devices because this form of bonding is used to encapsulate channels without the use of an adhesive.

Figure 5-8 shows some example images of a functioning microfluidic device, which was fabricated using centrifugal casting and fast curing. The centrifugally cast and fast cured PDMS component was bonded to a glass slide by exposing the PDMS and the glass surfaces to air plasma for less than a minute. The glass slide and the PDMS part were then brought in contact with each other, and a bond was formed. The completed device was then connected to tubing (two streams) and two syringes on a syringe pump. The syringe pump assembly acted as a flow source and had two different syringes: one filled with green dye and one filled with clear water. When the pump was turned on, the syringes provided two streams

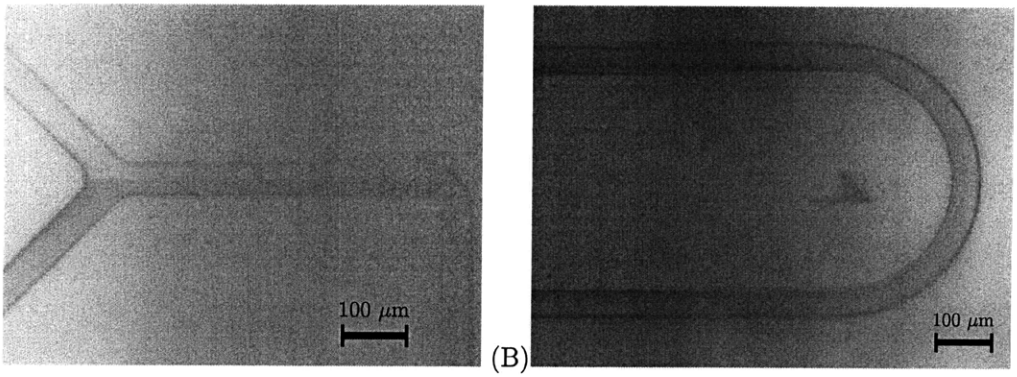

Figure 5-8: (A) Image of green dye and clear water going around a bend in a functioning microfluidic device. (B) Image of green dye and clear water streams being brought together in a Y-mixer. Images courtesy of Eehern Wong.

of fluid, which mixed within the microfluidic device. Figure 5-8 A shows the two streams being brought together at the Y-mixer junction (fluid enters from the left). Within the microfluidic channel, the green dye and clear water experience laminar flow and only mix by diffusion. Figure 5-8 B shows the two streams within one channel going around a bend.

Overall, this section shows that centrifugal casting and the fast curing methods described in this thesis do not hinder micro and nano feature replication in PDMS. With the centrifugal casting of PDMS, the spin times can be as short as 30 seconds (not including the deceleration of the centrifuge), and the cure times were a modest 8 minutes. In addition, the centrifugally cast and fast cured PDMS also retains its ability to have its surface modified by plasma treatment. To support this, images of an example device assembled by plasma treatment are shown in Figure 5-8. This device with a centrifugally cast component works as well as devices produced by conventional means of PDMS processing.

5.2 Mini Manufacturing Run

To evaluate the potential part-to-part variation of a large-scale manufacturing process based on centrifugal casting and fast curing, parts were produced in a mini-manufacturing run using the bulk metallic glass mold shown in Figure 4-29 B. A channel section 0.5 mm below the Y-junction where the two inlet streams meet and become one stream was measured on 20 consecutive parts. The height of the channels is approximately 40 μm and the width is approximately 50 μm. These parts were spun for approximately 1.5 minute (1 minute of energized spin time followed by approximately 30 seconds of deceleration). The set spin

speed was 7000 rpm, and the accelerating slew rate was approximately 300 rpm/s. The parts were then cured in 8 minutes with a maximum temperature of approximately 100 °C and temperature profiles similar to those shown in Figure 5-4. Example images of one of the channel sections measured are shown in Figure 5-9, and the height and width measurements were calculated using the algorithm described in Appendix B. Within the regions of interest for the 20 consecutive parts, only one bubble was observed.

Before measuring all the parts from the manufacturing run, two measurement tests were performed to estimate the variation of the channel and width measurements associated with the Zygo profilometer and the height-width measurement algorithm. In the first measurement test, a channel section was imaged repetitively 20 times without physically moving the part or adjusting any parameters. The 20 repetitive images were then processed using the custom height-width algorithm, and the results are shown in Figure 5-10 A. The standard deviations of the measured heights and widths are both less than 30 nm. In the second measurement test, a single part was physically loaded and unloaded onto the stage of the Zygo profilometer without changing any additional parameters. For each individual measurement, the part had to be aligned before an image was taken. The resulting measurements are shown in Figure 5-10 B. The resulting standard deviation for the height measurements is approximately 150 nm, and the resulting standard deviation for the width measurements is approximately 200 nm. Just by loading and unloading the same part, the standard deviation for the height/width measurements increased by a factor greater than 5.

After measuring the the same channel section as depicted in Figure 5-10, the series of 20 parts were then measured in the Zygo profilometer. The resulting measurements are shown in Figure 5-11. The standard deviation for the height measurements is less than 0.5 μm, and the standard deviation of the width measurements is less than 0.8 μm. With respect to both the height and width, the coefficient of variation (standard deviation divided by the measured mean) is less than 2%. In future manufacturing systems, this coefficient of variation metric may be reduced by reducing the variation in the channel measurement method, developing a more uniform demolding method, or better temperature process control. Regardless, the results from this manufacturing run show the centrifugal casting and fast curing process is able to maintain sub-micron channel variation.

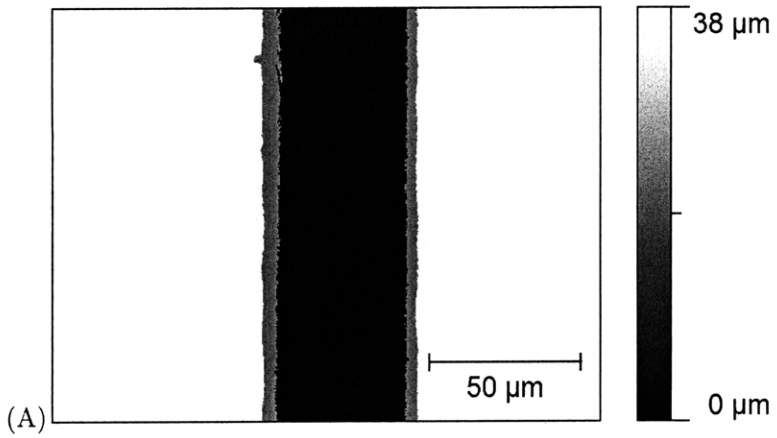

(A)

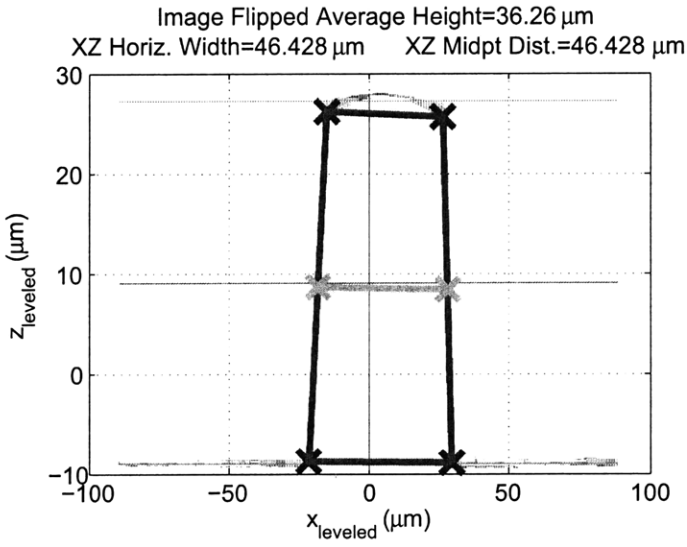

(B)

Figure 5-9: (A) Contour image of a channel section from the mini-manufacturing run. Fuzzy regions (red in digital version) along either side of the channel represent sections where no data was acquired by the Zygo profilometer. (B) Cross-sectional view and resulting measurements of the same channel section shown in A.

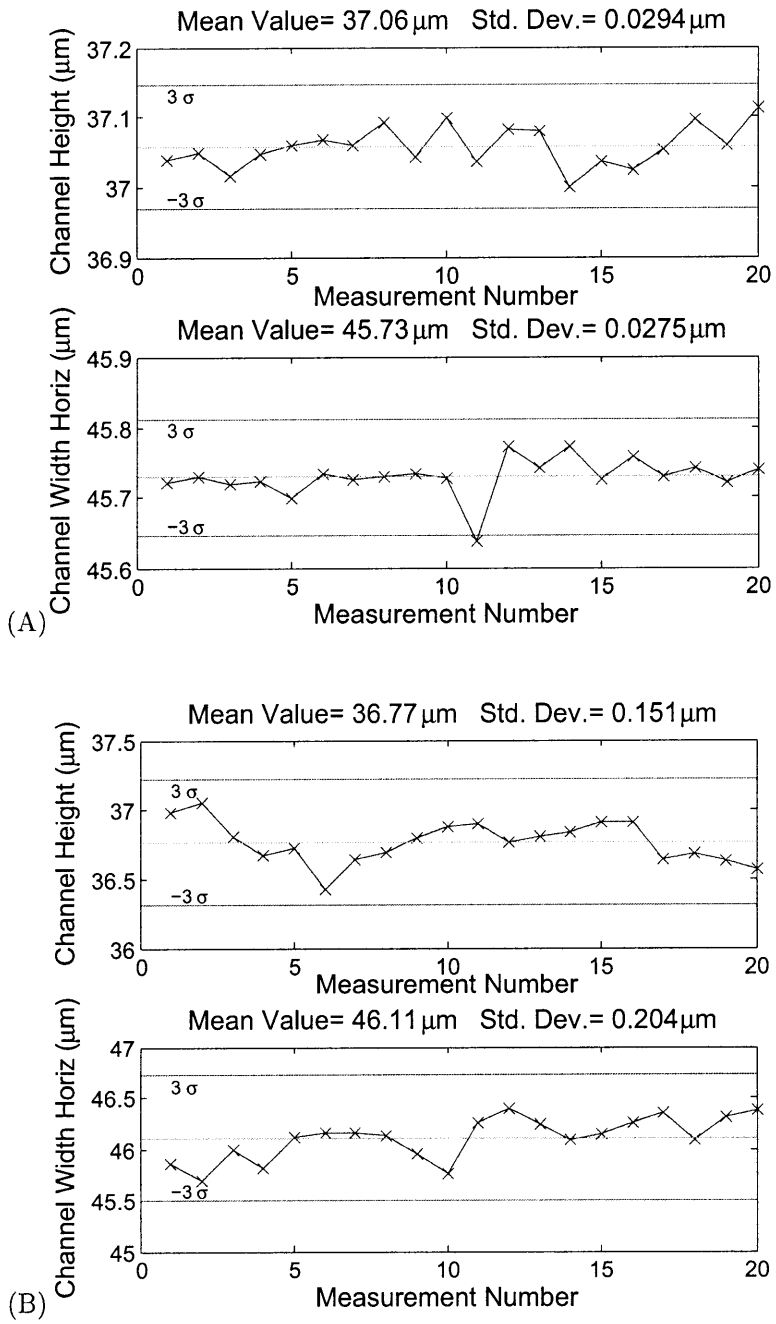

Figure 5-10: (A) Run chart of the same the same channel section measured 20 consecutive times without physically moving the part. (B) Run chart of the same channel section measured 20 times with physical loading and unloading of the part between each measurement.

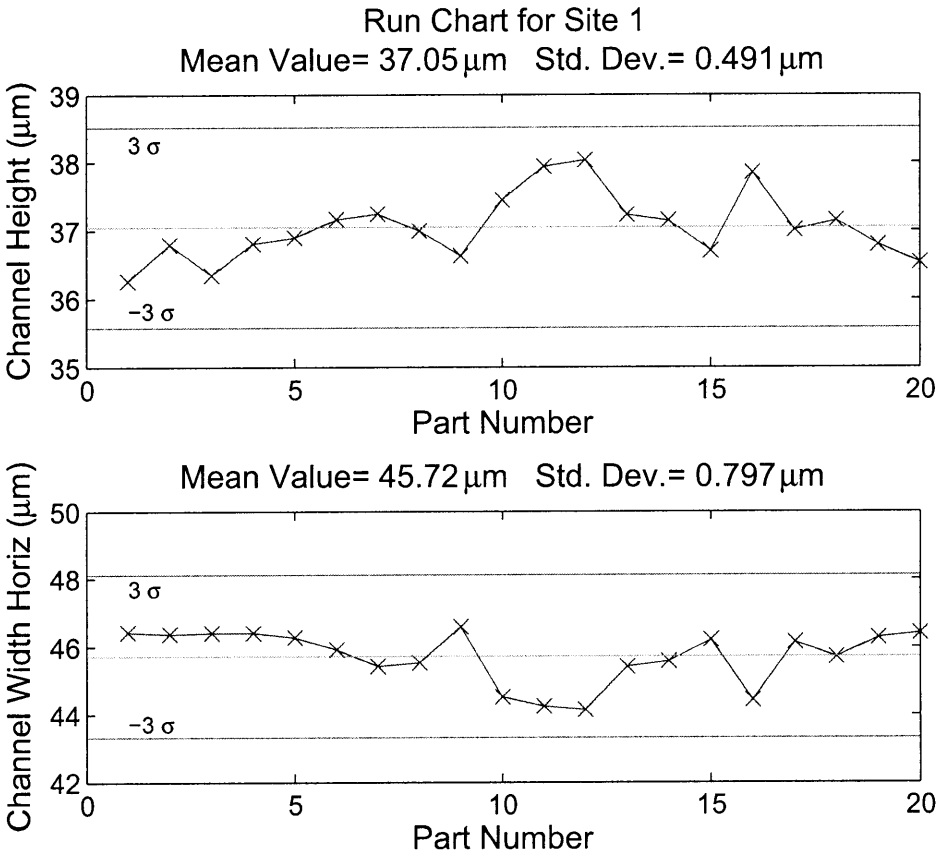

Figure 5-11: (A) Contour image of a channel section from the mini-manufacturing run. Fuzzy regions (red in digital version) along either side of the channel represent sections where no data was acquired by the Zygo profilometer. (B) Cross-sectional view of the same channel section shown in A analyzed to determine height and width measurements.

5.3 Example problem

As a case study, consider the hypothetical production of a PDMS component with lateral dimensions of 30 cm x 30 cm. This case study is performed to demonstrate the potential utility of centrifugal casting with respect to the production of parts almost ten times larger than the ones produced at this point. A part with lateral dimensions of 30 cm x 30 cm may be useful for microcontact printing or soft lithography applications, where large PDMS stamps are desirable.

Three possible mold designs are shown in Figure 5-12. In Figure 5-12 A, the molding region is placed near the center axis of rotation, which means the overall outer diameter can remain small. In Figure 5-12 B, the molding region is placed much farther away from the axis of rotation. In Figure 5-12 C, the molding region is elongated, and the diameter of the rotor is the same as in Figure 5-12 B. In this last case, only the top half of the molding region needs to be bubble free and the bottom half material will be trimmed off and removed.

The case shown in Figure 5-12 A is analyzed here because it requires the least amount of material/inertia in the rotor assembly and can be spun at the highest speeds. The case shown in Figure 5-12 B is analyzed here to determine whether or not higher bubble removal times can be reduced by increasing the part's distance from the center axis of rotation. Figure 5-12 C is included to see whether or not having additional fluid and hydrostatic pressure is beneficial for bubble dissolution and spin time reduction. The case shown in 5-12 C has the addtional cost associated with trimming away 50% of the completed part.

The objective is to determine which of these mold designs would be best for manufacturing with respect to cost, quality, and rate. In this case, flexibility is not too great a concern, since the lateral dimensions are fixed at 30 cm x 30 cm. In all three cases, the centrifuge is able to accelerate the rotor at a rate of 300 rpm/s and has the same initial speed of 100 rpm used in prior simulations. Finally, the mold material is to be aluminum with a yield strength of 20 MPa, a Poisson's ratio of 0.3, and a density of 2700 kg/m^3. These three cases represent extreme designs for a desired part size. In a real manufacturing setting, the distance from the center axis of rotation and the amount of excess material to be trimmed off of the completed part might be more thoroughly optimized to produce some combination of the proposed variations in this case study. These two parameter, distance from the center axis of rotation and quantity of excess material for trimming, might also be combined with

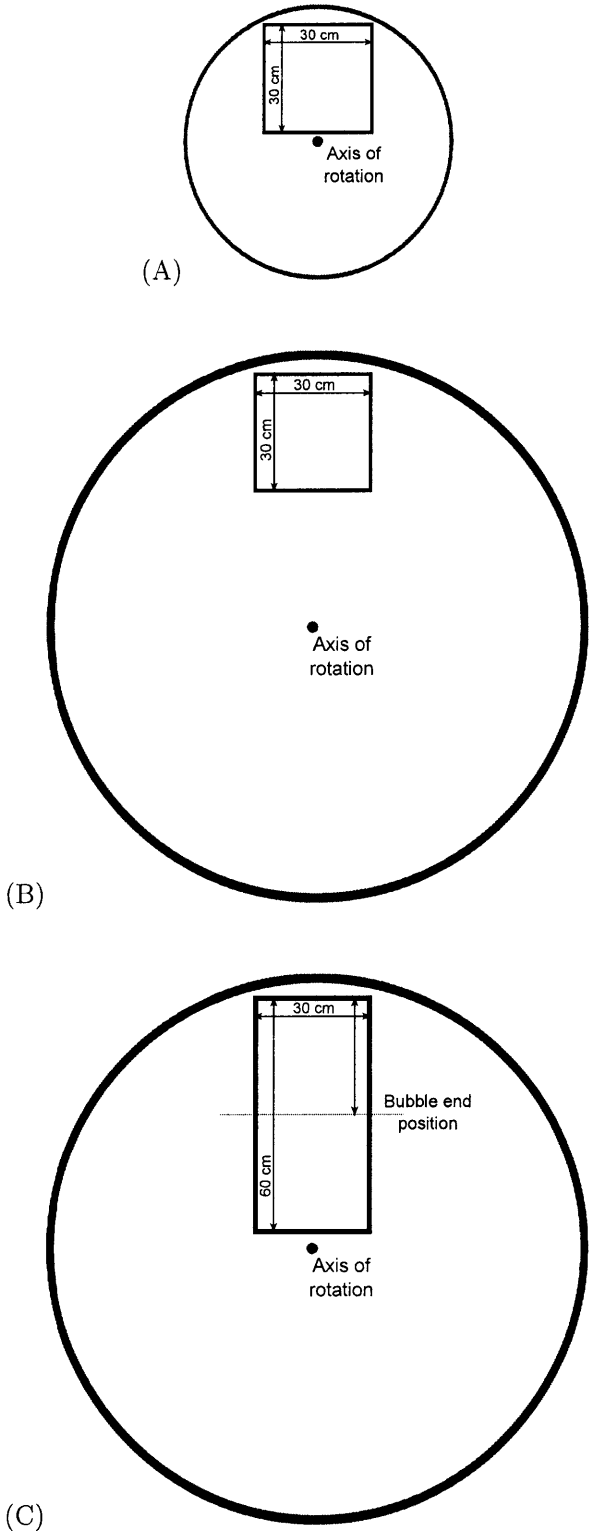

Figure 5-12: Diagram depicting three possible geometrical configurations for molding a 30 cm x 30 cm part.

attempting to fit more individual parts in the same rotor about the center axis of rotation to increase throughput.

5.3.1 Part with small outer diameter rotor

In the design shown in Figure 5-12 A, the outer radius of the rotor is set to 37 cm. Approximating the rotor geometry as a solid disc, Equation 2.8 can be used to estimate the maximum radial or circumferential stress at the center axis of rotation:

$$T_{\theta,max} = T_{r,max} = \frac{3+\nu}{8}\rho\left(r_o\omega^2\right). \tag{5.1}$$

With a safety factor of 2, the maximum permissible stress would be 10 MPa. Given the outer radius of 37 cm, the maximum spin speed of the centrifuge is approximately 1500 rpm.

The objective is to then estimate the amount of time required to degas the PDMS material given a maximum spin speed of 1500 rpm. Using the model outlined in Section 4.4, it is possible to simulate the bubble speed and time requirements for removal. Table 5.1 shows the parameters used for this simulation. The results of these simulations provide calculations for the amount of time required for bubbles to exit given initial diameters ranging from 0 μm to 1 mm and varied bubble starting locations ranging from near the center axis of rotation to the outer edge of the part along the centerline of the PDMS part being cast.

Figure 5-13 shows the simulated time for bubble removal results plotted against initial diameter bubble sizes at different starting positions for two different spin speeds. In Figure 5-13 A and Figure 5-13 B, the bubble starting position for each curve is shown above the curve's peak time value. The peak time for a bubble to be removed from solution represents the amount of time for a bubble of a critical size to be removed from solution. For a given curve, all the points left of the peak generally represent bubbles that were removed by being dissolved into solution. All the points right of the peak generally represent bubbles that were removed by buoyant forces eventually driving the bubble to the liquid-air interface. As shown in Figure 4-13, the optimized critical initial diameter yielding a maximum time for removal represents a bubble that takes the longest amount of time to exit the solution at the liquid-air interface or to dissolve very close to the liquid-air interface.

In Figure 4-13, the peaks shift to the right as the bubble starting location gets further

Table 5.1: Parameter values used in simulating combined bubble speed and diffusion behavior for 30 cm x 30 cm part with small rotor.

Parameter	Value	Description
bubble_start_pos	0.026 m 0.076 m 0.126 m 0.176 m 0.226 m 0.276 m 0.325 m	Bubble start distance from center axis of rotation
bubble_end_pos	0.025 m	Bubble ending distance from center axis of rotation
r_{fstart}	0.025 m	Liquid-air interface distance from center axis of rotation
dt	0.02 s	Time step
d_o domain	0 μm to 1 mm	Initial bubble diameter domain
d_o spacing	0.1 μm	Initial bubble diameter spacing
spin_speed	1000 rpm 1500 rpm 2000 rpm 2500 rpm 3000 rpm 3500 rpm 4000 rpm	Set spin speed
slew rate	300 rpm/s	Spin speed acceleration (slew rate)
offset	100 rpm	Spin speed at start
T	298 K	Temperature during spinning
σ	0.02 N/m	Liquid-gas surface tension
μ	3.9 Pa s	Liquid viscosity
ρ_f	1030 kg/m^3	Liquid density
P_{cham}	101.3 kPa	Chamber pressure
ϕ	0°	Mold tilt angle
κ	1.47×10^{-9} m^2/s	Diffusion coefficient (Air in PDMS)
k_D	1.927×10^{-6} kg (gas) / m^3(polymer)/ Pa	Henry's coefficient
M	0.02897 kg/mol	Molecular weight of gas
c_{f_init}	1.05	Initial supersaturation fraction
D_c	2	Drag force coefficient (used in this work)

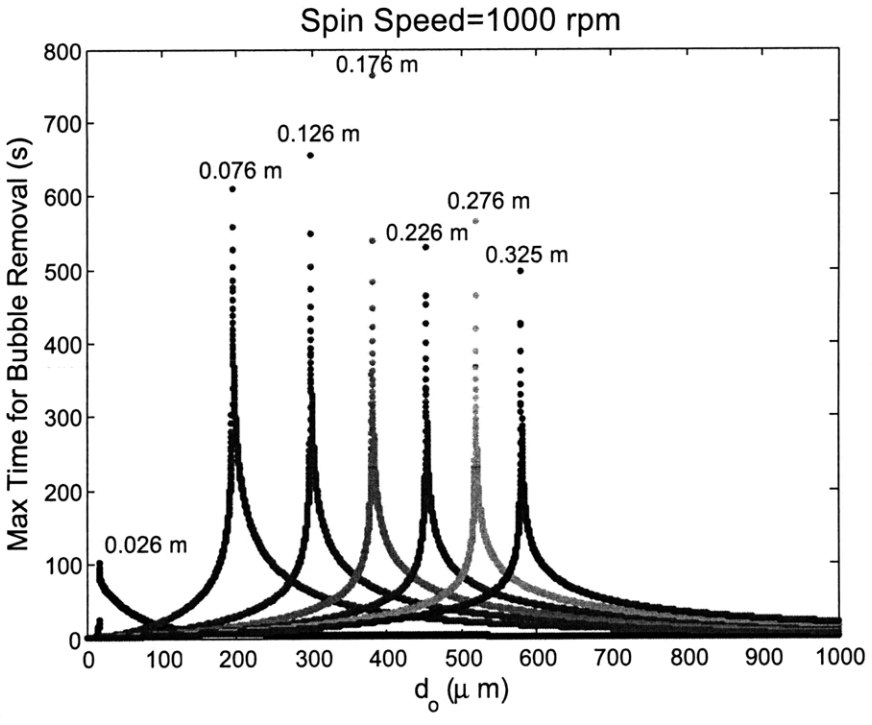

(A)

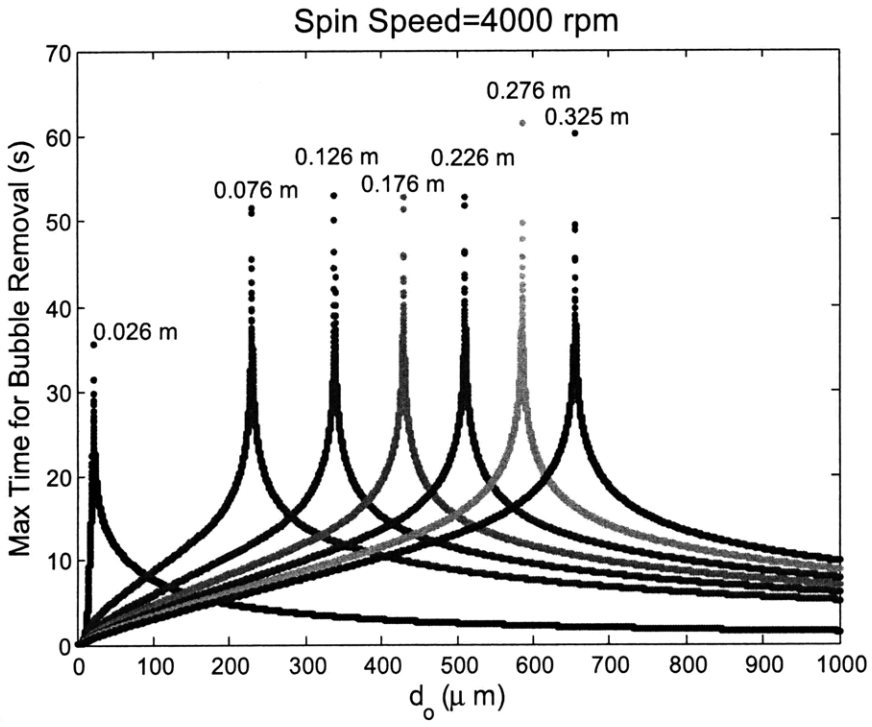

(B)

Figure 5-13: Simulated times for bubbles to be removed from PDMS plotted against a domain of initial bubble diameters. Simulations are for the scenario with a 30 cm x 30 cm part and a spinning rotor with small outer radius. Cases for two spin speed profiles and a few different initial bubble starting positions are shown.

from the center axis of rotation. This shift right because of larger bubble starting locations is a result of the initial diameter of the bubbles needing to be larger in order to make the complete trip to the liquid-air interface. A bubble starting farther from the center axis of rotation without a change in the spin speed or initial diameter will dissolve faster because the pressure is higher farther from the center axis of rotation. The higher pressure surrounding the bubble will cause an increase in the concentration gradient between the air concentration in the bubble wall and in the surrounding solution, which will cause faster dissolution. The greater pressure increase associated with a greater distance from the center axis of rotation will also cause a greater volume decrease of a bubble by the Ideal Gas Law. To compensate for faster dissolution rates and/or smaller bubble volumes at farther distances from the center axis of rotation, the critical bubble diameter increases, which means the initial bubble diameter needs to be larger for the bubble to survive its journey to the liquid-air interface near the center axis of rotation.

In Figure 4-13, the maximum peaks also shift to the right with an increase in the spin speed from 1000 rpm to 4000 rpm. This shift to the right is again because of a pressure increase. In this case, the pressure increase comes from an increase in spin speed. This pressure increase causes the bubbles to dissolve or to decrease in volume, which means the bubble diameter needs to be greater for it to survive its journey to the liquid-air interface near the center of the centrifuge.

Figure 5-14 shows simulated results based off of the results shown in Figure 4-13. Using the method shown in Figure 4-15, a maximum time value corresponding to a removal of 99% of the bubbles with initial diameters ranging from 0 μm to 1 mm is determined over domains of initial bubble diameters at a given speed and bubble starting location. Using these 3-dimensional simulated results, it is possible to estimate the spin time required for a given spin speed profile. Looking at the contour plot in Figure 5-14 B, it is possible to estimate that using a set spin speed of 1500 rpm will require at least 100 seconds of spinning and that the most time consuming bubbles to remove will start somewhere between 0.026 m and 0.1 m from the center axis of rotation.

5.3.2 Part with large outer diameter rotor

In the design shown in Figure 5-12 B, the outer radius of the rotor is set to 65 cm. Approximating the rotor geometry as a solid disc, Equation 2.8 or Equation 5.1 can be used again to

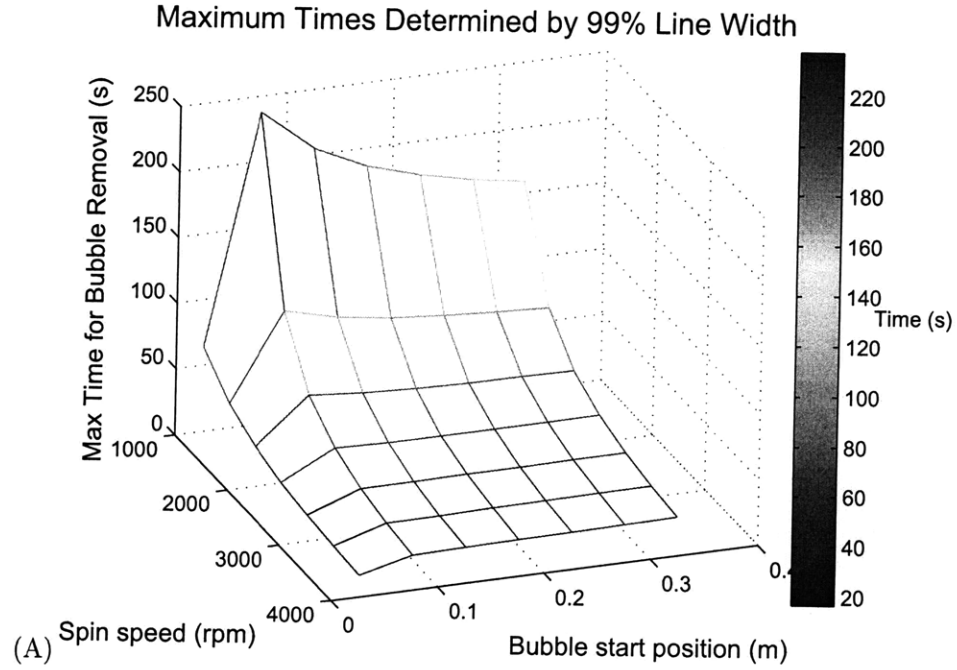

(A)

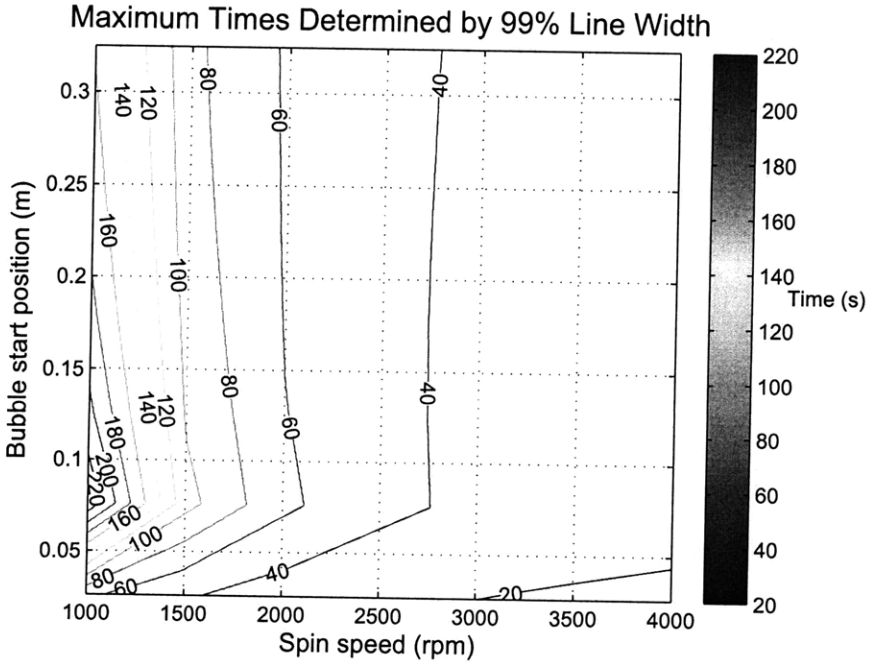

(B)

Figure 5-14: Simulated times for bubbles to be removed from PDMS plotted against set spin speeds and bubble starting positions. Simulations are for scenario with 30 cm x 30 cm part and spinning rotor with small outer radius. (A) 3-D depiction of simulated results. (B) Contour representation of the same numerical results.

estimate the maximum radial or circumferential stress at the center axis of rotation. With a safety factor of 2, the maximum permissible stress would be 10 MPa. Given this maximum permissible stress and the outer radius of 65 cm, the maximum spin speed of the centrifuge is approximately 1130 rpm.

Figure 5-15 and Figure 5-16 show simulated results for the case depicted in Figure 5-12 B. Most of the parameters shown in Table 5.1 remained the same for this simulation, but the first three listed were changed to reflect the different geometry. In this case, the fluid starts 32.5 cm from the center axis of rotation, and the bubble starts at the following distances from the center axis of rotation: 0.326 m, 0.376 m, 0.426 m, 0.4760 m, 0.526 m, 0.576 m, and 0.625 m. The bubble either dissolves as it moves toward the center during spinning or exits at the liquid-air interface 32.5 cm from the center axis of rotation.

Looking at the contour plot in Figure 5-16 B, it is possible to estimate the time required for removing the bubbles from the PDMS part depicted in Figure 5-12 B. Given the maximum spin speed for the rotor is approximately 1130 rpm, it will require approximately 50 seconds of spinning to produce a bubble free part. The most time consuming bubbles will start near the outer edge of the mold.

5.3.3 Long part with large diameter rotor

In the design shown in Figure 5-12 C, the outer radius of the rotor is again set to 65 cm, which means the estimated maximum spin speed of the centrifuge is approximately 1130 rpm. Figure 5-15 and Figure 5-16 show simulated results for the case depicted in Figure 5-12 C. Most of the parameters shown in Table 5.1 again remain the same for this simulation, but the first three listed are changed to reflect the different geometry. In this case, the fluid starts 2.5 cm from the center axis of rotation, and the bubble starts at the following distances from the center axis of rotation: 0.326 m, 0.376 m, 0.426 m, 0.4760 m, 0.526 m, 0.576 m, and 0.625 m. The bubble either dissolves as it moves toward the center during spinning or exits at the specified location of 32.5 cm from the center axis of rotation. In this case, the bubble can keep traveling past the specified location, but the objective is to ensure that no bubbles remain in the specified region 32.5 cm to 62.5 cm from the center axis of rotation.

Looking at the contour plot in Figure 5-18 B, it is possible to estimate the time required for removing the bubbles from the PDMS part depicted in Figure 5-12 C. Given the maximum spin speed for the rotor is approximately 1130 rpm, it will require approximately

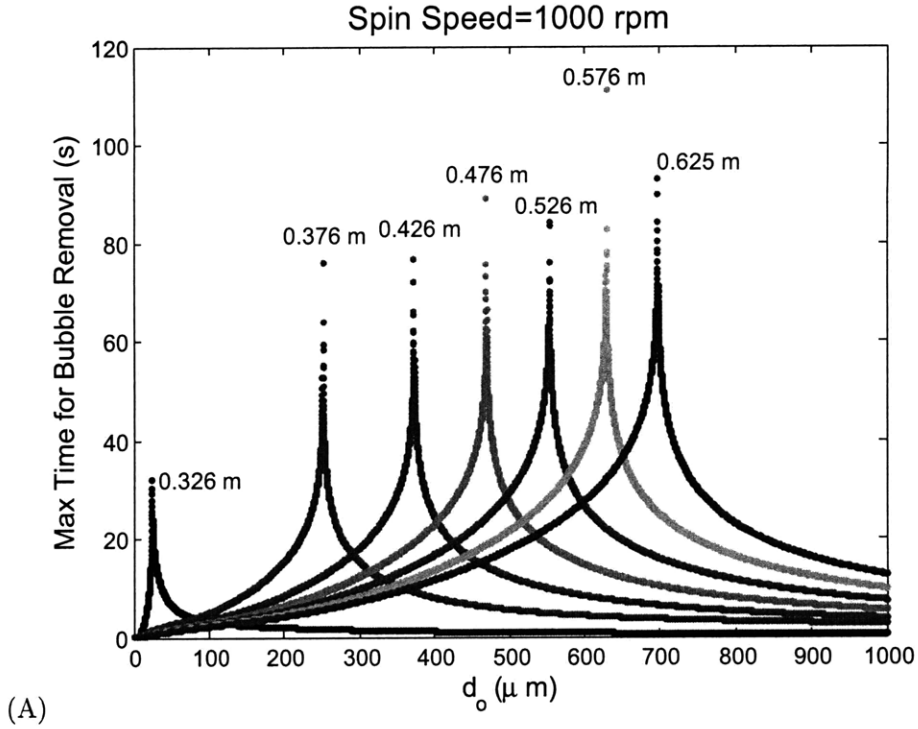

(A)

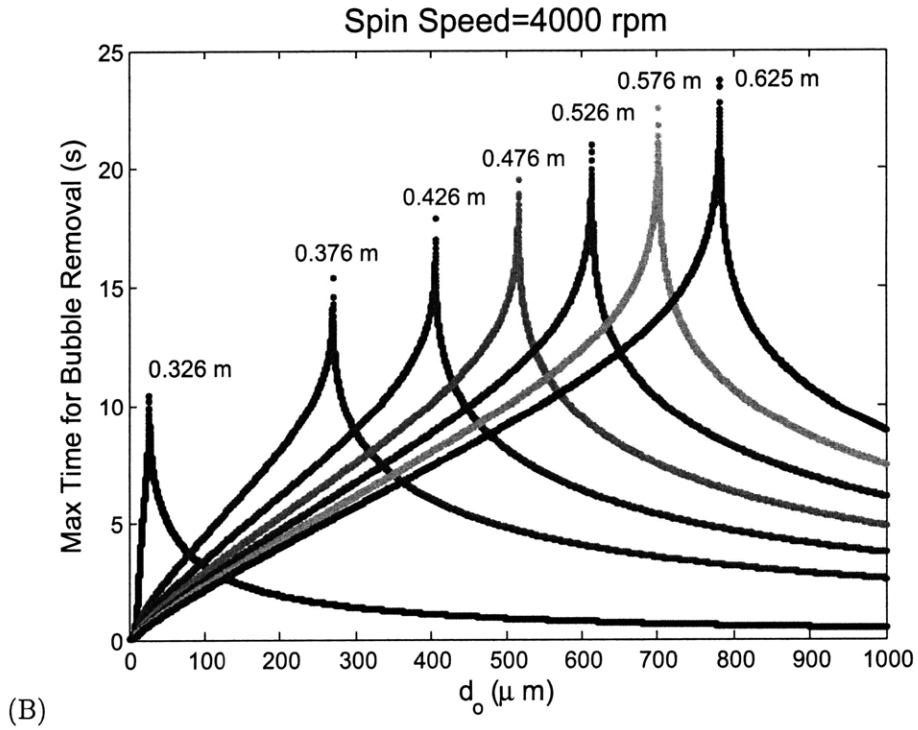

(B)

Figure 5-15: Simulated times for bubbles to be removed from PDMS plotted against a domain of initial bubble diameters. Simulations are for scenario with 30 cm x 30 cm part and spinning rotor with large outer radius. Cases for two spin speed profiles and a few different initial bubble starting positions are shown.

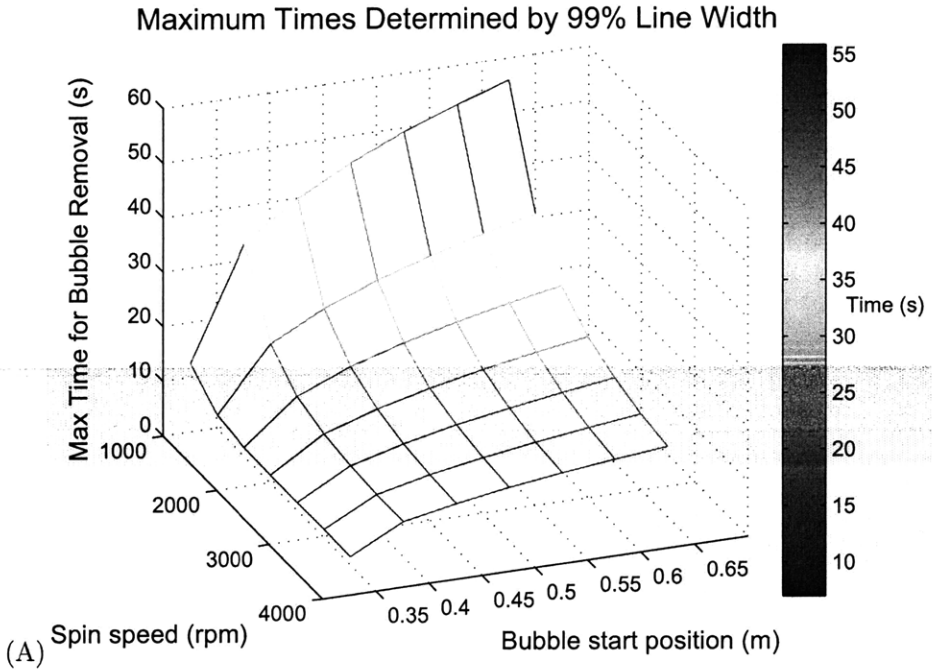

(A)

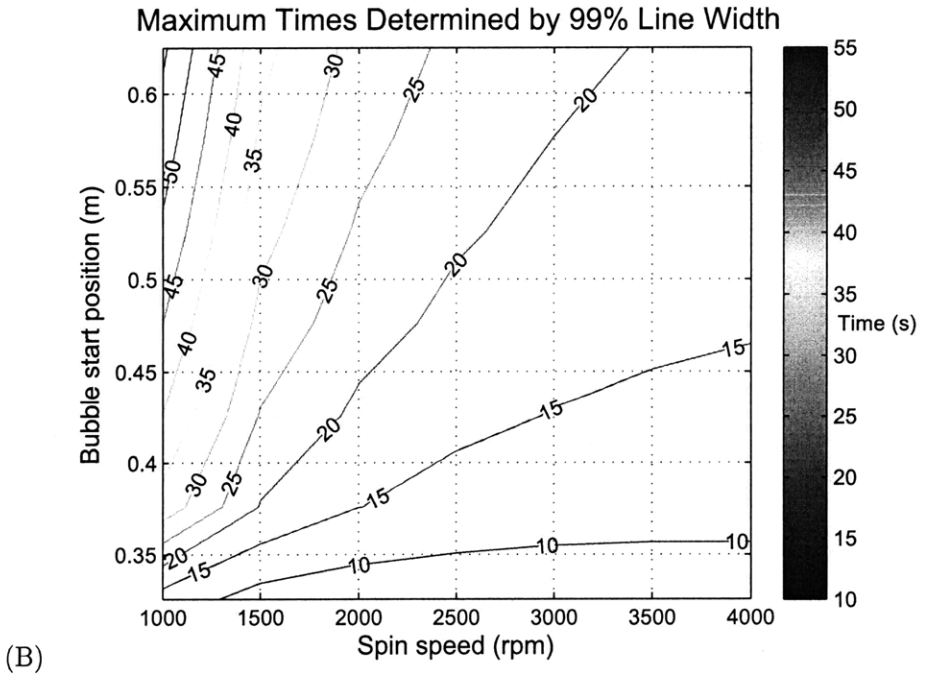

(B)

Figure 5-16: Simulated times for bubbles to be removed from PDMS plotted against set spin speeds and bubble starting positions. Simulations are for the scenario with a 30 cm x 30 cm part and a spinning rotor with large outer radius. (A) 3-D depiction of simulated results. (B) Contour representation of the same numerical results.

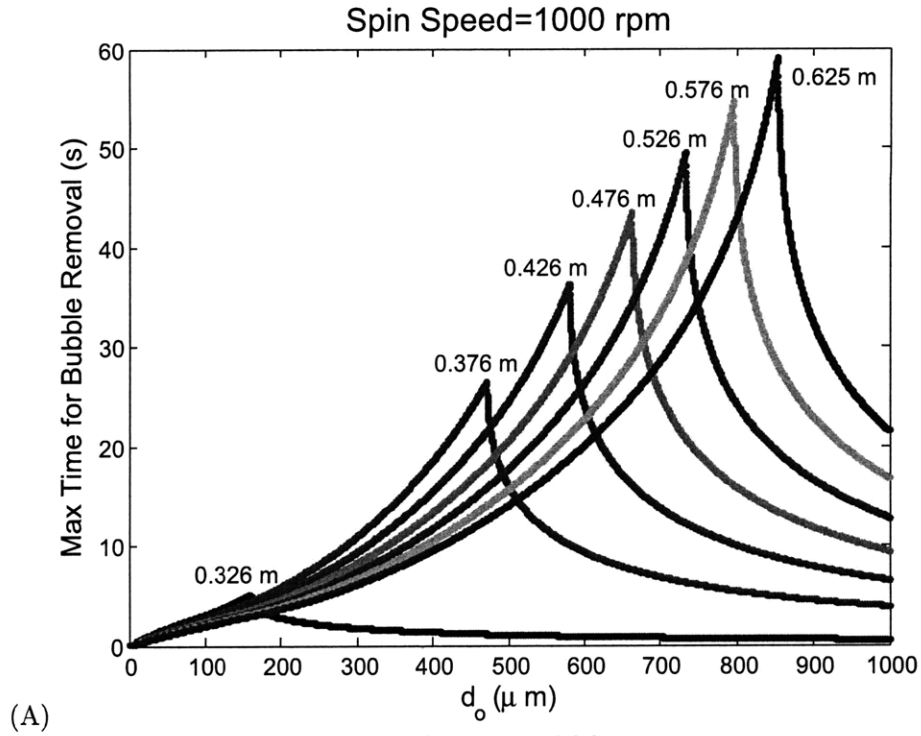

(A)

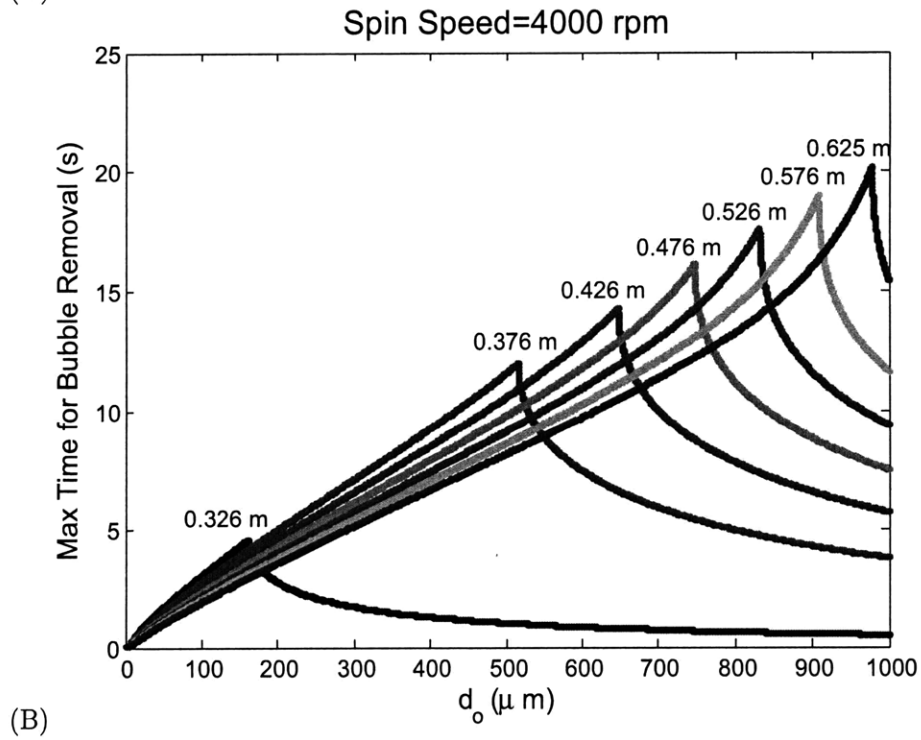

(B)

Figure 5-17: Simulated times for bubbles to be removed from PDMS plotted against a domain of initial bubble diameters. Simulations are for the scenario with a 60 cm x 30 cm part and a spinning rotor with large outer radius. Cases for two spin speed profiles and a few different initial bubble starting positions are shown.

Table 5.2: Comparisons for three potential designs for centrifugal casting a large PDMS part (30 cm x 30 cm).

Case #	Design type	Spin speed (rpm)	Spin time (seconds)	Comments
1	Small outer diameter	1500	> 100	Most time consuming bubbles are not located at outer edge of mold.
2	Large outer diameter	1130	~ 50	Most time consuming bubbles are located at outer edge of mold.
3	Long part, large outer diameter	1130	~ 50	Similar time requirements as case #2, but excess material wasted.

50 secondsof spinning to produce a bubble free part. The most time consuming bubbles will start near the outer edge of the mold.

Table 5.2 compares the results of the three cases shown in Figure 5-12 and the last few subsections. Case #1 requires the longest spinning time to remove the bubbles, even though the rotor can be spun approximately 30% faster than the rotor in the other cases. Case #2 and case #3 both require about the same amount of spinning time, but case #3 involves trimming away half of the spun PDMS. Thus, case #2 is probably the best option from a spinning and degassing perspective. That said, case #2 with the larger rotor diameter than case #1 could have more material/thermal mass than case #1, which could translate into longer curing times. To avoid this problem, a removable sub-mold assembly might be designed to be spun at a fixed distance away from center axis of rotation. After spinning, this sub-mold assembly could be removed and cured in a heating and cooling station without having to heat and cool the entire thermal mass of the spinning rotor.

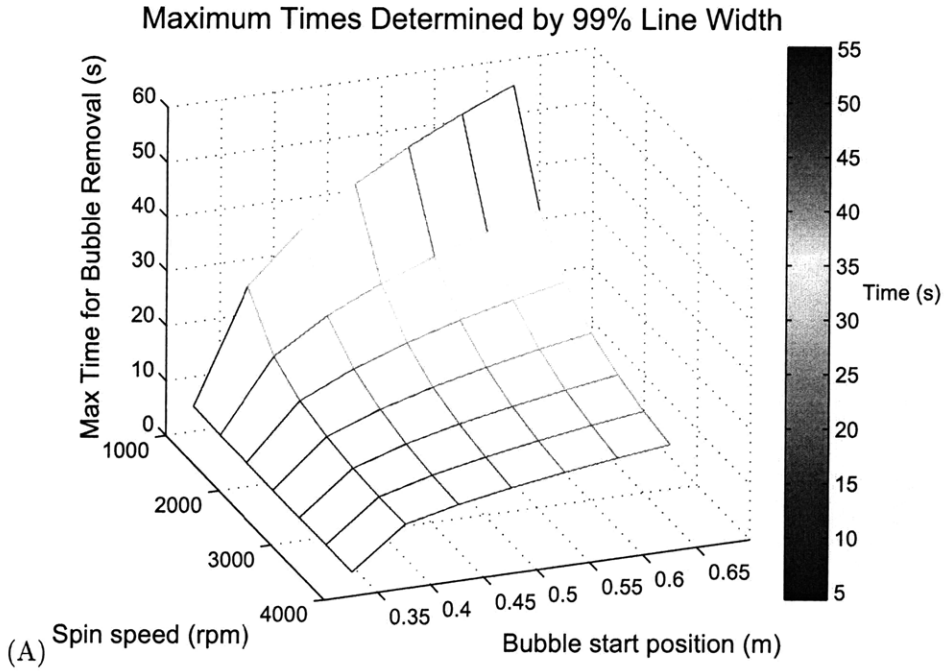

(A)

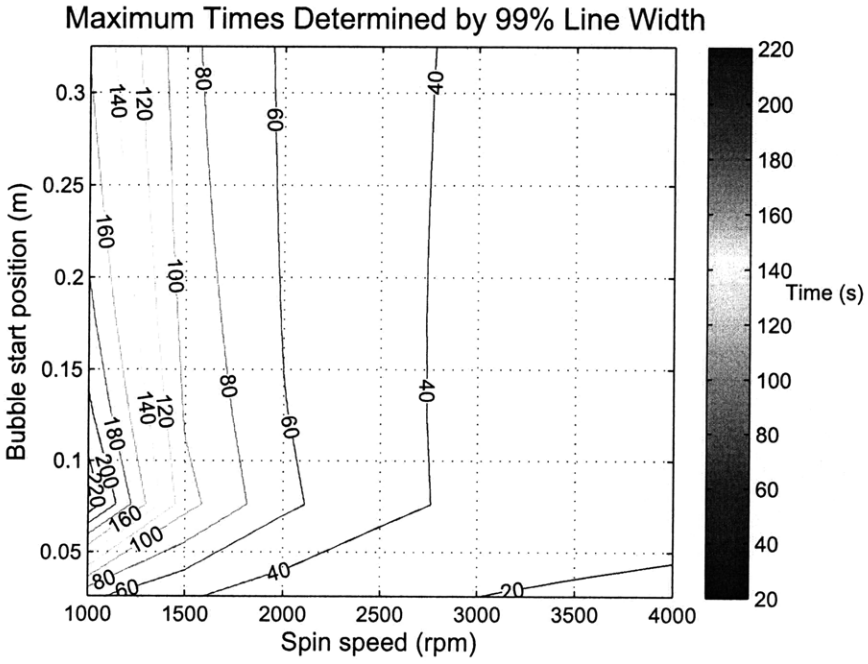

(B)

Figure 5-18: Simulated times for bubbles to be removed from PDMS plotted against set spin speeds and bubble starting positions. Simulations are for the scenario with a 60 cm x 30 cm part and a spinning rotor with large outer radius. (A) 3-D depiction of simulated results. (B) Contour representation of the same numerical results.

Chapter 6

Conclusions

This thesis has reviewed typical PDMS prototyping processes for the production of micro and nano features and has suggested novel methods for improving the quality and rate of production efforts. With respect to rate of PDMS device production, the two main time-limiting steps in the typical prototyping process are degassing (bubble removal) and curing. This thesis has introduced bubble removal via a new centrifugal casting procedure, along with a thermal management system for curing.

6.1 Contributions

The main contribution of this work is the application of centrifugal casting to PDMS micro and nano replication. The idea was conceived in a matter of minutes when AJ Schrauth suggested spinning the PDMS. The proof-of-concept experiments followed, and centrifugal casting now appears to be a viable method for degassing and molding micro/nano featured components. Through study and experimentation, this thesis has specifically contributed to improving the rate of PDMS component production, simultaneously molding multiple sides of a part, and predicting the amount of time required to spin the polymer given a number of parameters.

6.1.1 Rate

In the outlined centrifugal casting process for this thesis, the resin is mixed and poured into a mold reservoir, which is then spun at thousands of revolutions per minute for times ranging from 30 seconds (not including deceleration time) to a few minutes. For example, a bubble-

free part can be produced with a total spin time of only 45 seconds (30 seconds of energized spinning and 15 seconds of deceleration) and set spin speed of 7000 rpm. This total spin time of 45 seconds is approximately 5-15 times faster than degassing methods typically employed using a vacuum chamber. An example part, which was degassed in less than a minute is shown in Figure 4-29 D with some of its micro features displayed in Figure 5-3. Using higher spin speeds, it should be possible to further reduce the amount of spinning/degassing time required to produce bubble-free parts.

In addition to improving the production rate through bubble removal improvements provided by centrifugal casting, a novel thermal management system was designed and demonstrated for quickly curing PDMS parts. Using this thermal management system, high-temperature processing ($\sim$ 100 °C) was performed to cure PDMS parts in 8 minutes. With just a hot plate, PDMS parts have been exposed up to almost 300 °C during the curing process. Puddles of PDMS Sylgard 184 have been cured in 30 seconds (see Figure 2-11). To the author's knowledge, no other research groups have demonstrated PDMS curing of micro/nano features in less than 10 minutes [92]. However, silicone injection molders are well-aware of the potential to cure silicone products rapidly. Jefferson Rubber Works, Inc. claims that its average cycle time for silicone molding ranges between 25 to 50 seconds [9]. Thus, high-temperature processing of PDMS has the potential to improve the rate of microfluidic device production, but further work needs to be done to thoroughly understand resulting shrinkage and distortion in quickly cured PDMS parts [78, 115].

6.1.2 Quality

Centrifugal casting and fast curing has been applied to a mini manufacturing run of 20 parts with channel widths of approximately 50 μm and channel heights of approximately 40 μm. The parts were spun for less than 2 minutes with a top spin speed of 7000 rpm. After being degassed, the parts were then cured in 8 minutes with a maximum temperature of approximately 100 °C. A corresponding section on each part was measured, and the resulting standard deviations for the width and height measurements were sub-micron. For these 20 parts, only one bubble was observed within the specified region of interest.

6.1.3 Double-sided parts

The centrifugal casting process permits the simultaneous patterning of multiple surfaces of a part. The need for a large free surface (almost half the total surface area of a typically cast PDMS part for microfluidic applications) for bubble escape is eliminated. The thickness of a designed part can also be precisely controlled without the need for measuring the volume of dispensed PDMS. Centrifugal casting also has the potential to eventually produce the control-flow architecture utilized by Quake and others [110, 107].

6.1.4 Bubble behavior modeling

Two different but similar models have been explored to predict the amount of time required to produce bubble-free parts given the spin speed profile, geometry considerations, and fluid properties. In the first model, buoyant forces are balanced against drag forces on a bubble to predict the bubble's speed at any given location. The mass of the bubble is assumed to be constant throughout its journey toward the center axis of rotation, although the bubble diameter can change given the fluid pressure surrounding the bubble [106]. These bubble speeds can be integrated to calculate the bubble's position as time progresses. Using this method, it is possible to determine the amount of time required for a bubble of a given size at a specified location to exit the molding region of interest. Combining this modeling technique with experimental results, it is then possible to predict time requirements for spinning the resin within a given mold geometry at different spin speeds based on the experimentally derived critical bubble diameter (see Figure 4-24) for a specified starting bubble location.

The second model uses the same buoyancy and drag principles as the first model but adds one more important property; a bubble can lose or gain air by diffusion, and the gain or loss of air is dependent on the concentration gradient between the air concentration in the bubble wall and the air concentration in the PDMS solution surrounding the bubble. If the air concentration in the bubble wall is greater than in the surrounding solution, the bubble will shrink and eventually dissolve. The air concentration in the bubble wall is determined by the pressure within the bubble and Henry's Law.

Because centrifugal casting leads to pressurizing the fluid surrounding and the air within trapped bubbles without increasing the air concentration in the bulk of the PDMS, the concentration of gas in the bubble wall increases according to Henry's Law. Thus, unless

the bulk PDMS started out supersaturated with air, all bubbles will diffuse air into solution. That said, a bubble in a spinning solution is moving toward the center axis of rotation, and the pressure surrounding the bubble decreases as the bubble gets closer to the center. So, it is possible for the volume of the bubble to actually increase even though its actual mass is decreasing, if the bubble is moving fast enough toward the center axis of rotation.

A model has been developed to capture the combined buoyancy, drag, and diffusion effects, which predicts the time required for bubbles to either dissolve into solution or leave the region of interest with a given spin profile and bubble starting location. This model is implemented numerically and only requires solving a pair of 1st-order non-linear differential equations. The numerical implementation was performed in MATLAB, and the code is included within the appendix of this thesis. Both the model and numerical implementation were verified using high speed video imaging and a designed set of experiments.

6.2 General principles

The simulated time predictions for bubble removal in centrifugal casting have been applied to a single liquid resin (PDMS) and a few different geometries. Predictions for other resins could be made by changing the fluid properties, which would affect bubble speeds or diffusion rates. For example, lower viscosities would lead to faster traveling bubbles and reduced spin times. Higher Henry's coefficients would lead to higher concentration gradients, which would lead to faster bubble dissolution assuming no change to the diffusion coefficient and an initial non-supersaturated fluid state. A larger diffusion coefficient would also lead to faster bubble dissolution if the solution is initially in a non-supersaturated state. Predictions for varied geometries can be performed as shown in Section 5.3.

To provide more physical understanding for the cause and effect relationships concerning diffusion and bubble speed modeling, the numerous equations used in this thesis can be summarized in Table 6.1.

Table 6.2 shows the physical properties for the variables, which play a role in describing the relationships for centrifugal bubble removal. These relationships help describe the balance that exists between bubble dissolution and buoyant forces carrying bubbles out of solution. Changing parameters that make both dr/dt and dR/dt more negative will tend to decrease the time for bubble removal. Changing parameters that make both dr/dt and dR/dt

Table 6.1: General equations that govern the time required for bubble removal in centrifugal casting.

Name	Equation
Bubble speed	$\frac{dr}{dt} \propto -\frac{\rho_f g_r}{\mu} R^2$
Centrifugal gravity	$g_r = r\omega^2$
Bubble radius	$R \propto \frac{1}{\sqrt[3]{p}}$
Pressure of surrounding fluid	$p \propto \rho_f \left(r^2 - r_{fstart}^2\right) \omega^2$
Rate of diffusive bubble growth or shrinkage	$\frac{dR}{dt} \propto -\sigma p \kappa k_D \left\{\frac{1}{R} + \frac{1}{(\pi\kappa t)^{1/2}}\right\}$
Maximum rotor stress	$T_{max} \propto r_o \omega^2$.

Table 6.2: Variables associated with dominant physical properties for centrifugal bubble removal.

Variable	Property
r	Bubble's distance from axis of rotation (m)
R	Bubble radius (m)
p	Liquid pressure surrounding bubble (Pa)
ρ_f	Liquid density (kg/m^3)
μ	Liquid viscosity (Pa s)
ω	Spin speed (rad/s)
g_r	Centrifugal acceleration (m^2/s)
$\frac{dr}{dt}$	Bubble speed relative to axis of rotation (m/s)
r_{fstart}	Liquid-air interface's distance from axis of rotation (m)
$\frac{dR}{dt}$	Bubble radius rate of change (m/s)
t	Time (s)
σ	Liquid-air surface tension (N/m)
κ	Diffusion coefficient (m^2/s)
k_D	Henry's coefficient (kg gas/ (m^3 polymer Pa))
T_{max}	Maximum radial or circumferential stress in the rotor (Pa)
r_o	Outer diameter of rotor (m)

get closer to zero (less negative) will tend to increase the time for bubble removal. Changing parameters that will make either dr/dt and dR/dt more negative while not affecting the other one will also decrease the amount of spin time required.

6.3 Future work

Centrifugal casting research has been a field of study for many years. However, the numerical method outlined in this thesis for predicting spin times based on bubble diffusion and bubble buoyancy is new. This work also appears to be the first attempt to use centrifugal casting for the production of micro and nano featured components. In addition, a novel ther-

mal management system to assist the centrifugal casting system in part production holds potential. One of the aspirations for this work is that centrifugal casting and fast curing may find a way to improve the molding of micro and nano featured components. In an effort toward improving the centrifugal casting process for micro and nano featured components, here are a few suggested topics for future work.

6.3.1 Shrinkage and distortion with high temperature curing

High temperature curing and centrifugal casting are promising techniques for PDMS micro/nano feature production. However, additional work needs to be performed to better characterize shrinkage and/or thermal degradation of the material as it is exposed to temperatures higher than those used by the microfluidic device prototyping community. Eehern Wong in the MIT Laboratory for Manufacturing and Productivity is currently studying PDMS distortion and shrinkage by numerically simulating the curing behavior and heat generation of PDMS.

In addition to distortion and shrinkage, the biocompatibility and bondability of PDMS with other materials should be explored for PDMS cured at higher temperatures than those typically used by the microfluidics community. It may turn out that high temperature curing is good for high throughput, but that it alters the functionality of the material. It may be necessary to apply high temperature curing only long enough to partially cure the material. If the material remains a little tacky after being partially cured at a high temperature, it may bond better to a glass slide or another substrate.

6.3.2 Material selection

PDMS was selected for this thesis because of its widespread use in micro and nano technology applications. In the future, there is no reason centrifugal casting and fast curing could not be applied to other thermosetting resins such as acrylates and urethanes. With proper high melt flow index thermoplastics, centrifugal casting might also be applied for producing micro and nano featured components. Finally, biomaterials, composites, ceramics, or even shape memory polymers (inspired by Vikas Srivastava's recent work) might be potentially utilized with centrifugal casting. Centrifugal casting has already been applied to some of these materials, but improvements can be made, along with adaptations for micro and nano scaled features.

6.3.3 Thin part production

As explained in Figure 1.7, one of the objectives of this work is to develop double-sided patterning capability to facilitate the production of multi-layered devices. While this work has demonstrated the capability of producing functioning microfluidic devices and components with intentional features on multiple sides, not much effort has been expended in attempting to make a multi-layered functioning device with centrifugal casting. To make multi-layered functioning devices with centrifugal casting, demolding of thin layers of PDMS needs to be furthered explored. Work by Sriram Krishnan explored demolding of very thin layers of spin-coated PDMS [73], but demolding PDMS sandwiched between two hard molds is probably going to have a better chance of success using some sort of liquid parting method [64, 65].

6.3.4 Process control

This thesis covers the process shown in Figure 1-4. With the addition of a fast part measuring method, it should be possible to implement a process control manufacturing system similar to the one shown in Figure 6-1. In process control manufacturing with cycle-to-cycle feedback, a completed part is measured and then controller parameters are adjusted for the next part [56].

In the proposed system in Figure 6-1, the one major missing link is part measurement method for characterizing shrinkage. In reality, there could be a variety of methods for characterizing part shrinkage. On the macro scale, it might be possible to measure the outer dimensions of the part to characterize a certain degree of shrinkage with calipers or some other handheld measuring device. On the micro/nano scale, it might be possible to use an optical profilometer to take in-process measurements. Brian Anthony and others have been working on methods for fast in-process measurements, such as using a flatbed scanner to image micro features [51].

6.3.5 Numerical modeling

The modeling of the combined diffusion and buoyancy forces acting on the bubble ignores advection. Bubbles traveling with some speed through a medium are expected to have higher air diffusion rates than those predicted by the Epstein-Plesset bubble dissolution model [39].

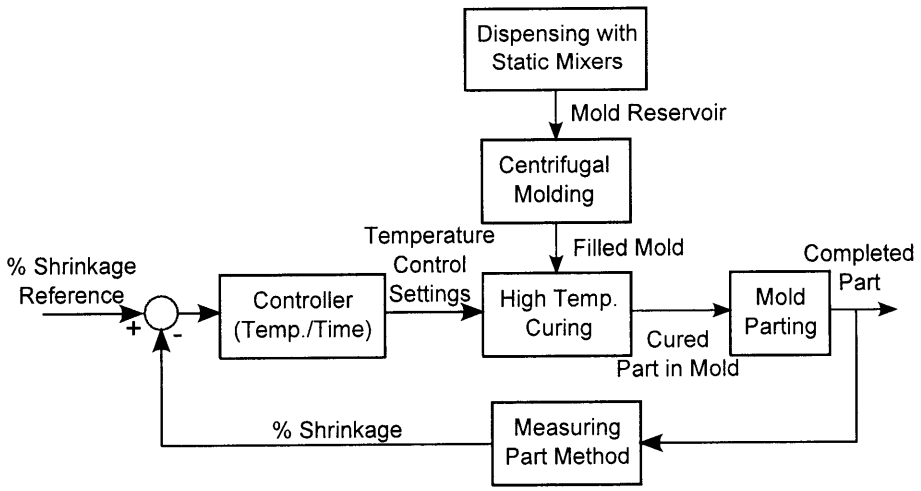

Figure 6-1: Idealized centrifugal process with cycle-to-cycle process control.

Additional work could incorporate a more complex model for more accurate into making spin time predictions. Better numerical methods or modeling could also be employed to explain the bubble growth behavior recorded in Section 3.4.4. Changes in viscosity and elasticity during PDMS curing went unmodeled in this work, but could also be incorporated into future models.

6.3.6 Simultaneous curing and spinning

To avoid the opportunity for bubbles to form when the spinning PDMS decelerates and depressurizes, simultaneously curing the PDMS while spinning may prove useful. In the centrifugal casting of thermoplastics, the thermoplastic is effectively cured by cooling down the mold assembly during spinning. To parallel the thermoplastic hardening performed by cooling, there are a variety of ways thermoset curing might be performed during spinning. One of which is simply placing the spinning region in a heated oven. Another might be to pass electrical wiring through a rotary junction to power heaters being spun within the rotor.

6.3.7 Mold handling improvements

The centrifugal casting system is a good prototype wok cell capable of producing approximately 6 parts per hour by running three cycles (two parts per cycle). With a spin time as low as 30 seconds and a curing time of approximately 8 minutes, the rest of the cycle time

(approximately 10 minutes) is spent dispensing, handling the mold assembly, and demolding the part. These three additional aspects of the PDMS processing cycle could be improved, especially the handling of the mold assembly. The current mold assembly design requires that 12 bolts be screwed and unscrewed either manually or with an electrical drill to clamp and unclamp the two mold halves used in the mold assembly. There should be a better way to engineer a quick clamping mechanism that can keep the mold halves together without the need for tightening and loosening so many bolts.

6.3.8 Air concentration adjustments

In thermosetting manufacturing production, vacuum reservoirs are often used for storing the thermosetting resin ingredients [8]. In the numerical simulations of this thesis, PDMS was assumed to be slightly supersaturated (5%) with dissolved air at the start of spinning. By having the PDMS constituents in vacuum reservoirs before dispensing and spinning the PDMS, the initial dissolved air content could be significantly less, which would result in faster bubble dissolution of newly entrapped bubbles during spinning.

6.3.9 Energy/ecological footprint analysis

A cursory energy consumption analysis was performed in Section 1.6.4 to estimate the cost of energy being consuming during the centrifugal casting cycle. However, it would be possible to measure the actual electrical consumption of the manufacturing process during molding using methods proposed by Tim Gutowski and others [47]. In addition, it would be interesting to look at the ecological footprint of producing micro and nano featured PDMS devices with special consideration for the synthesis of the PDMS constituents, along with the final disposal of the PDMS. PDMS is a thermosetting resin, which means it is not easily recycled.

6.4 Closing remarks

George Whitesides has said, "there will probably be several such technologies [for microfluidic device manufacturing], but in the early stages the definition of a single set of materials and processes to convert laboratory demonstrations into working commercial devices is an important step [114]." Centrifugal casting and fast curing are a new set of processes for

PDMS and possibly other materials that hold the potential of bringing microfluidics closer to successful commercialization. In addition to helping microfluidics grow, centrifugal casting will hopefully allow chemists and biologists to create micro or nano devices that were not before possible.

Appendix A

MATLAB Code

This section contains some of the MATLAB code generated for modeling bubble velocities in a centrifuge and modeling bubble growth using the Epstein-Plesset model. Only code that can run on its own has been included. Each section requires that all the subsections be included in the same file directory/folder in order for the code to run properly. It should be possible to copy and paste the code into appropriately named files and generate results in a matter of minutes. Other lines of code for processing high speed video, temperature, LabView, or Zygo profilometer data were generated but are not included in this appendix. For further information or to make suggestions, please feel free to contact the author.

A.1 Epstein-Plesset bubble growth

The following two subsections contain a MATLAB script and a function for calculating bubble growth or dissolution given a set of specified c_f parameters (see Section 3.3.2), initial bubble diameter, surface tension of the liquid, pressure of the solution, the Henry's coefficient, and the diffusion coefficient. By copying and pasting the following subsections into two files, it is possible to make bubble growth/shrinkage predictions in a few minutes.

A.1.1 simplified_epstein_plesset_script_without_ode45.m

```
%Script for simulating Epstein-Plesset bubble modeling with surface tension
%% Initialization
clc
clear all;
close all;
c_f=[1.00]; %Ratio of c_i to c_sinfty
%% Cycle through values of c_f
for i=1:length(c_f),
tspan = [.00001 5000]; %s Time
```

```
x0 = 50e-6; %m Initial Radius
B=8.314; %J/(mol K) Universal Gas Constant
T=273+25; %K Temperature
sigma=0.02; %N/m Surface Tension
kappa=1.47e-9; %m^2/s Diffusion Coefficient
p=101.3e3; %Pa Pressure surrounding system
HenryCoef=78.08/100*1.567e-6+20.95/100*3.158e-6+...
0.93/100*4.506e-6; %kg/m^3/Pa
M=28.97/1000; %kg/1000mol
d=HenryCoef*B*T/M;
%% Non-Runge-Kutta Solver (Eulerian)
dt=0.001;
t=tspan(1):dt:tspan(2);
x=zeros(1,length(t))+x0;
dxdt=zeros(1,length(t));
for j=1:(length(t)-1),
dxdt(j)=simplified_epstein_plesset_ode(t(j), x(j), c_f(i),...
sigma, kappa, p, HenryCoef, M, T);
x(j+1)=dxdt(j)*dt+x(j);
end
%% Temporarily store data for given c_f
tsave(i).Data=t;
xsave(i).Data=x;
%Calculate times required for bubble to reach 10*Ro, 50 microns, or
%dissolve
if mean(xsave(i).Data)>x0,
t_10Ro(i)=interp1(xsave(i).Data,tsave(i).Data,10*x0);
t_50microns(i)=interp1(xsave(i).Data,tsave(i).Data,50e-6);
else
t_o(i)=tsave(i).Data(min(find(xsave(i).Data<=0)));
end
end
%% Plot Results
figure
for i=1:length(c_f),
if mean(xsave(i).Data)<x0,
DissolutionIndices=find(tsave(i).Data<=t_o(i));
plot(tsave(i).Data(DissolutionIndices),...
xsave(i).Data(DissolutionIndices),'.-')
else
plot(tsave(i).Data,xsave(i).Data,'.-')
end
title(['Initial Bubble Radius=',num2str(x0*1e6),' \mum'])
hold on
set(gca,'FontSize',12)
xlabel('Time (s)','FontSize',14)
ylabel('Radius (m)','FontSize',14)
end
```

A.1.2 simplified_epstein_plesset_ode.m

```
function dxdt = ...
simplified_epstein_plesset_ode(t, x, c_f, sigma, kappa, p, ...
HenryCoef, M, T)
%Epstein-Plesset Bubble ODE with surface tension
B=8.314; %J/(K mol) Universal Gas Constant
rho_inf=M/(B*T)*p; %kg/m^3 Density of air in system (not within bubble)
c_sinfty=HenryCoef*p; %kg/m^3 Concentration of air in wall of bubble with
%infinite radius
Tau=2*M*sigma/(B*T);
dxdt=kappa*(c_sinfty*(c_f-1)-2*HenryCoef*sigma./x)./...
(rho_inf+1*Tau./(3*x)).*(1./x+1./(pi*kappa.*t).^0.5); %Rate of change
%in bubble radius
if x<=0,
dxdt=0;
end
```

A.2 Bubble time for exit without diffusion

This set of MATLAB scripts calculates the time required to remove bubbles during centrifugal casting assuming the bubbles do not dissolve or grow by diffusion (see Section 4.3 and Section 4.5.1). By copying and pasting the following subsections into three files, it is possible to make predictions for the amount of spinning time required to remove bubbles for specified initial bubble sizes.

A.2.1 time_crit_center_diameter_with_slew.m

```
%Script for plotting time for bubble to exit solution against set
%spin speed with a spin speed profile assuming no diffusion.
clear all;
close all;
bubble_start_pos=0.0615; %Dist from center axis (m)
bubble_end_pos=0.0343; %Dist from center axis (m)
rfstart=bubble_end_pos; % Liquid-air interface (m)
T=298; %Temperature (K)
sigma=.02; %Surface tension (N/m)
mu=3900*1e-3; %Dynamic viscosity (Pa s)
rhof=1030; %Density (kg/m^3)
spin_speed=[500:100:10000]; %Set spin speeds (rpm)
Patm=101.3e3; %Atmospheric Pressure (Pa)
phi=0; %Mold tilt angle (rad)
Pcham=Patm; %System pressure surrounding centrifuge assembly (Pa)
slewrate=300; %Acceleration slew rate for centrifuge (rpm/s)
offset=100; %Initial centrifuge speed at time=0 (rpm)
Dc=4*pi*mu; %Drag term. If Dc=6*pi*mu, Stoke's flow around sphere.
do=[80e-6:20e-6:160e-6]; % (m) Initial bubble diameter at ...
for i=1:length(do),
i
for j=1:length(spin_speed),
[xspeed(i,j),yspeed(i,j),d_start(i,j), rhoa(i,j), Vb(i,j),...
gr(i,j),Pb(i,j), Pfluid(i,j)]=...
bubble_speed(spin_speed(j),do(i),bubble_start_pos,rfstart,...
T,phi,mu,sigma,Pcham,rhof,Dc);
[time_to_exit(i,j), r_bubble, ...
spinspeedprofile(i,j).Data, ...
timeforspinspeedprofile(i,j).Data]=...
bubble_exit_time_func_with_slew(spin_speed(j),...
do(i),bubble_start_pos,...
rfstart,T,mu, sigma, Pcham, rhof,slewrate,offset,Dc);
end
end
for i=1:length(do)
figure(1)
plot(spin_speed,d_start(i,:),'.-')
text(spin_speed(1)-300,d_start(i,1)+0.5e-6,...
['d_o=',num2str(do(i)*1e6),'\mum'],'FontSize',12)
hold on
xlabel('Spin Speed (rpm)','FontSize',14)
ylabel('Pressurized Bubble Diameter (m)','FontSize',14)
set(gca,'FontSize',14)
figure(2)
plot(spin_speed,time_to_exit(i,:),'.')
text(spin_speed(1)-300,time_to_exit(i,1),...
['d_o=',num2str(do(i)*1e6),'\mum'],'FontSize',12)
hold on
xlabel('Spin Speed (rpm)','FontSize',14)
ylabel('Time for Bubble to Exit (seconds)','FontSize',14)
set(gca,'FontSize',14)
end
```

A.2.2 bubble_exit_time_func_with_slew.m

```
function [time_to_exit, r_bubble, spinspeedprofile, timeforspinspeedprofile]=...
bubble_exit_time_func(spin_speed,do,rbstart,rfstart,T,mu,...
sigma, Pcham, rhof, slewrate,offset,Dc)
%This function outputs the time required for a bubble to leave the region
%of interest. It makes use of bubble_speed4.m
gb=9.8; %m/s^2
R=8.314; %Ideal Gas Constant m^3 Pa /(K mol)
Rs=287.05; %Specific gas constant J/(kg K)
bi=do/2; %Initial bubble radius (m)
Ti=273+25; %K
Pchami=Pcham; %Absolute Pressure (Pa)
ro=rfstart; %Initial bubble starting position relative to center (m)
Pair=0;
N=spin_speed;
phi=0;
dt=1;
bubble_exit=0;
r_bubble(1)=rbstart;
i=1;
current_time=0;
timeforspeedprofile(i)=current_time;
spinspeedprofile(i)=0;
while bubble_exit==0,
est_spin_speed=slewrate*current_time+offset;
if est_spin_speed>spin_speed,
est_spin_speed=spin_speed;
end
[xspeed(i),yspeed(i),d(i), rhoa(i), Vb(i), gr(i),Pb(i), Pfluid(i) ]=...
bubble_speed(est_spin_speed,do,r_bubble(i),rfstart,T,phi,mu, sigma, ...
Pcham, rhof,Dc);
r_bubble(i+1)=r_bubble(i)-xspeed(i)*dt;
current_time=current_time+dt;
i=i+1;
timeforspinspeedprofile(i)=current_time;
spinspeedprofile(i)=est_spin_speed;
if r_bubble(i)<=rfstart,
bubble_exit=1;
end
end
time_to_exit=current_time;
```

A.2.3 bubble_speed.m

```
function [xspeed,yspeed,d, rhoa, Vb, gr,Pb, Pfluid ]=...
bubble_speed(spin_speed,do,r,rfstart,T,phi,mu, sigma, Pcham, rhof,Dc)
%Bubble speed output (m/s) for a given spin speed (rpm), initial bubble
%diameter (m) at Pcham, distance from center axis of rotation (m), distance
%of fluid start from center of axis of rotation (m), Temperature T
%in Kelvin, phi is in radians, mu is in Pa s, sigma is in N/m, rhof is in
%kg/m^3.
gb=9.8; %m/s^2
R=8.314; %Ideal Gas Constant m^3 Pa /(K mol)
Rs=287.05; %Specific gas constant J/(kg K)
bi=do/2;
Ti=273+25; %K
Pchami=Pcham; %Absolute Pressure (Pa)
ro=rfstart;
length_r=length(r);
Pair=0; %Pressure due to air at liquid-air interface (Pa)
N=spin_speed;
w=N*2*pi/60; %0*2*pi/60; %rad/s
%Calculations
for i=1:length(w)
Pgb(:,i)=rhof*gb*sin(phi)*(r-rfstart);
Pfluid(:,i)=Pcham+Pgb(:,i)+Pair+1/2*rhof*w(i).^2*(r.^2-rfstart^2);
%Assumes density of air has negligible effect
%Calculate initial pressure inside bubble and moles of gas in bubble
Pbi=2*sigma./bi+Pchami; %Pa
Vbi=4/3*pi*bi.^3; %m^3
```

```
n=Pbi.*Vbi./(R.*Ti);
%Calculate internal bubble pressure
Pb(:,i)=2/3*sigma./n./R./T*2.^(1/3).*...
(pi.*(9.*Pfluid(:,i)+(-(128.*pi*sigma^3-81.*...
n.*R.*T.*Pfluid(:,i).^2)./n./R./T).^(1/2)).*...
n.^2.*R^2.*T.^2).^(1/3)+8/3*pi*sigma.^2*2.^(2/3)./...
(pi.*(9.*Pfluid(:,i)+...
(-(128*pi*sigma^3-81.*n.*R.*T.*Pfluid(:,i).^2)./n./R./T).^(1/2)).*...
n.^2*R.^2*T.^2).^(1/3)+Pfluid(:,i);
Vb(:,i)=n*R*T./(Pb(:,i));
b(:,i)=(3*Vb(:,i)./(4*pi)).^(1/3);
rhoa(:,i)=Pb(:,i)./(Rs*T); %kg/m^3
gr=r.*w(i).^2; %m/s^2
vxss(:,i)=(rhoa(:,i)-rhof).*...
(gb*sin(phi)+gr.*cos(phi))./Dc.*(4*pi/3).^(1/3).*Vb.^(2/3);
vyss(:,i)=(rhof-rhoa(:,i)).*...
(gb*cos(phi)+gr.*sin(phi))./Dc.*(4*pi/3).^(1/3).*Vb.^(2/3);
end
xspeed=-vxss;
yspeed=vyss;
d=2*b;
```

A.3 Centrifugal bubble velocity with diffusion

The following three subsections contain a MATLAB script and three MATLAB functions for calculating the bubble velocities in a spinning body of fluid. The bubble velocity model outlined in this thesis is utilized and combined with the Epstein-Plesset model for bubble diffusion. By copying and pasting the four files and naming the functions appropriately, it is possible to make bubble velocity/position predictions in a few minutes.

A.3.1 bubble_tracking_for_centrifugal_casting_with_diffusion.m

```
%Script for plotting position of a bubble moving from the outer edge to the
%inner edge of part being spun in a centrifuge, along with a variety of
%other parameters. Models bubble velocities and their diffusional growth or
%shrinkage using the Epstein-Plesset model.
%Requires three additional functions:
% bubble_exit_time_func_with_slew_and_diffusion_speed_factor.m
% bubble_speed_with_epstein_plesset_diffusion_func_speed_factor.m
% delta_m_epstein_plesset_ode.m
%Last modified by Aaron Mazzeo on 3-27-09
clear all;
close all;
clc
bubble_start_pos=0.0615; %Dist from center axis (m)
bubble_end_pos=0.0343; %Dist from center axis (m)
rfstart=bubble_end_pos; % (m) 1.404 in = 0.0357 (m)
T=298; %Temperature during spin assuming initial bubble diameter
%was at 298 K
sigma=.02; %Surface tension of PDMS (N/m)
mu=3900*1e-3; %Dynamic viscosity of PDMS (Pa s)
rhof=1030; %Density of PDMS (kg/m^3)
Patm=101.3e3; %Atmospheric pressure (Pa)
phi=0; %Tilt angle of mold
Pcham=Patm;
spin_speed=[1000 2000 4000 8000]; %Max spin speeds (rpm)
slewrate=300; %Constant angular acceleration until reaching
%max speed (rpm/s)
offset=100; %Spin speed at time=0 (rpm)
kappa=1.47e-9; %Diffusion Coefficient (m^2/s)
HenryCoef=78.08/100*1.567e-6+20.95/100*3.158e-6+0.93/100*4.506e-6; %Henry's
```

```
% coefficient (%kg (gas)/m^3 (polymer)/Pa)
M=28.97/1000; %Molecular weight of air (kg/mol)
c_f_init=1.05% Initial fraction of air saturation in PDMS (c_f is defined
%in thesis)
dt=0.01; %Time step for each numerical step (s)
Dc=2; %Dc parameter as defined in thesis and is related to drag on a sphere
speed_factor=0; %Extra speed_factor parameter for estimating effect of
%convection on mass diffusion into or out of a bubble.
do=[75e-6 100e-6 0.000132118527930570 157.2e-6 0.000165322774052620 ...
0.000166241230964661 175e-6 200e-6 250e-6]; % (m) Initial bubble
%diameters at atmospheric pressure.
for i=1:length(do),
i
for j=1:length(spin_speed),
[time_to_exit(i,j), r_bubble, ...
spinspeedprofile(i,j).Data, ...
timeforspinspeedprofile(i,j).Data, ...
d(i,j).Data,c_f(i,j).Data]=...
bubble_exit_time_func_with_slew_and_diffusion_speed_factor(...
spin_speed(j),...
do(i),bubble_start_pos,...
rfstart,T,mu, sigma, Pcham, rhof,slewrate,offset,...
HenryCoef,M,kappa,c_f_init,dt,Dc,speed_factor);
r_bubbledata(i,j).Data=r_bubble;
end
end
save centrifugal_modeling_data_with_diffusion
%% Load and Plot Data
close all;
clear all;
clc
load centrifugal_modeling_data_with_diffusion
for i=1:length(do)
figure(2)
plot(spin_speed,time_to_exit(i,:),'.')
text(spin_speed(1)-300,time_to_exit(i,1),...
['d_o=',num2str(do(i)*1e6),'\mum'],'FontSize',12)
hold on
xlabel('Spin Speed (rpm)','FontSize',14)
ylabel('Time for Bubble to Exit (seconds)','FontSize',14)
grid on
set(gca,'FontSize',14)
end
figure(3)
plot(timeforspinspeedprofile(1,1).Data,spinspeedprofile(1,1).Data)
xlabel('Time (s)')
ylabel('Spin Speed (rpm)')
title('Spin Profile for first d_o and first spin speed')
set(gca,'FontSize',12)
grid on
figure(4)
for i=1:length(do),
for j=1:length(spin_speed)
subplot(length(spin_speed)/2,length(spin_speed)/2,j)
timeforspinspeedprofiletemp=timeforspinspeedprofile(i,j).Data;
dtemp=d(i,j).Data;
plot(timeforspinspeedprofiletemp,dtemp*1e6,...
'-.','LineWidth',3)
xlabel('Time (s)','FontSize',14)
ylabel('Bubble Diameter (\mum)','FontSize',14)
set(gca,'FontSize',14)
hold on
endpointlength=length(dtemp);
endpoint=dtemp(endpointlength);
text(max(timeforspinspeedprofile(i,j).Data),endpoint*1e6-2,...
['d_o=',num2str(do(i)*1e6,4), '\mum'])
title(['Spin Speed=',num2str(spin_speed(j)),' RPM'])
grid on
end
end
figure(5)
for i=1:length(do),
for j=1:length(spin_speed)
subplot(length(spin_speed)/2,length(spin_speed)/2,j)
r_bubbledatatemp=r_bubbledata(i,j).Data;
```

```
dtemp=d(i,j).Data;
%dtemp=[dtemp dtemp(length(dtemp))];
plot(r_bubbledatatemp(1:length(dtemp)),dtemp*1e6,...
'-.','LineWidth',3)
xlabel('Bubble Position (m)','FontSize',14)
ylabel('Bubble Diameter (\mum)','FontSize',14)
set(gca,'FontSize',14)
hold on
endpointlength=length(dtemp);
endpoint=dtemp(endpointlength);
text(min(r_bubbledata(i,j).Data),endpoint*1e6-2,...
['d_o=',num2str(do(i)*1e6,4), '\mum'])
title(['Spin Speed=',num2str(spin_speed(j)),' RPM'])
grid on
end
end
figure(6)
for i=1:length(do),
for j=1:length(spin_speed)
subplot(length(spin_speed)/2,length(spin_speed)/2,j)
timeforspinspeedprofiletemp=timeforspinspeedprofile(i,j).Data;
c_ftemp=c_f(i,j).Data;
plot(timeforspinspeedprofiletemp,c_ftemp,...
'-.','LineWidth',3)
xlabel('Time (s)','FontSize',14)
ylabel('c_f','FontSize',14)
set(gca,'FontSize',14)
hold on
endpointlength=length(c_ftemp);
endpoint=c_ftemp(endpointlength);
text(max(timeforspinspeedprofile(i,j).Data),endpoint,...
['d_o=',num2str(do(i)*1e6,4), '\mum'])
title(['Spin Speed=',num2str(spin_speed(j)),' RPM'])
grid on
end
end
figure(7)
for i=1:length(do),
for j=1:length(spin_speed)
subplot(length(spin_speed)/2,length(spin_speed)/2,j)
r_bubbledatatemp=r_bubbledata(i,j).Data;
c_ftemp=c_f(i,j).Data;
%c_ftemp=[c_ftemp c_ftemp(length(c_ftemp))];
plot(r_bubbledatatemp(1:length(c_ftemp)),c_ftemp,...
'-.','LineWidth',3)
xlabel('Bubble Position (s)','FontSize',14)
ylabel('c_f','FontSize',14)
set(gca,'FontSize',14)
hold on
endpointlength=length(c_ftemp);
endpoint=c_ftemp(endpointlength);
text(max(r_bubbledata(i,j).Data),endpoint,...
['d_o=',num2str(do(i)*1e6,4), '\mum'])
title(['Spin Speed=',num2str(spin_speed(j)),' RPM'])
grid on
end
end
figure(8)
for i=1:length(do),
for j=1:length(spin_speed)
subplot(length(spin_speed)/2,length(spin_speed)/2,j)
timeforspinspeedprofiletemp=timeforspinspeedprofile(i,j).Data;
r_bubbledatatemp=r_bubbledata(i,j).Data;
plot(timeforspinspeedprofiletemp,...
r_bubbledatatemp(1:length(timeforspinspeedprofiletemp))*1e3,...
'-.',...
[min(timeforspinspeedprofiletemp)...
max(timeforspinspeedprofiletemp)],...
[bubble_start_pos bubble_start_pos]*1e3, ...
[min(timeforspinspeedprofiletemp)...
max(timeforspinspeedprofiletemp)],...
[bubble_end_pos bubble_end_pos]*1e3,'LineWidth',3)
xlabel('Time (s)','FontSize',14)
ylabel('Position (mm)','FontSize',14)
```

```
set(gca,'FontSize',14)
hold on
endpointlength=length(r_bubbledatatemp);
endpoint=r_bubbledatatemp(endpointlength);
text(max(timeforspinspeedprofile(i,j).Data),endpoint*1e3-2,...
['d_o=',num2str(do(i)*1e6,4), '\mum'])
title(['Spin Speed=',num2str(spin_speed(j)),' RPM'])
grid on
end
end
```

A.3.2 bubble_exit_time_func_with_slew_and_diffusion_speed_factor.m

```
function [time_to_exit, r_bubble, spinspeedprofile, ...
timeforspinspeedprofile, d,c_f]=...
bubble_exit_time_func_with_slew_and_diffusion_speed_factor(...
spin_speed,do,rbstart,rfstart,T,mu,sigma, Pcham, rhof, slewrate,...
offset,HenryCoef,M,kappa,c_f_init,dt,Dc,speed_factor)
%This function outputs the time required for a bubble to leave the region
%of interest. It requires another function:
% bubble_speed_with_epstein_plesset_diffusion_func_speed_factor.m
%Created by Aaron Mazzeo
%Last updated on 3-27-09
phi=0;
bubble_exit=0;
r_bubble(1)=rbstart;
j=1;
bi=do/2;
Pbi=2*sigma./bi+Pcham; %Pa
Vbi=4/3*pi*bi.^3; %m^3
R=8.314; %Universal gas constant (J/(K mol))
n(j)=Pbi.*Vbi./(R.*T);
ntemp=n(j);
dtemp=0;
current_time=0.0001;
spinspeedprofile(j)=0;
bubble_speed(j)=0;
while bubble_exit==0, %Numerical forward time-step integration loop
est_spin_speed=slewrate*current_time+offset;
if est_spin_speed>spin_speed,
est_spin_speed=spin_speed;
end
[xspeed(j),yspeed(j),d(j), rhoa(j), Vb(j), gr(j),Pb(j), ...
Pfluid(j), c_f(j),n(j) ]=...
bubble_speed_with_epstein_plesset_diffusion_func_speed_factor...
(est_spin_speed,do,...
r_bubble(j),rfstart,T,phi,mu, sigma, Pcham, rhof,...
current_time,j, dt, HenryCoef,M,kappa,dtemp,c_f_init,Dc,...
bubble_speed(j), speed_factor,ntemp);
r_bubble(j+1)=r_bubble(j)-xspeed(j)*dt;
current_time=current_time+dt;
dtemp=d(j);
ntemp=n(j);
bubble_speed(j+1)=xspeed(j);
timeforspinspeedprofile(j)=current_time;
spinspeedprofile(j)=est_spin_speed;
j=j+1;
if (r_bubble(j)<=rfstart)||(dtemp<=0),
bubble_exit=1;
end
end
time_to_exit=current_time;
```

A.3.3 bubble_speed_with_epstein_plesset_diffusion_func_speed_factor.m

```
function [xspeed,yspeed,d, rhoa, Vb, gr,Pb, Pfluid, c_f,n ]=...
bubble_speed_with_epstein_plesset_diffusion_func_speed_factor(...
spin_speed,do,r,rfstart,T,phi,mu, sigma, Pcham, rhof, t,TimeIndex, ...
dt, HenryCoef,M,kappa,d,c_f_init,Dc,bubble_speed,speed_factor,n)
%Bubble speed output (m/s) for a given spin speed (rpm), initial bubble
%diameter (m) at P_atm, distance from center axis of rotation (m), distance
%of fluid start from center of axis of rotation (m), Temperature T
%in Kelvin, phi is in radians, mu is in Pa s, sigma is in N/m, rhof is in
%kg/m^3. This script uses the Epstein-Plesset derivation for diffusion and
%changes of bubble diameter by diffusion.
%Created by Aaron Mazzeo
%Last updated: 3-27-09
gb=9.8; %m/s^2
R=8.314; %Ideal Gas Constant m^3 Pa /(K mol)
Rs=287.05; %Specific gas constant J/(kg K)
b=d/2;
Pchami=Pcham; %Absolute Pressure (Pa)
w=spin_speed*2*pi/60; %0*2*pi/60; %rad/s
%Calculations
Pgb=rhof*gb*sin(phi)*(r-rfstart);
Pfluid=Pcham+Pgb+1/2*rhof*w.^2*(r.^2-rfstart^2);
%Assumes density of air near center axis of rotation has negligible effect
c_i=c_f_init*HenryCoef*Pchami;
c_f=c_i/(HenryCoef*Pfluid);
if TimeIndex==1,
%Calculate internal bubble pressure
Pb=2/3*sigma./n./R./T*2.^(1/3).*...
(pi.*(9.*Pfluid+(-(128.*pi*sigma^3-81.*...
n.*R.*T.*Pfluid.^2)./n./R./T).^(1/2)).*...
n.^2.*R^2.*T.^2).^(1/3)+8/3*pi*sigma.^2*2.^(2/3)./...
(pi.*(9.*Pfluid+...
(-(128*pi*sigma^3-81.*n.*R.*T.*Pfluid.^2)./n./R./T).^(1/2)).*...
n.^2*R.^2*T.^2).^(1/3)+Pfluid;
Vb=n*R*T./Pb;
b=(3*Vb./(4*pi)).^(1/3);
rhoa=Pb./(Rs*T); %kg/m^3
else
m=M*n;
dmdt=delta_m_epstein_plesset_ode_with_speed_factor(t, b, c_f, ...
sigma, kappa, Pfluid, ...
HenryCoef, M, T,bubble_speed,speed_factor);
m=dmdt*dt+m;
if m>0
n=m/M;
Pb=2/3*sigma./n./R./T*2.^(1/3).*...
(pi.*(9.*Pfluid+(-(128.*pi*sigma^3-81.*...
n.*R.*T.*Pfluid.^2)./n./R./T).^(1/2)).*...
n.^2.*R^2.*T.^2).^(1/3)+8/3*pi*sigma.^2*2.^(2/3)./...
(pi.*(9.*Pfluid+...
(-(128*pi*sigma^3-81.*n.*R.*T.*Pfluid.^2)./n./R./T).^(1/2)).*...
n.^2*R.^2*T.^2).^(1/3)+Pfluid;
Vb=n*R*T./Pb;
b=(3*Vb./(4*pi)).^(1/3);
rhoa_inf=M/(R*T)*Pfluid;
Tau=2*M*sigma/(R*T);
rhoa=rhoa_inf+Tau/b;
Pb=R*T/M*rhoa;
else
Vb=0;
b=0;
rhoa=0;
Pb=0;
end
end
gr=r.*w.^2; %m/s^2
vxss=(rhoa-rhof).*...
(gb*sin(phi)+gr.*cos(phi))./(2*Dc.*pi*mu)*(4*pi/3).^(1/3).*Vb.^(2/3);
vyss=(rhof-rhoa).*...
(gb*cos(phi)+gr.*sin(phi))./(2*Dc.*pi*mu).*(4*pi/3).^(1/3).*Vb.^(2/3);
xspeed=-vxss;
yspeed=vyss;
d=2*b;
```

A.3.4 delta_m_epstein_plesset_ode.m

```
function dmdt = ...
delta_m_epstein_plesset_ode(t, R, c_f,...
sigma, kappa, p, HenryCoef, M, T)
%Epstein-Plesset bubble problem with surface tension.
%Our problem only involves a first derivative and this function calculated
%the change in mass of a given bubble in solution.
%Created by Aaron Mazzeo
%Last modified on 3-27-09
c_sinfty=HenryCoef*p;
dmdt=4*pi*R.^2.*kappa*(c_sinfty*(c_f-1)-2*HenryCoef*sigma./R).*...
(1./R+1./(pi*kappa.*t).^0.5);
if R<=0,
dmdt=0;
end
```

Appendix B

Measurement and part-to-part variation at the micro and nano scales

Measurement is an extremely important component of micro and nano scale manufacturing. It is necessary to measure the product being produced for quality control purposes. In the large-scale manufacturing of microfluidic devices, robust methods may be necessary for characterizing part-to-part variation of the individual components being produced. To begin to address these measurement issues, a Zygo optical profilometer has been used, along with some custom measurement algorithms to characterize part-to-part variation of micro channels replicated in PDMS. The PDMS was molded against a variety of materials such as polymethylmethacrylate (PMMA), polycarbonate (PC), polychlorotrifluorethylene (PCTFE), polytetrafluoroethylene (PTFE), and aluminum. To summarize these results, the following from a paper presented at the International Symposium on Nanomanufacturing in January of 2008 is included [87].

The liquid curable resin polydimethylsiloxane (PDMS) Sylgard 184, a silicon-based thermoset, is cast on a variety of molds composed of polytetrafluoroethylene (PTFE), polycarbonate (PC), polychlorotrichlorofluoroethylene (PCTFE), aluminum, and polymethylmethacrylate (PMMA). The PDMS is allowed to cure at room temperature on these molds to avoid the introduction of bubbles or residual stresses that might introduce additional variation to channel widths or depths. The nominal height for the channels is $50\,\mu$mand the nominal width is $250\,\mu$m. To measure the channel widths and depths, an optical profilometer and a simple, robust algorithm are used to characterize part-to-part dimensional

variation of PDMS parts molded against various mold materials. The average standard deviation for part-to-part channel height measurements is approximately 300 nm, and the average standard deviation for part-to-part channel width measurements is approximately 1.2 μm. Both the channel height and width part-to-part averaged standard deviations are less than 1% of the averaged measured channel depths and widths.

B.1 Introduction

PDMS is well-suited for the prototyping of microfluidic devices [88]. PDMS has been shown to replicate features less than 2 nm in height [45] and tens of nanometers in width [120]. Even though PDMS has been shown to be an excellent material for microfluidic device production, no prior studies have been found discussing part-to-part variation of the geometrical dimensions of micro or nano channels formed in PDMS parts.

In an effort toward the characterization and design of an effective manufacturing process for the production of micro and nano features in curable liquid resins, a study addressing the gauge repeatability and part-to-part variation of the width and depths of micro channels replicated in PDMS has been performed. The replicated PDMS channels were molded against a variety of different materials including PTFE, PC, PCTFE, and PMMA. The channels in these thermoplastic materials were formed using the hot embossing process. The mold used in the hot embossing process is a micro machined piece of aluminum, which was also used to mold PDMS directly.

After the PDMS parts were produced, selected sites at approximately the same locations for each part were measured using an optical profilometer. The optical profilometer alone is not capable of calculating channel widths and depths. To accomplish this task, a simple, robust algorithm for determining widths and depths of single channel sections was developed using some previously used techniques and work [83]. Using this width and depth measuring technique, a gauge repeatability and part-to-part variation study were performed on micro channels molded in PDMS.

B.2 PDMS Casting

In prototype PDMS device fabrication, there are generally five steps. First, the two-part PDMS solution is mixed by hand or a mixing device. Second, the PDMS is dispensed on

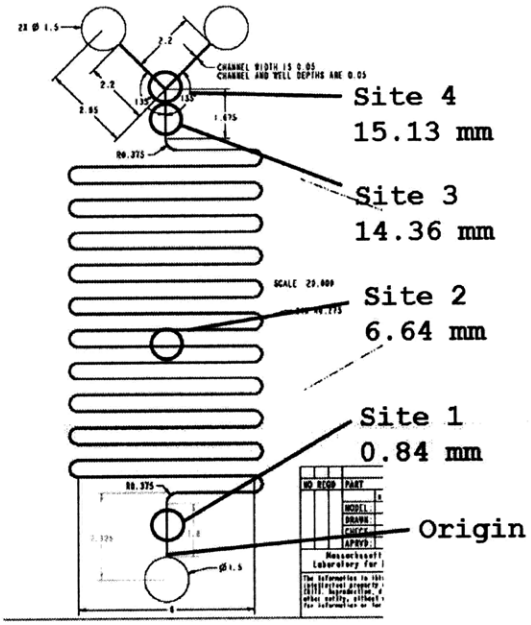

Figure B-1: Micro mixer design sent to Microlution for micro machining in aluminum. Distances indicated below site numbers are relative to origin.

the mold. Third, the PDMS and mold are placed in a vacuum jar or chamber to degas the PDMS and remove unwanted bubbles. Fourth, the PDMS is cured in an oven. Last, the PDMS and mold are separated from each other.

In this study, MCX 08-24 static mixers were used to mix and dispense the PDMS at the standard 10:1 ratio on the plastic and aluminum molds. The PDMS and the molds then sat at room temperature for at least 24 hours. The resulting thickness of the parts was less than a few millimeters. Degassing was not necessary because bubbles were able to escape before the PDMS cured. After the PDMS cured on the molds, the PDMS was peeled from the molds by hand. The entire cycle was then repeated to produce a series of parts for the reproducibility study. In addition to eliminating the need for oven cure and degassing steps, this simplified process reduced the possibility of introducing additional stress/strain in molded PDMS parts due to thermal contraction/shrinkage.

B.3 Height and Width Analysis

In order to quantify part-to-part variation of PDMS parts molded against a variety of materials, a Zygo NewView 5000 optical profilometer was used to measure selected sites. The

sites used for the height and width analysis on multiple parts are sites 1, 2, and 3 shown in Figure B-1. The data from these sites were used with custom algorithms to interpret the data and determine channel heights and widths.

B.3.1 Optical Profilometer

Generally speaking, SEM images as those shown in Figure B-2 are excellent for qualitatively describing replication results at the length scales of concern in this work. However, SEMs generally do not provide quantitative dimensional data. To generate quantitative dimensional data, an optical profilometer is used. The Zygo optical profilometer used has lateral resolution on the order of a micron and depth resolution on the order of a nanometer. To collect data, the sample is placed on the x,y stage and is moved to a pre-designated location in the camera view. The optical profilometer has a motor-driven x,y stage, which is capable of translating the part laterally to pre-programmed positions. The x,y stage is moved appropriately, and images are taken at the designated locations. After images are captured as shown in Figure B-3, three-dimensional Zygo (x,y,z) coordinate data can then be exported, manipulated, and processed in MATLAB or some other numerical computing package.

B.3.2 Height and Width Calculation Algorithm

To calculate channel height and width dimensions, images at the desired sites are first taken with the optical profilometer. The (x,y,z) coordinate data are then manipulated as shown in Figure B-4. The data are centered by calculating the centroid of all the data points and subtracting the centroid from all the data. Next, the data are projected into the x,z plane, and a line in the x,z plane is fit using the MATLAB polyfit command. The angle of the fitted line to the horizontal is calculated, and all the data are rotated about the y-axis by this angle to better level the data as shown in Figure B-5 A. The newly rotated data are then projected into the y,z plane, and a line in the y,z plane is fit using the MATLAB polyfit command. The angle of the fitted line to the horizontal is calculated, and all the data are rotated about the x-axis by this angle to complete the leveling of the data as shown in Figure B-5 A. This same leveling technique has been used with atomic force microscope scans[83].

After the data have been leveled, the x,z plane is split into two regions: one above the "zero" line and one below the "zero" line. The "zero" line can be defined as the horizontal line running parallel to the x-axis in the x,z plane and going through the centroid of the

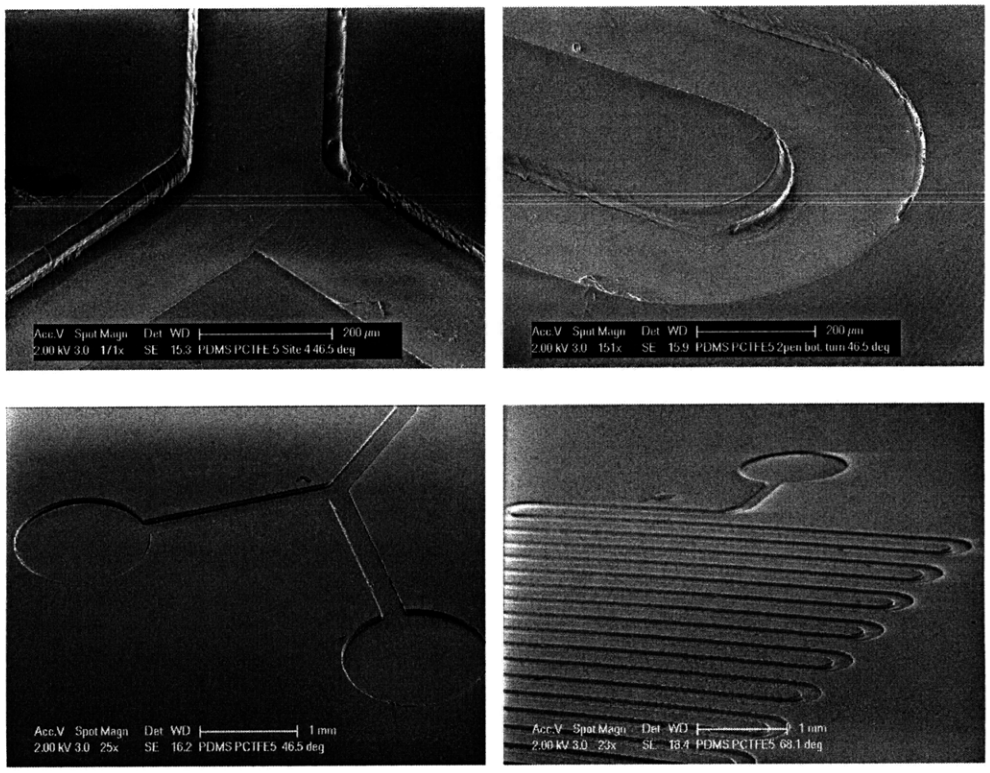

Figure B-2: SEM images of a resulting PDMS part, which was molded on a hot embossed PCTFE mold.

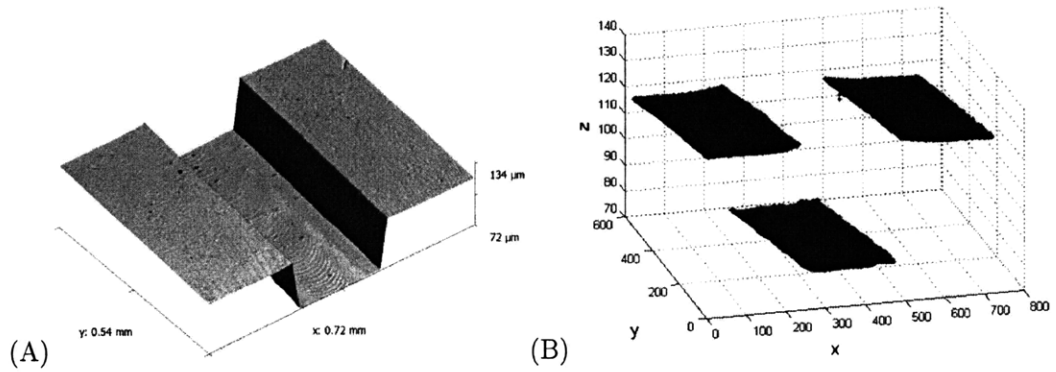

Figure B-3: (A) Site 1 of a PDMS part depicted using the Laplace correction rendering provided by the free, open source Gwyddion software. (B) The same optical interferometer data rendered in a MATLAB figure showing plotted points and missing sidewall data. The number values are in units of microns.

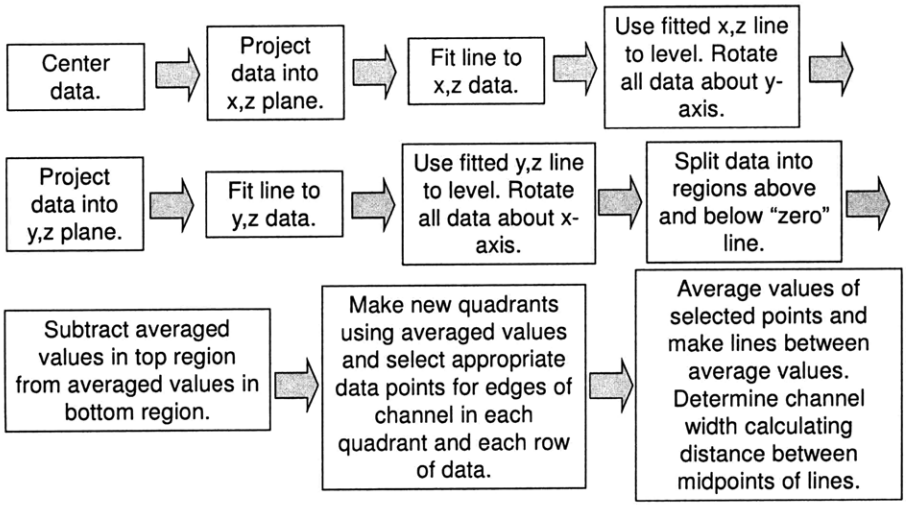

Figure B-4: Algorithm for calculating height and width values.

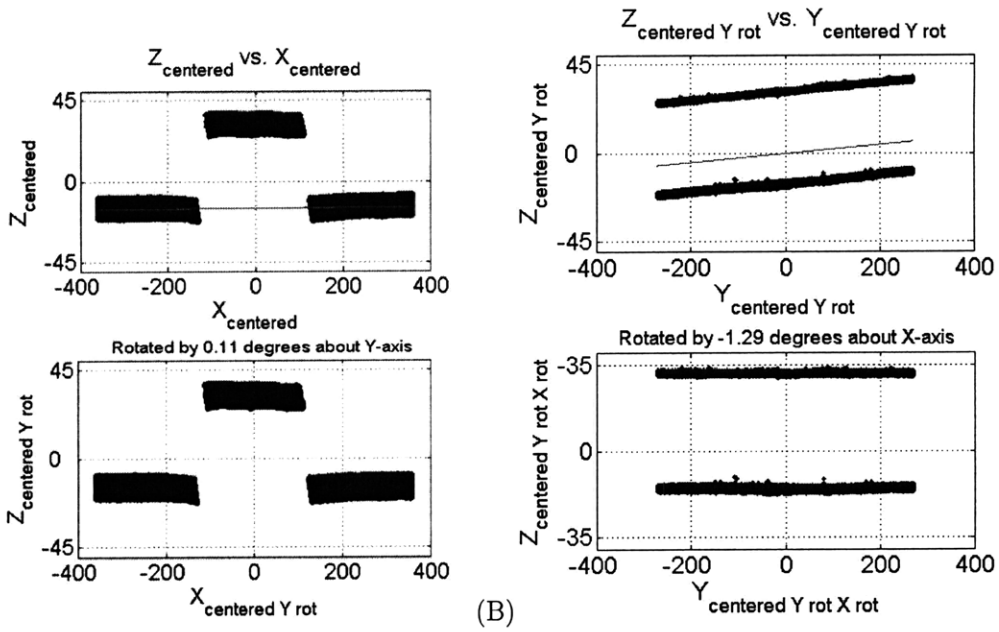

Figure B-5: (A) Data from Figure B-3 projected into the x,z plane and rotated about the y-axis. (B) Data from A projected into the y,z plane and rotated about the x-axis. The number values are in units of microns.

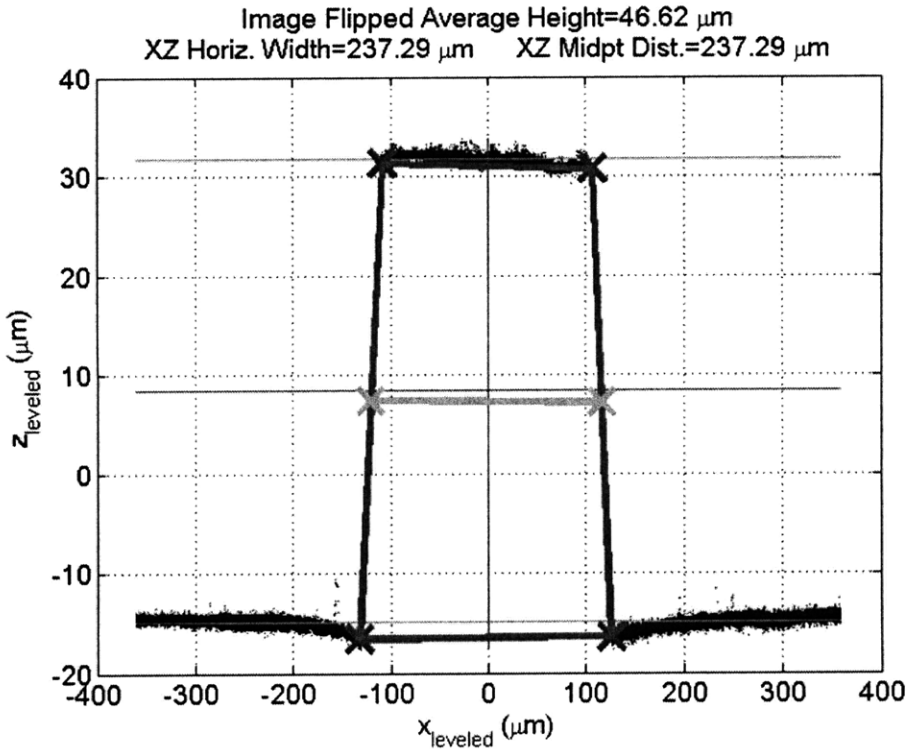

Figure B-6: Leveled channel data from Figure B-5 B in the x,z plane split into four quadrants. The height is the difference between the top horizontal line and the bottom horizontal line. The width is the horizontal distance between the two midpoints of the almost vertical lines drawn.

leveled data. The z-values for the data above the "zero" line are then averaged, and the z-values for the data below the "zero" line are also averaged. The difference between these two average values is then reported as the height or depth of the channel. The top and bottom lines running parallel to the x-axis as shown in Figure B-6 run through the z-values averaged above and below the "zero" line.

To calculate the width of the channel, four quadrants are defined in the x,z plane as shown in Figure B-6. The difference between either the top or bottom line and half the calculated height is used to draw a horizontal line running parallel to the x-axis, which splits the channel data into a new top region and a new bottom region. A new vertical line running parallel to the z-axis is drawn through the centroid of the leveled data. The new horizontal and vertical lines define the four quadrants. The channel data in each of these quadrants are then used to calculate average corner/edge values used for calculating the channel width. In the upper left quadrant shown in the x,z plane projection, the most negative point is selected in each

row of data (parallel to the y-axis), and the x,z-values of the selected points in each row are averaged to determine the upper left corner/edge of the channel. Similarly, the most negative points are selected and averaged in the bottom left quadrant, and the most positive points are selected and averaged in the upper right and bottom right quadrants. Lines are then drawn in the x,z plane between these corner/edge points as shown in Figure B-6. The midpoints of the two most vertical lines are then calculated, and the horizontal distance between the two midpoints is calculated and declared to be the width of the channel.

B.4 Results

PDMS parts were molded as outlined in Section B.2, and the resulting parts were measured as described in Section B.3 using an optical profilometer and original MATLAB scripts. With these measurement tools and parts, the gauge repeatability of the measurement system has been characterized for PDMS parts with channel widths and depths of approximately 250 μm and 50 μm, respectively. Using the results of the repeatability study and the custom measurement algorithms on PDMS parts produced from the room temperature curing process, part-to-part variation of the PDMS molding process is explored.

B.4.1 Gauge Repeatability

To determine the repeatability of the channel height and width measurement process, site 1 on a part formed in PDMS from a hot embossed PCTFE mold was repetitively measured. The PDMS part was removed from the x,y stage of the Zygo optical profilometer after each measurement. The microscope objectives were generally switched back and forth between measurements, and the tilt of the x,y stage was occasionally adjusted. These disturbances were purposefully introduced to replicate measurement conditions and variability that might normally be expected.

The width and height measurements for a series of 20 measurements at site 1 of a PDMS part cast off PCTFE are shown in Figure B-7. The standard deviation for the height measurements is 0.28 μm, which is 0.60% of the averaged mean height of 46.49 μm. The standard deviation of the repetitive width measurements is 0.17 μm, which is 0.072% of the average channel width of 237.46 μm.

Table B.1 gives repeatability data for 20 measurements at three sites of the PDMS

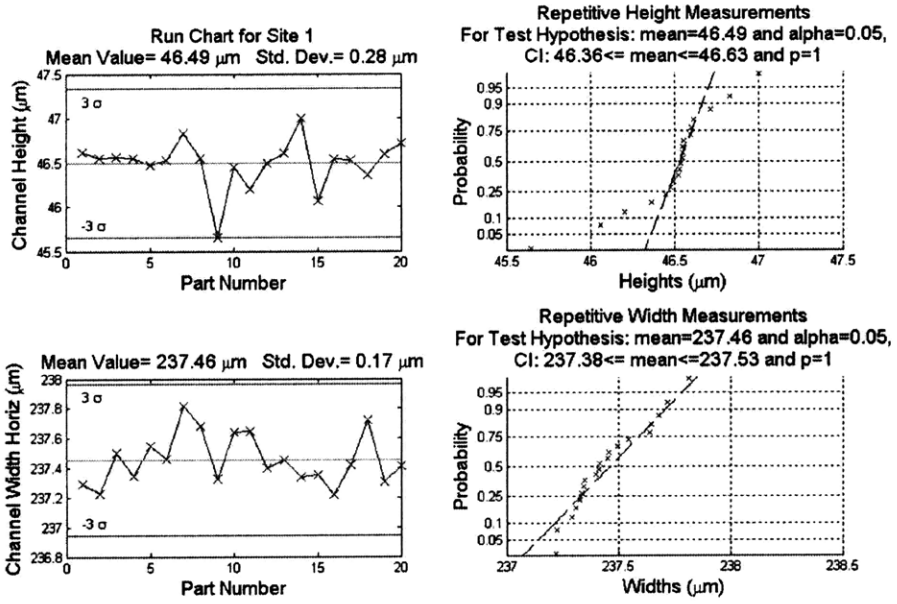

Figure B-7: Run chart showing the repeatability of the channel and width height channel measurement system.

Table B.1: Measured and averaged repeatability values at 3 sites for a single PDMS part.

Site # and Dim.	Ave. (μm)	Std. dev. (μm)	Std. dev. /Ave (%)	Max. (μm)	Min. (μm)
1-height	46.49	0.28	0.60	47.01	45.65
1-width	237.46	0.17	0.07	237.81	237.22
2-height	45.49	0.24	0.53	46.29	45.22
2-width	241.47	0.17	0.07	241.81	241.16
3-height	45.60	0.17	0.37	46.18	45.35
3-width	227.25	0.78	0.35	229.31	225.94

part cast off of PCTFE. The site number and whether the row represents depth or width measurements are given in the first box of each row. The standard deviations, the relative percentages of the standard deviations to the averages, and minimum and maximum values for the depths and widths are reported.

B.4.2 Part Variation

In the part-to-part variation experiment, the same molds and approximately the same processing conditions (cured at room temperature for at least 24 hours) were used to produce series of parts. These parts were then measured, and their height and width values were

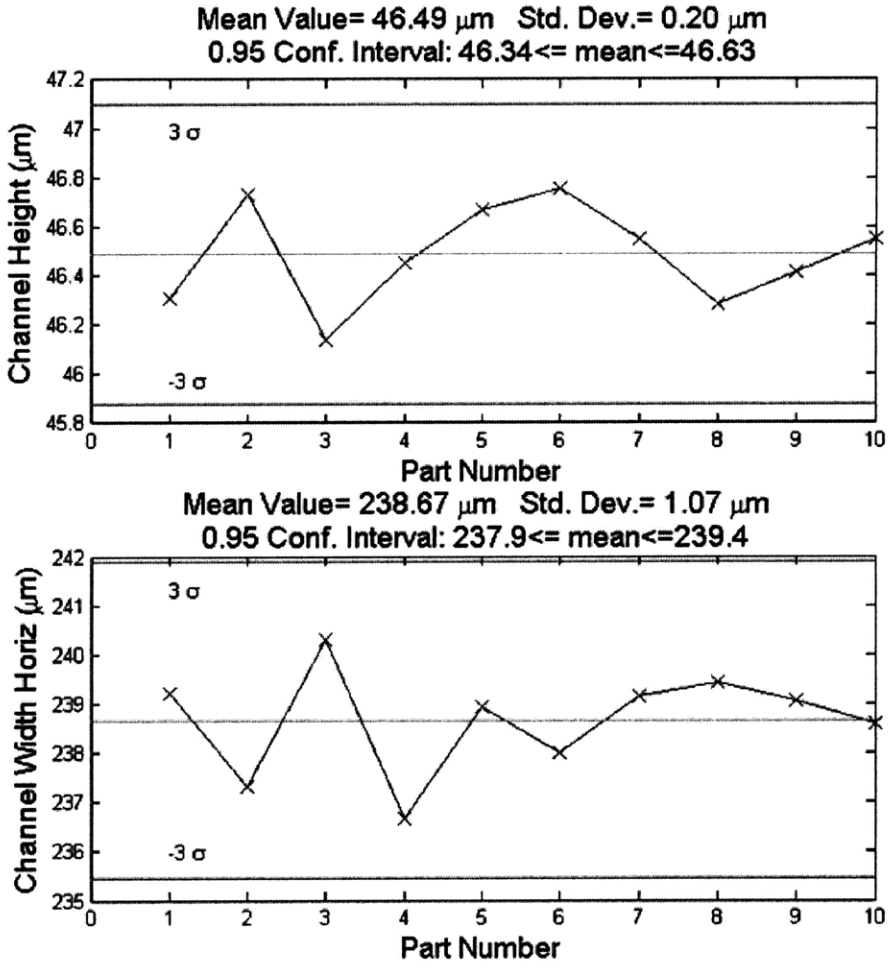

Figure B-8: Part-to-part experiment for site 1 of PDMS part cast on PCTFE. The same site was measured on 10 different replicated parts.

recorded in run charts like the ones shown in Figure B-8.

The measurement data are compiled in Table B.2. For this study, mold heights and widths are represented by only one measurement and do not represent multiple repeated measurements of the same site. There were 11 PDMS parts molded against PMMA, 10 PDMS parts molded against aluminum, 11 parts molded against PCTFE, and 9 PDMS parts molded against PC. The average values in the bottom row of Table B.2 are just the averages of all the values included in each column.

It was previously mentioned that PTFE (Teflon) was used as a mold for PDMS, but data for the mold and the PDMS parts are not included in Table 5. The data are not included because of the difficulty our measurement system had in getting clean data from

Mold Material and Site	Mold Height (μm)	Ave. Part Height (μm)	Std. Dev. Part Height (μm)	Mold Width (μm)	Ave. Part Width (μm)	Std. Dev. Width (μm)
PC-1	49.6	50.16	0.29	240.5	236.62	0.73
PC-2	47.2	47.77	0.33	190.1	177.88	2.89
PC-3	48.9	48.82	0.50	247.9	245.46	0.63
PMMA-1	49.6	49.63	0.22	245.2	243.55	0.81
PMMA-2	47.9	48.02	0.25	246.8	244.67	0.70
PMMA-3	47.6	47.57	0.27	256.6	249.24	0.90
PCTFE-1	46.8	46.49	0.20	240.3	238.67	1.07
PCTFE-2	46.0	45.78	0.27	242.4	239.2	1.13
PCTFE-3	45.9	45.46	0.19	230.6	227.08	1.84
Al-1	50.5	50.39	0.16	251.7	249.27	0.88
Al-2	49.2	48.82	0.24	251.8	253.39	1.44
Al-3	49.4	48.92	0.21	250.8	251.59	1.14
Ave.	48.2	48.15	0.26	241.2	238.05	1.18

Table B.2: Measured and averaged height and width values for molds and PDMS parts.

the PTFE mold and PDMS parts cast against PTFE. The optical profilometer was not able to completely map the surfaces of the PTFE mold and the PDMS part cast off of the corresponding PTFE mold. The images taken suggest that the PTFE mold produced in the hot embossing process has a rough surface texture that cannot be easily measured with our optical profilometer.

B.5 Observations

Molding PDMS against thermoplastic and aluminum molds lead to part-to-part standard deviations of less than 1% of the mean channel depths and widths. To arrive at this conclusion, channel width and height repeatability and part-to-part variation studies on series of PDMS parts were performed. To quantitatively compare channel widths and heights, a simple, robust algorithm was developed that can be used with an optical profilometer to calculate channel widths and depths. The average standard deviation for part-to-part channel height measurements is approximately 300 nm, and the average standard deviation for part-to-part channel width measurements is approximately 1.2 μm. Again, both the channel height and width part-to-part averaged standard deviations are less than 1% of the averaged measured channel depths and widths.

Bibliography

[1] World Microfluidics / Lab-on-a-Chip Markets. Frost and Sullivan, Jan 2003.

[2] Information about Dow Corning Brand Silicone Encapsulants. Form No. 10-898F-01 on http://www.dowcorning.com, 2005.

[3] U.S. Microfluidics/Lab-on-a-chip Markets. Frost and Sullivan, May 2006.

[4] Bristol Myers Squibb Co. Form 10-K Annual Report for 2008, Feb. 2009.

[5] Bulletproof Acrylic. Pacific Bulletproof Co. (http://www.pacificbulletproof.com), Accessed March 2009.

[6] Compliance Assistance-Fair Labor Standards Act. United States Department of Labor (http://www.dol.gov/esa/whd/flsa/), Accessed April 2, 2009.

[7] Electric Power Monthly with data for December 2008. Energy Information Administration (US Department of Energy) http://www.eia.doe.gov/cneaf/electricity/epm/table5_6_a.html, March 2009.

[8] GPFR 1000 Rapid-Pro Series Resin Processing System. Ashby Cross Website (http://ashbycross.com/gpfr1000.htm), Accessed April 13, 2009.

[9] Injection Molding: Liquid Silicone Molding. http://www.jeffersonrubber.com/ liquid_silicone.html, Accessed on April 11, 2009.

[10] Lilly Eli & Co. Form 10-K Annual Report for 2008, Feb. 2009.

[11] Liquid Silicone Molding and Tooling for Prototyping. Albright Technologies, Inc. (http://www.albright1.com/resources.php), Accessed April 2, 2009.

[12] Merck & Co Inc. Form 10-K Annual Report for 2008, Feb. 2009.

[13] Pfizer Inc. Form 10-K Annual Report for 2008, Feb. 2009.

[14] Product Q&A #5: Adhesion Problems on Cast Aluminum. Dow Corning Website (http://www.dowcorning.com/FAQ/faq_search.asp?DCWS=Electronics&DCWSS=Encapsulants &ind=009&2ndlevel=&e=Product+Resources), Accessed March 27, 2009.

[15] Thinky Planetary Centrifugal Mixer. http://thinkyusa.com/, Accessed February 28, 2009.

[16] Vapor Pressure Chart. Clearco Products Website (http://www.clearcoproducts.com/silicones_library.html), Accessed March 25, 2009.

[17] Vapor Pressure Data for Clearco Pure Silicone Fluids. Clearco Products Website (http://www.clearcoproducts.com/silicones_library.html), Accessed March 25, 2009.

[18] Viscosity to Temperature Chart: Clearco Pure Silicone Fluids. Clearco Products Website (http://www.clearcoproducts.com/silicones_library.html), Accessed March 18, 2009.

[19] Wacker Silicone Fluids AK. Amber Composites Website (http://www.ambercomposites.com/downloads/datasheet/silicones-ak.pdf), Accessed March 26, 2009.

[20] D. Armani, C. Liu, and N. Aluru. Re-configurable fluid circuits by PDMS elastomer micromachining. pages 222–227, 1999.

[21] R. Battino, T.R. Rettich, and T. Tominaga. The Solubility of Nitrogen and Air in Liquids. *J. Phys. Chem. Ref. Data*, 13(2), 1984.

[22] P. M. Biesheuvel, A. Nijmeijer, and H. Verweij. Theory of batchwise centrifugal casting. *AIChE J*, 44(8):1914–22, 1998.

[23] Joseph L. Katz Milton Blander. Bubble nucleation in liquids. *AICHE Journal*, 21(5):833–848, 1975.

[24] N. Bontoux, L. Dauphinot, T. Vitalis, V. Studer, Y. Chen, J. Rossier, and MC Potier. Integrating whole transcriptome assays on a lab-on-a-chip for single cell gene profiling. *Lab on a Chip*, 8(3):443–450, 2008.

[25] A. Bubendorfer, X. Liu, and A. V. Ellis. Microfabrication of PDMS microchannels using SU-8/PMMA moldings and their sealing to polystyrene substrates. *Smart Materials and Structures*, 16(2):367–371, 2007.

[26] J.J. Carroll, J.D. Slupsky, and A.E. Mather. The solubility of carbon dioxide in water at low pressure. *J. Phys. Chem. Ref. Data*, 20(6):1201–1209, 1991.

[27] J. H. Chen. Method of manufacturing a hollow silicon rubber doll. US Patent 2005/0194715 A1, Sept. 8, 2005.

[28] Nikolai Chernov. Circle Fit (Pratt Method). MATLAB File Exchange (http://www.mathworks.com/matlabcentral/fileexchange/22643), January 2009.

[29] R. Clift, J.R. Grace, and M.E. Weber. *Bubbles, Drops, and Particles.* Academic Press San Diego, Calif, 1978.

[30] T.S. Coffey. Diet Coke and Mentos: What is really behind this physical reaction? *American Journal of Physics*, 76:551, 2008.

[31] JS Colton and NP Suh. The nucleation of microcellular thermoplastic foam with additives: Part I: Theoretical considerations. *Polymer Engineering and Science*, 27(7), 1987.

[32] Dow Corning. Dow Corning Reply Sylgard 184 Viscosity. Email Communication (tech.info@dowcorning.com), Email received on March 17, 2009.

[33] Crawford and Throne. *Rotational Molding Technology.* Plastics Design Library, 2002.

[34] M. Dirckx, A. D. Mazzeo, and D. E. Hardt. Production of micro-molding tooling by hot embossing. In *Proceedings of the 2007 International Manufacturing Science and Engineering Conference*, October 15-17, 2007.

[35] Matthew Dirckx and David E. Hardt. A review of hot micro-embossing manufacturing process research. In *Proceedings of the 1st International Conference on Micromanufacturing*, pages 340–345, 2006.

[36] Matthew Dirckx, Aaron D. Mazzeo, and David E. Hardt. Evaluation of thermoplastic materials for hot micro-embossing tooling. In *Proceedings of the International Symposium on Nanomanufacturing*, Singapore, Jan 23-25, 2008 2008.

[37] Z. Duan and R. Sun. An improved model calculating CO2 solubility in pure water and aqueous NaCl solutions from 273 to 533 K and from 0 to 2000 bar. *Chemical Geology*, 193(3-4):257–271, 2003.

[38] K. Efimenko, W.E. Wallace, and J. Genzer. Surface modification of Sylgard-184 poly (dimethyl siloxane) networks by ultraviolet and ultraviolet/ozone treatment. *Journal of colloid and interface science*, 254(2):306–315, 2002.

[39] P. S. Epstein and M. S. Plesset. On the stability of gas bubbles in liquid-gas solutions. *The Journal of Chemical Physics*, 18(11):1505–1509, November 1950 1950.

[40] E. Eteshola and D. Leckband. Development and characterization of an elisa assay in pdms microfluidic channels. *Sensors and Actuators B: Chemical*, 72(2):129–133, 2001.

[41] GK Fleming and WJ Koros. Dilation of polymers by sorption of carbon dioxide at elevated pressures. 1. silicone rubber and unconditioned polycarbonate. *Macromolecules*, 19(8):2285–2291, 1986.

[42] A. Folch, S. Mezzour, M. Du ring, O. Hurtado, M. Toner, and R. Müller. Stacks of microfabricated structures as scaffolds for cell culture and tissue engineering. *Biomedical Microdevices*, 2(3):207–214, 2000.

[43] A. Y. Fu, H. P. Chou, C. Spence, F. H. Arnold, and S. R. Quake. An integrated microfabricated cell sorter. *Analytical Chemistry*, 74(11):2451–2457, Jun 1 2002. LR: 20061115; PUBM: Print; GR: HG 01642-04/HG/NHGRI; JID: 0370536; ppublish; printed on 5-04-07.

[44] J. X. Gao, L. P. Yeo, M. B. Chan-Park, J. M. Miao, Y. H. Yan, J. B. Sun, Y. C. Lam, and C. Y. Yue. Antistick postpassivation of high-aspect ratio silicon molds fabricated by deep-reactive ion etching. *Microelectromechanical Systems, Journal of*, 15(1):84–93, 2006.

[45] B. D. Gates and G. M. Whitesides. Replication of vertical features smaller than 2 nm by soft lithography. *Journal of the American Chemical Society*, 125(49):14986–14987, 2003.

[46] G. Gogos. Bubble removal in rotational molding. *Polymer Engineering and Science*, 44(2):388–94, 02 2004. M1: Copyright 2005, IEE.

[47] T. Gutowski, J. Dahmus, A. Thiriez, M. Branham, and A. Jones. A thermodynamic characterization of manufacturing processes. In *IEEE International Symposium on Electronics and the Environment, Orlando, Florida, USA, May*, pages 7–10, 2007.

[48] W. M. Haines. Polyurethane molding techniques. *Elastomerics*, 110(9):26–32, 1978.

[49] Melinda Hale. Development of a Low-Cost, Rapid-Cycle Hot Embossing System for Microscale Parts. Master's thesis, Massachusetts Institute of Technology, 2009.

[50] B. J. Hamrock, S. R. Schmid, and B. Jacobson. *Fundamentals of Machine Elements.* McGraw-Hill, second edition, 2005.

[51] D. E. Hardt, B. W. Anthony, and S. B. Tor. A teaching factory for polymer microfabrication - MuFac. In *6th International Symposium on Nanomanufacturing (Athens)*, March 2008.

[52] David Hardt, Matthew Dirckx, Grant Shoji, Kunal Thacker, and Qi Wang. Process control for microembossing: Basic characterization studies. In *Symposium of the Singapore MIT Alliance Programme in Innovation in Manufacturing Systems and Technology*, 2006.

[53] David Hardt, Bala Ganesan, Matthew Dirckx, Grant Shoji, and Kunal Thacker. Process variability in micro-embossing. In *Symposium of the Singapore MIT Alliance Programme in Innovation in Manufacturing Systems and Technology*, 2005.

[54] David Hardt, Bala Ganesan, Qi Wang, and Matthew Dirckx. Process control in microembossing: A review. In *Symposium of the Singapore MIT Alliance Programme in Innovation in Manufacturing Systems and Technology*, 2004.

[55] David E. Hardt, Bala Ganesan, Wang Qi, Matthew Dirckx, and Adam K. Rzepniewski. Process control in micro-embossing: A review, Jan 2004.

[56] David E. Hardt and Tsz-Sin Siu. Cycle to cycle manufacturing process control. In *First Annual Singapore-MIT Alliance Symposium*, Singapore, 2002.

[57] D. Henann and L. Anand. A constitutive theory for the mechanical response of amorphous metals at high temperatures spanning the glass transition temperature: Application to microscale thermoplastic forming. *Acta Materialia*, 2008.

[58] R. C. Huang and L. Anand. Non-linear mechanical behavior of the elastomer polydimethylsiloxane (PDMS) used in the manufacture of microfluidic devices. DSpace at MIT, Jan 2005.

[59] P.W. Hum. *Exploration of large scale manufacturing of polydimethylsiloxane (PDMS) microfluidic devices.* PhD thesis, Bachelors Thesis, Massachusetts Institute of Technology, 2006.

[60] B. H. Jo, L. M. Van Lerberghe, K. M. Motsegood, and D. J. Beebe. Three-dimensional micro-channel fabrication in polydimethylsiloxane (PDMS) elastomer. *Microelectromechanical Systems, Journal of*, 9(1TY - JOUR):76–81, 2000.

[61] Byung-Ho Jo and David J. Beebe. Fabrication of three-dimensional microfluidic systems by stacking molded polydimethylsiloxane (PDMS) layers. volume 3877, pages 222–229. SPIE, August 19, 1999.

[62] Y. Kamiya, Y. Naito, T. Hirose, and K. Mizoguchi. Sorption and partial molar volume of gases in poly(dimethyl siloxane). *Journal of Polymer Science Part B Polymer Physics*, 28(8):1297–1308, 1990.

[63] E. P. Kartalov and S. R. Quake. Microfluidic device reads up to four consecutive base pairs in DNA sequencing-by-synthesis. *Nucleic Acids Research*, 32(9):2873–2879, 2004.

[64] A. M. Kendale. Automation of Soft Lithographic Microcontact Printing. Masters Thesis, Massachusetts Institute of Technology, 2002.

[65] A. M. Kendale and D. L. Trumper. Microcontact Printing. US Patent 7,117,790 B2, Oct. 10, 2006.

[66] A. A. Kendoush. The virtual mass of a growing and collapsing bubble. *AICHE Journal*, 52(6):2013–2019, 2006.

[67] C. Kennedy. Fabrication of microfluidic circuits by printing techniques. US Patent 6,509,085, January 21 2003.

[68] K.Y. Kim, S.L. Kang, and H.Y. Kwak. Bubble nucleation and growth in polymer solutions. *Polymer Engineering and Science*, 44(10), 2004.

[69] L. Kim, M. D. Vahey, H. Y. Lee, and J. Voldman. Microfluidic arrays for logarithmically perfused embryonic stem cell culture. *Lab on a chip*, 6(3):394–406, Mar 2006.

[70] K. G. Klemic, J. F. Klemic, and F. J. Sigworth. An air-molding technique for fabricating PDMS planar patch-clamp electrodes. *Pflugers Archiv : European journal of physiology*, 449(6):564–572, Mar 2005.

[71] W. Kloek, T. van Vliet, and M. Meinders. Effect of bulk and interfacial rheological properties on bubble dissolution. *Journal of Colloid And Interface Science*, 237(2):158–166, 2001.

[72] M. Kontopoulou and J. Vlachopoulos. Bubble dissolution in molten polymers and its role in rotational molding. *Polymer Engineering and Science*, 39(7), 1999.

[73] Sriram Krishnan. *On the Manufacture of Very Thin Elastomeric Films by Spin-coating.* PhD thesis, Massachusetts Institute of Technology, 2007.

[74] Paul Krugman. Health Care Now. New York Times (http://www.nytimes.com/2009/01/30/opinion/ 30krugman.html?_r=1), January 2009.

[75] A. Kumar, H. A. Biebuyck, and G. M. Whitesides. Patterning self-assembled monolayers: Applications in materials science. *Langmuir*, 10(5):1498–1511, 1994.

[76] W. M. Larson. Method of centrifugally casting a tire. US Patent 3,956,448, May 11, 1976.

[77] H. L. Lee, P. Boccazzi, R. J. Ram, and A. J. Sinskey. Microbioreactor arrays with integrated mixers and fluid injectors for high-throughput experimentation with ph and dissolved oxygen control. *Lab on a chip*, 6(9):1229–1235, Sep. 2006.

[78] S. W. Lee and S. S. Lee. Shrinkage ratio of PDMS and its alignment method for the wafer level process. *Microsystem Technologies*, 2007.

[79] S.T. Lee. *Foam Extrusion: Principles and Practice.* CRC Press, 2000.

[80] David R. Lide, editor. *CRC Handbook of Chemistry and Physics.* CRC Press/Taylor and Francis, 89th (internet version 2009) edition, 2009.

[81] H.B. Liu, N. Ramalingam, Y. Jiang, C.C. Dai, K.M. Hui, and H.Q. Gong. Rapid distribution of a liquid column into a matrix of nanoliter wells for parallel real-time quantitative PCR. *Sensors & Actuators: B. Chemical*, 135(2):671–677, 2009.

[82] J. Liu, C. Hansen, and S. R. Quake. Solving the "world-to-chip" interface problem with a microfluidic matrix. *Anal.Chem*, 75(18):4718–4723, 2003.

[83] Aaron D. Mazzeo. Accurate capacitive metrology for atomic force microscopy, 2005.

[84] Aaron D. Mazzeo, Nancy Diaz, Matthew Dirckx, and David E. Hardt. Single-step through-hole punching and double-sided hot embossing of microfluidic channels. In *Proceedings of the 2nd International Conference on Micromanufacturing*, 2007.

[85] Aaron D. Mazzeo, Matthew Dirckx, and David E. Hardt. Process selection for microfluidic device manufacturing. In *Society of Plastics Engineers Annual Technical Conference*, 2007.

[86] Aaron D. Mazzeo, Matthew Dirckx, and David E. Hardt. Single-step through-hole punching by hot embossing. In *Society of Plastics Engineers Annual Technical Conference*, 2007.

[87] Aaron D. Mazzeo and David E. Hardt. Toward the manufacture of micro and nano features with curable liquid resins: Mold materials and part-to-part dimensional variation. In *Proceedings of the International Symposium on Nanomanufacturing*, Singapore, Jan 23-25, 2008.

[88] J. C. McDonald and G. M. Whitesides. Poly(dimethylsiloxane) as a material for fabricating microfluidic devices. *Accounts of Chemical Research*, 35(7):491–499, 2002.

[89] Henry Müller, B. Küper, U. Maier, and L. Pierkes. The latest on molding of polyurethane. *Advances in Polymer Technology*, 5(4):257–304, 1985.

[90] Barack Obama. Presidential inauguration address. New York Times (http://www.nytimes.com/2009/01/20/us/politics/20text-obama.htm), January 2009.

[91] A. Oláh, H. Hillborg, and G.J. Vancso. Hydrophobic recovery of UV/ozone treated poly (dimethylsiloxane): adhesion studies by contact mechanics and mechanism of surface modification. *Applied Surface Science*, 239(3-4):410–423, 2005.

[92] Adrian O'Neill, Jeffrey Soo Hoo, and Glenn Walker. Rapid curing of PDMS for microfluidic applications. *Lab on a Chip: Chips and Tips*, Oct. 23, 2006.

[93] Janet Rae-Dupree. Disruptive innovation, applied to health care. New York Times (http://www.nytimes.com/2009/02/01/business/01unbox.html?ref=business), January 2009.

[94] D.B. Roitman, K.P. Killeen, K.L. Seaward, H. Yin, and K. Robotti. PAEK embossing and adhesion for microfluidic devices. US Patent 7,314,599, Jan. 1, 2008.

[95] Adam Rosenthal, Alice Macdonald, and Joel Voldman. Cell patterning chip for controlling the stem cell microenvironment. *Biomaterials,*, 28(21):3208–3216, 7 2007.

[96] M. W. Rowell, M. A. Topinka, M. D. McGehee, H. J. Prall, G. Dennler, N. S. Sariciftci, L. Hu, and G. Gruner. Organic solar cells with carbon nanotube network electrodes. *Applied Physics Letters*, 88:233506, 2006.

[97] Bryan B. Sauer and Gregory T. Dee. Molecular weight and temperature dependence of polymer surface tension: comparison of experiment with theory. *Macromolecules*, 24(8):2124–2126, 1991.

[98] Leonard S. Schaer. Rubber-mold spin-casting for low-cost prototype or production parts. *Machine Design*, 49(2):113–117, 1977.

[99] K. Shah, W. C. Shin, and R. S. Besser. A PDMS micro proton exchange membrane fuel cell by conventional and non-conventional microfabrication techniques. *Sensors and Actuators B: Chemical*, 97(2-3):157–167, 2004. printed on 5/23/07.

[100] Eric A. Sheard. Removing bubbles from castable liquid polyurethane raw materials. *Elastomerics*, 122(10):49–50, 1990.

[101] Y. S. Shin, K. Cho, S. H. Lim, S. Chung, S. J. Park, C. Chung, D. C. Han, and J. K. Chang. PDMS-based micro PCR chip with Parylene coating. *Journal of Micromechanics and Microengineering*, 13(5):768–774, 2003.

[102] S. K. Sia and G. M. Whitesides. Microfluidic devices fabricated in poly(dimethylsiloxane) for biological studies. *Electrophoresis*, 24(21):3563–3576, 2003.

[103] A. Singh, B. D. Freeman, and I. Pinnau. Pure and Mixed Gas Acetone/Nitrogen Permeation Properties of Polydimethylsiloxane (PDMS). *J.Polym.Sci.Part B.Polym.Phys*, 36:289–301, 1998. printed on 5/23/07.

[104] F.L. Smith and A.H. Harvey. Avoid common pitfalls when using Henry's Law. *Chemical Engineering Progress*, 103(9):33–39, 2007.

[105] A. G. Spence and R. J. Crawford. Removal of pinholes and bubbles from rotationally moulded products. *Proceedings of the Institution of Mechanical Engineers, Part B: Journal of Engineering Manufacture*, 210:521–533, 1996. .

[106] C. D. Spencer. Centrifugal casting of thermoplastics. *Society of Plastics Engineers - Journal*, 18(7):774–779, 1962.

[107] T. Thorsen, S. J. Maerki, and S. R. Quake. Microfluidic large-scale integration. *Science*, 298(5593):580–584, 2002 2002.

[108] A. Tourovskaia, X. Figueroa-Masot, and A. Folch. Long-term microfluidic cultures of myotube microarrays for high-throughput focal stimulation. *Nature a-z index*, 1(2):1092–1104, 2006.

[109] Y. C. Tung, M. Zhang, C. T. Lin, K. Kurabayashi, and S. J. Skerlos. PDMS-based opto-fluidic micro flow cytometer with two-color, multi-angle fluorescence detection capability using PIN photodiodes. *Sensors and Actuators B: Chemical*, 98(2-3):356–367, 2004.

[110] M. A. Unger, H. P. Chou, T. Thorsen, A. Scherer, and S. R. Quake. Monolithic microfabricated valves and pumps by multilayer soft lithography. *Science*, 288(5463):113–116, 2000.

[111] J. A. van Kan, L. P. Wang, P. G. Shao, A. A. Bettiol, and F. Watt. High aspect ratio PDMS replication through proton beam fabricated Ni masters. *Nuclear Instruments and Methods in Physics Research Section B: Beam Interactions with Materials and Atoms*, 260(1):353–356, 2007.

[112] G. Vozzi, C. Flaim, A. Ahluwalia, and S. Bhatia. Fabrication of PLGA scaffolds using soft lithography and microsyringe deposition. *Biomaterials*, 24(14):2533–2540, 2003.

[113] Giovanni Vozzi, Christopher J. Flaim, Francesca Bianchi, Arti Ahluwalia, and Sangeeta Bhatia. Microfabricated PLGA scaffolds: a comparative study for application to tissue engineering. *Materials Science and Engineering: C,*, 20(1-2):43–47, 5/31 2002.

[114] G.M. Whitesides. The origins and the future of microfluidics. *Nature*, 442(7101):368–373, 2006.

[115] E. Wong, V. Hong, A.D. Mazzeo, and J.H. Chun. Polydimethylsiloxane (PDMS) shrinkage for the manufacturing of microfluidic devices. In *In Proceedings of the 5th International Symposium on Nanomanufacturing (ISNM)*, 2008.

[116] S. Wu. *Polymer Interface and Adhesion.* Marcel Dekker, Inc., 1982.

[117] S. Wu. *Surface and Interfacial Tension of Polymers, Oligomers, Plasticizers, and Organic Pigments*, pages 521–540. Polymer Handbook (4th Edition). John Wiley & Sons, 2005.

[118] Y. Xia, J. J. McClelland, R. Gupta, D. Qin, X. M. Zhao, L. L. Sohn, R. J. Celotta, and G. M. Whitesides. Replica molding using polymeric materials: A practical step toward nanomanufacturing. *Advanced Materials*, 9(2):147–149, 1997.

[119] Y. Xia, J. Tien, D. Qin, and G. M. Whitesides. Non-photolithographic methods for fabrication of elastomeric stamps for use in microcontact printing. *Langmuir*, 12(16):4033–4038, 1996.

[120] Younan Xia and George M. Whitesides. Soft Lithography. *Annual Review of Materials Science*, 28(1):153–184, 1998.

[121] L. Xu and R. J. Crawford. Analysis of the formation and removal of gas bubbles in rotationally moulded thermoplastics. *Journal of Materials Science*, 28(8):2067–2074, 1993.

[122] E. Zana and L. G. Leal. Dissolution of a stationary gas bubble in a quiescent, viscoelastic liquid. *Industrial & Engineering Chemistry Fundamentals*, 14(3):175–182, 1975.

[123] Jun Zhang, Mary B. Chan-Park, and Samuel R. Conner. Effect of exposure dose on the replication fidelity and profile of very high aspect ratio microchannels in SU-8. *Lab on a Chip*, 4:646–653, 2004.